Purdue University

Purdue e-Pubs

5-2018

Novel Multiphysics Phenomena in a New Generation of Energy Storage and Conversion Devices

Arpan Kundu
Purdue University

Recommended Citation

NANOSCALE MULTIPHYSICS PHENOMENA FOR A NEW GENERATION OF

ENERGY STORAGE AND CONVERSION DEVICES

A Dissertation

Submitted to the Faculty

of

Purdue University

by

Arpan Kundu

In Partial Fulfillment of the

Requirements for the Degree

of

Doctor of Philosophy

May 2018

Purdue University

West Lafayette, Indiana

THE PURDUE UNIVERSITY GRADUATE SCHOOL
STATEMENT OF DISSERTATION APPROVAL

Dr.Timothy S. Fisher, Chair

    School of Mechanical Engineering

Dr.Xiulin Ruan

    School of Mechanical Engineering

Dr.Supriyo Datta

    School of Electrical and Computer Engineering

Dr.Ali Shakouri

    School of Electrical and Computer Engineering

Approved by:

    Dr. Jay P. Gore

        Head of Graduate Program, School of Mechanical Engineering

To my loving and caring mother

ACKNOWLEDGMENTS

I feel extremely fortunate to have had the opportunity to work under the able guidance of Prof. Timothy S. Fisher during my doctoral study. This dissertation would not have taken shape without his continuous encouragement and advice. Despite his overarching vision towards dreaming big, he always provided me the freedom to pursue the research topics of my choice. His consolation and mental support proved to be most valuable to me during times when my experiments turned out to be futile and I seeked his permission towards pursuing other research projects. He is very supportive and always makes himself available for his students, despite his several responsibilities.

Furthermore, I would like to express my gratitude towards my collaborators. I really enjoyed working with Prof. Ali Shakouri and Dr. Kerry Maize who helped me in validating my circuit model to experimental results on electroreflectance imaging and guided me for the entire duration of the project. I am also thankful to Prof. Laurent Pilon, Jeep Ampol and Obaidallah Munteshari for sharing their thermal measurements on my supercapacitor samples. Furthermore, I would like to express my gratitude towards Prof. Supriyo Datta who has helped me hone my presentation skills and communicate effectively with the audience while presenting my work. I must also thank Prof. Xiulin Ruan and Prof. Amy Marconnet for their guidance on teaching ME315 for the first time as a Lambert fellow. In addition, I thank my fellow members of the research group, past and present with whom I have had many fruitful discussions on research topics as well as graduate life. I would like to particularly thank Sridhar, Ishan, Kim, Anurag, Majed, Yuan, Brian, Rajat, Aaditya, Pingge, Kwesi, Joel, Guoping, Ritu, Rajib, Anurup, Aniruddha, Rahul for their help and their time spent with me. Last, but not the least, I would like to thank my parents and God Almighty whose blessings have blossomed in the form of this work.

TABLE OF CONTENTS

LIST OF TABLES

LIST OF FIGURES

Figure   Page

ABSTRACT

Kundu, Arpan PhD, Purdue University, May 2018. Nanoscale Multiphysics Phenomena For a New Generation of Energy Storage and Conversion Devices. Major Professor: Timothy S. Fisher.

The swelling demand for storing and using energy at diverse scales has stimulated the exploration of novel materials and design strategies applicable to energy storage systems. The most popular electrochemical energy storage systems are batteries, fuel cells and capacitors. Supercapacitors, also known as ultracapacitors, or electrochemical capacitors have emerged to be particularly promising. Besides exhibiting high cycle life, they combine the best attributes of capacitors (high power density) and batteries (high energy storage density). Consequently, they are expected to be in high demand for applications requiring peak power such as hybrid electric vehicles and uninterruptible power supplies (UPS). This dissertation aims to make advancements on the following two topics in supercapacitor research with the aid of modeling and experimental tools: applying various thermophysical effects to design supercapacitor devices with novel functionalities and studying degradation mechanisms upon continuous cycling of conventional supercapacitors.

The prime drawback of conventional supercapacitors is their low energy density. Most research in the last decade has focused on synthesizing novel electrode materials. Although such novel electrodes lead to high energy density, they often involve complicated synthesis process and result in high cost and low power density. A new concept of inducing pseudocapacitance developed in recent years is by introducing redox additives in the electrolyte that engage in redox reactions at the electrode/electrolyte interface during charge/discharge. The first section of this dissertation reports the performance of fabricated solid-state supercapacitors composed

of redox-active gel electrolyte (PVA-K3Fe(CN)6-K4Fe(CN)6). The electrochemical performance has been studied extensively using cyclic voltammetry, constant current charge/discharge and impedance spectroscopy techniques, and then the results are compared with similar devices composed of conventional gel electrolytes such as PVA-H3PO4 and PVA-KOH on the basis of capacitance, internal resistance and stable voltage window.

The second section explores the utility of the thermogalvanic property of the same redox-active gel electrolyte, PVA-K3Fe(CN)6-K4Fe(CN)6 in the construction of a thermoelectric supercapacitor. The integrated device is capable of being electrically charged by applying a temperature gradient across its two electrodes. In the absence of available temperature gradient, the device can be discharged electrically through an external circuit. Therefore, such a device can be used to harvest waste heat from intermittent heat sources. An equivalent circuit elucidating the mechanisms of energy conversion and storage applicable to thermally chargeable supercapacitors is developed. A fitting analysis aids in the evaluation of model circuit parameters providing good agreement with experimental voltage and current measurements.

The latter part of the dissertation investigates the factors influencing aging in conventional supercapacitors. In the first part, a new imaging technique based on the electroreflectance property of gold has been developed and applied to characterize the aging characteristics of a microsupercapacitor device. Previous aging studies were performed through traditional electrical characterization techniques such as cyclic voltammetry, constant charge/discharge, and electrochemical impedance spectroscopy. These methods, although simple, measure an average of the structures' internal performance, providing little or no information about microscopic details inside the device. The electroreflectance imaging method, developed in this work is demonstrated as a high-resolution imaging technique to investigate charge distribution, and thus to infer aging characteristics upon continuous cycling at high scan rates. The technique can be used for non-intrusive spatial analysis of other electrochemical systems in the future. In addition, we investigate heat generation mechanisms

that are responsible for accelerated aging in supercapacitors. A modeling framework has been developed for heat generation rates and resulting temperature evolution in porous electrode supercapacitors upon continuous cycling. Past thermal models either neglected spatial variations of heat generation within the cell or considered electrodes as flat plates that led to inaccuracies. Here, expressions for spatiotemporal variation of heat generation rate are rigorously derived on the basis of porous electrode theory. Detailed numerical simulations of temperature evolution are performed for a real-world device, and the results resemble past measurements both qualitatively and quantitatively.

In the last chapter of the thesis, a rare thermoelectric effect called the Nernst effect has been investigated in single-layer periodic graphene with the aid of a modified Boltzmann transport equation. Detailed formulations of the transport coefficients from the BTE solution are developed in order to relate the Nernst coefficient to the amount of impurity density, temperature, band gap and applied magnetic field. Detailed knowledge of the variation of the thermoelectric and thermomagnetic properties of graphene shown in this work will prove helpful for improving the performance of magnetothermoelectric coolers and sensors.

1. INTRODUCTION

Some of the material in this chapter has been published in

SpringerBriefs in Thermal Engineering and Applied Science [1]

1.1 Electrical Energy Systems

With growing energy demands and the looming depletion of fossil fuels, electrical energy storage (EES) systems are under aggressive development for current and future renewable energy needs [2]. EES systems with high energy and power density values are required to meet the energy requirements of hybrid electric vehicles (HEVs) and portable electronic devices such as mobile phones and laptops. The major types of EES systems are batteries, capacitors, fuel cells, and their combinations which are summarized in Fig. 1.1.
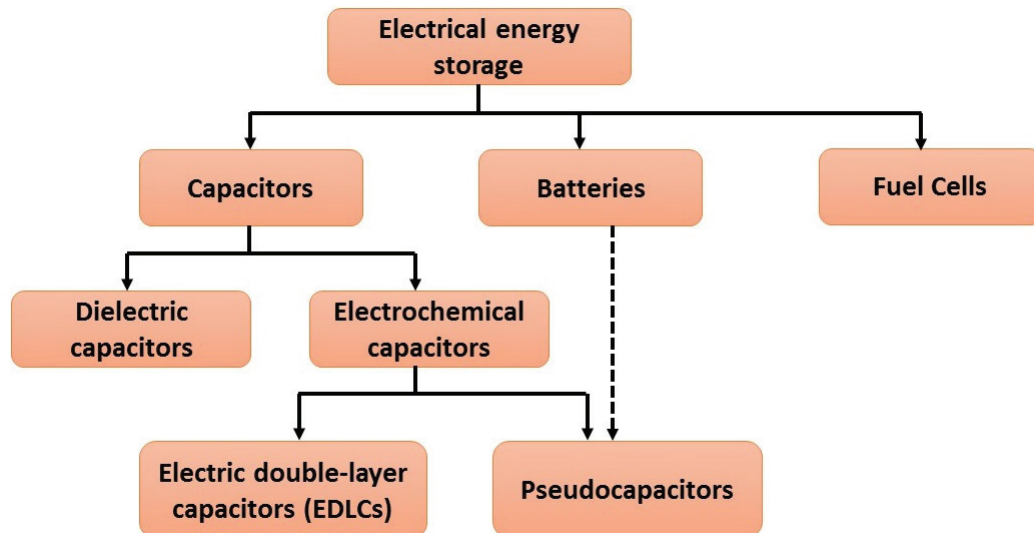
Fig. 1.1. Types of Electrical Energy Storage Systems.

Batteries store electrical energy via faradaic reactions at the interface of the electrode and electrolyte. A typical example of battery is lithium ion battery which is composed of lithium nickel manganese oxide ($LiMn_2O_4$) cathode, graphite anode and a lithium salt in the electrolyte. During charge, the lithium ions migrate to the negative electrode, while during discharge, they migrate to the positive electrode. Dielectric capacitors on the other hand, store charge electrostatically within two electrodes separated by a dielectric material. Finally, fuel cells use a continuous stream of hydrogen fuel and oxygen to sustain an electrochemical reaction that generates electricity.
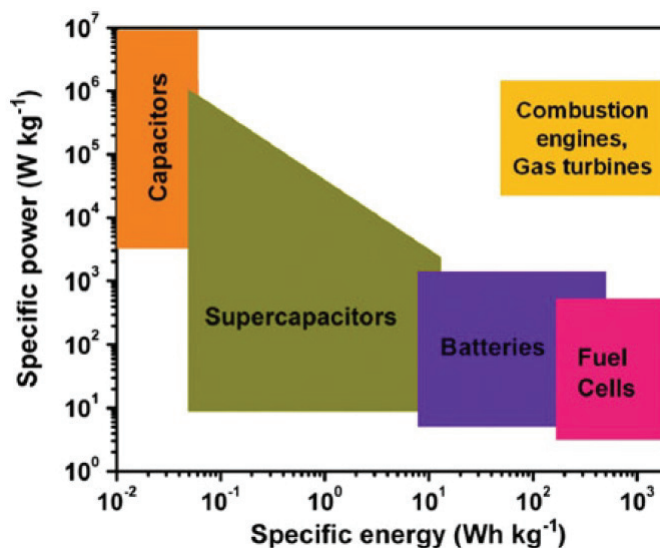
Fig. 1.2. Ragone plot of different major energy storage systems.

The prime performance metrics for comparing these technologies are reliability, power and energy density, cycle-life, temperature range and emission of pollutants. Batteries and capacitors are closed systems with anodes, cathodes and separators that are soaked with electrolytes and sealed in a single compartment. Conversely in fuel cells, the fuel, consisting of hydrogen at the anode and oxygen at the cathode, is supplied from a tank. Fig. 1.2 provides a Ragone plot that compares different electrochemical energy storage systems to internal combustion engines and turbines, and

electrolytic capacitors. As apparent from the simplified Ragone plot, supercapacitors bridge the gap between conventional electrolytic capacitors and batteries in terms of specific energy and power densities. The terms specific energy (Wh kg^{-1}) and energy density (Wh L^{-1}) are generally used to assess energy storage systems, whereas their rate capability is represented by specific power (W kg^{-1}) or power density (W L^{-1}).
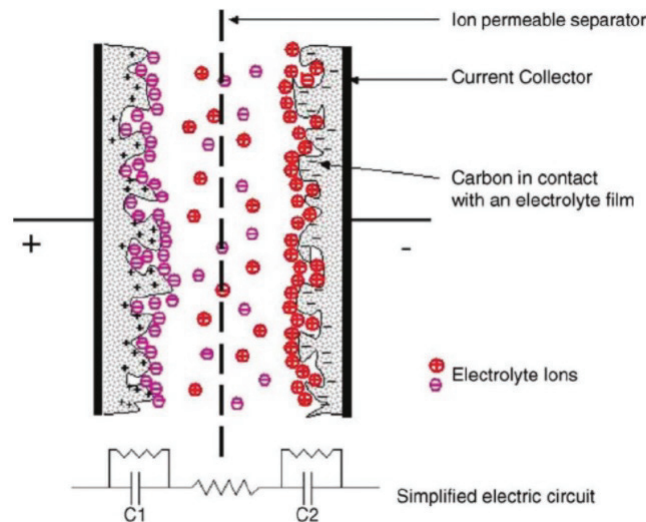
Fig. 1.3. Schematic of an electrochemical double layer capacitor based on porous electrode materials [3]

1.2 Supercapacitors

Supercapacitors are referred to as electric double-layer capacitors (EDLCs), electrochemical capacitors, electrochemical supercapacitors, and ultracapacitors. The concept of supercapacitors derives from conventional electrolytic capacitors, which consist of two electrically conducting plates or electrodes separated by a dielectric such as air, glass or ceramic. The plates hold equal and opposite charge on their opposing faces, and the dielectric composition develops an electric field. The capacitance (C) is,

$$C = \frac{\epsilon_0 \epsilon_r A}{d} \tag{1.1}$$

where ϵ_0 is the permittivity of vacuum 8.85×10^{-12} F m^{-1}; ϵ_r is the relative permittivity of the dielectric, A is the cross-section area of the conducting plate, and d is the distance between the plates. Unlike electrolytic capacitors, charge in supercapacitors is stored at the interface between an electrode and an electrolyte, in which case each electrode-electrolyte interface represents a capacitor. Consequently, a two-terminal supercapacitor device is equivalent to two conventional capacitors in series. Supercapacitors bridge the gap between batteries by featuring higher energy density but lower power density and conventional capacitors that offer higher power density but relatively low energy density. They are termed super because of the high surface area (A) of their electrodes (e.g., porous carbon with a specific surface area of 2000-3000 m^2 g^{-1}), and the very small separation distance (d) between the positive and negative charge, on the order of Angstroms. The advantages of supercapacitors include high power density, low maintenance and long cycle life. Comprehensive reviews of supercapacitor fundamentals are provided in Ref. [4].

Supercapacitors can be classified into two main types based on their working mechanisms [4]: (i) Electric double-layer capacitors (EDLCs): Energy is stored through physical ion adsorption. Charge accumulation is achieved with electrostatically positive and negative charge separately residing in a Helmholtz double layer at the boundary between an electrolyte and a conductor electrode. The charge transfer is non-faradic without redox reactions taking place within or across the electrode interface as shown in Fig. 1.3. EDLCs typically exhibit rapid cycling, longer cycle life and higher coulombic efficiencies than batteries. (ii) Pseudocapacitors: Energy is stored through fast redox reactions at the interface between the electrolyte and electroactive materials. Charge transfer is faradic in nature. Pseudocapacitors have higher energy density compared to EDLCs, but they suffer from lower cycleability due to quasi-reversible redox reactions during the cyclic charge and discharge processes. Pseudocapacitors typically consist of metal oxides (e.g., MnO_2, RuO_2, and Fe_2O_3) or conducting polymers coated on porous electrodes (typically porous carbon). The primary challenges supercapacitor manufacturers now face are to improve energy density and reduce fab-

rication costs without sacrificing power, cycle life and safety. The energy density of typical supercapacitors is limited to several watt hours per kilogram, which cannot meet the requirements of hybrid vehicles, and consequently they have been used as ancillary components in battery systems that require short power bursts. To resolve this issue, extensive efforts have been dedicated to further enhance the overall performance by adopting new nanostructures for electrodes, new types of electrolytes and innovative structural designs. For instance, ionic liquid electrolytes with a large voltage window ($\geq$4 V) are promising potential replacements of currently used organic electrolytes [5], which possess an operational voltage window of 2.7 V.
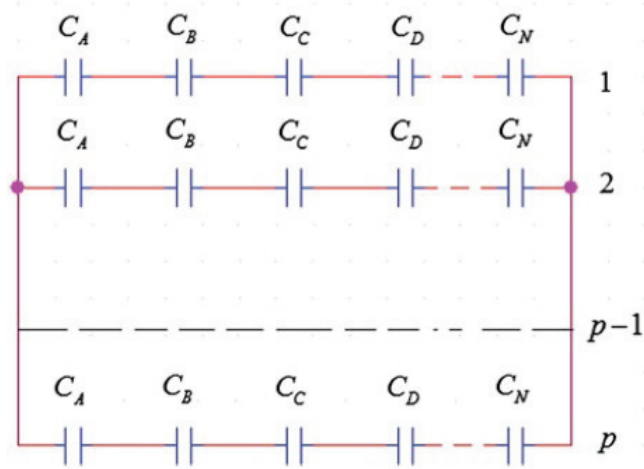
Fig. 1.4. Equivalent circuit of a supercapacitor stack

The maximum operating voltage and charge storage capacity of a single supercapacitor cell is quite low, and therefore a large number of cells are generally connected to form a stack that meets the requirements of voltage and current in a particular application. In most cases, the input parameter is the stored energy W_{max} and the equivalent capacitance of the stack C_{eq}. A schematic of a supercapacitor stack is shown in Fig. 1.4. The maximum stored energy W_{max} is,

$$W_{max} = \frac{C_{eq}V^2}{2} \tag{1.2}$$

The number of series-connected cells in a stack N_s (C_A, C_B,.C_N) is,

$$N_s = \frac{V_{max}}{V_{cell}} \tag{1.3}$$

where V_{max} is the maximum voltage of the supercapacitor stack, and V_{cell} is the nominal voltage of each supercapacitor cell. The number of parallel branches N_p is,

$$N_p = \frac{N_s C_{eq}}{C_{cell}} \tag{1.4}$$

The total number of cells in the supercapacitor stack (N_t) is,

$$N_t = N_s N_p \tag{1.5}$$

Thermal analysis and management of supercapacitors is also critical for practical applications. Operating supercapacitors at off-design temperatures for long durations leads to safety, reliability and performance issues. Therefore, it is essential to understand the temperature variation in supercapacitors during their operation, from both experimental and theoretical analyses. Supercapacitor temperatures typically increase during charge and discharge processes due to Joule heating. Heat dissipation occurs by conduction within the cell and by convection and radiation from the capacitor wall to the ambient. The amount of Joule heating is related to the charging current and the electrical resistance of the cell. Apart from internal heat generation, capacitor temperatures also depend on the ambient temperature especially if they operate under extreme temperature conditions. Typical high temperature applications include military applications and underground drilling. Another common example is capacitor banks used in hybrid electric vehicles that may heat up by a nearby combustion chamber [6]. Cold temperature applications include cold cranking in vehicles and space missions. The performance of supercapacitors under such extreme conditions is quite different from their rated performance. Thus, understanding thermal influences on supercapacitor performance with regard to capacitance and cycle-life is of vital significance for their use in various applications.

Prolonged use of supercapacitors leads to aging, i.e., deterioration in performance. The aging of supercapacitors occurs at different rates for different electrode and electrolyte materials, and is a function of cycling parameters (maximum voltage, number

of cycles and duty cycle). Hence, understanding the decomposition mechanisms leading to aging is essential for estimating their aging rate and lifetime [6]. Such analyses can aid in the design of appropriate thermal management systems, and hence alleviate safety issues in practical operation. In recent years, much progress in supercapacitors has been accomplished from both experimental and theoretical perspectives, showing great promise to complement or replace batteries in energy conversion and storage applications [7].

Commercial Supercapacitors

Supercapacitors typically possess a long-term life of millions of charge/discharge cycles and a low equivalent internal series resistance, allowing them to provide much higher power than battery packs of similar total energy ratings. Although ultracapacitor packs are relatively more expensive and store less energy per unit mass compared to batteries, they are expected to last the life of electric vehicles and are found to provide more fuel-efficient power in heavy electrical applications (e.g., automotive, hybrid transport). Combining supercapacitors with batteries can enhance performance in hybrid electric vehicles, including more powerful acceleration, braking energy recovery, outstanding cold-weather starting and increased overall system life. For instance, pulsed power during startups to reduce the duty cycle on a battery prolongs battery life, which can dramatically reduce battery replacement costs and improve reliability in vehicles. Because of their outstanding recharging capability and reasonable energy density, they provide applications such as automotive, heavy transportation, marine and traction with reliable engine starting over a wider temperature range than batteries. Commercial supercapacitors have been successfully used in many applications such as electrical vehicles (EVs) and hybrid electric vehicles (HEVs) for capturing and storing energy from regenerative braking and supplying vehicle acceleration power. For instance, supercapacitors are rapidly recharged at bus stops with charging stations to power EV buses in Shanghai, and supercapacitor

modules are used as a power buffer in Honda fuel cell cars, which can respond to rapid changes in power in a few seconds. The excellent low-temperature performance of supercapacitor modules makes them appealing to replace batteries as power supplies for cold cranking trucks in freezing weather, because batteries usually cannot provide enough power required to start the engine, whereas supercapacitors exhibit reliable performance even down to -40 °C. Supercapacitors with excellent low temperature performance can easily satisfy the power needs in extreme weather conditions in heavy electrical applications. The automotive sector is now a steady source of revenue for supercapacitor manufacturers. Moreover, supercapacitors are also used in wind turbine pitch control, rail, and heavy industrial equipment.

1.3 Electrode and Electrolyte Materials for Supercapacitors

1.3.1 Electrode Materials

Conventional supercapacitor electrodes usually consist of active electrode material (e.g., activated carbon), binder and conducting agent (e.g., carbon black). Each of the components makes contribution to the electrochemical performance in terms of specific capacitance, rate capability, and cycle life. High specific surface area, high electrical conductivity and good electrolyte accessibility to intra-pore regions are usually the qualities of a high-performance supercapacitor electrode. Apart from those requirements to ensure good electrochemical performance, other qualities such as good thermal stability and high thermal conductivity are also essential to determine thermal performance of the supercapacitors in practical applications, especially in extreme temperature conditions. In order to attain both high power and energy density, the constituent electrode materials should be capable of undergoing rapid, reversible redox reactions.The most common pseudocapacitive electrode materials used in the past are metal oxides such as MnO_2, RuO_2, VO) . Although RuO_2 exhibits high specific capacitance (720 F g^{-1}), its high cost prohiibts commercialization. On the other, MnO_2 has attracted much attention as a pseudocapacitive electrode mate-
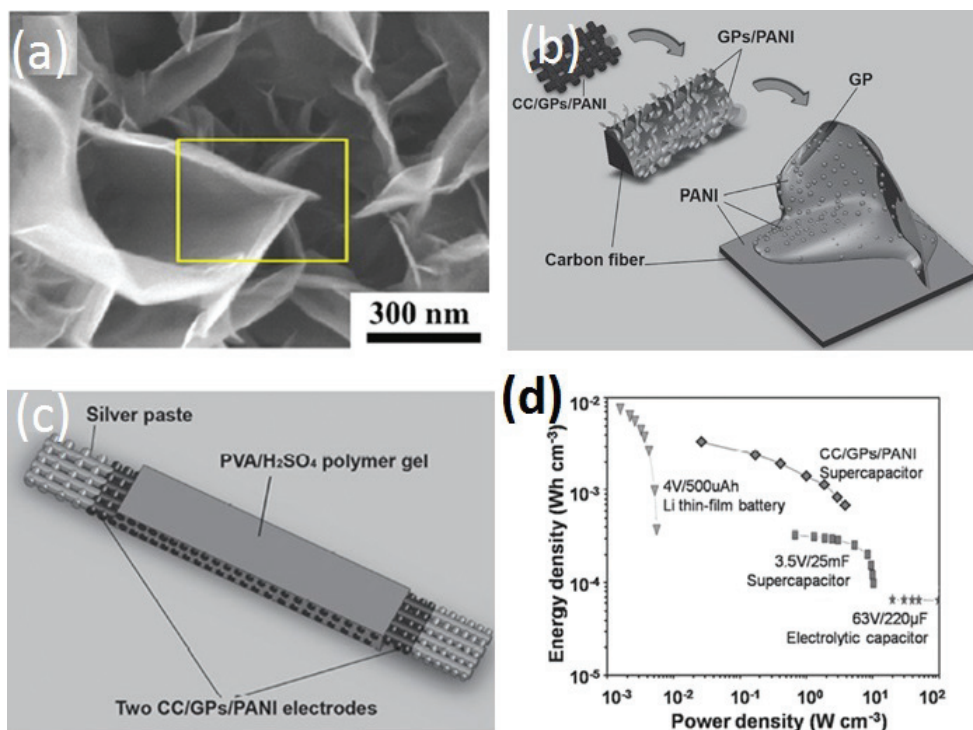
Fig. 1.5. (a) Buckypaper(BP)/MnO$_2$ electrode [8] (b) Polyaniline coated on graphene petals on top of carbon cloth (CC/GP/Pani) (c) A symmetric two-terminal device composed of CC/GP/Pani device and (d) Ragone plot comparing the performance of the fabricated device with the state-of-the-art [9]

rial due to its low cost, low toxicity, and high theoretical specific capacitance (1370 F g^{-1}). On the flip side, its poor electric conductivity prevents realization of high theoretical capacitance. Electrically conducting polymers such as polypyrrole (PPy), polyaniline (PANI) and polythiophene (PTP) are generally used as pseudocapacitive materials to boost energy and power density. Fig. 1.5 displays a snapshot of the several types of pseudocapacitive electrodes employed in the past to fabricate high performance supercapacitors.

1.3.2 Electrolyte Materials

The electrolytes used in supercapacitors can be classified into 4 major categories namely organic electrolytes, aqueous electrolytes, ionic liquids and polymer gel eelctrolytes. Fig. 1.6 maps the electrochemical performance and thermal stability of the various types of electrolytes in a radar plot.

Organic Electrolytes

Organic electrolytes possess a relatively large operational potential window and high ionic conductivity, but face shortcomings of high viscosity, cost and volatility. The most commonly used organic solvents in commercial supercapacitors are propylene carbonate (PC), acetonitrile (ACN), and dimethyl carbonate (DMC). Organic electrolytes based on ACN and PC solvents are limited to a potential window of about 2.7 V, but their conductivity of about 100 mS cm^{-1} comes close to aqueous electrolytes such as sulfuric acid (850 mS cm^{-1}) and potassium hydroxide (620 mS cm^{-1}).

Aqueous Electrolytes

Aqueous electrolytes possess high ionic conductivity of the order of 1 S cm^{-1}. Supercapacitors based on aqueous electrolytes usually exhibit higher capacitance than other types of electrolytes because of many reasons. Apart from high ionic conductivity, small solvated ion size in aqueous electrolytes makes it easier for them to penetrate into small pores leading to higher charge storage compared to organic electrolytes [43]. Aqueous electrolytes exhibit advantages in terms of high ionic conductivity, low cost, non-flammability and environmental benignity, which makes supercapacitors based on aqueous electrolytes attractive. However, some operational difficulties are associated with the aqueous electrolytes: (i) Supercapacitors based on aqueous electrolytes can be operated to 1 V because of the limitation by the decomposition voltage of
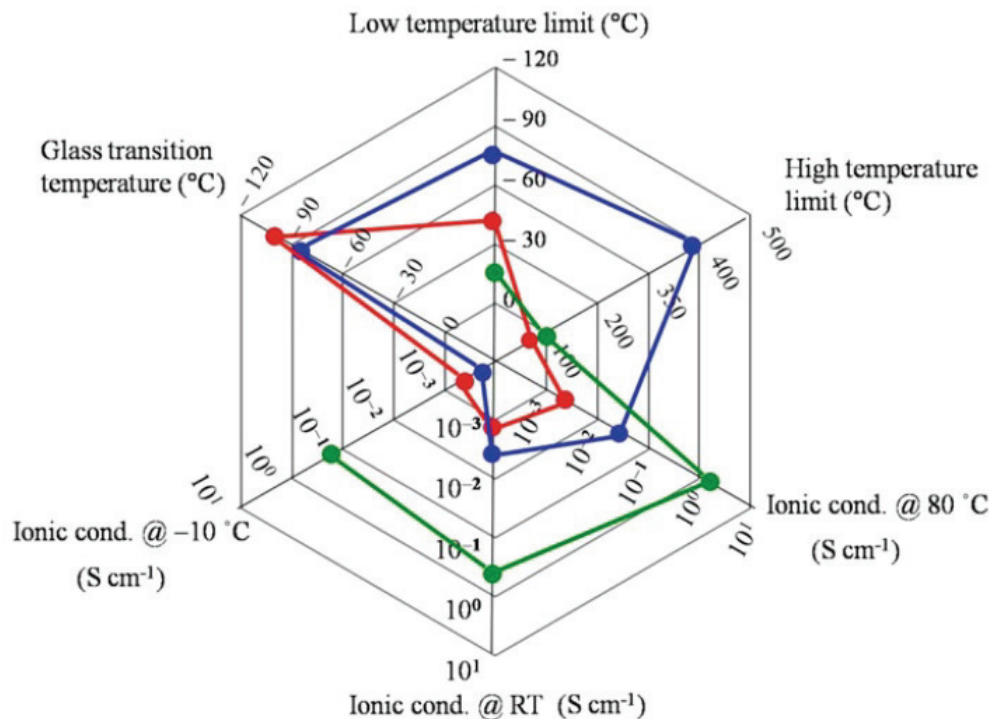
Fig. 1.6. Comparative radar plots of the thermophysical properties of organic (red), aqueous (green) and ionic liquid (blue) electrolytes. A data point is not plotted in the green curve, indicating that the information about that category is unavailable in the reference.

water ($\approx$ 1.23 V [41]), except for asymmetric supercapacitors, the operational voltage window of which can be extended to 2 V. Asymmetric supercapacitors employ a pseudocapacitive (e.g., MnO_2) positive electrode that relies on faradaic reactions for charge storage and a high-surface-area carbon as a negative electrode. These low-cost aqueous electrolyte-based asymmetric supercapacitors could potentially satisfy the power and energy demands of practical applications. However, they also face potential problems such as gas evolution during charge/discharge processes. Such problems might be avoided or mitigated by adding alternative catalysts to the system or using carbon materials as catalysts for water recombination. (ii) The choice of current collectors used in aqueous electrolytes is limited to several metal materials (e.g., stainless steel, nickel, Pt, and Au) to avoid the corrosion of these metals during

charge/discharge processes. Corrosion of the current collectors in aqueous electrolytes should be minimized to ensure good long-term cycling performance. These current collectors are generally heavier and more costly than the thin (25 μm) aluminum foil current collectors used in non-aqueous supercapacitors.

Ionic Liquids

Ionic liquids (ILs) are low-temperature molten salts (composed of only ions) with a large liquid range. ILs with melting temperature and glass transition temperature below room temperature are called room-temperature ionic liquids (RTILs). They are attracting extensive interest as electrolytes in supercapacitors because of their low flammability, low volatility, low corrosivity, high chemical and electrochemical stability, large voltage window ($\geq$3.5 V) and wide temperature range. Moreover, the use of neat ILs facilitates device flexibility and packaging because of the absence of any solvent. However, IL electrolytes face many drawbacks such as high viscosity and low ionic conductivity (10^{-5} S cm^{-1}) at room temperature. Increasing amount of work has been reported on exploring the potential of using such electrolytes in commercial products, particularly at high temperatures.

The viscosity and ionic conductivity of IL electrolytes have been discussed in prior work. Their room temperature ionic conductivity generally lies between 10^{-3} and 10^{-2} S cm^{-1} with some even comparable to that of aqueous electrolytes. Their ionic conductivity is generally low at room temperatures. Their enhanced ionic conductivity at high temperatures (typically above 60 °C) renders them favored candidates in high-temperature applications.

Polymer Gel Electrolytes

A polymer electrolyte is generally a mixture of a gel agent, solute and a solvent. Based on the type of solute and solvent that is spread into polymer matrix, polymer electrolytes can be classified as organic solvent-containing, water-containing (includ-

ing acidic, neutral and alkaline solute), and IL-containing electrolytes. The most common polymer matrices in electrochemical energy devices are polyvinyl alcohol (PVA), polyacrylonitrile (PAN), polyvinyl chloride (PVC), polyvinyl sulfone (PVS), polyvinyl pyrrolidinone (PVP), polyethylene glycol diacrylate (PEGDA), polymethyl methacrylate (PMMA), and polyvinylidene fluoride (PVdF). Solid-state polymer gel electrolytes hold some distinct advantages over their liquid counterparts such as reduced leakage, improved safety, better shape versatility, lightness and better manufacturing integrity. Moreover, their unique bifunctional role as both electrolyte and separator requires no additional separator materials.

Polymer electrolyte-based supercapacitors primarily find applications in consumer electronics, micro-electronics, and wearable or printable electronics because of their high reliability, ease of handling, scalability, good electrochemical and chemical stability, flexibility, and wide operating temperature range. Polymer gel electrolytes can be applied into many supercapacitor structures such as sandwich, interdigitated, coaxial fiber, and braided cells. The advantage of solidstate/ polymer gel electrolytes have been addressed in prior work. However, typical polymer electrolytes such as anhydrous protonic electrolytes PEO/H_3PO_4 or PVP/H_3PO_4 possess a relatively low ionic conductivity of 10^{-6} to 10^{-5} S cm^{-1} at 25 °C. Thermal stability and ionic conductivity of the polymer electrolytes need to be further improved in order meet the requirements in practical applications. Much work has been reported on lithium-conducting polymer electrolytes prepared by immobilizing various lithium salts in a polymer matrix and solid-state lithium ion conductors. Although possessing a wide electrochemical voltage window, those electrolytes generally exhibit a relatively low ionic conductivity. New IL electrolytes for lithium ion batteries are being developed intensely in many industrial and academic laboratories. Many popular concepts of fabricating high-performance of polymer electrolytes for lithium ion batteries can be applied in supercapacitor polymer electrolyte fabrications.

1.3.3 Redox Electrolytes

An innovative approach to boost the energy density of supercapacitors is by introducing redox species in the electrolyte. As displayed in Fig. 1.7, the redox species undergo oxidation at the positive electrode and reduction at the negative electrode thereby inducing pseudocapacitance. Prior studies have demonstrated enhanced performance by incorporating redox additives such as hydroquinone [10, 11], p-phenylenediamine [12], KI [13–16], Na_2MoO_4 [17] and $K_3Fe(CN)_6$ [18] in the electrolyte.
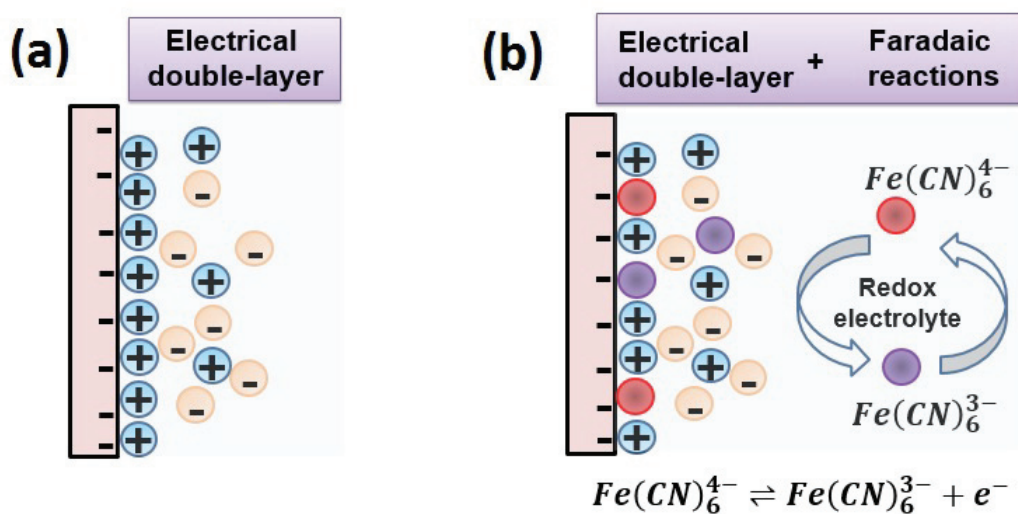
Fig. 1.7. (a) Schematic of energy storage mechanisms in a pure double-layer electrolyte system (b) Schematic of energy storage mechanisms in a redox-active electrolyte system

1.4 Thermo-Electrochemical Cells for Waste Heat Harvesting

Apart from research into energy storage systems, substantial work is ongoing in harvesting waste heat and directly converting thermal energy from sources such as industrial waste streams, solar heat to electrical energy. This section presents an introduction to the various thermo-electrochemical energy conversion methods used for waste heat harvesting.

1.4.1 Liquid-based Thermoelectric Generator

The conventional method to convert thermal to electrical energy is through solid-state thermoelectrics. They work on the principle that electronic charge carriers in a semiconductor thermodiffuse when subjected to a temperature gradient which leads to a thermo-voltage called the Seebeck voltage. A plethora of materials including semi-metals, inorganic semiconductors, and electronically conducting polymers have been explored for use in such applications. However, such devices suffer from drawbacks such as high cost, intrinsically low Seebeck coefficient (10-100 mV/K) and rigid structure. Alternative thermoelectric conversion techniques are thus being explored using temperature dependence of voltage in a liquid electrochemical cell. Such a dependence is known to primarily originate from two types of phenomenon depending upon the choice of the electrolyte, namely the thermogalvanic effect and the Soret effect. Their operating principles differ slightly from solid-state thermoelectrics in which electrons are the charge carriers through the entire circuit.

1.4.2 Soret Effect

Soret effect is the phenomenon observed in a mixture of ions where the different types of ions exhibit different mobilities upon application of a temperature gradient. This effect has been found to lead to a thermovoltage for electrolytes such as polystyrene sulfonic acid (PSSH) [2] and polyethylene oxide-sodium hydroxide (PEO-

NaOH) [3] with Seebeck coefficients of 7.9 mV/K and 11 mV K^{-1} respectively. For an electrochemical cell composed of PSSH electrolyte, a temperature gradient across the two electrodes leads to diffusion of mobile H$^+$ to the cold side, while leaving less mobile PSS behind. An excess of H$^+$ ions near the cold electrode leads to the formation of an electric double layer which results in an open-circuit voltage that can be described using the Nernst equation:

$$E_{cell} = E_{cell}^0 - \frac{RT}{F} ln \frac{[H_{hot}^+]}{[H_{cold}^+]} \tag{1.6}$$

where E_{cell}° is the potential difference between the cold and hot electrodes, E_{cell} is
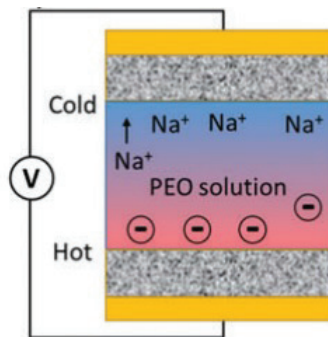
Fig. 1.8. Soret effect in polyethylene oxide (PEO)-NaOH electrolyte [19]

the standard cell potential for the two electrodes, $[H_{hot}^+]$ and $[H^+{}_{cold}]$ are the molar concentration close to the hot and cold electrodes respectively, R is the universal gas constant, T is the temperature and F is the Faraday constant. The schematic of the phenomenon is displayed in Fig. 1.8.

1.4.3 Thermogalvanic Effect

Thermogalvanic effect is caused by a temperature-dependent entropy change during electron exchange between a redox ion and the electrode surface. The electrochemical Seebeck coefficient S for a hypothetical reaction B→A+ne$^-$ is given by

$$S = \frac{\partial V}{\partial T} = \frac{\Delta s_{B,A}}{nF} \tag{1.7}$$

where V is the electrode potential, T is the temperature, $\Delta s_{B,A}$ is the reaction entropy
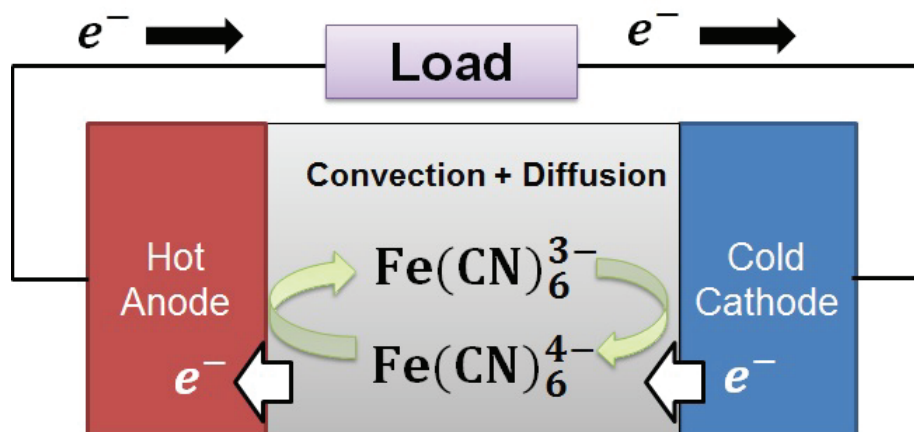
Fig. 1.9. Working mechanism of a thermo-electrochemical cell

for the redox couple and n is the number of electrons involved in the reaction. The Seebeck coefficient is found to be quite high for redox couples such as $Fe(CN)_6^{4-}/$ $Fe(CN)_6^{3-}$ (-1.21 mV K^{-1})[4], Fe^{2+}/Fe^{3+} (1.02 mV K^{-1}) [5] and I^{3-}/I^- (0.5-2.0 mV K^{-1}) [6]. The most widely used electrolyte is ferro/ferricyanide liquid electrolyte due to its favorable properties such as high Seebeck coefficient and non-toxicity.
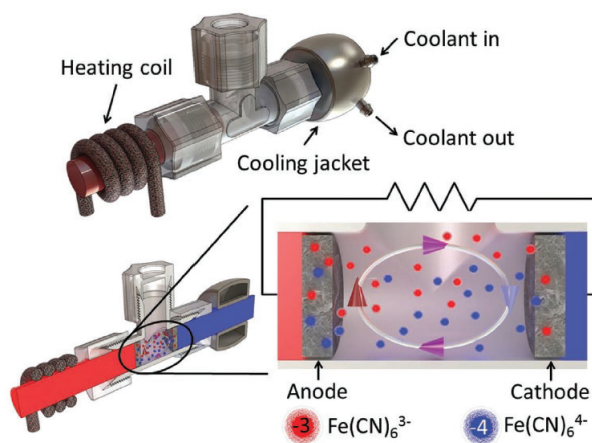
Fig. 1.10. Schematic of a thermocell harvesting waste heat from a hot water pipe [20]
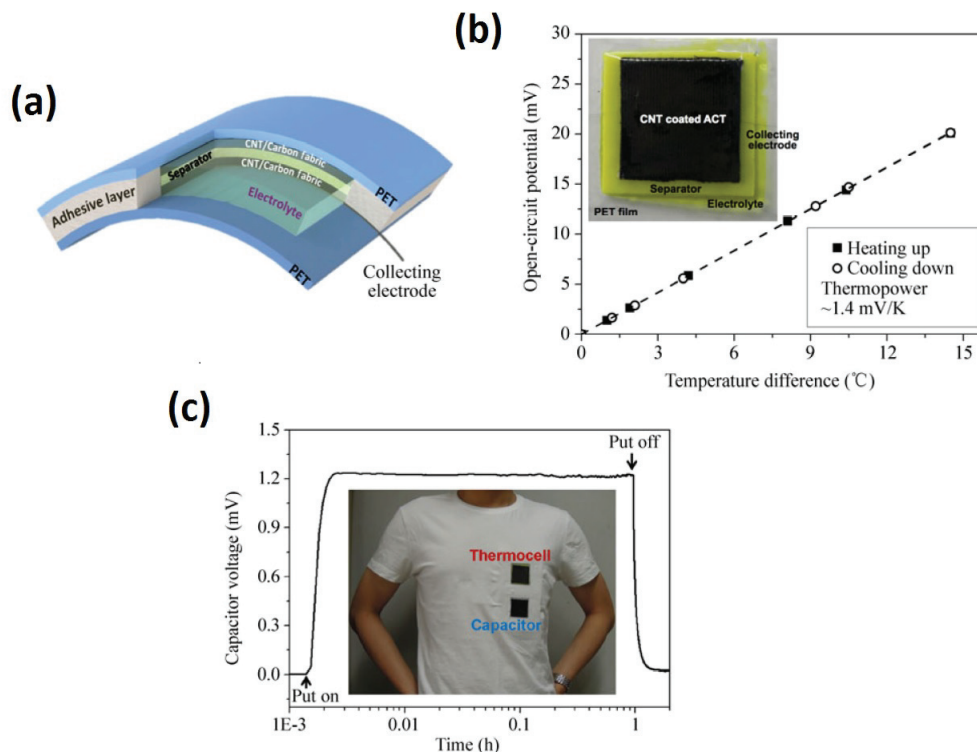
Fig. 1.11. (a) Schematic depicting the structure of a flexible thermocell. (b) Dependence of open-circuit voltage on the temperature difference between hot and cold electrodes. (c) Photograph of a T-shirt embedded with the thermocell and capacitor [21]

1.4.4 Thermo-Electrochemical Cell

Thermo-electrochemical cells (also known as thermocells or thermogalvanic cells) work on the principle of temperature dependence of electrochemical redox potentials to generate electrical power. They may turn as an attractive alternative to harvest low-grade heat, because of their simple design, direct thermal-to-electric energy conversion, continuous operation and low expected maintenance. A thermo-electrochemical force (EMF) is produced by the free energy difference of products and reactants upon application of a temperature difference across the electrodes. The products after being oxidized/reduced due to thermogalvanic effect migrate to opposite electrodes inside the electrolyte, while the electrons generated at the an-

ode due to the oxidation of ions move through the external circuit from anode to cathode. For aqueous electrolyte water molecules carry heat from hot to cold side. Thermocells using aqueous potassium ferrocyanide/ferricyanide redox solution have been thoroughly studied in the past because the reaction leads to exchange of one electron per iron atom and yields a large Seebeck coefficient (≥ 1 mV/K) and high exchange current density. The power conversion efficiency of a thermocell is expressed as

$$\eta = \frac{1/4 V_{oc} I_{sc}}{Ak(\Delta/D)} \tag{1.8}$$

and the power conversion efficiency relative to Carnot cycle is

$$\eta_r = \frac{\eta}{(\Delta T/T_h)} \tag{1.9}$$

where I_{sc} is the short circuit current, V_{oc} is the open circuit voltage, A is the electrode cross-section, ΔT is the temperature difference between the electrodes, d is the electrode separation distance, k is the effective thermal conductivity of the electrolyte and separator, and T_h is the temperature at the hot side. In order to obtain a high exchange current density $j_{sc} = I_{sc}/A$, the charge transfer resistance (R_{ct}) and mass transfer resistance (R_{mt}), need to be minimized. For this reason, various nanocarbon electrodes such as single-walled and multi-walled carbon nanotubes with favorable properties such as intrinsically high surface area and fast electron conductivity to/from the electrolyte, have beeen employed in the past [22, 23] for superior power output. A collection of the most recent works on thermo-electrochemical cells is displayed in Fig. 1.10 and Fig. 1.11.

1.5   Motivation of The Present Study

Electrochemical capacitors are promising for serving the energy requirements for hybrid electrical vehicles and portable electronics. In a conventional electrical double-layer capacitor (EDLC), the charge is stored at the electrode/electrolyte interface by electrostatic attraction forces. Although EDLCs are capable of generating high power, they lack in energy density and are hence considered inferior to other energy

storage devices. One option to boost the capacitance is to induce faradaic reactions at the electrode/electrolyte interface. The conventional technique to attain pseudo-capacitance is by fabricating electrodes with reactive materials such as manganese dioxide, ruthenium dioxide, etc. However, these options carry disadvantages such as high cost, complicated synthesis procedures and short cycle life due to rapid material degradation. Furthermore, integrated energy storage devices required to power low-power devices such as microprocessors, sensors and wireless communication chips need to interface with external power supplies. Here, we employ a redox electrolyte to build supercapacitors with enhanced performance without the involvement of complicated synthesis steps. Furthermore, we demonstrate a novel integrated thermoelectric supercapacitor device that is capable of converting waste heat directly into stored charge.

Similar to other energy storage systems, supercapacitors dissipate heat during charging and discharging. The dissipated heat leads to elevated temperatures which causes material degradation, aging, low cycle life and high self-discharge rates. In order to avoid such harmful effects, proper thermal strategies need to be developed. A thorough understanding of the underlying mechanisms of heat generation needs to be developed. Here, we propose a new continuum model to investigate the heat generation rate in supercapacitors and its dependence on the various system and operating parameters. Furthermore, we develop a new non-contact imaging technique to investigate the degradation of microsupercapacitor electrodes during continuous cycling.

1.6   Contributions and Organization of the Thesis

In this dissertation, we aim to investigate various multi-physics phenomena in supercapacitors. The two primary objectives of the work presented here are: (i) performance enhancement of supercapacitors using novel electrolytes and (ii) an in-depth

analysis of various heat generation and degradation mechanisms in supercapacitors upon continuous cycling. A brief overview is represented in Fig. 1.12.

Chapter 2: We develop a thin, lightweight, symmetric and all-solid-state pseudo-capacitor employing a redox-active gel electrolyte $K_3Fe(CN)_6$- $K_4Fe(CN)_6$ and electrodes composed of graphene petals coated on carbon nanotube paper. A thorough investigation of the electrochemical performance of all-solid-state supercapacitor devices fabricated with such redox-active electrolyte is performed in terms of capacitance, internal resistance and operating voltage window. Furthermore, detailed comparison is performed with similar devices composed of pure double-layer gel electrolytes such as $PVA-H_3PO_4$ and PVA-KOH gel electrolytes.
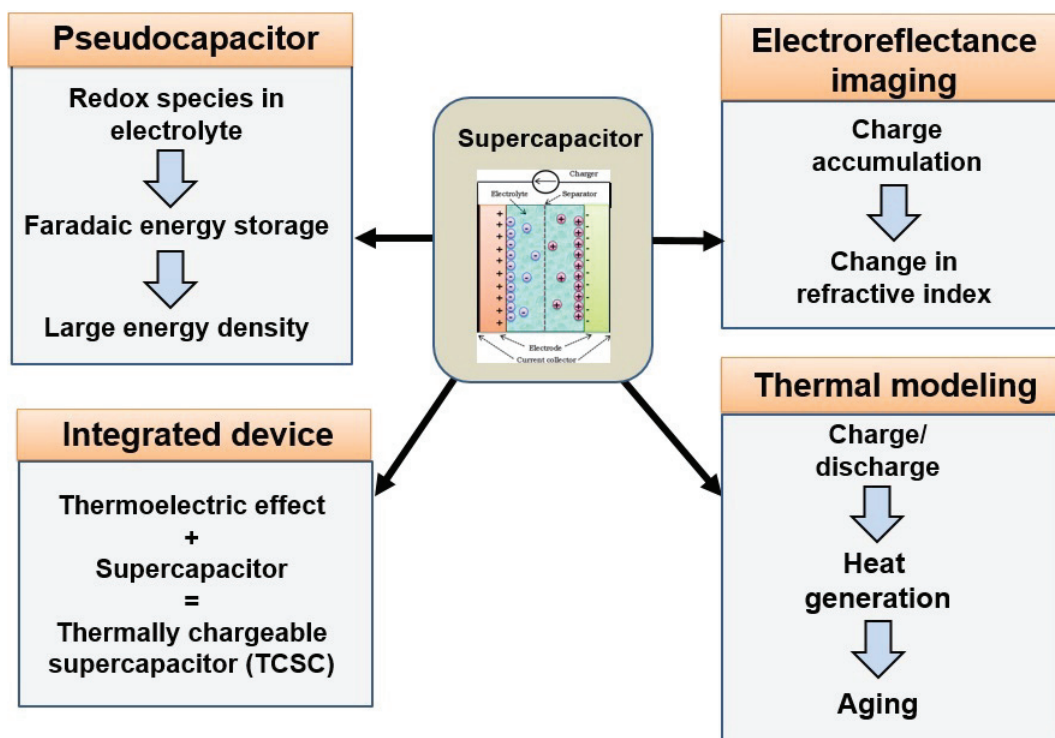
Fig. 1.12. A summary of various multi-physics effects studied in this thesis

Chapter 3: In addition to inducing pseudocapacitance, the ferrocyanide/ferricyanide redox couple also exhibits thermogalvanic property. Such interesting property enables the successful conversion of waste heat energy into electricity. We establish

the connection between pseudocapacitance and thermogalvaic property of the ferro-cyanide/ferricyanide redox couple to conceptualize an integrated thermoelectric su-percapacitor. We design, build and test the device and demonstrate its capability to directly convert waste heat into stored electrical energy thus circumventing the need for an external energy storage device in systems that are conventionally used to harvest waste heat from intermittent heat sources. Furthermore, we develop an equivalent circuit model to elucidate the working mechanisms of energy conversion and storage applicable to thermally chargeable supercapacitor devices in general. A fitting analysis aids in the evaluation of model circuit parameters providing good agreement with experimental voltage and current measurements.

Chapter 4: The following two chapters of the thesis focuses on developing novel techniques to characterize and predict degradation of supercapacitor components dur-ing continuous cycling. With age, its capacitance degrades and internal resistance rises. Aging is also strongly dependent on the operating temperature. Typically, the lifetime of a supercapacitor is halved for every 10 K rise in operating tempera-ture. Thermal modeling is an effective technique to predict temperature evolution in supercapacitors. Previous models oversimplified heat generation rate calculation by considering it spatially uniform and estimating it as Joule heating evaluated from the current imposed and experimentally measured electrical resistance. Here, for the first time, we develop a one-dimensional continuum model to predict temperature evolution in a full device composed of several sandwich EDLC structures. We employ porous electrode theory in derivation of expressions for total heat generation rate as a function of the solid and liquid phase currents in the electrodes. Such model is an improvement over the first principles flat plate electrode model and takes into consideration factors such as electrode porosity, volumetric surface area and electrode and electrolyte conductivity. Furthermore, we present a scaling analysis of the model which simplified the problem. Eleven independent design parameters were simplified to seven dimensionless similarity parameters which govern the spatio-temporal evolu-

tion of electrode and electrolyte phase potentials, ion concentration, heat generation rates and temperature evolution.

Chapter 5: The performance degradation of supercapacitors has traditionally relied on electrical characterization methods such as cyclic voltammetry and electrical impedance spectroscopy which measure an 'average' of the performance of its internal components. In chapter 4, we leverage the electroreflectance property of gold electrodes to propose a new high-resolution, non-contact technique to image dynamic charge distribution in integrated microsupercapacitor during fast voltage cycling. The novel technique was used to study electrode degradation in the microsupercapacitor devices upon cycling over a period of 4.1 million charge/discharge cycles.

Chapter 6: Thermoelectric materials are commonly used for continuous generation of electricity in response to a temperature gradient without involvement of moving parts. Here, we study a new thermoelectric effect called Nernst effect which involves the generation of electric current in the cross product direction between a temperature gradient and an applied magnetic field. In the past, such phenomena has been demonstrated to have a simpler design than conventional thermoelectric devices based on Seebeck effect. Using a semiclassical Boltzmann transport equation (BTE) approach, we derive analytical expressions for electric and thermoelectric transport coefficients of graphene in the presence and absence of a magnetic field. The Nernst coefficient is thoroughly characterized as functions of impurity concentrations, temperature, carrier concentration and magnetic field, and valuable insights emerge in comparing model results with previously published experimental data.

2. EFFECT OF REDOX-ACTIVE GEL ELECTROLYTE ON GRAPHITIC PETAL BASED SOLID-STATE SUPERCAPACITORS [†]

Some of the material in this chapter is being prepared for publication in *ACS Energy Letters.*

2.1 Introduction

In recent years, thin, flexible and lightweight energy storage devices have undergone rapid development to satisfy the growing energy demand for miniaturized consumer electronic devices [24, 25]. Among various alternatives, supercapacitors have emerged to be promising for their fast power delivery, excellent cyclic stability and low maintenance costs. Past studies have predominantly targeted novel electrode materials to promote storage through electrical double layer formation and pseudo-capacitance. Carbon-based electrodes have been used because of their high surface area, low cost and high electrical conductivity. Furthermore, pseudocapacitive electrode materials such as transition metal oxides [26] and conducting polymers [27] have been employed to attain high energy density. However, these options carry disadvantages such as high cost, complicated synthesis, low power density and short cycle life [28, 29].

Recently, several groups have reported a different approach to promote energy density, by introducing redox species into the electrolyte. Such species undergo oxidation at the positive electrode and reduction at the negative electrode during charging, thus producing pseudocapacitance. These electrolytes allow the use of less-expensive carbon electrodes to build devices with high energy density while ideally maintaining

high power and cycle life. Oftentimes, such liquid electrolytes are encapsulated in a polymeric network to form gel electrolytes for building solid-state devices that are compact, durable and have longer shelf life in comparison to liquid electrolyte devices.

Redox electrolytes can be broadly classified into two types [11, 30, 31]: redox-additive electrolyte obtained by addition of redox-active species to a supporting electrolyte, or the exclusive use of a redox-active electrolyte. Numerous prior studies have demonstrated enhanced performance of supercapacitors in terms of high capacitance and low internal resistance by incorporating redox additives such as hydroquinone [10,11], p-phenylenediamine [12], KI [13–16], Na_2MoO_4 [17] and $K_3Fe(CN)_6$ [18].

Reports of redox-active electrolytes are comparatively more scarce. Lota et al. [15] and Tian et al. [32] obtained large values of capacitance from three-electrode measurements with aqueous KI and $K_4Fe(CN)_6$ as electrolytes due to pseudocapacitive contributions of the redox ions. Lota et al. [15] found that the KI solution led to higher capacitance (261 F g^{-1}) compared to aqueous H_2SO_4 electrolyte (160 F g^{-1}) using activated carbon electrodes. The authors also inferred that the redox species (I^-) engaged in redox reactions only at positively charged electrode which is indicated by relatively higher capacitance value while applying positive bias across the working electrode in three-electrode measurements. It is well known that in a capacitor, both the electrodes contribute cumulatively to the performance, according to [28]:

$$\frac{1}{C_{dev}} = \frac{1}{C_+} + \frac{1}{C_-}.$$ (2.1)

Thus for exceptional device performance, both cationic and anionic species must be present in the electrolyte. One proposed approach is to introduce separate redox additives in two compartments partitioned by a Nafion separator in a sandwich-type configuration [28, 29, 33]. For example, Frackowiak et al. [28] applied potassium iodide solution as catholyte (electrolyte for the positive electrode) and vanadyl sulfate solution as anolyte (electrolyte for the negative electrode). Similarly, Zhong et al. [29] assembled a solid-state supercapacitor using hydroquinone (HQ) and methylene blue (MB) as the catholyte and anolyte respectively. Such a strategy is reported to produce a three to four-fold improvement in specific energy density based on the active mass

of the electrodes. However the large thickness of the electrolyte/separator layer(4 mm) in such devices is expected to cause low volumetric capacitance.

Potassium ferricyanide ($K_3Fe(CN)_6$) and potassium ferrocyanide ($K_4Fe(CN)_6$) salts have been previously used as electrochemical probe reagents to investigate electron transfer kinetics at the surface of single- and multi-walled carbon nanotubes [34, 35]. Studies on the electrochemical performance in supercapacitor applications are relatively scarce. Tian et al. [32] obtained higher single-electrode capacitance in aqueous 0.1 M $K_4Fe(CN)_6$ electrolyte (232 F g^{-1}) compared to 144 F g^{-1} in 0.1 M KOH. Ma et al. [18] constructed a solid-sate supercapacitor composed of PVA-KOH-$K_3Fe(CN)_6$ gel electrolyte and demonstrated its superior electrochemical performance compared to PVA-KOH gel electrolyte. Yang et al. [36] prepared PVA-$K_3Fe(CN)_6$-$K_4Fe(CN)_6$ (PVA-PFC) gel electrolyte and leveraged its thermogalvanic property to build of a flexible and wearable thermo-electrochemical cell. The ionic conductivity of the gel electrolyte was found to be ≈ 6 mS cm^{-1} which is much lower than its liquid counterpart, (168.4 mS cm^{-1} for 0.4 M $K_3Fe(CN)_6$ [37]). The weight percentage of $K_3Fe(CN)_6$/$K_4Fe(CN)_6$ in the gel corresponded to its maximum solubility, which has also been confirmed in this study.

Here, we investigate the electrochemical properties of the PVA-PFC gel when employed in the form of an electrolyte for a lightweight, solid-state supercapacitor device with electrodes composed of vertical graphene petals (GPs) grown by microwave plasma chemical vapor deposition (MPCVD) on flexible buckypaper (BP) substrates. Furthermore, we compare its performance with devices composed of PVA-H_3PO_4 and PVA-KOH gel electrolytes in terms of capacitance, internal resistance, operating voltage window and self-discharge rate. Such influences have not been studied systematically previously for graphene- based supercapacitors. The different blends of gel electrolytes are prepared by mixing poly(vinyl alcohol) (PVA) with liquid potassium ferrocyanide/ferricyanide, phosphoric acid and potassium hydoxide. The preparation technique of the PVA- $K_3Fe(CN)_6$-$K_4Fe(CN)_6$ gel electrolyte (denoted PVA-PFC), PVA-H_3PO_4 gel electrolyte and PVA-KOH gel electrolyte is adopted from Yang et
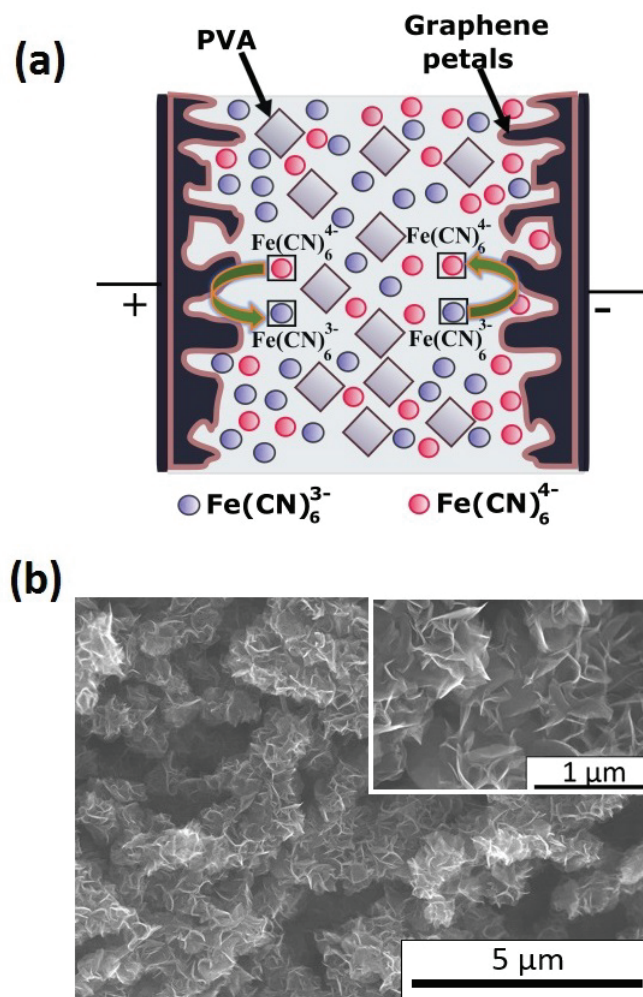
Fig. 2.1. (a) Schematic representation of a symmetric two-terminal supercapacitor device with BP/GP electrodes and PVA-K$_3$Fe(CN)$_6$-K$_4$Fe(CN)$_6$ gel polymer electrolyte. (b) SEM image of GPs fully covering CNTs at low and high (inset) magnifications.

al. [36], Hashmi et al. [38] and Ma et al. [18] respectively. Two BP/GP electrodes were assembled with a piece of a particular variety of gel electrolyte film to assemble an all-solid-state supercapacitor. The redox electrolyte device is found to exhibit larger energy and power densities compared to the other devices, owing to its high capacitance and wider operating voltage window (1.5 V). All reported results are based on the projected (Euclidean) area of the electrodes.

2.2   Experimental

2.2.1   Polymer Gel Electrolyte Preparation

4g PVA powder (molecular weight 89,000-98,000, 99% hydrolyzed, Sigma-Aldrich) was dissolved in 40 ml deionized water with continuous stirring at 85 °C for 20 min. In order to synthesize PVA- $K_3Fe(CN)_6$-$K_4Fe(CN)_6$ gel (denoted PVA-PFC), 10 ml 0.1 M $K_3Fe(CN)_6$ and $K_4Fe(CN)_6$ was added to the PVA solution. To prepare PVA-H_3PO_4 gel, 4g concentrated H_3PO_4 was added to the PVA solution. Similarly, in order to prepare PVA-KOH gel electrolyte, 2.7g KOH was added to the PVA solution. The gel electrolytes were subsequently allowed to cool to room temperature. Finally, this homogeneous viscous solution was poured onto a PTFE evaporating dish and allowed to dry at room temperature for 24 hours. The prepared film was cut into small pieces and then used for supercapacitor assembly.

2.2.2   Electrode Fabrication

Commercial buckypaper substrates (5×10 mm^2 , Nanotech Labs Inc., USA), elevated 9 mm on top of a Mo puck, were subjected to MPCVD growth conditions of H_2 (50 sccm) and CH_4 (10 sccm) at 30 Torr total pressure. At first, the substrates were exposed to hydrogen plasma for approximately 2 min, during which the plasma power was gradually raised from 300 to 600 W. The growth time was 20 min to ensure complete coverage of GPs over the entire substrate. Detailed steps involved in the growth process are provided in ESI. GPs grown in the presence of H_2 plasma are highly graphitic and thus hydrophobic. The activation of the GPs requires functionalization with oxygen-containing functional groups which is accomplished by electrochemical oxidation process performed at 1.9 V in 1 M H_2SO_4 for 20 min.
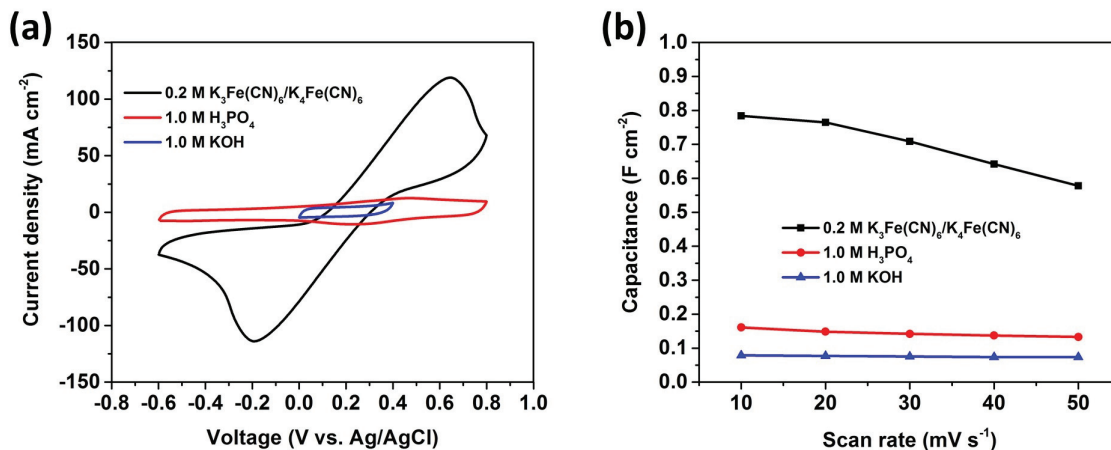
Fig. 2.2. Electrochemical performance of BP/GP electrodes in aqueous 1 M H_3PO_4 electrolyte, mixture of aqueous 0.2 M $K_3Fe(CN)_6$ and 0.2 M $K_4Fe(CN)_6$, and aqueous 1 M KOH. (a) CV curves acquired at a scan rate of 50 mV s^{-1} in a voltage window from -0.6 V to +0.8 V for the H_3PO_4 and 0.2 M $K_3Fe(CN)_6/K_4Fe(CN)_6$ electrolytes, and in the voltage window of 0-0.4 V for the KOH electrolyte. (b) Area-specific capacitance derived from the CV curves plotted as a function of scan rate.

2.2.3   Supercapacitor Assembly

To construct a solid-state supercapacitor, two BP/GP electrodes were dip coated with the corresponding gel electrolyte solution and then assembled with the film electrolyte. The as-synthesized device was kept at room temperature for 1 h prior to operation.

2.2.4   Characterizations

The surface morphology of the electrodes was characterized by field emission scanning electron microscope (SEM, Hitachi S-4800). Electrochemical measurements were performed in both a three-electrode and two-terminal cells using the Gamry Echem Testing System, Gamry Instruments, Inc., USA under ambient conditions. In the
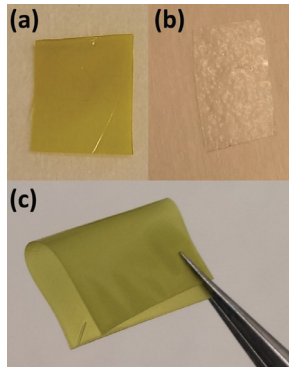
Fig. 2.3. Photograph of gel polymer electrolyte film samples. (a) PVA-K$_3$Fe(CN)$_6$-K$_4$Fe(CN)$_6$ (b) PVA-H$_3$PO$_4$ and (c) folded PVA-K$_3$Fe(CN)$_6$-K$_4$Fe(CN)$_6$ film

three-electrode cell, the BP/GP electrode is considered as the working electrode, platinum mesh as the counter electrode, and saturated calomel electrode (SCE) as the reference electrode. For the two-terminal cells, cyclic voltammetry (CV) measurements were performed at scan rates ranging from 5 to 50 mV s^{-1}. Galvanostatic charge/discharge tests were performed for currents ranging from 1 to 20 mA cm^{-2}. The device-specific areal capacitance (C_{dev}) and electrode-specific areal capacitance (C_{el}) were obtained from galvanostatic current curves using [18, 29, 33]:

$$C_{dev} = (I \times \Delta t)/(A \times (\Delta V - IR_{drop})) \tag{2.2}$$

$$C_{el} = 4C_{cell} \tag{2.3}$$

where C represents areal capacitance (F cm^{-2}), $I(A)$ is the applied current, Δt is the discharge time, ΔV is the voltage window, IR_{drop} is the voltage drop at the beginning of discharge and A is the projected (Euclidean) area of the electrodes. The energy density E_{dev} (W h cm^{-3}) and power density P_{dev} (W cm^{-3}) are estimated from [18, 29, 33, 39]

$$E_{dev} = C_{dev}\Delta V^2/7200 \tag{2.4}$$

$$P_{dev} = E_{dev} \times 3600/\Delta t \tag{2.5}$$

Electrochemical impedance spectroscopy (EIS) measurements were also carried out with an AC voltage amplitude of 5 mV in the frequency range of 0.1 Hz and 100 kHz and a dc bias voltage of 0 V. Conventionally, the device capacitance is normalized by the mass of active electrode materials. Such an aprroach may be ambiguous for comparison purposes because the mass of the metallic current collectors and electrolytes are ignored in the process. Therefore, we have reported the performance parameters of our devices in terms of the geometric area of the electrodes.

2.3   Results and Discussion

2.3.1   Electrode Characterization

Scanning electron microscopy (SEM) images in Fig. 2.1b show the morphology and microstructure of GPs synthesized by MPCVD on commercial buckypaper. The petals protrude approximately 500 nm from the BP surface, while the span width of a single petal was found to range from 100 nm to 500 nm. A comparison of the microstructure before and after GP growth is provided in Fig. 8.1. Besides generating high surface area, GP-coated CNT arrays have been found to be more mechanically stable than bare CNT arrays in a past study [40]. Furthermore, unlike bare CNTs, they retain their morphology during solvent immersion and evaporation cycles. Thus, attributes such as robust mechanical properties, high surface area and small thickness makes BP/GP an ideal choice for supercapacitor electrodes.

The capacitive performance of the BP/GP electrode was tested in a three-electrode configuration cell, as described in the Experimental section. Fig. 2.2a shows CV curves acquired at a scan rate of 50 mV s^{-1} in three different electrolytes: solution of 0.2 M K$_3$Fe(CN)$_6$ and 0.2 M K$_4$Fe(CN)$_6$, 1 M H$_3$PO$_4$ and 1 M KOH. A quasi-rectangular CV shape is observed for the 1 M H$_3$PO$_4$ and KOH electrolytes while a pair of broad peaks originating from pseudocapacitive contributions of the redox species is observed for the redox electrolyte. The CV curves obtained at different scan rates ranging from 10 to 50 mV s^{-1} are displayed in Fig 8.2. The area-normalized

specific capacitance is found to be significantly higher for the redox electrolyte at all scan rates as indicated by the larger area in the CV curves. At a scan rate of 10 mV s^{-1}, the capacitance is found to be 0.79 F cm^{-2} for the redox electrolyte which is approximately 5 times that for H$_3$PO$_4$ aqueous electrolyte (0.16 F cm^{-2}) and 10 times that for KOH aqueous electrolyte (0.08 F cm^{-2}). However, the capacitance retention rate at high scan rates is quite low for the redox electrolyte. The Nyquist plots obtained from EIS measurements show a lower x intercept for the redox electrolyte, suggesting higher ionic conductivity compared to H$_3$PO$_4$ electrolyte, which has also been confirmed in past studies (168.4 mS cm^{-1} for 0.4 M K$_3$Fe(CN)$_6$ [37] compared to 59.4 mS cm^{-1} for 1 M H$_3$PO$_4$ [41]).

2.3.2 Symmetric Supercapacitors Based on PVA-PFC Polymer Gel Electrolyte

Symmetric two-terminal devices were assembled by sandwiching polymer gel electrolyte film between two BP/GP electrodes. For all the fabricated devices, the BP/GP electrodes and electrolyte film are each approximately 0.1 mm thick, leading to an overall device thickness of around 0.3 mm. Cut pieces of the polymer gel electrolyte films are shown in Fig. 2.3. The film can be easily bent into a circular arc, and does not fracture even when bent over 180°. The film quickly recovers upon releasing, thereby exhibiting robust mechanical properties.

The structure of the fabricated PVA-PFC device is schematically illustrated in Fig. 2.1a. The redox species engage in reversible Faradaic charge transfer in addition to forming a double layer by virtue of their charge. CV curves of the device in the voltage window -1.5 to +1.5 V are displayed in Fig. 2.4a for scan rates ranging from 5 to 50 mV s^{-1}. The ferrocyanide ion (Fe(CN)$_6^{4-}$) reacts to form ferricyanide (Fe(CN)$_6^{3-}$) ion during the forward scan and vice-versa during the reverse scan, represented by the oxidation and reduction peaks. The oxidation and reduction peaks move in the positive and negative voltage directions respectively as the scan rate

rises, thus demonstrating the quasi-reversible nature of the reactions [42]. The inset of Fig. 2.4a shows that both the oxidation and reduction peak current densities almost vaies linearly with the square root of scan rate, implying that the reactions are diffusion-controlled [29, 43].

The electrochemical performance of the device is further examined by galvanostatic charge/discharge (GCD) measurements at current densities ranging from 1 to 20 mA cm^{-2} in the voltage window of 0 to 1.5 V. Fig. 2.4b shows the GCD curves for current densities of 2, 3 and 4 mA cm^{-2}. The charge and discharge time durations can be observed to be almost equal in all the curves, which is indicative of high coulombic efficiency and favourable electrochemical reversibility. Voltage non-linearity points observed in the charge/discharge curves are found to be similar to the redox peaks observed in the CV curves.

Electrode-specific areal capacitance determined from the charge/discharge curves is plotted as a function of the current density in Fig. 2.4c. At a low current density of 1 mA cm^{-2}, the electrode-specific areal capacitance $C_{A,el}$ is 0.95 F cm^{-2} based on a single electrode, which is comparable to devices with pseudocapacitive electrodes studied in the past [44]. As the current density increases from 1 to 20 mA cm^{-2}, $C_{A,el}$ undergoes a gradual depletion from a value of 0.95 to 0.14 F cm^{-2} . The device shows a relatively low capacitance retention (15%) at high current density (20 mA cm^{-2}). The dwindling capacitance may be attributed to incomplete participation of the ferro/ferricyanide ions during rapid cycling. The volumetric capacitance based on the entire device volume is calculated to be 7.9 F cm^{-3} at a low current density of 1 mA cm^{-2}, which is significantly higher than previous reports of solid-state supercapacitors (graphene based SCs 0.45 F cm^{-3} [45], carbon onion/MnO$_2$ based SCs 0.68 F cm^{-3} [46], H-TiO$_2$ based SCs 0.7 F cm^{-3} [47], carbon fiber/MnO$_2$ based SCs 2.5 F cm^{-3} [48], WO$_{3-x}$/MoO$_{3-x}$ asymmetric SCs 3.8 F cm^{-3} [48])

Life cycle tests were conducted over 5000 cycles for the symmetric device at a current density of 5 mA cm^{-2} using galvanostatic charge/discharge cycling in a potential window from 0 to 0.8 V. Fig. 2.4d shows that the device exhibits a capacitance loss of

$\approx 13\%$ at the end of 5000 cycles, indicating good long-term stability. Such stability surpasses the results obtained in previous studies on redox electrolytes [18, 49–51]. The coulombic efficiency, also plotted in Fig. 2.4d, maintains a high value (¿98%) throughout the course of 5000 cycles, suggesting high charge transfer efficiency during long term cycling. The constant current charge discharge profiles for the first cycle and the 5000th cycle displayed in the inset of Fig. 2.4d shows no significant change in electrochemical response after the long-term cycling test.

The primary drawback of redox electrolytes is that they cause rapid self-discharge under open-circuit conditions, making them unsuitable for applications requiring long-term energy storage. Rapid self-discharge primarily occurs due to shuttling of mobile redox species and cyclic instability due to intermixing redox couples [11, 52, 53]. For most devices based on redox electrolytes, self-discharge characteristics are not studied. A recent study by Chen et al. [53] proposes employing an ion exchange membrane such as Nafion instead of a porous separator to mitigate the shuttling of the redox species. However, the high cost of Nafion membranes is prohibitive to mass production.

The leakage current was measured on our PVA-PFC based device while maintaining a constant voltage of 0.8 V for 10 h. The results in Fig. 2.5a indicate that the leakage current drops rapidly from its initial value, before reaching a steady state value of 50 μA cm^{-2} (see in inset). This leakage current is slightly higher than that observed for devices based on electrochemically inert electrolytes like PVA-H$_2$SO$_4$ [54]. In order to investigate the charge retention capability, self-discharge characteristics were measured under open-circuit condition. The device was initially held at 0.8 V. The hold duration was also varied to study its influence. The results shown in Fig. 2.5b show that for all hold durations, there is a quick drop in cell voltage initially, followed by a slow decay. Furthermore, long hold times mitigate the voltage drop to a certain extent, possibly due to longer equalization time allowing for charge distribution [53].

The inset of Fig. 2.5b compares the charge retention capability of our device with past measurements on aqueous redox electrolyte (0.4 M HQ + 1 M H$_2$SO$_4$)

devices [53]. Plots are shown for two devices, one with porous cellulose separator and the other with Nafion 117 membrane. Our device exhibits superior charge retention capability compared to the porous separator device indicating that the PVA polymer chains present in the gel electrolyte are quite efficient in suppressing self-discharge occurring due to shuttling of the redox species. The self-discharge rate of the PVA-H_3PO_4 electrolyte device is found to be much slower than the PVA-PFC electrolyte device as shown in Fig. S6, due to the absence of any redox species.

2.3.3   Performance Comparison with Various Gel Electrolytes

In this section, we compare the performance of devices based on redox electrolyte PVA-PFC with devices consisting of pure double layer electrolytes PVA-H_3PO_4 and PVA-KOH. A lone study [55] on graphene-based supercapacitors comparing the performance of various pure double layer gel electrolytes demonstrated that PVA-H_3PO_4 electrolyte outperforms other electrolytes such as PVA-H_2SO_4, PVA-KOH, PVA-NaOH in terms of capacitance and stable voltage window. The small radius of H^+ ions present in the PVA-H_3PO_4 electrolyte compared to the other ions (K^+, OH^-) was proposed to allow them to easily diffuse between graphene layers, leading to high capacitance. We find similar trends while comparing the performance of PVA-H_3PO_4 and PVA-KOH gel electrolytes.

Voltage Window

The operating voltage window of a supercapacitor is a critical factor in determining its energy and power density, and it primarily depends on the stability of the electrolyte. In order to achieve a large potential window, electrolytes based on organic solvents or ionic liquids [56, 57] are generally preferred over aqueous electrolytes, although the volatility of organic liquids and the high cost of ionic liquids are major concerns. Asymmetric cell configurations based on a plethora of electrode materials [58, 59] have been also deployed in the past to attain a wide potential win-
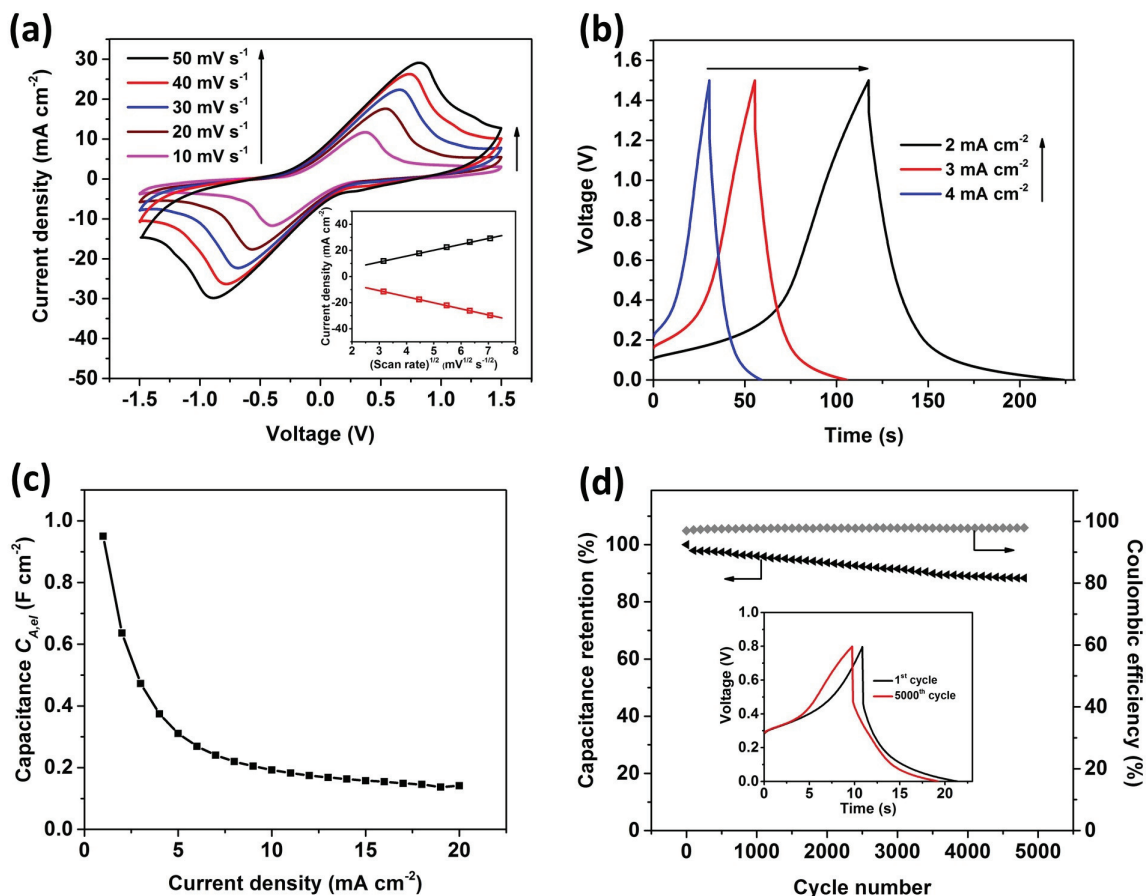
Fig. 2.4. Electrochemical performance of a two-terminal symmetric supercapacitor device with PVA-PFC gel electrolyte. (a) CV curves acquired at scan rates ranging from 5 to 50 mV s^{-1} in the voltage window -1.5 to +1.5 V. The inset shows peak current density in the forward and reverse sweeps as a function of the square root of scan rate. (b) GCD curves for current densities in the range 2 to 5 mA cm^{-2} in the potential window 0 to 1.5 V. (c) Electrode-specific areal capacitance $C_{A,el}$ calculated from galvanostatic charge/discharge curves as a function of current density. (d) Cycling stability test performed at a current density of 5 mA cm^{-2} showing 13% loss after 5000 cycles (inset showing GCD at the 1st and 5000th cycles).

dow. However, such approaches involve intricate and expensive electrode synthesis techniques that are generally not favorable for mass production.

In a recent study, Lee et al. [30] demonstrated stability up to 1.8 V in a symmetric device employing aqueous potassium ferricyanide electrolyte. The large potential window was attributed to suppressed potential rise at the positive electrode due to the ferricyanide/ferrocyanide redox reaction, causing biased potential development at the negative electrode. This effect may in turn cause the potential at each individual electrode to remain below the decomposition voltage of water, thus leading to stability up to 1.8 V.

Here, we study the voltage window of a device based on gel-based potassium ferrocyanide/ferricyanide electrolyte instead of its aqueous counterpart. S-value analysis has been performed to determine the stable voltage window. The S-value, an index of stability, is defined as [30, 60, 61],

$$S = \frac{Q_{char}}{Q_{dis}} - 1 \tag{2.6}$$

where Q_{char} is the charge stored during charging and Q_{dis} is the charge released during disharging. When the applied voltage exceeds the chemical decomposition potential of the electrolyte, Faradaic leakage currents become significant, leading to a non-zero second derivative of S with respect to applied potential V. Two types of criteria were applied by Weingarth et al. [60] to determine the stable potential window of ionic liquids, namely $S¡0.1$ and $\frac{d^2S}{dV^2}¡0.05$. For a GCD measurement, S can be shown to be inversely proportional to the coulombic efficiency η_{coul} as

$$S = 1/\eta_{coul} - 1. \tag{2.7}$$

Fig. 2.6a displays the variation of S with voltage window for devices based on PVA-PFC, PVA-H$_3$PO$_4$ and PVA-KOH gel electrolytes. The S-values were derived from GCD measurements performed at a current density of 2 mA cm^{-2} while extending the operating voltage window from 0.5 to 1.5 V, 0.5 to 1.1 V and 0.2 to 0.5 V, respectively for the PVA-PFC, PVA-H$_3$PO$_4$ and PVA-KOH electrolyte based devices. For the

PVA-PFC based device, S can be observed to reach the cutoff value of 0.1 at 1.5 V, while for the PVA-H$_3$PO$_4$ and PVA-KOH devices, S reaches the cutoff value at 1.0 V and 0.4 V respectively. In other words, the coulombic efficiency drops below 90 % for wider voltage windows as shown in the inset of Fig 6a. The GCD curve for the PVA-PFC device retains its shape while extending the voltage window from 0.5 V to 1.5 V as displayed in Fig. 2.6b.

S-values were also evaluated from CV curves acquired during operation at different voltage windows. Fig. 2.6c shows that the S-value for the PVA-PFC device deviates significantly from 0.1 for voltages above 1.5 V and also deviates from linear variation, implying non-zero second derivative. The CV curve can also be observed to retain its shape while expanding the voltage window from 0.5 to 1.5 V, shown in Fig. 2.6d.

In comparison, for the PVA-H$_3$PO$_4$ device, S exceeds 0.1 at 1.0 V and rises abruptly to 0.65 at 1.2 V, indicating the occurrence of chemical decomposition. The CV curves shown in Fig. 2.6e display a high current response at 1.2 V caused by contributions from Faradaic leakage. From this analysis, the safe potential window for the PVA-H$_3$PO$_4$ device can be inferred to be 1.0 V. Similarly, the window for the PVA-KOH device is inferred to be 0.4 V. These results are in agreement with a past study by Chen et al. [55] which reports voltage windows of PVA-H$_3$PO$_4$ and PVA-KOH devices as 0.8 V and 0.4 V. Fig. S9 compares the GCD profiles obtained for voltage windows below and above the stability point for the three devices, revealing the loss of symmetric shape as the voltage window exceeds the stability limit.

Capacitance and ESR

Fig. 2.7 compares the performance of the present devices in terms of capacitance, cyclic stability and impedance characteristics. Fig. 2.7a displays the GCD profiles obtained at a constant current denisity of 2 mA cm^{-2} for the three devices. A clear deviation from the ideal trangular shape is observed for the PVA-PFC device. The plateau characteristics represent redox reactions that occur at a constant potential

and are typical for pseudocapacitors. The electrode-specific areal capacitance ($C_{A,el}$) values evaulated from the GCD curves are shown for the three devices as a function of current density in Fig. 2.7b. At a small current density of 1 mA cm^{-2}, the PVA-PFC device exhibits a capacitance $C_{A,el}$ of 0.95 F cm^{-2} that is four times that of the PVA-H$_3$PO$_4$ device (0.23 F cm^{-2}) and about eight times that of the PVA-KOH device (0.12 F cm^{-2}). At a high current density of 10 mA cm^{-2}, although the capacitance retention is lower for the PVA-PFC device (20%) compared to the PVA-H$_3$PO$_4$ device (65%) and PVA-KOH device (73%), its capacitance value is larger than the PVA-H$_3$PO$_4$ and PVA-KOH devices by factors of 1.3 and 2.2 respectively. The electrode-specific areal capacitance is also derived from the CV characteristics at different scan rates. The results depicted in Fig. S3 shows higher capacitances for the PVA-PFC electrolyte device at all scan rates. However, the capacitance retention is higher for the PVA-H$_3$PO$_4$ and PVA-KOH devices (79% and 78% respectively) compared to the PVA-PFC device (64%) at a scan rate of 50 mV s^{-1}. The CV curves for the PVA-H$_3$PO$_4$ and PVA-KOH devices acquired in voltage windows of 1.0 V and 0.4 V respectively at scan rates ranging from 10 to 50 mV s^{-1} are shown in Fig. S7a and S8a respectively. The CV curves are almost rectangular in shape, indicating a predominant double-layer effect. Similar conclusions can be drawn from the GCD curves shown in Fig. S7b and S8b for the respective devices.

The cyclic durability of the PVA-PFC and PVA-H$_3$PO$_4$ devices was evaluated by repeating the GCD measurements at a current density of 5 mA cm^{-2} over 5000 cycles. As shown in Fig. 2.7c, 87% and 73% of the initial capacitance is retained after 5000 cycles for the PVA-PFC device and the PVA-H$_3$PO$_4$ device, respectively. Both the devices retain a coulombic efficiency of $\approx$ 98% at the end of the cyclic test. The high cyclic stability of the PVA-PFC device is indicative of fast redox reactions occurring during charge/discharge. The equivalent series resistance (ESR) calculated from the x intercept are evaluated to be 2.87, 7.44 and 13.47 Ω cm^2 for the PVA-H$_3$PO$_4$, PVA-KOH and PVA-PFC devices, respectively. The higher ESR of the PVA-PFC device

can also be inferred from the larger IR voltage drop occurring at the beginning of discharge in the GCD curve of Fig. S5.

A Ragone plot displaying the volumetric energy and power densities of the devices fabricated in the present work, electrolytic capacitors, commercial supercapacitors, batteries and other solid-state symmetric and asymmetric supercapacitors reported in prior work is shown in Fig. 8. The average energy density (derived from GCD profile at a constant current density of 1 mA cm^{-2}) of the PVA-PFC device is evaluated to be 7.4 mWh cm^{-3} which exceeds that for PVA-H$_3$PO$_4$ and PVA-KOH based devices by 9 and 111 times, respectively. Furthermore, the average power density (derived from GCD at a constant current density of 20 mA cm^{-2}) of the PVA-PFC supercapacitor is 8.2 W cm^{-3} which exceeds values evaluated for the PVA-H$_3$PO$_4$ device (1.6 W cm^{-3}) and PVA-KOH device (0.56 W cm^{-3}). A simple calculation shows that the energy densities of the PVA-PFC and the PVA-H$_3$PO$_4$ devices are 22.7 and 2.5 times greater than the maximum energy density of a 3.5 V/25 mF commercial supercapacitor. Meanwhile, their power densities are 1535 and 300 times greater than that of a standard lithium thin-film battery. Additionally, both the energy and power densities are superior to those of similar solid-state devices fabricated in prior work [45,62–64], thereby highlighting the extraordinary performance of the symmetric redox-active gel electrolyte based supercapacitors developed in this work.
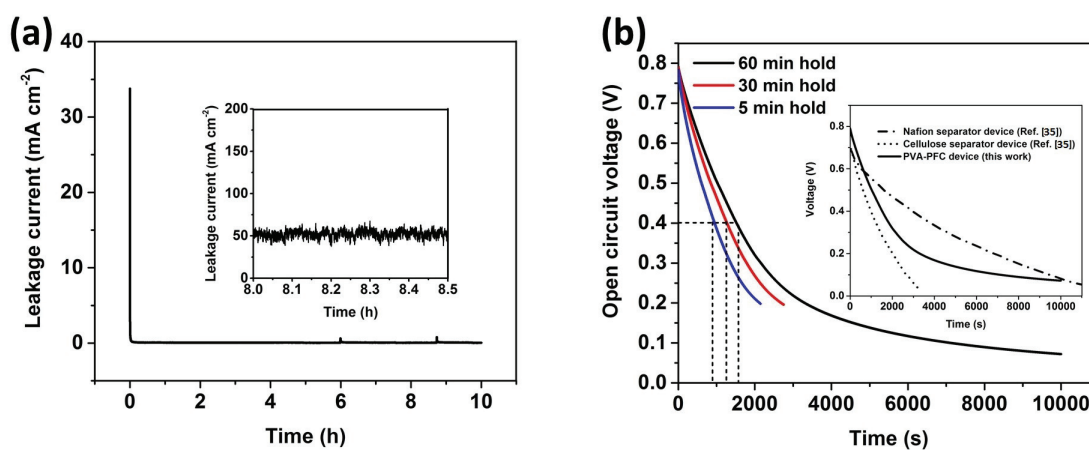
Fig. 2.5. (a) Leakage current of the PVA-PFC based symmetric device charged to a floating potential of 0.8 V and kept at 0.8 V for 10 h. The inset is a magnified view of the leakage current at long time instants after it reaches saturation. (e) Open-circuit voltage profiles for the device after being held at 0.8 V for different time durations. The inset shows comparison of self-discharge curve of the device (hold time of 1 hr) with a past study [53].
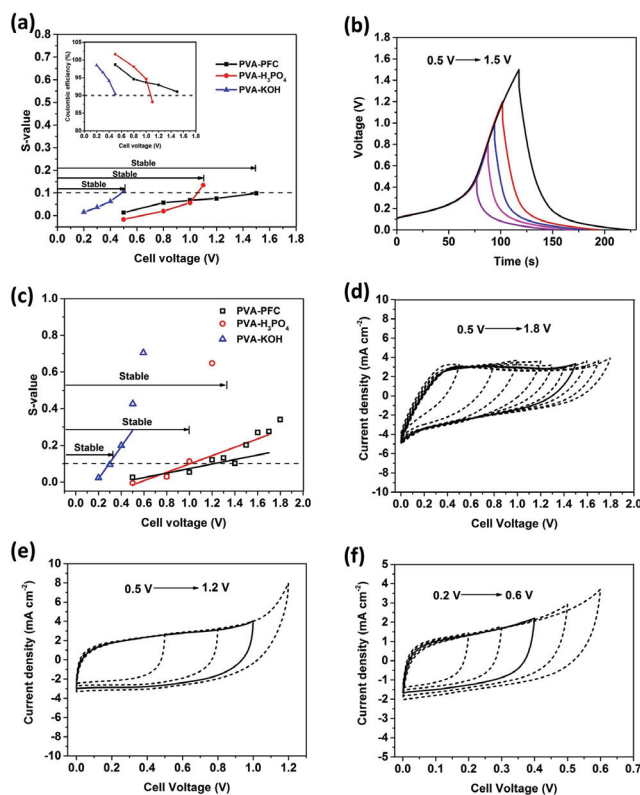
Fig. 2.6. Stability analysis for the two-terminal symmetric devices. (a) S-value evaluated from GCD measurements performed at a constant current density of 2 mA cm^{-2} with different operating voltage windows for the PVA-PFC, PVA-H$_3$PO$_4$ and PVA-KOH devices. The inset shows the variation of coulombic efficiency with cell voltage. (b) GCD profiles for the PVA-PFC device measured at a constant current density of 2 mA cm^{-2} while raising the operating potential window from 0.5 V to 1.5 V. (c) Variation of S with voltage window, derived from CV profiles acquired at a scan rate of 50 mV s^{-1} from the PVA-PFC, PVA-H$_3$PO$_4$ and PVA-KOH devices. (d) CV profiles measured on the PVA-PFC device at a scan rate of 50 mV s^{-1} while increasing the potential window from 0.5 V to 1.8 V. (e) CV profiles measured on the PVA-H$_3$PO$_4$ device at a scan rate of 50 mV s^{-1} while raising the potential window from 0.5 V to 1.2 V. (f) CV profiles measured on the PVA-KOH device at a scan rate of 50 mV s^{-1} while raising the potential window from 0.2 V to 0.6 V. The bold curves in (d)-(f) represent CV curves measured in the voltage window of maximum stability for the respective devices.
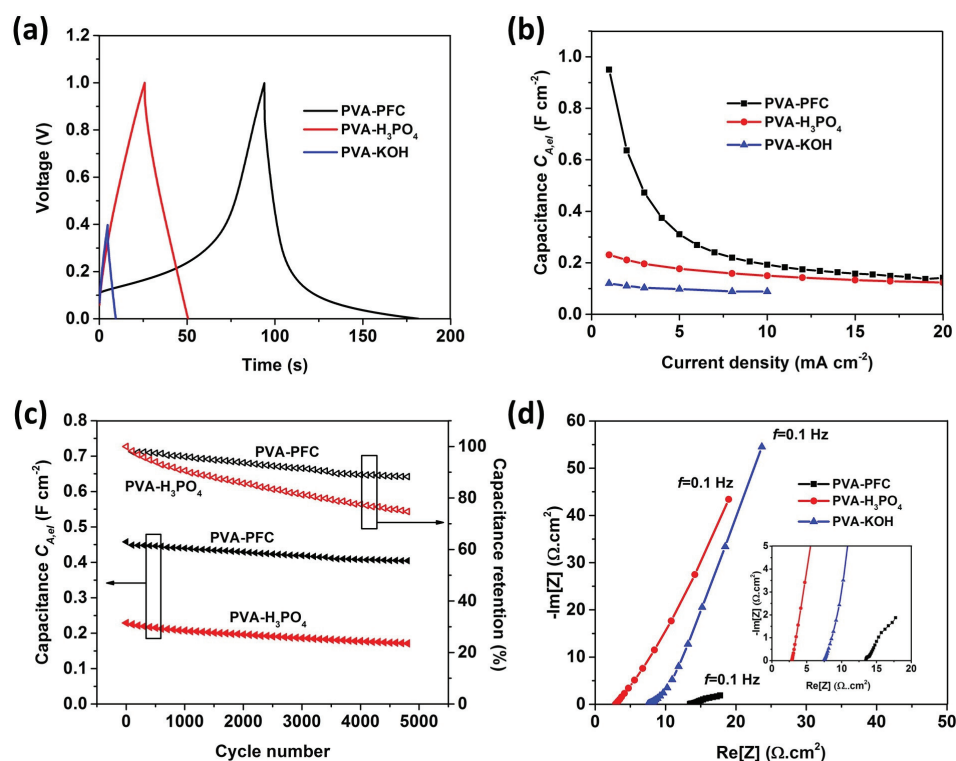
Fig. 2.7. Comparison of electrochemical performance of the fabricated two-terminal symmetric supercapacitor devices. (a) Constant current charge/discharge cycling profiles performed at a current density of 2 mA cm^{-2} in the voltage range of 0 and 1.0 V for the PVA-PFC and PVA-H$_3$PO$_4$ electrolyte based device, and in the voltage range of 0 and 0.4 V for the PVA-KOH device. (b) Electrode-specific areal capacitance $C_{A,el}$ evaluated from GCD curves, plotted as a function of current density in the range of 1 to 20 mA cm^{-2} (c) Capacitance retention (%) and absolute value of electrode-specific areal capacitance during cyclic GCD test performed in a potential window of 0 and 0.8 V. (d) Nyquist plot in the frequency range of 0.1 Hz and 100 kHz.
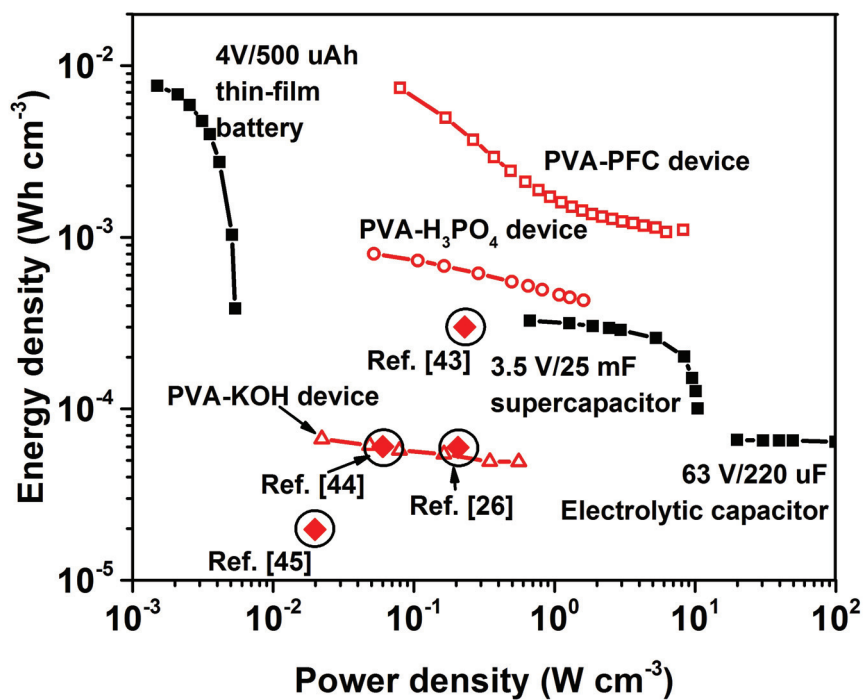
Fig. 2.8. Comparative volumetric energy and power densities (Ragone plot) of the fabricated devices with a typical Li-ion thin-film battery, electrolytic capacitor, a commercial supercapacitor (from ref. [65]), and other solid-state supercapacitors cited from refs. [45, 62–64]

2.4   Conclusions

In summary, we have fabricated and compared the electrochemical performance of two-terminal all-solid-state supercapacitor devices composed of redox-active gel electrolyte $PVA-K_3Fe(CN)_6-K_4Fe(CN)_6$ with electrochemically inert $PVA-H_3PO_4$ and PVA-KOH electrolytes. A nanoarchitecture based on BP/GP was selected as the electrode material by virtue of its mechanical robustness and large electrochemical surface area. The redox reactions of the ferrocyanide/ferricyanide redox couple lead to large capacitance especially at small current densities. Furthermore, the device exhibits a wider potential window compared to the other electrolytes, leading to larger overall energy and power density.

3. HARNESSING THE THERMOGALVANIC EFFECT OF THE FERRO/ FERRICYANIDE REDOX COUPLE IN A THERMALLY CHARGEABLE SUPERCAPACITOR
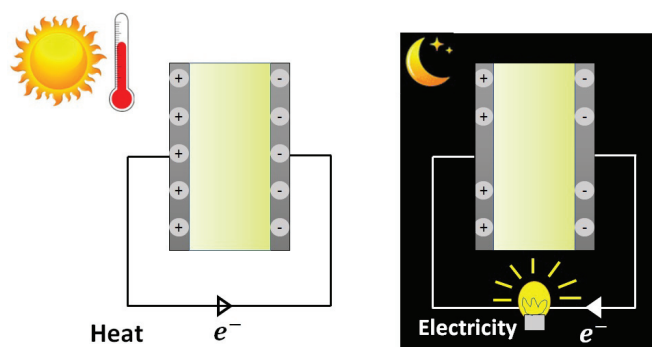
Some of the material in this chapter is currently under review in *Electrochimica Acta*.

3.1 Introduction

The requirements of today's portable and wearable electronic equipment have prompted the need to integrate 'on-chip' power supplies. Integrated flexible and compact energy storage permits low-power devices such as microprocessors, sensors and wireless communication chips to operate without any direct interface to an external power supply [24, 25]. One viable approach for such integrated stand-alone devices is to harness energy from low-grade waste heat that is abundantly available from various sources such as solar energy or automobile exhaust. Conventional thermoelectrics, typically inorganic semiconductors, are expensive which exhibit low Seebeck coefficients (10-100 μV/K). Hence new routes for thermoelectric conversion are be-

ing explored such as thermally driven ion migration [19, 66–68], mixed ion/electron diffusion [69, 70] thermogalvanic [37, 71] and thermomagnetic [72] effects .

Thermo-electrochemical cells (or thermocells) that exploit the thermogalvanic effect are quite appealing due to their low cost, simple design and operation near room temperature. Such devices based on the thermogalvanic effect generate steady electrical power upon application of a temperature gradient across two electrodes. The thermogalvanic Seebeck coefficient S_e due to a generic electron transfer reaction B→A+ne$^-$ is

$$S_e = \frac{\partial V}{\partial T} = \frac{\Delta s_{B,A}}{nF},$$
(3.1)

where V is electrode potential, T is temperature, $\Delta s_{B,A}$ is the reaction entropy for the redox couple, n is the number of electrons involved in the reaction, and F is the Faraday constant. Ikeshoji [73], Quickenden [74] and Burrow [75] were the first to report a high S_e value of -1.4 mV K^{-1} for ferrocyanide/ferricyanide aqueous solutions; this value is approximately one order of magnitude higher than those reported for conventional thermoelectric materials such as Bi$_2$Te$_3$ (ca. 0.2 mV K^{-1} [76]). Significantly high Seebeck coefficients have also been reported for electrolytes composed of cobalt complexes [77](1.9 mV K^{-1}) and triiodides [78] (2.0 mV K^{-1}).

In the past, researchers have demonstrated thermocells with enhanced performance by employing large surface area carbon electrodes [79–81]. The electrolyte most commonly used is aqueous ferrocyanide/ferricyanide due to its favourable properties, namely high Seebeck coefficient, low cost and high ionic conductivity. Furthermore, in order to boost the overall conversion efficiency, the electrical and thermal resistances were tuned by mixing carbon nanotube additives to such aqueous electrolytes [37, 82]. However, despite possessing high ionic conductivity values, aqueous electrolytes make large-scale integration and packaging cumbersome. Solid-state polymer gel electrolytes, in contrast, offer easy handling, improved safety, low internal corrosion, lightness, shape versatility and manufacturing simplicity. In a past report, Yang et al. [83] fabricated a pair of thermogalvanic gel electrolytes for use in wearable applications.

Although thermocells can generate continuous power from a steady temperature gradient, for intermittent sources additional energy storage devices are required to store the harvested energy. Recent studies have attempted to integrate both functionalities into a single device leading to overall system simplicity and suitability for waste heat harvesting. Zhao et al. [19, 66] demonstrated thermal charging with PEO-NaOH liquid polymeric electrolyte operating on the basis of Soret effect with a Seebeck coefficient greater than 11 mV/K. Similarly, Kim et al. [84] fabricated a thermally chargeable solid-state supercapacitor with polystyrene sulfonic acid electrolyte exhibiting a Seebeck coefficient of 8 mV/K. However, Zhao's device suffered from high self-discharge rates and other drawbacks associated with liquid electrolytes. Kim's solid-state device, the first of its kind, consisted of polyaniline coated electrodes that are expensive and complicated to implement. Moreover, the high thermo-induced voltage demonstrated in these studies does not translate to high energy density. Although the converted voltage can be easily amplified using an inexpensive voltage converter circuit, the low amount of stored energy is unaltered by voltage conversion.

A TCSC's net energy density [85] expressed as $E = 1/2C(S\Delta T)^2$ is influenced by both the capacitance C and the Seebeck coefficient S. The conventional approach to obtain high capacitance involves constructing electrodes consisting of electrochemically active materials coated on carbon materials with high surface area (e.g., graphene [86], activated carbon [87], carbon nanotubes [88], carbon fibers [89], vertical graphene nanosheets or graphene petals (GPs) [8]). However, such electrodes can exhibit low electrical conductivity and poor cyclic stability [90]. An innovative approach involves introducing redox additives such as quinone/hydroquinone [49, 91] or p-phenylenediamine [12, 39] into liquid or gel electrolyte that enhance capacitance through electron transfer redox reactions. Interestingly, the ferro/ferricyanide redox couple, in addition to being used as an electrolyte in thermocells for its thermogalvanic effect, also finds application as a redox additive to electrolytes in supercapacitors [92–94]. The electron transfer reaction at the electrode/electrolyte interface $Fe(CN)_6^{3-} + e^- \rightleftharpoons Fe(CN)_6^{4-}$ is found to be highly reversible and produces a consider-

able improvement in the overall capacitance. Ma et al. [94] found that the addition of potassium ferricyanide to PVA/KOH gel electrolyte improved ionic conductivity and increased capacitance from 137.8 F g^{-1} to 431 F g^{-1}. To date, this redox couple has not been systematically employed in any device to exploit both its thermogalvanic and pseudocapacitive properties at the same time.

In the present work, we combine this new thermogalvanic gel electrolyte, PVA/K$_3$Fe(CN)$_6$/ K$_4$Fe(CN)$_6$, with inexpensive carbon cloth electrodes to build an all-solid-state, lightweight, flexible thermally chargeable supercapacitor (TCSC). This device can be used as a stand-alone component to store charge from intermittent temperature gradients and then to supply on-demand power to portable electronic devices. It possesses high overall area-specific capacitance and low self-discharge rate, resulting in high energy density that can be harvested with minimum loss over a long period of time after 'thermal' charging. An equivalent circuit model of the device is also presented that produces identical voltage and current profiles as measured experimentally. This model furthermore is used to study the influence of parameters such as applied temperature gradient and load resistance on the energy storage characteristics of the device.

3.2   Results

3.2.1   Electrochemical Characterization of Electrodes

Carbon cloth (CC) has previously been employed as electrodes for supercapacitors primarily due to its large surface area. Scanning electron microscopy (SEM) images in Fig. 9.1 reveal the microstructure of pure carbon cloth at low and high magnifications. The average diameter of a single carbon fiber inferred from Fig. 9.1c is ≈ 9 μm. The porous nature of the carbon cloth allows for a large number of reaction sites for the ferro/ferricyanide ions to exchange electrons leading to large overall capacitance. In order to clarify the role of electrolyte on the overall electrochemical performance, cyclic voltammetry experiments were conducted in a three-electrode

configuration cell in a voltage window of 0-0.8 V, for two different electrolytes: (i) 0.2 M $K_3Fe(CN)_6/K_4Fe(CN)_6$ aqueous electrolyte and (ii) 1.0 M H_3PO_4. The CV curves corresponding to a scan rate of 50 mV s^{-1} are compared in Fig. 3.1a, while the area-specific capacitance values derived from the CV curves are shown as a function of scan rate in Fig. 3.1b. The CV curve for the ferrocyanide/ferricyanide electrolyte exhibits a large redox peak at 0.71 V which can be attributed to redox reaction through direct electron transfer process from $Fe(CN)_6^{4-}$ to $Fe(CN)_6^{3-}$. On the other hand, the CV for the H_3PO_4 electrolyte exhibits a more rectangular shape indicating only electrical double-layer contribution. At a scan rate of 5 mV s^{-1}, the area-normalized capacitance based on the projected area of the carbon cloth for the redox electrolyte is evaluated to be 2.8 F cm^{-2} that is almost 10 times larger than for the pure double-layer electrolyte. However, with rise in scan rate, the capacitance value declines rapidly for the redox electrolyte. At a scan rate of 100 mV s^{-1}, the areal capacitance value for the redox electrolyte is 0.25 F cm^{-2} which is merely 4 times that for the double-layer electrolyte. Past studies [32, 95] suggest that such observation can be attributed to insufficient time available for adsorption of $Fe(CN)_6^{4-}/Fe(CN)_6^{3-}$ ions onto the electrode surface at fast scan rates. In summary, the potassium ferrocyanide/ferricyanide electrolyte acts as a redox mediator which leads to large values of capacitance especially at low cycling rates.

The carbon cloth electrodes can be functionalized with different graphene nanostructures in order to attain high electrochemical surface area. In the past, GPs grown on carbon cloth (SEM images shown in Fig. 3.2) without any binder has shown promising results as active electrode materials in supercapacitors [9]. Thus, in order to investigate the influence of GPs on electrochemical performance, a comparison study was performed between bare carbon cloth (CC) and carbon cloth coated with graphene petals (CC/GP) as the working electrodes. Fig. 3.2 displays the three-electrode configuration cell test results for two working electrolytes: (i) a solution of 0.2 M $K_3Fe(CN)_6$ and 0.2 M $K_4Fe(CN)_6$, and (ii) 1.0 M H_3PO_4. The CC/GP electrode was oxidized in 1 M H_2SO_4 for 15 mins prior to the run, to turn the GPs
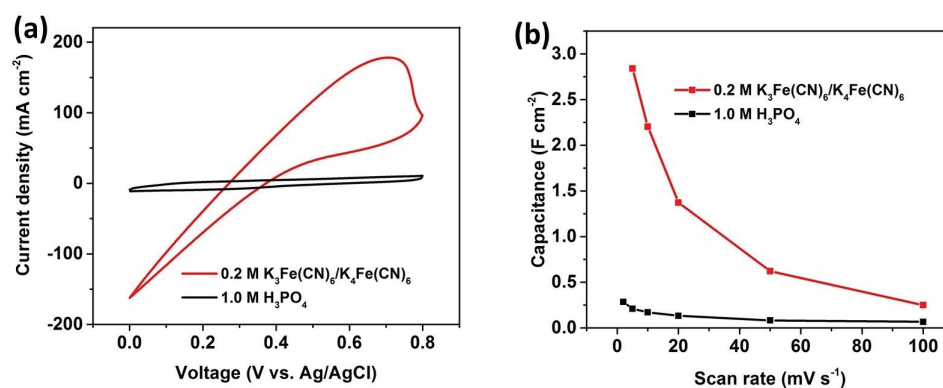
Fig. 3.1. (a) Electrochemical performance of bare carbon cloth (CC) in a three electrode configuration. Two electrolytes are used for comparison: (i) solution of 0.2 M $K_3Fe(CN)_6$ and 0.2 M $K_4Fe(CN)_6$ and (ii) 1.0 M H_3PO_4. Figure (a) displays the CV plot for scan rate 50 mV s^{-1} and Figure (b) shows the capacitance values derived from the CV curves at different scan rates.
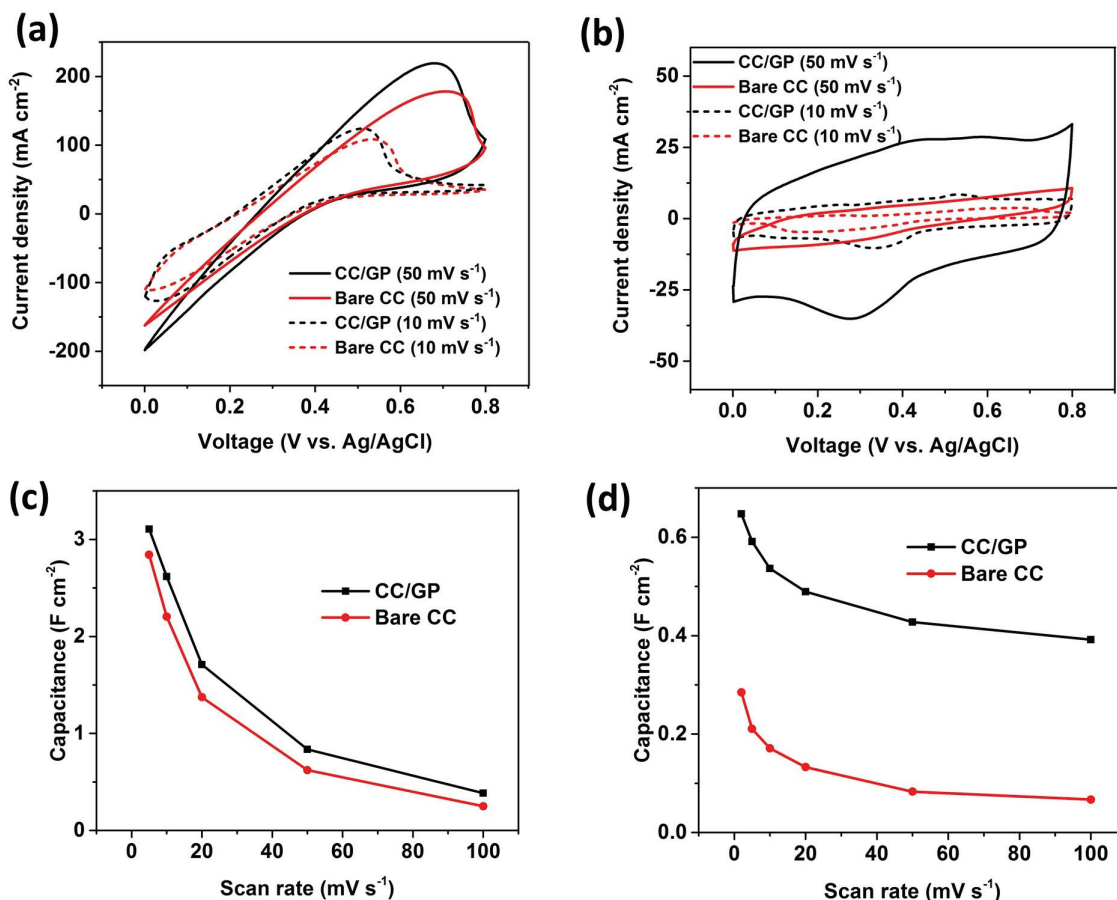
Fig. 3.2. Electrochemical performance of bare carbon cloth (CC) and graphene petal coated carbon cloth (CC/GP) electrodes in a three electrode configuration. (a) CV curves for a bare CC and CC/GP electrode at scan rates of 10 mV s^{-1} and 50 mV s^{-1} in mixture of 0.2 M $K_3Fe(CN)_6$ and 0.2 M $K_4Fe(CN)_6$ (b) CV curves for a bare CC and CC/GP electrode at scan rates of 10 mV s^{-1} and 50 mV s^{-1} in 1.0 M H_3PO_4 aqueous solution (c) Comparison of area-normalized specific capacitance of bare CC and CC/GP electrodes at different scan rates in 0.4 M $K_3Fe(CN)_6/K_4Fe(CN)_6$ aqueous solution (d) Comparison of area-normalized specific capacitance of bare CC and CC/GP electrodes at different scan rates in 1.0 M H_2SO_4 aqueous solution.

hydrophilic using the procedure described in a previous study [9]. Fig. 3.2b and 3.2d exemplify that the capacitance values for the pure double-layer electrolyte 1 M H_3PO_4 is larger in case of the CC/GP electrode compared to bare CC electrode. The CC/GP electrode offers a capacitance improvement of 2.3 and 5.9 times at scan rates of 2 and 100 mV s^{-1} respectively. Such result indicates that GPs offer larger electroactive surface area to ions present in the H_3PO_4 electrolyte. However, in case of the redox electrolyte, it is surprising that the GPs offer a minor improvement in capacitance at all scan rates as observed from Fig. 3.2a and 3.2c. Such result is presumed to be due to inaccessibility of the large ferrocyanide/ferricyanide ions to the porous structures of the GPs. In fact, such observation is quite common when the redox reactions at the electrode/electrolyte interface are diffusion controlled and the diffusion layer thickness is much larger than the size of the nanostructures [96]. Results shown in Fig. 9.3 illustrate that similar to present observations, two-electrode symmetric devices composed of CC/GP electrodes provide an insignificant improvement in electrochemical performance over devices composed of bare CC electrodes.

3.2.2 Thermally Chargeable Supercapacitor Based on PVA/$K_3Fe(CN)_6$/ $K_4Fe(CN)_6$ Polymer Gel Electrolyte

The all-solid-state symmetric supercapacitor device used to demonstrate thermal charging is fabricated by sandwiching a piece of gel electrolyte film between two bare carbon cloth electrodes. The gel electrolyte is composed of an aqueous solution of poly(vinyl alcohol) (PVA) and potassium ferricyanide/ferrocyanide redox couple (see Experimental section for preparation details). It serves the dual purpose of a solid electrolyte and a thermoelectric generator. The device is encased in a nylon film package to prevent electrolyte evaporation. The assembly consisting of the electrodes, gel film, nylon film packaging, fabrics and copper wires is flexible and pliable enough to accommodate a wide variety of heat source shapes. A sketch depicting the structure of the flexible TCSC is provided in Fig. 3.4a.

Before testing the thermoelectric properties of the two-terminal symmetric device, its electrochemical performance is characterized using galvanostatic charge/discharge (GCD), cyclic voltammetry (CV), electrochemical impedance spectroscopy (EIS) and cyclic stability tests. Galvanostatic charge/discharge (GCD) profiles are shown in Figure 3a for current densities ranging from 0.2 to 1.0 mA cm^{-2} in the potential window of 0 and 0.1 V (profile at current density of 0.1 mA cm^{-2} shown in Figure S5a). The semi-symmetric shape of the charge/discharge curves is indicative of high Coulombic efficiency and stable capacitance. The area-normalized specific capacitance can be derived from the curves using the relation [97],

$$C_{s1} = \frac{I_d}{\nu},\tag{3.2}$$

where I_d is the discharge current density and ν is the slope of the voltage profile after the IR drop. C_{s1} is shown as a function of the charge/discharge rate (current density) in Figure 3c. At a constant current density of 0.1 mA cm^{-2}, the calculated area-specific capacitance is 9.5 F cm^{-2}. This value is more than an order of magnitude higher than what was obtained in the past two studies on thermally chargeable supercapacitors [19, 84]. It can be attributed to the pseudocapacitive contribution of the redox species (also evident from the redox peaks in the CV curves shown in Figure S5c) which are absent in case of pure double-layer electrolytes. Furthermore, the area-specific capacitance shows a decreasing trend with discharge current density because at high cycling rates, the ions dont have enough time to exchange electrons with inner active sites of the porous carbon electrode [98]. The internal resistance calculated based on the IR voltage drop at the beginning of discharge (shown in Figure S5b) is 71 Ω at a current density of 1 mA cm^{-2} which can be considered quite large and is caused by the low ionic conductivity of the gel electrolyte.

Electrical impedance spectroscopy was carried out to probe the electrochemical behavior of the device in the frequency range of 10 mHz and 100 kHz with ac voltage amplitude set at 5 mV and dc bias at 0 mV. As shown in Figure 3b, the Nyquist plot displays the variation of the real part of the impedance $Z_{Re}(f)$ vs. the imaginary
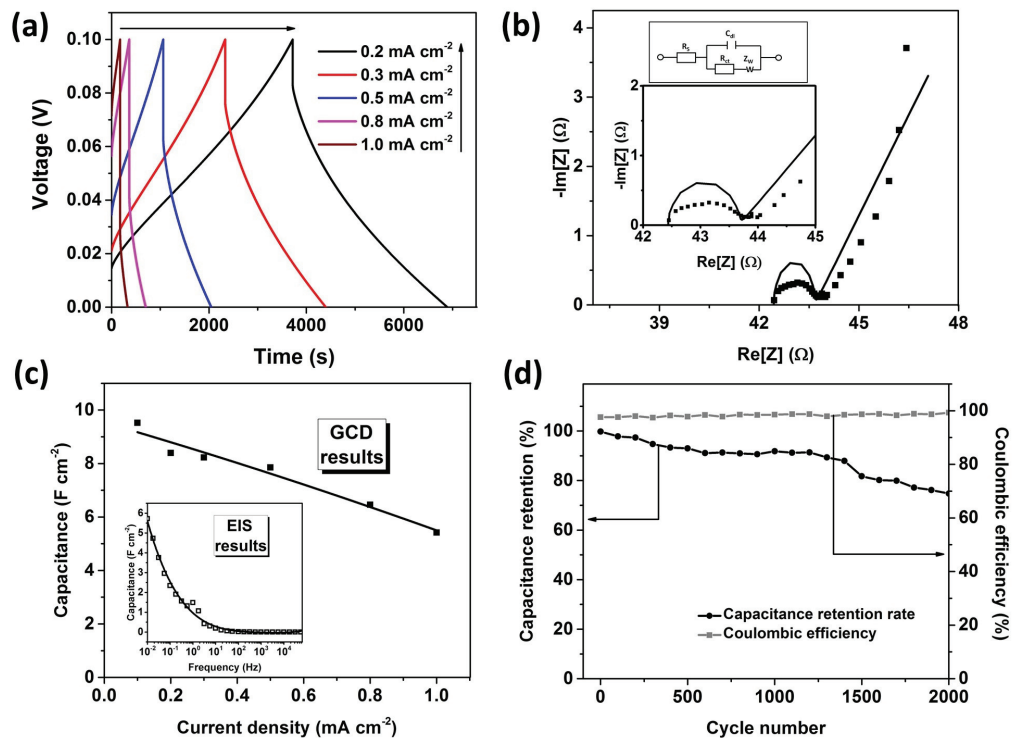
Fig. 3.3. Electrochemical performance of an all-solid-state two-terminal symmetric supercapacitor device consisting of bare carbon cloth electrodes and 1.5 mm thick gel electrolyte film. (a) Galvanostatic charge-discharge curves at constant-current densities in the range of 0.2 to 1.0 mA cm^{-2}. (b) Nyquist plot in the frequency range of 10 mHz and 100 kHz.(c) Area-specific capacitance versus current density obtained from constant current curves. The inset shows area-specific capacitance vs frequency obtained from Nyquist plot. (d) Charge/discharge cycling test at a current density of 5 mA cm^{-2}, showing $\approx 8\%$ loss over 1000 cycles and $\approx 25\%$ loss after 2000 cycles.

part, $-Z_{Im}(f)$ where f is the frequency. The plot consists of two distinct segments: a distorted semicircle in the high frequency region and a sloped line in the low frequency region. The x-intercept in the plot represents the internal resistance of the electrode material and electrolyte of the device, while the semicircle represents the charge transfer resistance corresponding to the Faradic reaction occurring at the electrode/electrolyte interface. The sloped line in the low frequency regime represents
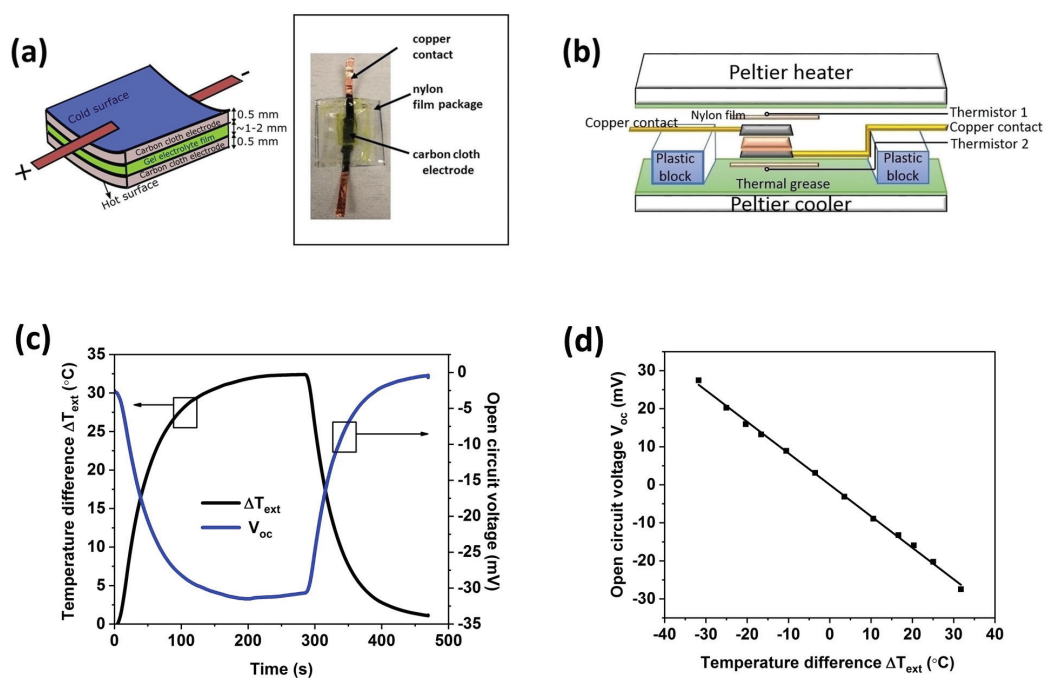
Fig. 3.4. (a) Sketch of the thermally chargeable supercapacitor (TCSC) and photograph of the actual device in inset. (b) Schematic of the test platform for thermoelectric measurements. (c) and (d) show thermoelectric properties of a symmetric device obtained by sandwiching a 1.5 mm thick PFC gel electrolyte film between two bare carbon cloth electrodes. Plot of open-circuit voltage V_{oc} and applied temperature difference ΔT_{ext} as a function of time is displayed in (c), while the plot of steady state V_{oc} versus ΔT_{ext} is shown in (d).

the ion diffusion/transport at the electrode surface [71]. The area-specific capacitance derived from the Nyquist plot using the relation [99],

$$C_{s2} = -1/(2\pi f A Z_{Im}).$$ (3.3)

is shown as a function of frequency in the inset of Figure 3c. Following the trend of C_{s1}, the calculated value decreases from 5.7 F cm^{-2} at a frequency of 10 mHz to 1.5 F cm^{-2} at a frequency of 1 Hz. Long-term cyclic life is a crucial factor for practical applicability of such devices. The cyclic stability tests for the device at a constant current density of 5 mA cm^{-2} show a mere 8% loss in specific capacitance after 1000 cycles and 25% loss after 2000 charge-discharge cycles with $\approx$100% Coulombic efficiency as shown in Figure 3d.

The thermoelectric properties of the device is tested by sandwiching it in beteeen a Peltier heater and cooler as shown in Figure 4b. A thermistor is attached to each face of the external casing in order to monitor the applied temperature difference ΔT_{ext}. The open circuit thermovoltage V_{oc} is recorded for different values of ΔT_{ext} by varying the hot and cold side temperatures in the range of 19 to 63 °C and 13 to 19 °C respectively. The transient plot shown in Figure 4c reveals that the open circuit voltage V_{oc} closely follows the variation of the applied temperature gradient ΔT_{ext} with respect to time. Furthermore, the steady state value of thermo-induced voltage was recorded for different ΔT_{ext} values (each held fixed for 3 min). The plot shown in Figure 4d establishes a linear relationship between the observed V_{oc} and the applied temperature gradient ΔT_{ext} (time-dependent results shown in Figure S6a) in both positive and negative regimes. The effective Seebeck coeffcient S_{eff}, is then back-calculated using the measured open circuit voltage V_{oc} and the measured temperature difference across the two faces of the device ΔT_{ext} through

$$S_{eff} = \frac{V_{oc}}{\Delta T_{ext}}.$$ (3.4)

As expected, the S_{eff} magnitude evaluated from the slope, 0.86 mV K^{-1} is lower than the characteristic Seebeck coefficient of the ferrocyanide/ferricyanide redox couple (1.21 mV K^{-1}). The ratio between the two is 0.71 which is about a factor of 7
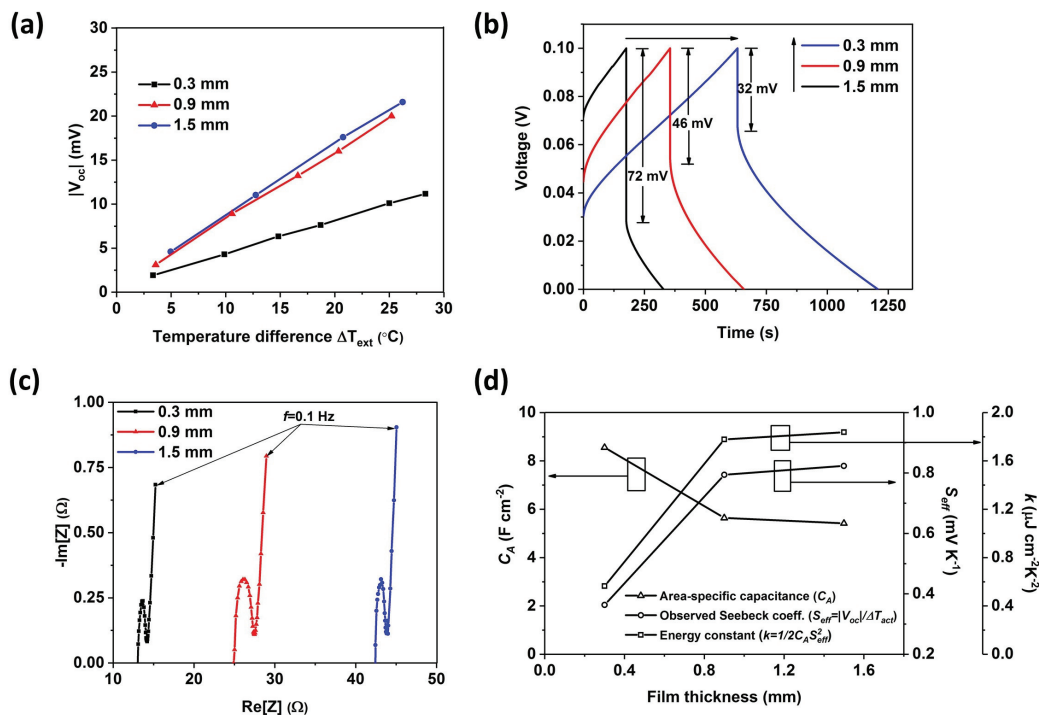
Fig. 3.5. (a) Thermally induced open circuit voltage as a function of the externally applied temperature gradient ΔT_{ext} for devices with gel film thickness 0.3 mm, 0.9 mm and 1.5 mm. (b) Galvanostatic charge/discharge profiles at a constant current density of 1 mA cm^{-2} for devices with gel film thickness 0.3 mm, 0.9 mm and 1.5 mm. (c) Nyquist plots for EIS tests conducted in the frequency range of 0.1 Hz and 100 kHz for TCSC devices with film thickness 0.3 mm, 0.9 mm and 1.5 mm. (d) Area-specific capacitance, C_A derived from galvanostatic charge/discharge cycling at a current density of 1 mA cm^{-2}, effective Seebeck coefficient S_{eff} and energy constant $k = 1/2C_A S_{eff}^2$ plotted as a function of gel film thickness.

higher than found for a plastic thermocell based on ferrocyanide/ferricyanide redox electrolyte [71].

3.2.3 Thermally Chargeable Supercapacitor Design Parameters

Cyclic voltammetry tests performed in a three-electrode configuration cell descibed previously in Section 2.1 illustrate the role of the ferrocyanide/ferricyanide ions

present in the aqueous electrolyte as a redox mediator. In addition to double-layer formation, the ions engage in redox reactions at the electrode/electrolyte interface during charge/discharge that results in enhanced capacitance. In order to confirm the pseudocapacitive behavior of the ferrocyanide/ferricyanide redox couple present in the gel electrolyte, a comparison of electrochemical performance is conducted between solid-state devices composed of PVA/H_3PO_4 and $PVA/K_3Fe(CN)_6/K_4Fe(CN)_6$ gel electrolyte films each 0.9 mm thick. Both devices are built of bare CC electrodes. The galvanostatic charge/discharge (GCD) curves corresponding to a current density of 1 mA cm^{-2} are displayed in Figure S4. For both devices, the curves are symmetric in nature. However, the curve for the redox electrolyte exhibits a larger area that corresponds to larger capacitance. The areal capacitance values are evaluated to be 5.5 F cm^{-2} for the device composed of $PVA/K_3Fe(CN)_6/K_4Fe(CN)_6$ gel electrolyte, and 0.167 F cm^{-2} for the device composed of PVA/H_3PO_4 gel electrolyte. Thus, the pseudocapacitive contribution of the ferrocyanide/ferricyanide ions leads to 33 times higher capacitance for a small operating current density of 1 mA cm^{-2}.

Furthermore, in order to investigate the influence of electrode surface area on the device performance, a comparison of area-normalized specific capacitance was performed for TCSC devices composed of bare CC and CC/GP electrodes at a low current density of 0.1 mA cm^{-2}. The results shown in Fig. 9.3 indicates that the device capacitance improves by ¡5% at all scan rates upon replacing bare CC electrodes with CC/GP electrodes. This corroborates with the inference drawn from three-electrode cell configuration test results shown in Fig. 3.2. Because the GPs contribute marginally to the performance, bare CC is used to prepare electrodes for the TCSC device.

The thickness of the gel electrolyte film plays a major role in determining the device performance. A thick film is expected to boost the effective Seebeck coefficient S_{eff}, however it may adversely affect ion transport leading to poor areal capacitance. As explained earlier, the energy storage in the device is proportional to the product of areal capacitance and square of S_{eff} . Therefore, both parameters need to be

maximized in order to attain high energy storage density. Here, we have investigated these two performance parameters separately for devices with film thickness values of 0.3 mm, 0.9 mm and 1.5 mm. Fig. 3.5a shows the thermo-induced open circuit voltage V_{oc} as a function of ΔT_{ext} for the three devices. The thermo-induced V_{oc} can be observed to rise linearly with applied temperature gradient in all cases (time-dependent results shown in Fig. 9.6). However, the slope is much larger for the 0.9 mm film device compared to the 0.3 mm film device that corresponds to higher temperature difference induced across the two faces of the film. The slope increases marginally with rise in film thickness from 0.9 mm to 1.5 mm, which indicates that the ratio of the thermal resistance of the film to thermal resistance of the overall device does not vary significantly for film thickness greater than 0.9 mm.

Fig. 3.5b shows the galvanostatic charge/discharge curves for the three devices, all at a constant current density of 1 mA cm^{-2}. The areal capacitance derived from the CV curves is shown as a function of the gel film thickness in Fig. 3.5d. It can be observed that the areal capacitance drops in value with rise in film thickness. The areal capacitance decreases from a value of 8.6 F cm^{-2} for a film thickness of 0.3 mm to a value of 5.5 F cm^{-2} for a film thickness of 0.9 mm. In order to compare the thermally-induced energy storage for the films, the energy coefficient defined as $k = 1/2 C S_{eff}^2$ is evaluated for all three devices. Fig. 3.5d shows that k follows the trend of the effective Seebeck coefficient and is highest for the 1.5 mm thick film. Therefore, we decided to use the 1.5 mm thick film in our thermoelectric measurements.

The Nyquist plot shown in Fig. 3.5c exhibits rising value of x intercept with increase in film thickness. Using the slope of rise of the x intercepet with thickness, the bulk ionic conductivity of the electrolyte using

$$\sigma = \frac{1}{s.A} \tag{3.5}$$

is estimated to be 5.44 mS cm^{-1} which is similar to the value determined by Yang et al. [83] for the same gel electrolyte (6 mS cm^{-1}) at room temperature. Here, s
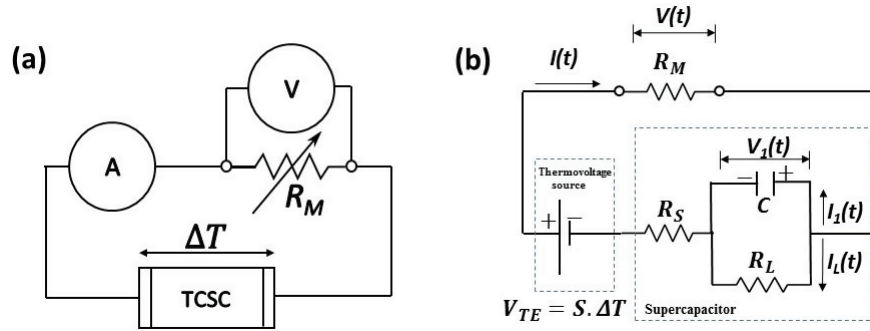
Fig. 3.6. (a) Bias circuit used for the thermoelectric measurements. (b) Equivalent circuit for the device and the load resistor. The device is modeled as a series combination of a thermovoltage power source and supercapacitor (represented by a Randles circuit).

represents the slope of variation of x-intercept in the Nyquist plot with film thickness, and A is the projected area of each electrode.

3.2.4 Demonstration of Thermal Charging Phenomenon

Fig 3.6a shows the bias circuit used to investigate the thermal charging phenomenon. The device is connected in series with a variable resistor R_M while a temperature gradient ΔT_{ext} is applied across its two surfaces. The time variant voltage and current across the variable resistor is recorded with the help of data acquisition boards NI-DAQ 9215 and NI-DAQ 9203 respectively at a sampling rate of 100 samples per second. Fig. 3.7 shows the measured transient electrical response of the device during one typical thermal charging cycle. In order to charge the device thermally, a steady temperature gradient ΔT_{ext} of 50 °C was applied across its faces, while shorting its two terminals externally. The charging current density induced by the thermovoltage rises from 0 to a value of -0.6 mA cm^{-2}, as the external temperature gradient attains its steady-state value. As the device continues to charge gradually under application of the constant temperature gradient, the current decays slowly to finally reach a value close to 0. The long charging time (3600 s) can be attributed to
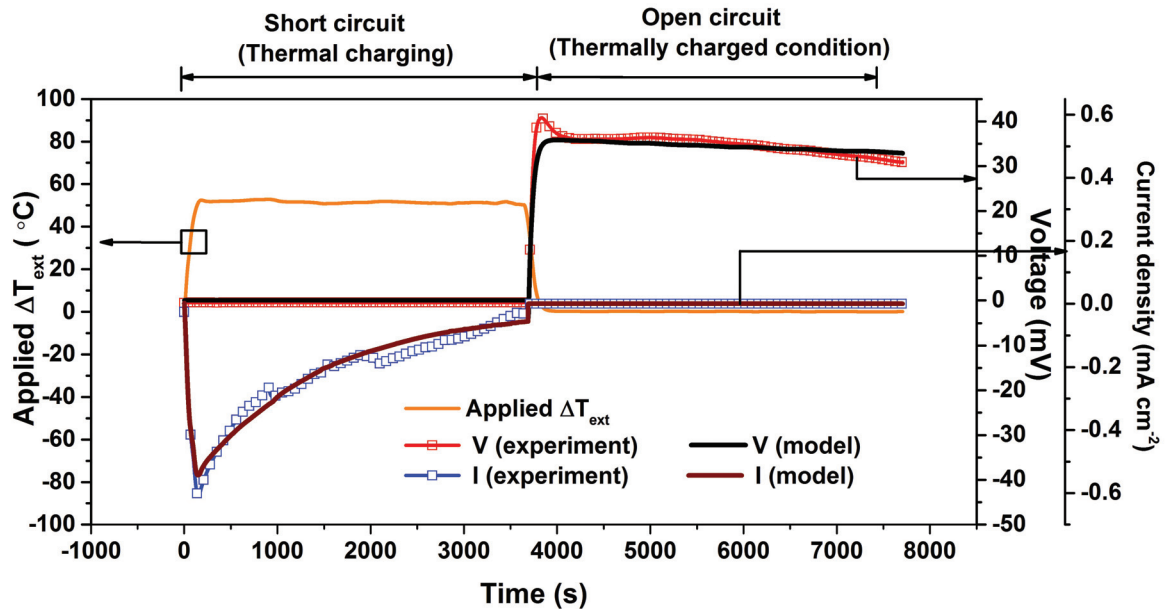
Fig. 3.7. Demonstration of thermal charging with a ΔT_{ext} value of 50 °C. To begin with, the device is externally short-circuited while the temperature gradient is applied. When the charging current approaches zero, the circuit is opened and the temperature gradient is removed. The thermally charged V_{oc} is observed for a period of 5000s.

the high RC time constant of the device. At the end of the thermal charging process, the circuit is opened and the voltage across the terminals is recorded as a function of time. As soon as the temperature gradient is removed, the open circuit voltage increases from 0 to 41 mV. Because of self-discharge, the thermo-induced open circuit voltage drops to 31 mV in the next 4100 s. We note that the observed charge retention capability compare favorably to a similar TCSC device [19] (decay from 150 mV to 0 in 1600s).

Fig. 3.8 compares the thermo-induced voltage corresponding to ΔT_{ext} of 30 and 50 °C. In both the cases, the rise in thermo-induced voltage coincides with decline in the applied temperature gradient. The thermo-induced V_{oc} for $\Delta T_{ext} =$30 °C peaks at 22.2 mV which slowly declines to 16.3 mV at the end of 2500 s due to self-discharge. In the latter case, the decay in V_{oc} is comparatively less abrupt at the beginning, and the thermal charging time (for the charging current to reach 0) is much lower, 1041 s compared to 3600s for $\Delta T_{ext} =$50 °C.

The observed thermal charging phenomenon can be explained by the sequence of steps shown in Fig. 3.9. Initially, the gel electrolyte consists of ferrocyanide and ferricyanide ions randomly oriented in a polymer matrix (State 1). When the temperature of one electrode is raised with the aid of waste heat, it causes a change in the redox potential of the electrolyte, triggering the reaction $\text{Fe(CN)}_6^{4-} \rightarrow \text{Fe(CN)}_6^{3-} + \text{e}^-$. The reverse reaction does not occur at the cold electrode due to dearth of excess electrons. The accumulation of electrons at the hot electrode leads to a negative open circuit voltage (State 2). When the electrodes are externally connected through a load resistor, electrons flow from the hot to cold electrode where they reduce the neighboring ferricyanide ions to ferrocyanide ions (State 3) while also generating some useful electrical work in the load resistor. This process represents 'thermal charging' of the supercapacitor and continues until the ion concentrations near the electrodes reach saturation, at which point the current through the external circuit decays to zero (State 4).
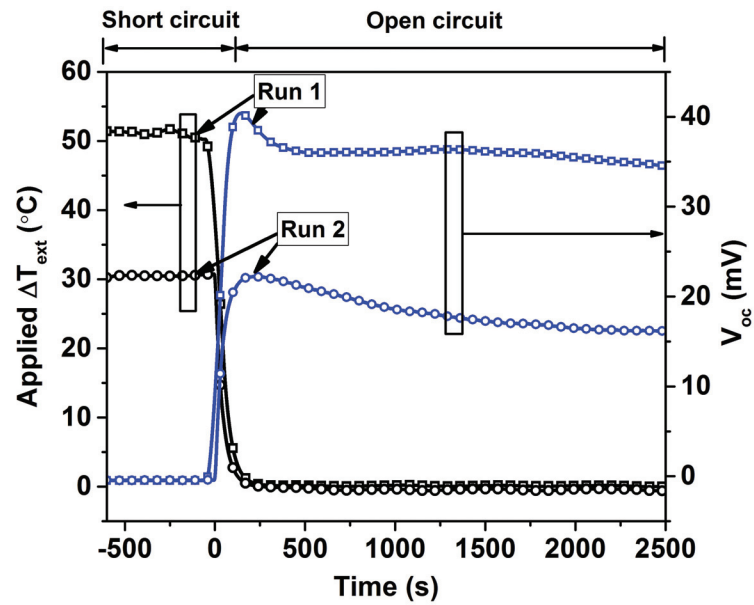
Fig. 3.8. Open circuit voltage profiles for two runs with ΔT_{ext} values of 50 ° C and 30° C. In both the runs, the device is thermally charged at a constant ΔT_{ext} under a short-circuit condition, following which the temperature gradient is removed and the open circuit voltage is measured.
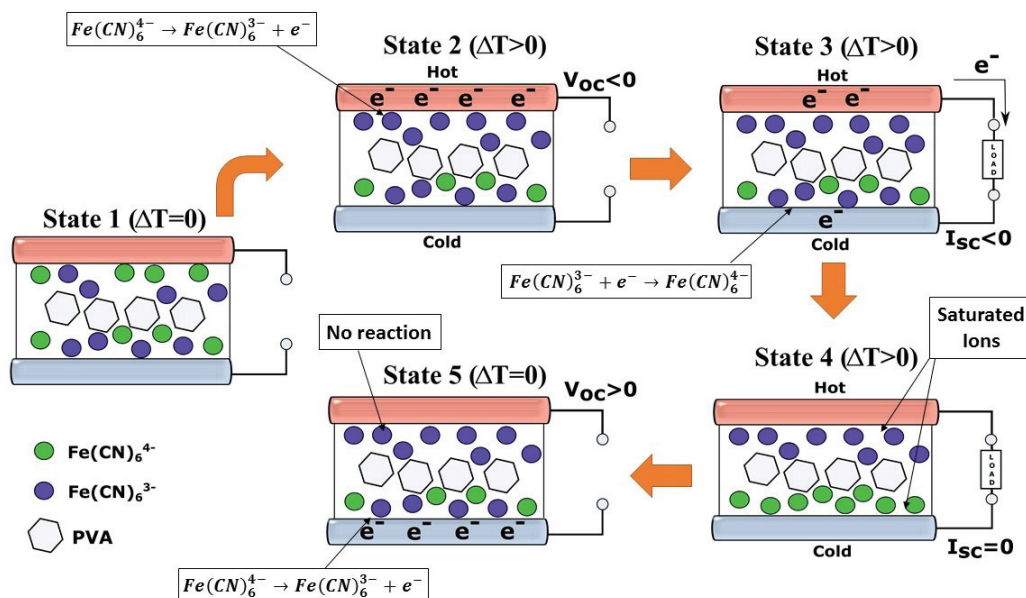
Fig. 3.9. Working mechanism of the thermally chargeable supercapacitor (TCSC). State 1:Discharged (initial) state with ferro/ferricyanide ions dispersed randomly in PVA matrix. State 2: When a temperature gradient is applied under open-circuit condition, the ferrocyanide ions at the hot electrode react to generate ferricyanide ions and electrons. State 3: Electrons generated by the reaction transfer to the cold side and reduce the neighboring ferricyanide ions to ferrocyanide ions upon shorting the two electrodes externally with a load resistor. State 4: The current drops to zero when all the ions on the hot (cold) side are oxidized (reduced). State 5: When the temperature gradient is removed and the load resistor is disengaged, the ferrocyanide ions at the cold electrode react to generate electrons. These electrons on the cold side produce an open circuit voltage present across the device at zero temperature gradient.

The reaction products remain localized near the hot and the cold electrodes due to their inability to travel through the tortuous path of the PVA polymer matrix. Such a characteristic is evidenced by the low ionic conductity of the PVA/$K_3Fe(CN)_6$/ $K_4Fe(CN)_6$ gel electrolyte used in this work (6 mS cm^{-1} [83]) compared to that of 0.4 M $K_3Fe(CN)_6$/ $K_4Fe(CN)_6$ aqueous electrolyte (170 mS cm^{-1} [37]). Upon removing the temperature gradient, both electrodes return to ambient temperature causing the electrolyte redox potential near the electrodes to change, this time in the direction opposite to State 2. The ferrocyanide ions near the cold electrode become oxidized to generate ferricyanide ions and electrons at the electrode, leading to a positive open circuit potential (State 5). We note that the reverse reaction does not occur at the hot electrode upon equilibration due to lack of excess electrons. State 5 represents the 'thermally charged' state of the supercapacitor.

3.2.5   Equivalent Circuit Model

The mechanism of TCSC operation explained in the previous subsection is further elucidated here with the help of an equivalent circuit model. Because the TCSC performs the dual function of a thermoelectric generator and a supercapacitor, we propose that it can be effectively modeled by a series combination of a thermo-induced voltage source and a supercapacitor. The supercapacitor is modeled as a Randles equivalent circuit as shown in Fig. 3.6b. The voltage source V_{TE} is assumed to be the product of the Seebeck coefficient S of the gel electrolyte and the temperature difference across the faces of the gel film, ΔT_{act} across the two surfaces of the gel electrolyte. S was found to be -1.21 mV/K for the gel electrolyte [83] over the range of ΔT from 0-20 K, and the same value is used here. The parameter R_S represents the ion transport resistance in the electrolyte, C represents an ideal capacitor at the electrode-electrolyte interface that stores charge during charging and releases charge during discharging, while R_L represents the leakage resistance in the device that causes self-discharge under an open-circuit condition. The load resistance used in

the thermal charging and discharging phases are termed R_{mc} and R_{md} respectively. The voltage across the load resistor and the capacitor C are denoted by V and V_1 respectively. The current flowing through the load resistor, capacitor C and the leakage resistor R_L are represented by I, I_1 and I_L respectively. The model values of V and I across the load resistor are later used to validate the experimental results.

The timeline can be broken into 3 phases: thermal charging (Phase 1), hold (Phase 2) and discharge (Phase 3). Initially, the TCSC circuit is open, and both V_{TE} and V_1 are zero. In Phase 1, a load resistance R_{mc} is installed while maintaining a positive temperature gradient ΔT across the device. The thermo-induced voltage V_{TE} rises to $S\Delta T$, which then charges the capacitor C. The capacitor voltage V_1 increases gradually with time, while the charging current I decays slowly. The charging current is determined from

$$V_{TE} - V - V_1 - IR_S = 0. \tag{3.6}$$

In Phase 2, the temperature gradient is removed, and the external load is disengaged. This causes the thermovoltage V_{TE} to disappear and the open circuit voltage to attain the value of $-V_1$. Under open-circuit conditions, the TCSC should ideally maintain a constant voltage; however the presence of parasitic shunt paths in the device results in self-discharge that causes a slight decay in the open circuit voltage. V_1 is obtained from

$$
\begin{aligned}
I_L R_L + V_1 &= 0, \\
I_L &= C\frac{dV_1}{dt}.
\end{aligned}
\tag{3.7}
$$

In Phase 3, the circuit is closed once again with a load resistor R_{md}, and the unknown voltage and current values are determined using

$$V_1 = -I(R_S + R_{md}). \tag{3.8}$$

Detailed analytical expressions of voltage and current across the load resistor during different phases of the cycle are listed in the Supplementary Information. t_1, t_2 and t_3 represent time values from the beginning of Phases 1-3 respectively. The durations of

Phases 1-3 are t_1, t_2, and t_3 respectively. The unknown parameters in the model are obtained by fitting expressions for voltage and current with the measurements. The procedure used for fitting is illustrated in Fig. 3.10. The combination of parameters resulting in the minimum value of the total mean square error (MSE_{tot}) is selected to represent the circuit parameters. MSE_{tot} is chosen to be the sum of the normalized mean square error for voltage and for current, thereby giving them equal weight. The normalized MSE for the ith combination of parameters is defined as

$$MSE_{X,i} = \frac{\sum_{t=0}^{t=t_f}(X_{model,i}(t) - X_{exp}(t))^2}{\sum_{i=1}^{n}\sum_{t=0}^{t=t_f}(X_{model,i}(t) - X_{exp}(t))^2}, \tag{3.9}$$

where X stands for voltage or current, and n is the number of combinations of the fitting parameters.

Because the equivalent circuit is found to provide an excellent fit with the experimental results, it can be used as a convenient tool to analyze the role of the tunable parameters namely load resistance in the thermal charging phase R_{mc}, thermal charging phase duration, and hold phase duration. The performance indices obtained from the model are as follows.

The amount of charge stored in the capacitor in the thermal charging phase Q_c is obtained by integrating the capacitor charging current I_1 over time from 0 to t_1. During charging, I_1 decreases exponentially with time while V_1 gradually rises to the equilibrium voltage. The value of Q_c upon complete charging (I_1=0) can be expressed as CV_{eff} where V_{eff} is $S\Delta T\frac{R_L}{R_L+R_S}$. However, we note that the duration required for the device to charge completely may be quite long. For small charging durations, the capacitor is not completely charged by the end of the thermal charging phase. The charge released by the capacitor during discharge Q_{dc} is calculated by integrating I_1 with time from $(t_1 + t_2)$ to $(t_1 + t_2 + t_3)$. The charge retention ratio is defined as $\beta = \frac{Q_{dc}}{Q_c}$ and denotes the fraction of charge retained by the device during the hold phase.
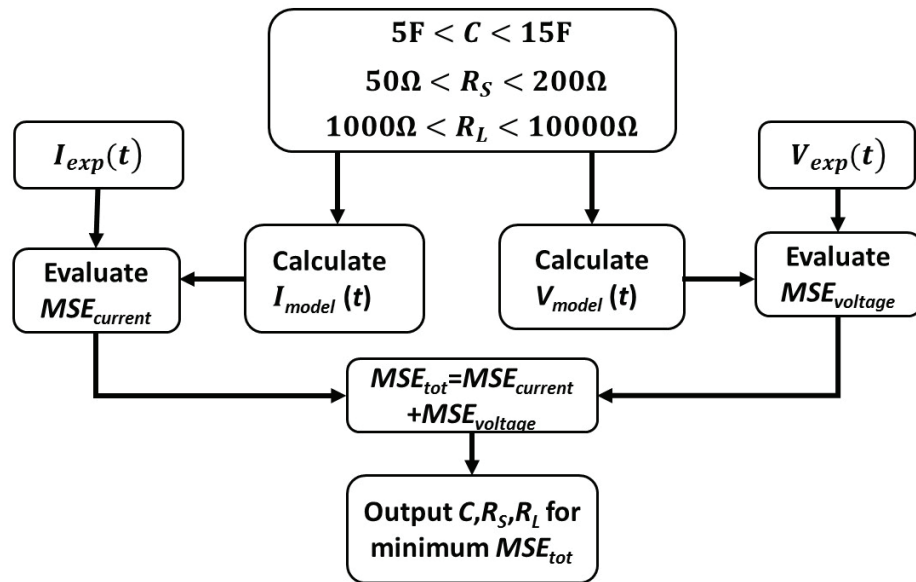
Fig. 3.10. Flow chart for calculating Randles circuit parameters for the thermally chargeable supercapacitor.

The amount of energy supplied by the thermovoltage source during the thermal charging phase is given by

$$E_{in,ch} = \int_0^{t_1} I.V_{TE}dt. \tag{3.10}$$

This energy is distributed among the circuit elements R_{mc}, R_S, C and R_L:

$$E_{in,ch} = E_{Rm,ch} + E_{C,ch} + E_{Rs,ch} + E_{Rl,ch} \tag{3.11}$$

$E_{Rs,ch}$ and $E_{Rl,ch}$ are energy losses in the series and leakage resistors, while $E_{Rm,ch}$ is the energy output in the load resistor. $E_{C,ch}$ is the energy stored in the capacitor. A fraction of this energy is lost during the hold phase due to current flow through the leakage resistance R_L. In the discharging phase, the stored energy is distributed among the load resistor R_{md}, series resistor R_S and the leakage resistor R_L. The thermovoltage source is absent in both the hold and discharging phases. The energy balance in the discharging phase can be written as,

$$-E_{C,dc} = E_{Rm,dc} + E_{Rs,dc} + E_{Rl,dc} \tag{3.12}$$

where $E_{C,dc}$ represents energy stored in the capacitor C, and $E_{Rm,dc}$, $E_{Rs,dc}$ and $E_{Rl,dc}$ represent energy lost in R_{md}, R_S and R_L respectively. A point to note here is that $E_{C,dc}$ is negative because the capacitor loses energy during discharge.

3.2.6 Model Fitting

To estimate the areal capacitance of the TCSC device, model fitting based on the full equivalent circuit in Fig. 3.6b was performed on the measured voltage and current profiles. Current and voltage profiles were fitted by iterating over combinations of the free parameters in the Randles equivalent circuit. Values of the parameters that resulted in optimal voltage and current fit are: R_S=144 Ω, R_L=4100 Ω, C=10 F. Fig. 3.7 shows that the fitted model current and voltage profiles follow the experimental results quite closely. The value of MSE_{total} obtained for the optimal fit is evaluated to be 6.59×10^{-5}, which is indicative of a very good fit. The areal capacitance 13.3 F

cm^{-2} is comparable to that derived from galvanostatic charge/discharge cycling at a current density of 0.1 mA cm^{-2} (9.5 F cm^{-2}).

3.2.7   Stored Charge and Energy Calculations

In Section 2.4, the thermal charging phenomenon was demonstrated by allowing the device to 'thermally' charge under closed circuit codition. Furthermore, the thermally induced open-circuit voltage was retained for a long time to investigate its self-discharge rate. This time, in order to estimate the amount of charge and energy stored in the TCSC device corresponding to the thermo-induced voltage, the 'thermally' charged TCSC device is connected in series to a load resistor after a hold period of 1000 s, and the voltage and current across the load resistor is monitored. Similar changes are made during the 'thermal' charging phase, the device is connected to a 330 Ω resistor instead of short-circuiting. Thus, even during the 'thermal' charging stage, some useful amount of work is obtained. In principle, the load resistor can be varied to tune the useful work output and the charging speed of the device.

Fig. 3.11a displays the voltage profiles obtained across the load resistor corresponding to applied ΔT_{ext} values of 25, 35 and 50 °C. The current profiles in phases 1 and 3 can be obtained by dividing the measured voltage V by R_M. The voltage variation is similar in all three runs and has a negative peak during phase 1 which thereafter slowly saturates to zero. Upon open-circuiting, the voltage rises to a positive value swiftly. This positive voltage value representing the thermo-induced voltage is discharged with a load resistor during the discharge phase. The output energies in phase 1, $E_{Rm,ch}$ and in phase 3, $E_{Rm,dc}$ are evaluated by integrating V^2/R_M with time. The negative peak voltage value as well as the charging time can be observed to rise with applied ΔT_{ext}. Similarly, the open circuit voltage during phase 2 increases proportionately with ΔT_{ext}. We note that during the 1000 s hold time in phase 2, the decay is quite significant (41.4 to 38.3 mV) for $\Delta T_{ext}= 50$ °C, while in the other two runs, the variation is marginal. Such behavior may be due to auxillary reactions
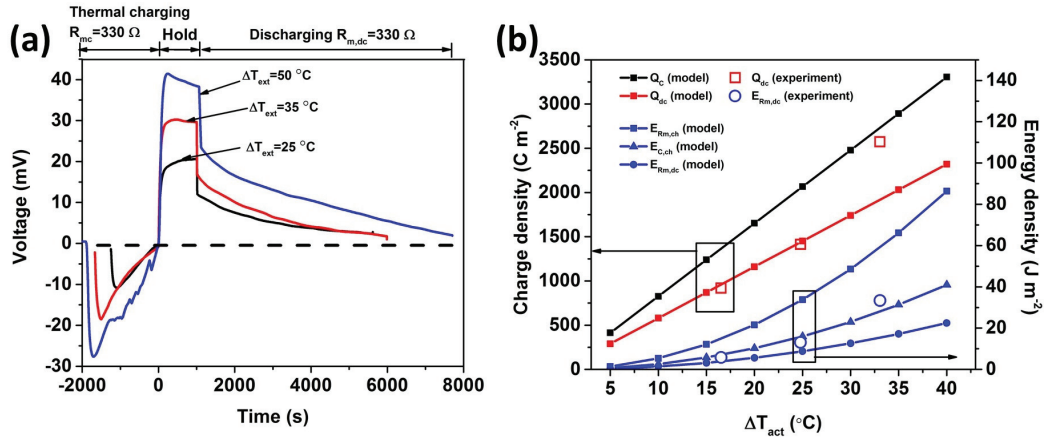
Fig. 3.11. (a) Measured voltage across the load resistor R_M corresponding to runs with ΔT_{ext} of 25, 35 and 50 °C. Each run consists of a thermal charging phase, a hold phase and a discharging phase. The load resistance is set at 330 W in both the thermal charging phase and the discharging phase. The hold phase duration is 1000 s. (b) Measured and modeled values of charge and energy storage density as a function of the temperature difference across the faces of the gel film,, ΔT_{act}. The geometric area of the electrodes is used for normalization. Q_C denotes the charge input to the capacitor C in the thermal charging phase while Q_{dc} denotes the charge released by the capacitor in the discharging phase. $E_{C,ch}$ represents the energy stored in the capacitor C in the thermal charging phase, while $E_{Rm,ch}$ and $E_{Rm,dc}$ represent the energy output in the load resistance during thermal charging and discharging respectively.

triggered at high temperatures. During phase 3, the net discharge time (time until voltage dips below 1 mV) is higher for large values of ΔT_{ext} due to greater stored energy in the device.

The equivalent circuit model used to fit the measured voltage and current profiles may be perceived as a convenient tool to analyze the influence of controllable parameters such as the temperature difference across the faces of the gel film, ΔT_{act}, external load resistance during thermal charging R_{mc}, and hold phase duration. Fig. 3.11b shows the impact of the actual temperature difference ΔT_{act} across the electrolyte film on the charge and energy storage in the device during phase 1 and 3. The stored

charge density in the capacitor element C rises approximately linearly with ΔT_{act} with a slope of 83 C m^{-2}K^{-1}. Owing to self-discharge during the hold phase, the output charge density in the discharge phase is lower with a slope of 58 C m^{-2}K^{-1}. The output charge in phase 3, evaluated from measurements shown in Fig. 3.11a can be observed to follow the trend of the model data.

The influence of the applied temperature gradient on the energy stored and energy output has also been evaluated using the model. Fig. 3.11b shows the variation of the energy output in the load resistor during thermal charging ($E_{Rm,ch}$), energy stored in the capacitor C during thermal charging ($E_{C,ch}$) and energy output in the discharge phase ($E_{Rm,dc}$). As expected, all three vary quadratically with the applied ΔT_{act}. Due to loss in the various circuit elements, E_{Rmdc} is lower than the stored energy $E_{C,ch}$. Furthermore, $E_{Rm,dc}$ calculated from the measured voltage profiles displayed in Fig. 3.11a, which is also shown in the same plot, shows a close resemblance to that calculated using the model.

A load resistance R_{mc} applied during the charging phase may be beneficial for extracting some useful work, although it may lead to low charging currents (Fig. 9.8b), implying slow charging rates. Consequently, with a rise in the value of the load resistance R_{mc} and considering a fixed thermal charging phase duration, the charge stored (Q_C) and energy stored ($E_{C,ch}$) decline due to insufficient charging, while the energy output during the thermal charging phase (E_{Rmch}) rises.

Figure 9.9 displays the influence of the applied hold time on the charge and energy output characteristics of the device. During the hold phase, the capacitor loses charge due to self-discharge through the leakage resistance R_L. This is due to decay in the capacitor voltage V_1 . The charge retention ratio and the energy retention ratio are given by $\beta_Q = Q_{dc}/Q_C$ and $\beta_E = E_{Rm,dc}/E_{C,ch}$ respectively. For zero hold time, β_Q is close to 100% while β_E is 62% because of energy loss in the circuit elements other than the load resistor, which occur even at zero hold time. With a rise in hold time from 0 to 3000s, the value of β_Q falls to 89 %, while β_E falls to 54%.

Table 3.1.

Comparison of devices with different solid-state electrolytes for energy capture from intermittent heat sources for a ΔT_{act} of 10 ° C.

Electrolyte	Capacitance C (F cm^{-2})	Seebeck Coefficient S_e (mV K^{-1})	Energy stored $E_{ch} = \frac{1}{2}C(S_e\Delta T)^2$ (μJ cm^{-2})	Charge stored $Q_{ch} = C(S_e\Delta T)$ (mC cm^{-2})	Ref.
PEO-NaOH	0.00103	11.1	6.3	0.11	[19]
PSSH	0.12	7.2	311.0	8.64	[84]
PVA/K$_3$Fe(CN)$_6$ /K$_4$Fe(CN)$_6$	13.3	1.2	973.6	160.90	This Work

3.2.8   Performance Comparison

We now compare the performance parameters of our device with similar TCSC devices demonstrated in recent studies. Table 1 shows that the area-specific capacitance of our device (13.3 F cm^{-2}) exceeds the PSSH device (120 mF cm^{-2}) and the PEO-NaOH device (1031 μF cm^{-2}) by 110 and 13000 times respectively. On the other hand, the Seebeck coefficient of our device (1.21 mV K^{-1}) is inferior to that for the PSSH device [84] (7.2 mV K^{-1}) and the PEO-NaOH device [19] (11.1 mV K^{-1}) by 6 and 10 times respectively. However, considering the effects of both areal capacitance and Seebeck coefficient, the net thermally induced charge and energy density values turn out to be much greater for our device compared to the PSSH device and the PEO-NaOH device. Furthermore, a comparison study has been conducted with a conventional energy havesting and storage system consisting of a single leg thermoelectric generator (TEG) based on Bi_2Te_3 connected in series to the same supercapacitor. Besides larger space requirements and circuit complexity, the Seebeck coefficient of Bi_2Te_3 (190 μV K^{-1}) is approximately six times lower than our gel electrolyte which results in 41 times lower energy density (Table S2). Also, we evaluate the efficiency η in converting heat to electricity defined as the ratio between energy stored in the device during thermal charging ($E_{C,ch}$) and waste heat input during that time (Q_{in}), using the the equation S16 developed recently by Wang et al. [66]. The efficiency of our device is quite low (5×10^{-5} %) when compared to the circuit composed of a conventional TEG in series to the same supercapacitor. The low efficiency can be attributed primarily to the low ionic conductivity of the electrolyte used in this study (detailed in Table S2). Future research on electrolytes displaying such thermoelectric effects is anticipated to produce a higher efficiency.

3.3   Conclusions

We have demonstrated for the first time that the thermogalvanic effect of the ferrocyanide/ferricyanide redox couple can be used to construct a solid-state ther-

moelectric supercapacitor. The device stays charged even after the thermal gradient is removed and thus can be discharged by delivering power to an external circuit. Our TCSC consists of two carbon cloth electrodes sandwiching a potassium ferrocyanide/ferricyanide gel electrolyte film. In addition to thermogalvanic effect, the potassium ferrocyanide/ferricyanide redox couple also generates high capacitance due to its redox action, that has been demonstrated through comparison studies with pure double-layer electrolytes. The fabricated symmetric TCSC device exhibits excellent electrochemical performance in terms of enhanced capacitance, self-discharge behavior and cyclic stability. Hence, such thermal charging concept offers a simple, low-cost method of storing large amount of energy in a given footprint area from intermittent heat sources without involving any complex electrode fabrication process. An equivalent circuit model representing the device is shown to provide a satisfactory fit with the current and voltage profiles measured during thermal charging. Based on a fitting technique, the area-specific capacitance value is inferred to be 13.3 F cm^{-2} which is more than two orders of magnitude larger than TCSC devices demonstrated in the past.

3.4 Experimental Section

$PVA/K_3Fe(CN)_6/K_4Fe(CN)_6$ *gel fabrication:* 4g PVA powder was dissolved in 40 ml deionized water along with 10 ml solution containing a mixture of 0.1M K$_3$Fe(CN)$_6$ and K$_4$Fe(CN)$_6$. The solution was heated to 85°C under continuous stirring, until the solution became clear. The viscous solution was then poured onto a 60 mm PTFE evaporating dish and allowed to evaporate slowly in hood at room temperature for around 3 days. Upon complete evaporation of excess water, a flexible, thin, free standing and semi-transparent polymer gel electrolyte membrane was obtained. It was then cut to the desired shape for supercapacitor assembly. By altering the volume of the viscous gel electrolyte allowed to dry, the membrane thickness could be controlled.

Two-electrode device assembly: Two CC electrodes were immersed into the 85 °C PVA/$K_3Fe(CN)_6$/$K_4Fe(CN)_6$ gel electrolyte (the copper contacts kept out) for 10 min and then taken out. The hot electrolyte soaked and penetrated the porous electrodes thoroughly. To assemble the TCSC device, the wet electrodes were clamped together with a polymer gel electrolyte membrane of appropriate thickness, sandwiched in between. The assembly was dried at room temperature for 12 h. Thereafter, the device was immersed in a solution of 0.2 M $K_3Fe(CN)_6$ and 0.2 M $K_4Fe(CN)_6$ for 1 hr to ensure complete soakage of the electrodes prior to packaging in a nylon film bag.

Material characterization: The surface morphology of electrodes was characterized by field emission scanning electron microscope (SEM, Hitachi S-4800).

Electrochemical measurements: The electrochemical performance of the device and individual electrodes was evaluated using a Gamry Echem Testing System, Gamry Instruments, Inc., USA. Electrochemical tests were conducted in a three-electrode configuration cell at room temperature using either 1.0 M H_3PO_4 or a mixture of 0.2 M $K_3Fe(CN)_6$ and 0.2 M $K_4Fe(CN)_6$ as the electrolyte. Pt foil, bare carbon cloth or CC/GP electrode was used as working electrode with Pt mesh and standard calomel electrode (SCE) as the counter and reference electrodes respectively.

Thermistor calibration: The thermistor used in the experiments is a micro-betachip thermistor probe procured from Mouser electronics. It was calibrated with a standard Parr 6775 digital thermometer. A comparison of the temperature readings shown in Table S1 shows a maximum error of 0.1 %.

4. HEAT GENERATION IN SUPERCAPACITORS

Some of the material in this chapter has been accepted for publication in
SpringerBriefs in Thermal Engineering and Applied Science [1]

4.1 Introduction

Repetitive charge/discharge cycling of a supercapacitor causes significant amounts of heat generation leading to substantial temperature rise. In absence of proper cooling systems, the operating temperature of EDLCs may exceed the temperature rated by manufacturers which is typically around 70 °C. Elevated temperatures have undesirable effects on EDLCs such as accelerated aging, high self-sischarge rates and increased cell pressure and electrolyte evaporation. With age, the internal resistance of EDLCs rise and their capacitance fades. Furthermore, temperature anomalies between series-connected EDLCs may lead to overvoltage in indicidual cells. All these factors make it essential to build a thorough understanding of the underlying heat generation mechanisms and thus predict the operating temperature for the given operating conditions.

4.1.1 Aging

The electrochemical performance of supercapacitors deteriorates with prolonged use. This process is called aging, during which the components of a supercapacitor cell (e.g., electrolytes) undergo redox reactions to form decomposition products that block the electrode pores, leading to higher ESR and lower capacitance. Both high operating temperatures and high applied voltages accelerate the aging of supercapacitors. A study on the aging characteristics of commercially available supercapacitors

reveals that the aging rate increases by a factor of 64 by either increasing the temperature by about 40 °C above room temperature (25 °C) or by charging to a voltage of 200 mV above the rated voltage [100]. For example, supercapacitors with a rated lifetime of 15 years meet their end-of-life criteria within 3 months of operation under such conditions. Commercial supercapacitors used in room-temperature conditions generally age at a slow speed and possess a cycle lifetime of a few years. It is possible to study the aging characteristics under such conditions but requires an unreasonable amount of time for the experiments to end. In order to avoid this problem, accelerated aging tests can be performed by operating supercapacitors at high temperatures and voltages. EIS is an efficient experimental technique to study the aging parameters (e.g., ESR and capacitance) during cyclic charge-discharge cycles of a capacitor under varying conditions. Although both high voltage and high temperature promote aging, their individual influence is difficult to disentangle. For this purpose, experiments can be carried out to study the aging characteristics by varying one parameter while keeping the other one fixed. However, the results vary with many factors such as cell design, electrode and electrolyte material and testing conditions. The supercapacitors tested are usually commercial supercapacitors consisting of activated carbon electrodes and organic electrolyte.

4.1.2 Thermal Modeling

Thermal modeling is an effective technique to predict the spatial and temporal variation of temperature under the prescribed operating conditions. The operating temperature rise is typically caused by either internal heat generation or heat transfer from external sources. Most studies estimate the internal heat gener tion rate and the corresponding temperature profiles in commercial supercapacitors for given charge/discharge current profiles. The temperature reaches steady state after the heat generation rate equals the heat dissipation rate to the ambient. A higher heat dissipation rate leads to a lower steady-state temperature in supercapacitors. Heat
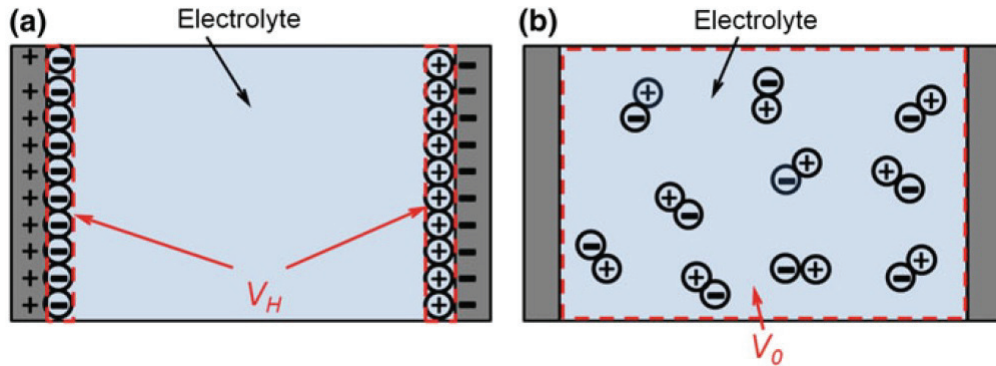
Fig. 4.1. Mechanism of reversible heat generation. a Charged; b discharged state. V_H represents the volume occupied by the ions in the charged state and V_0 represents the volume of the entire electrolyte in the uncharged state, adapted from Ref. [101]

dissipation occurs by conduction from the core of the supercapacitors to the outer wall and by convection and radiation from the outer wall to the ambient. Heat is generated in supercapacitors primarily in the form of irreversible heating or Joule heating, and reversible heat. The irreversible heat is positive during both charge and discharge. In the most common form, it is expressed as,

$$\frac{dq_{Joule}}{dt} = I^2 R_S \tag{4.1}$$

where I is charging current, and R_S is the equivalent series resistance. The ESR is determined by: (i) interfacial resistance between the electrode and the current collectors; (ii) electronic resistance of the electrode material; (iii) ionic resistance of ions diffusing through the electrode pores; (iv) electrolyte resistance, and (v) resistance of ions migrating through the separator. Equation (4.1) reveals that the Joule heating is dominated much more by the charging current (proportional to square) than the series resistance (linearly proportional).

Apart from the irreversible Joule heating losses, reversible heat generation caused by entropic effect occurs during the charge/discharge processes of a supercapacitor. Unlike irreversible Joule heating, the reversible heat generation rate is positive during charging and negative during discharging. It is not accounted for in the heat gen-

eration term of many models because: (a) its neglect simplifies the models and (b) the thermal time constant of the supercapacitor material is larger than the periods of charge/discharge. Reversible heat generation is dictated by ion behavior. During charging, ions migrate to the electrodes to compensate for the positive and negative charge on the electrodes. In the charged state (see Fig. 4.1a), the ions are in a state of maximum order and minimum entropy. This causes the ions to release heat to the contacts, leading to a rise in temperature in the contacts (heating). In the discharged state (see Fig. 4.1b), however, the ions disperse into the electrolyte, causing them to reach a state of maximum disorder and hence maximum entropy. During this process, the ions absorb heat from the contacts and thus cool them. Therefore, the contacts alternately heat during charging and cool during discharging which causes the temperature-time profile to follow a saw-tooth shape. Based on the above analysis, the entropy of the enclosed system changes during charge/discharge processes. The entropy change of the closed system during charging is,

$$\Delta S = -\int_{T_1}^{T_2} \frac{dq_{rev}}{T} = -\int_{T_1}^{T_2} \frac{C_{Heat}dT}{T} = -C_{Heat}ln(\frac{T_2}{T_1}) \tag{4.2}$$

where ΔS is the entropy change of the ions, q_{rev} is the reversible heat, C_{Heat} is the heat capacity of the contacts, and T_1 and T_2 are the contact temperatures at the beginning and end of charging pulse. During discharging, the entropy change is the same in magnitude but negative in sign. The entropy change of the ion system during charging is defined by the Boltzmann relation which relates entropy (S) to the number of ways the ions can be arranged (p) and is,

$$S = k_b ln p = k_b ln(\frac{V_H}{V_0})^N = 2\frac{Ck_bV}{e}ln(\frac{V_H}{V_0}) \tag{4.3}$$

where k_b is Boltzmann constant (1.38058×10^{-23} J K^{-1}), V_H is the volume occupied by the ions in the charged state, namely the volume of the Helmholtz layer, V_0 is the volume of the entire electrolyte in the uncharged state (see Fig. 4.1), N is the number of ions forming the layer, C is the capacitance which is assumed to be constant, V

is the voltage, and e is the charge of an ion (assumed to be monovalent). The total entropy change due to ion formation at the two electrodes is,

$$\Delta S = 2\frac{Ck_b\Delta V}{e}ln(\frac{V_H}{V_0}), \tag{4.4}$$

where ΔV is the voltage applied during charging. Equating the change in entropy obtained from both relations reveals,

$$\Delta S = -C_{Heat}ln(\frac{T_2}{T_1}) = 2\frac{Ck_b\Delta V}{e}ln(\frac{V_H}{V_0}), \tag{4.5}$$

Hence, the temperatures before and after charging are related by,

$$T_2 = T_1\frac{a_0}{a_H}exp(-2\frac{Ck_b\Delta V}{eC_{Heat}}), \tag{4.6}$$

where a_H and a_0 are the thicknesses of the Helmholtz layer and electrolyte region, respectively. The dimensions in the other directions have been assumed to be constant during the charging process. The reversible heat generation term can be derived from the Eq. 4.2 as,

$$\frac{dq_{rev}}{dt} = -2T\frac{k_b}{e}ln(\frac{a_H}{a_0})I(t), \tag{4.7}$$

Since $I(t) = C\frac{dV}{dt}$, the heat generation rate becomes

$$\frac{dq_{rev}}{dt} = -T\frac{dS}{dt} = -2T\frac{Ck_b}{e}ln(\frac{a_H}{a_0})\frac{dV}{dt}, \tag{4.8}$$

Comparing Eqs. (4.1)-(4.7), we find that the irreversible heat generation term is proportional to the square of the current while the reversible heat generation term is linearly proportional to the current. The entropy change during a charge/discharge process is higher for higher currents. Gualous et al. [102] tested commercial supercapacitors at different currents and observed that the entropy change during charging increases from -0.37 J K^{-1} at a current of 10 A to -0.99 J K^{-1} at a current of 30 A. The temperature ripples caused by this phenomenon during the charge/ discharge process of a commercial capacitor (Nesscap 5000 F, 100 A) between 0.5 and 2.5 V with a pause of 150 s are as shown in Fig. 4.2 [101]. Generally, the temperature profiles observed experimentally during continuous charge/discharge cycling of a supercapacitor is a superposition of a linear profile caused by irreversible Joule heating
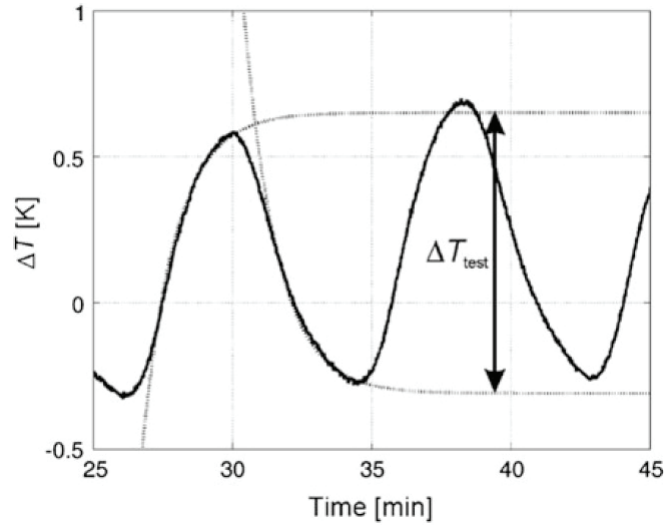
Fig. 4.2. Temperature ripple observed for the Nesscap 5000 F super-capacitor operating at 100 A in a voltage range of 0.5-2.5 V [101].

and oscillations caused by reversible heating. Following this trend, the typical temperature history of the Nesscap capacitor (5000 F, 1.5-2.5 V) at different currents is shown in Fig. 4.3 [101].

Similar temperature profiles have also been experimentally observed in other studies for charge/discharge cycling [102, 103]. The temperature oscillations due to the entropy effect are found to increase with increasing potential window and increasing charge/discharge duration. In supercapacitors with high thermal mass, these oscillations in temperature occur primarily at the core. The time required for them to propagate to the surface is substantially longer than the charge/discharge duration. Notably, these oscillations continue even after the supercapacitor reaches its steady-state temperature and lead to additional thermal stresses in the supercapacitor component materials and hence reduce their lifetime.
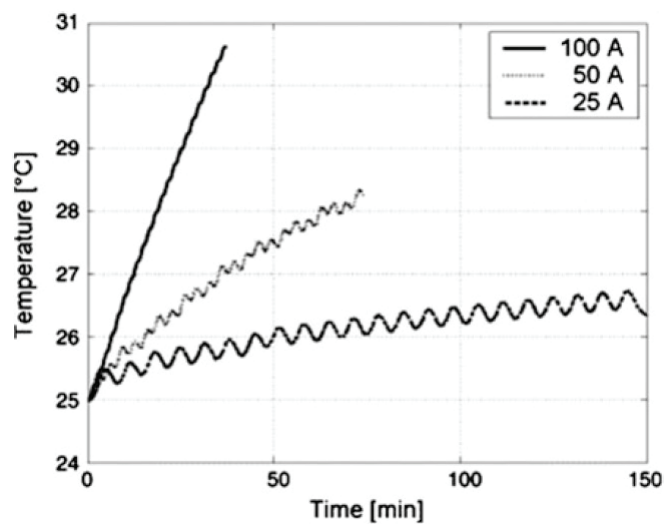
Fig. 4.3. Temperature profiles measured for a Nesscap 5000 F capacitor (1.5-2.5 V) at different currents. The duration of each step is 50 s for 100 A, 100 s for 50 A and 200 s for 25 A. The first step is charging and second step is discharging [101].

Types of Thermal Models

To date, numerous methods have been proposed to model temperature profiles of supercapacitors. Most thermal models make the following assumptions:

1. Heterogeneities in physical, electrical and structural properties of the different components are assumed to be absent.

2. Heat generation/absorption from redox exothermic/endothermic reactions during charging/discharging is neglected.

3. Thermal interface resistances at electrode/current collector interfaces and electrode/electrolyte interfaces are neglected.

4. Thermophysical properties of the materials are assumed to be the same at all temperatures.

5. Solvent species are not considered in ion transport.

6. Self-discharge and charge redistribution effects are neglected.

Comprehensive models that consider all the constituent species in the electrolyte and include reversible and irreversible heat generation, charge redistribution effects, self-discharge effects, and polarization and depolarization energy losses have not yet been developed. Most thermal models use approximations such as equivalent circuit models, lumped capacitance models and finite element models with effective medium approximations to obtain the temperature profiles. Equivalent circuit models are fit to the EIS results to derive unknown parameters. Thereafter, the heat generation is calculated from Joule heating in the resistances and then used in the Fourier heat conduction equation to obtain the temperature distribution. Such analyses are very approximate and grossly simplify the influence of cycle parameters and thermophysical properties of the materials. Physics-based analyses, on the other hand, are more elaborate as they use continuum models in the electrolyte to derive ion transport equations and heat generation parameters. However, they require high computa-

tional costs, and it is difficult to include details of components such as electrodes, separator and current collectors.

Electro-Thermal Model

The electrical performance and thermal behavior of supercapacitors are intricately related to numerous parameters such as operating cycle parameters, temperature history and material properties. Also, a large set of transport phenomena (e.g., ionic and electronic transport, heat and mass transport) are intertwined and difficult to model in a coupled manner. In order to incorporate the interdependence of electrical and thermal parameters, electro-thermal models are often used. The input current profiles are often adopted from typical duty cycles of hybrid electric vehicles (HEV) in order to obtain realistic results. Duty cycles for HEV often consist of discontinuous peaks for small time durations followed by large rest periods. The simplest and most common approach to model electrical and thermal behavior is to treat the supercapacitor as an equivalent circuit composed of several capacitive, resistive and inductive elements. Each element represents a certain type of physics that influences the charge/discharge characteristics. The advantage of such models is that they are simple and easy to compute, but their disadvantage is that they approximate real physical phenomenon and properties. Electrothermal modeling is an iterative process in which the output current and temperature are fed iteratively to change the Thermophysical properties until the results converge. The approach for electrothermal modeling proposed by Lajnef et al. [104] is shown in Fig. 4.4. Joule heating, which is the only thermal input to such models is obtained from the electrical model. In turn, the temperature obtained from the thermal model also influences the electrical parameters. The electrical and thermal models shown in Fig. 4.4 are described in the following paragraphs. Initially, an equivalent electrical circuit is established for a given supercapacitor. Thereafter, the unknown capacitance and resistance values are obtained by fitting to experimental EIS and power cycling test results. The simplest
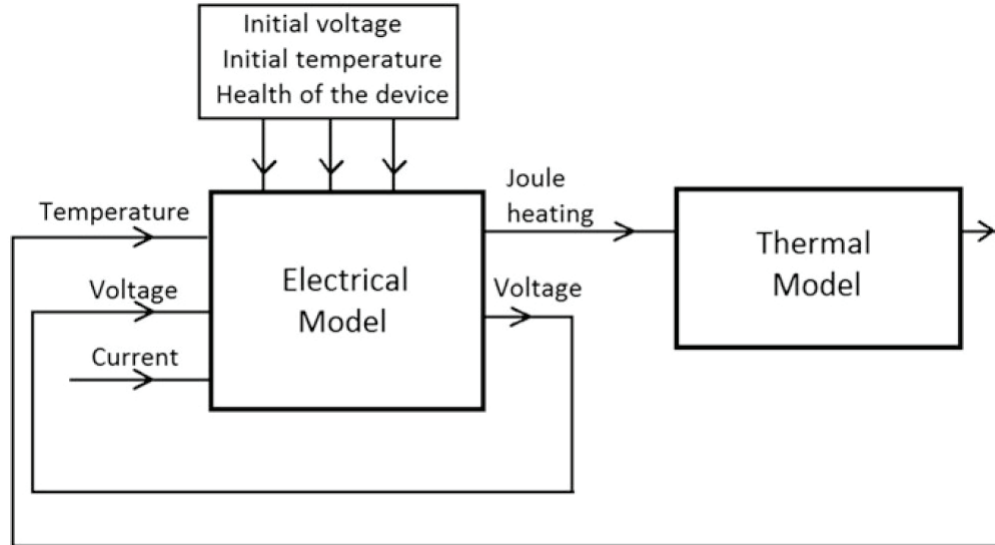
Fig. 4.4. Electro-thermal model of a supercapacitor

electrical equivalent circuit model of a double-layer capacitor is the series RC circuit. However, this simple model ignores important features such as charge transfer resistance due to faradaic reactions at the electrode surface, distributed charge storage in porous electrodes, and inductive effects that commonly occur in double-layer capacitors. To resolve these issues, a Randles circuit, shown in Fig. 4.5, incorporates the charge transfer resistance caused by faradaic reactions and semi-infinite linear diffusion of ions in the electrolyte. In this model, the charge transfer resistance R_{ct} models the impedance of the faradaic reaction at the interface, and the impedance parameter Z, also known as the Warburg parameter, models the diffusion behavior of ions.

However, this model neglects the porous nature of the electrodes and is often insufficient in describing experimentally observed current-voltage characteristics. The first attempt to model porous electrodes was made by De Levie [105] who suggested a transmission line model for each pore, a representation of which is shown in Fig. 4.6. The double-layer capacitances and resistances within the pores can be modeled by the transmission line model.
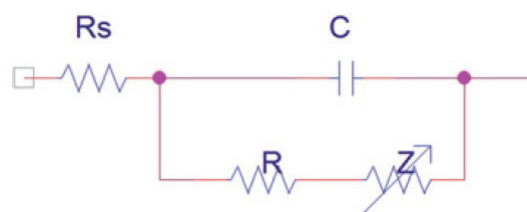
Fig. 4.5. Randles equivalent circuit
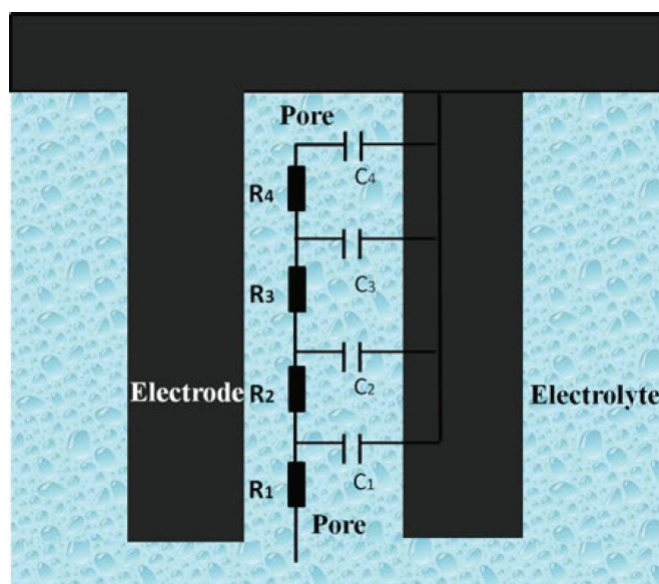
Fig. 4.6. Five-branch transmission line model for a porous electrode
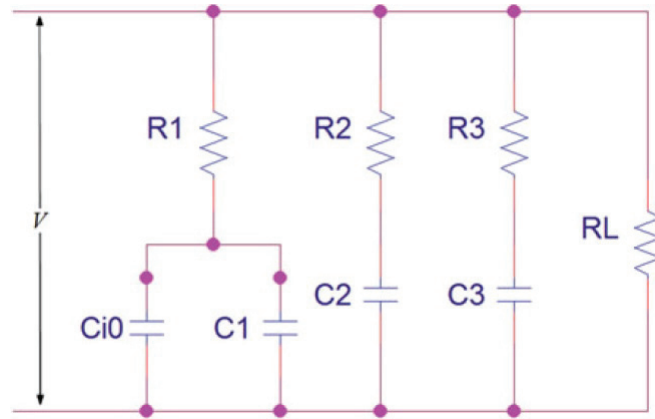
Fig. 4.7. Three-branch model

Zubieta and Bonert [106] found that an equivalent circuit consisting of three branches, as shown in the Fig. 4.7, is able to fit to certain experimental results well. In this equivalent circuit, each branch possesses a different time constant. The first branch containing R_1 (which is the ESR) denotes the immediate branch possessing a time constant of a few seconds. The branch consisting of R_2 and C_2 denotes the delayed branch which has a larger time constant. Finally, R_L represents the leakage resistance. Many other types of equivalent circuit models for porous electrodes have also been proposed. The heat generation rate due to Joule heating is calculated as,

$$\frac{dq_{Joule}}{dt} = \sum_{k=1}^{n} I_k(t)^2 R_k, \tag{4.9}$$

where R_k accounts for ESR as well as the resistances in the RC branches. The calculated power (Joule losses) is fed as input to the thermal model in order to estimate the average temperature. The thermal model (see Fig. 4.8) can be represented by a number of thermal RC branches in parallel to model the different time constants in the temperature-time characteristics. The average temperature is then obtained from the thermal model. Individual resistance and capacitance values are fitted to the experimental temperature-time characteristics for different current profiles.The temperature characteristics obtained from the previous step are used to adjust the parameters of the electrical models, namely resistance and capacitance. This itera-
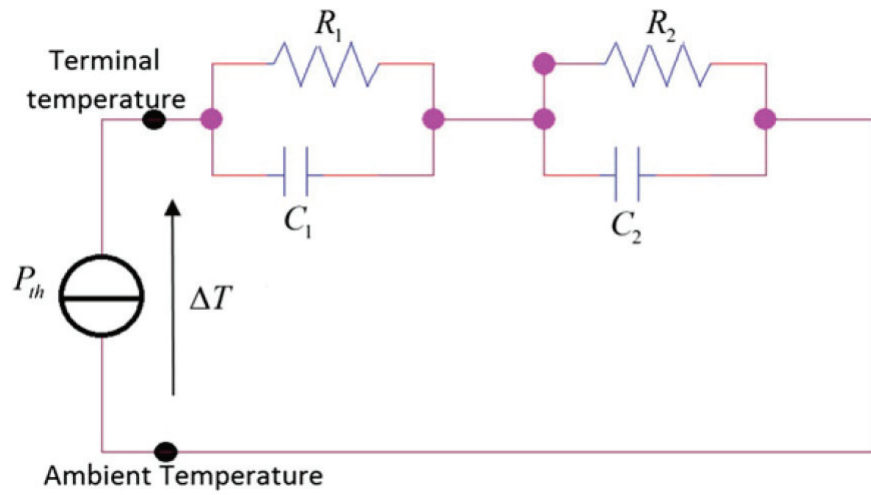
Fig. 4.8. Equivalent circuit thermal model
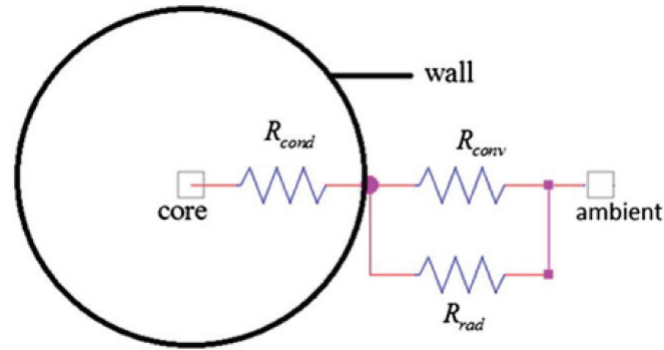
Fig. 4.9. Lumped capacitance model for heat transfer in a commercial supercapacitor

tion process continues until the changes in parameters from one iteration to the next reaches a threshold value i.e., convergence is reached.

Lumped Models

Lumped thermal models solve for average temperature values instead of the spatial temperature distribution in supercapacitors. An inherent assumption of such models is that temperature changes within the device are small compared to the temperature difference between the device and the ambient. This assumption was found to be quite reasonable particularly for large cycling currents, for which the temperature gradient within the device was found to be negligible in comparison with the difference of the outer surface temperature with the surroundings. Such models are more convenient to study the temperature evolution in commercial supercapacitors due to their inherent simplicity, low computation cost and easy comparison with experimental results. In some lumped models, termed single-temperature models here, only the average temperature of the device is evaluated and is subsequently compared to the experimental temperature values. However, this approach may involve significant error, since the experimental temperature is generally obtained from a thermocouple attached to the case of the device and can differ from the average temperature. In

order to obtain better estimates, two temperature values can be evaluated, namely the core temperature and case temperature. These are termed double-temperature models here. The core temperature is generally a few degrees higher than the case temperature.

Finite Element Models

In situations where a large spatial temperature variation exists, it is often essential to study the temperature distribution throughout the supercapacitor. Moreover, uneven temperature distribution leads to higher thermal stresses and accelerated aging. Many authors have studied the temperature distribution at various time instants during charging/discharging using the time-dependent heat diffusion equation [107],

$$\rho c_p \frac{\partial T}{\partial t} = k \nabla^2 T + \dot{q}_{gen} \tag{4.10}$$

where ∇^2 is the Laplacian operator, $\dot{q}_{gen}$ is the volumetric heat generation rate (W m^{-3}), ρc_p is the thermal mass of the capacitor, and k is the thermal conductivity of the capacitor material. If the supercapacitor is assumed to be axisymmetrical, i.e., the heat conduction is assumed to occur only in the radial and axial directions, the equation becomes,

$$\rho c_p \frac{\partial T(r,z,t)}{\partial t} = k_r \frac{\partial^2 T(r,z,t)}{\partial r^2} + \frac{k_r}{r} \frac{\partial T(r,z,t)}{\partial r} + k_z \frac{\partial^2 T(r,z,t)}{\partial z^2} + \dot{q}_{gen} \tag{4.11}$$

where k_r is the thermal conductivity along the radial direction, k_z is the thermal conductivity along the axial direction, and $r_i \leq r \leq r_o$, $0 \leq z \leq L$, $0 \leq t \leq t_f$. The heat generation term $\dot{q}_{gen}$ has contributions from the following sources:

(i) Joule heating during ion transport in electrolyte (within electrodes and separator) and electronic charge transport in current collectors and the solid phase of electrodes.

(ii) Exothermic/endothermic electrochemical reactions at the electrode/electrolyte interface.

(iii) Thermal contact and electrical resistances between layers.

In order to express the heat diffusion terms, the geometric features of the supercapacitors should be considered. A typical commercial supercapacitor takes a cylindrical shape consisting of two activated carbon electrodes separated by a porous membrane (separator) and impregnated with an organic electrolyte. The carbon electrodes are in direct contact with aluminum metallic current collectors to minimize internal resistance. These components are usually either rolled and sealed in a cylindrical container or stacked and sealed in a rectangular one.

Along the radial direction, the thermal resistances of the different layers lie in series,

$$R_{rad} = \sum_i \frac{L_i}{k_i A_i} \tag{4.12}$$

where L_i, k_i and A_i are the thickness, thermal conductivity and cross-sectional area of each layer. Since the thermal conductivity of activated carbon (0.5 W m^{-1} K^{-1}) is much lower than the thermal conductivity of aluminum (120 W m^{-1} K^{-1}), the thermal resistance in the radial direction is dominated by the carbon layers [10]. Along the axial direction, the thermal resistances are in parallel,

$$\frac{1}{R_{rad}} = \sum_i^N \frac{1}{R_{th,n}}, \tag{4.13}$$

where $R_{th,n}$ is the thermal resistance of the nth layer, and N is the total number of layers (including carbon, aluminum and separator). The thermal conductance of carbon and separator can often be neglected compared to that of aluminum, and hence the thermal path along the axial direction is largely determined by the thermal conductivity of aluminum. As the thermal resistance is lower in the axial direction, most of the heat generated is dissipated through the longitudinal surface of the supercapacitors rather than from the cylindrical surface. Moreover, due to the low thermal resistance, temperature is almost uniform along the axial direction. This is also the reason the terminal temperature is assumed equal to the core temperature in many studies [108, 109]. The terminal temperature is more convenient to be measured than the core temperature.
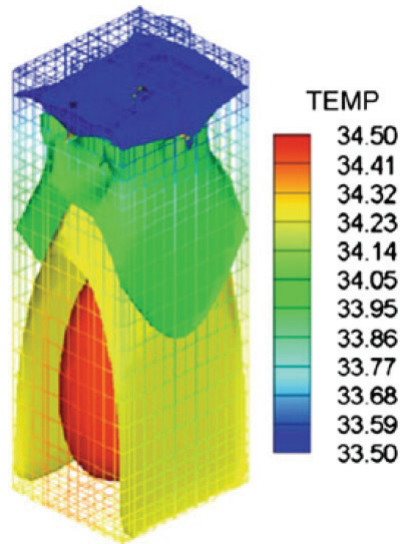
Fig. 4.10. Isothermal surface distribution of Nesscap 2.7 V/3500 F cell after 50 cycles [110].

The heat conduction equation is solved using the following initial and boundary conditions: (a) Initially, the temperature in the capacitor is assumed to be uniform,

$$T(r, z, 0) = T_0, \tag{4.14}$$

(b) The temperature gradient at the centerline is zero,

$$\lambda_r \frac{\partial T}{\partial r} = 0, \tag{4.15}$$

(c) On the supercapacitor casing, the heat conduction rate is equal to the convective heat loss rate,

$$-\lambda_r \frac{\partial T(r_0, z, t)}{\partial r} = h_{conv}(T - T_a) \tag{4.16}$$

where T_a is the ambient temperature. The governing Eq. 4.11 is solved with the initial and boundary conditions from Eqs. (4.14-4.16) to obtain temperature profiles at different time instants and locations.

Thermal Models for Supercapacitor Stack

Because of the relatively low maximum operating voltage and charge storage capacity of a single supercapacitor, a large number of cells are generally connected to form a circuit in order to meet the voltage and current requirements in hybrid electric vehicles. The heat dissipation problem under such circumstances is worse than for single cell units because of the higher power densities in comparison to available cooling area. The cooling strategy directly influences the temperature distribution of the supercapacitor pack. The average temperature, temperature uniformity and voltage uniformity in supercapacitor modules significantly influence the lifetime expectation of the entire module. In addition, the temperature distribution in the stack is also critical because temperature variations within the stack can lead to different aging rates and hence different charge/discharge characteristics. This phenomenon in turn may lead to electrically unbalanced stacks and reduced performance [111]. Simulation models make it possible to predict the temperature evolution in each cell and help design the cooling system (if necessary) with appropriate characteristics to maintain the temperature of all cells below the allowed maximum temperature. Many thermal models of supercapacitors packs have been developed in prior work [3, 9, 11, 47, 48].

Figure 4.11 shows an example of cooling supercapacitor modules by forced convection in the transverse and axial directions. Al Sakka et al. [103] modeled a supercapacitor stack with axial ventilation with a nodal thermal model. The supercapacitor stack was modeled using an electro-thermal approach as shown in Fig. 4.12. Each cell was represented by an equivalent circuit model, and the heat transfer between them or to the surroundings was represented by additional resistances. The heat generation term for each individual cell calculated from Joule heating occurring in the equivalent series resistance was as given in Eq. 4.1. The convection heat transfer from one cell to another cell or to the ambient was modeled by thermal resistances.

The modeling for transverse ventilation involves a more complicated procedure than for the axial ventilation because the ambient temperatures around all cells in
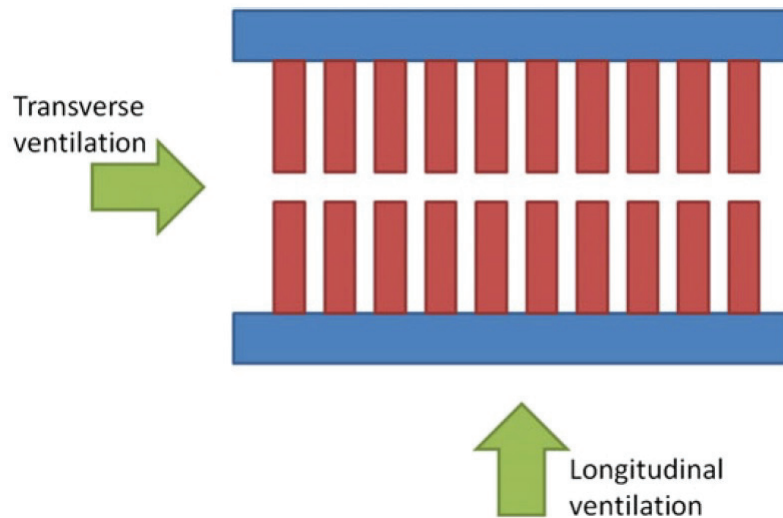
Fig. 4.11. Schematic of a supercapacitor bank
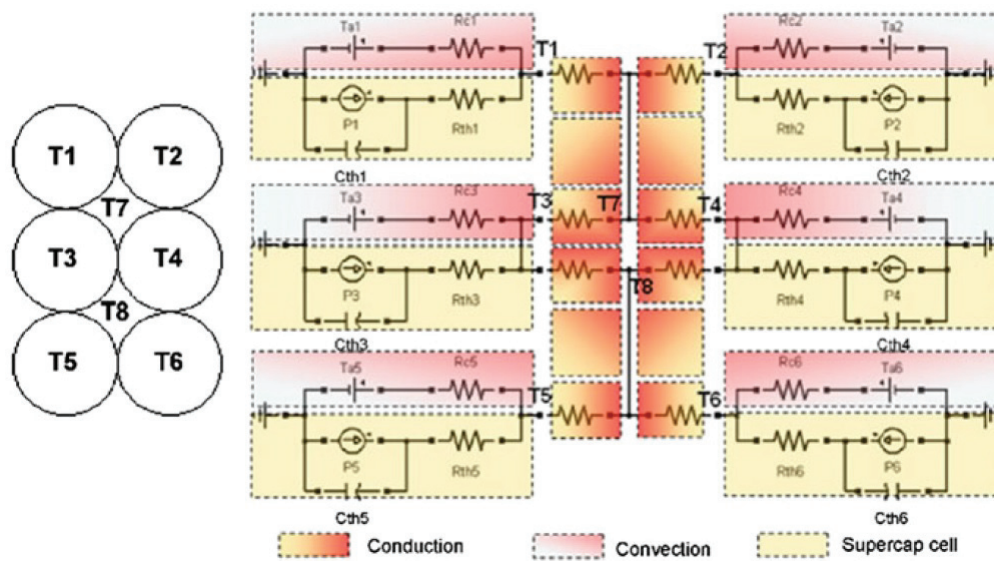
Fig. 4.12. Discretization of a supercapacitor tank [103]

the former case are different. In transverse ventilation, the air flows from the inlet to the outlet while ventilating components in the transverse direction. Hijazi et al. [109] presented a model for the temperature evolution in these stacks in which the system is divided into a number of elements. Each element is assumed to have a uniform temperature equal to that at its node. Heat exchange between the nodes occurs by conduction, convection and mass transfer, which is represented by thermal resistance (separately for conduction, convection and mass transport) in between contiguous nodes. The matrix representation of all the nodes is represented as,

$$mc_p \frac{\partial T}{\partial t} = [A_{cond} + A_{conv} + A_{trans}]T + \dot{q}_{gen}, \tag{4.17}$$

where T is the temperature vector of the nodes, mc_p is the heat capacity of each element and $\dot{q}_{gen}$ is the heat generation at each node in watts. G is the thermal conductance matrix which consists of conduction matrix A_{cond}, convection matrix A_{conv}, and mass transport matrix A_{trans} that represents the effects of heating of the cooling stream,

$$A_{cond}(i,j) = \begin{cases} \frac{1}{R_{cond}(i,j)} & if \ j \ a_i \\ 0 & otherwise \end{cases} \tag{4.18}$$

$$A_{conv}(i,j) = \begin{cases} \frac{1}{R_{conv}(i,j)} & if \ j \ a_i \\ 0 & otherwise \end{cases} \tag{4.19}$$

where a_i is the set of neighboring nodes that exchange heat with node i. The conduction resistance R_{cond} and the convection resistance R_{conv} are,

$$R_{cond} = \frac{T_{terminal} - T_{case}}{\dot{q}_{gen}}$$
$$R_{conv} = \frac{T_{case} - T_a)}{\dot{q}_{gen}} \tag{4.20}$$

where $T_{terminal}$ and T_{case} are the temperatures measured at the terminal and case of a particular cell, respectively. The heat generation rate $\dot{q}_{gen}$ is calculated as the difference between the power input during charging and power output during discharging.

The conduction and convection thermal resistances are calculated using Eq. 4.20. For systems with large number of nodes, the matrix G is sparse because the temperature of each node primarily depends on the temperature of its adjacent nodes. The evaluation of the coefficients of the matrix Atrans differs slightly from the calculation of the matrices A_{cond} and A_{conv}, since the heat exchange by mass flow in node i depends only on the upstream nodes and not all the neighboring ones. Consequently the terms are equal to,

$$A_{trans}(i,j) = \begin{cases} \dot{m}_{ij}c_p & if \ j \ u_i \\ 0 & otherwise \end{cases} \tag{4.21}$$

where $\dot{m}_{ij}$ is the mass flow rate (kg s^{-1}) from node i to j, and u_i is the set of nodes which are upstream with respect to i. The model is used to calculate temperatures of all node points at different charge/discharge currents, and the results are matched with experimental results. Sensitivity analysis shows that uncertainties in the air velocity and convection heat transfer coefficients have the greatest impact on model accuracy.

In the models mentioned above, only the cells are assumed to participate in heat generation and thermal transport. However, a packaged element also contains inactive components such as the case, current collector ends and electrical cables that do generate negligible if any heat. Incorporating the inactive components into models is necessary to make them more realistic and accurate particularly because they can represent extended heat transfer surfaces. Guillemet et al. [112] considered both active and inactive components in their compact thermal model. The active components were modeled as 2D blocks with uniform heat generation. Meanwhile the inactive components were represented by a collection of thermal resistances attached to the active components similar to the representation of heat dissipation to the ambient by convection and/or radiation.

First principles Thermal Models

The equivalent circuit models, lumped models and finite element models for thermal analysis described in the previous sections make many approximations. For instance, the equivalent circuit models and lumped models assume the temperature in the entire capacitor to be uniform or within individual elements such as current collectors, electrodes and electrolyte. Irreversible heat generation parameter is calculated from Joule heating through the ESR and is often assumed to be constant. Also, most models do not consider reversible heat generation, with a notable exception by Schiffer et al. [101] who considered reversible heat generation term by assuming a Stern layer of monovalent ions on the electrode surfaces. However, this model assumes that the ions compress to a layer of uniform thickness during charging.

An alternative is to make use of Poisson-Nernst-Planck (PNP) electro-diffusion theory to represent the transport of ions in the presence of voltage and concentration gradients. The model separates the electrolyte domain into two regions, namely an inner region called the Stern layer which is of known thickness (assumed to be equal to ion radius), and an outer region called the diffuse layer. The ion concentrations in the diffuse layer and electric potential are evaluated by solving the Modified Poisson-Nernst-Planck (MPNP) equations in the diffuse layer [107, 113] ,

$$\frac{\partial c_i}{\partial t} = -\bigtriangledown N_i \qquad for \quad i = 1, 2, ..., \tag{4.22}$$

where N_i is the local flux of species i. For a binary, symmetric electrolyte, N_i is expressed as follows,

$$N_i = -[D_i \quad c_i + \frac{z_i F D_i}{RT} c_i \quad \psi \tag{4.23}$$

where the first and second terms on the right side express ion diffusion and migration in an electric field, respectively. The third term expresses steric effects caused by finite ion size. In the above equations, ψ, j, a, $_0$, $_r$ and N_A represent electric potential, current density, ion radius, absolute permittivity, relative permittivity, and Avogadro number, respectively. D_i and c_i represent the diffusion coefficient and concentration of a particular ion species, respectively. R is the universal gas constant (R=8.314 J

mol^{-1} K^{-1}). ψ and j_s represent the electric potential and the current density at the electrode surface, respectively.

The accounting of finite size becomes particularly important for potentials above 1 V and concentrations over 1 mol L^{-1}. The simulation can be run with constant current or constant voltage boundary conditions,

$$- \epsilon_0 \epsilon_r \frac{d\psi(0,t)}{dx} = \begin{cases} j_s & for \ (n-1)t_c < t < (n-1/2)t_c \\ -j_s & for \ (n-1/2)t_c < t < nt_c \end{cases} \tag{4.24}$$

$$\psi(0,t) = \begin{cases} 0 & for \ t < 0 \\ \psi_s & for \ t > 0 \end{cases} \tag{4.25}$$

Temperature is evaluated by solving the time-dependent heat diffusion equation,

$$\rho c_p \frac{\partial T}{\partial t} = k \nabla^2 T + \dot{q}_{gen}, \tag{4.26}$$

where the heat generation term $\dot{q}_{gen}$ (W m^{-3}) consists of irreversible and reversible terms,

$$\dot{q}_{gen} = \dot{q}_{Joule} + \dot{q}_{rev}. \tag{4.27}$$

The irreversible heat generation term is due to Joule heating,

$$\dot{q}_{Joule} = \frac{j^2}{\sigma} \tag{4.28}$$

The above equation is equivalent to Eq. 4.1 if we consider current density j (A m^{-2}) instead of current I (A). The reversible term is a sum of ion diffusion, steric, concentration gradient and temperature effects,

$$\dot{q}_{rev} = \dot{q}_{rev,diff} + \dot{q}_{rev,steric} + \dot{q}_{rev,conc} + \dot{q}_{rev,temp} \tag{4.29}$$

$$\dot{q}_{rev,diff} = \frac{DzF}{\sigma} j \nabla (c_1 - c_2) \tag{4.30}$$

$$\dot{q}_{rev,steric} = \frac{DzFa^3 N_A(c_1 - c_2)}{\sigma(1 - a^3 N_A(c_1 + c_2))} j \nabla (c_1 - c_2) \tag{4.31}$$

$$\dot{q}_{rev,conc} = \frac{3}{32\pi} \frac{z^3 e F^2}{(\epsilon_0 \epsilon_r)^{3/2} R^{1/2} T^{1/2} (c_1 + c_2)^{1/2}} (N_1 + N_2) \nabla (c_1 + c_2) \tag{4.32}$$
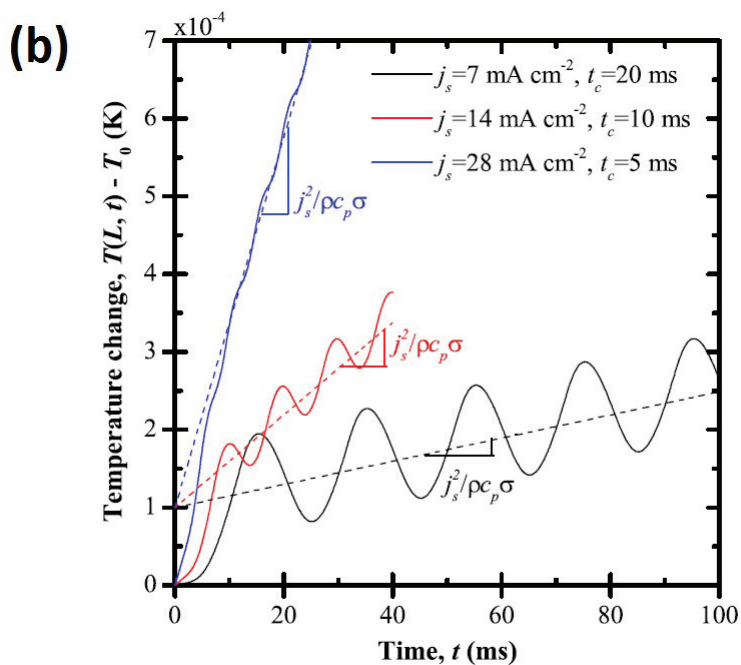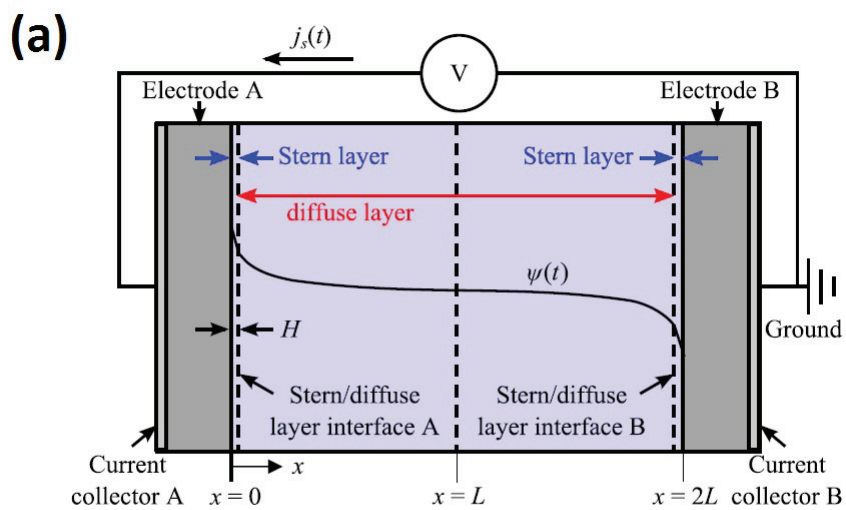
Fig. 4.13. (a) Illustration of simulated 1D cell and (b)Predicted temperature rise $T(L,t)$-T_0 at the centerline for cycling at three different current densities j_s over the same potential window [114].

$$\dot{q}_{rev,temp} = -\frac{3}{32\pi} \frac{z^3 e F^2 (c_1 + c_2)^{1/2}}{(\epsilon_0 \epsilon_r)^{3/2} R^{1/2} T^{3/2}} (N_1 + N_2) \quad T, \tag{4.33}$$

Detailed derivations of Eqs. 4.29-4.33 are provided in Ref. [115]. The Joules heating is positive both during charging and discharging, while the reversible heat is exothermic during charging and endothermic during discharging. This leads to large temperature oscillations in the Helmholtz layer. Moreover, the maximum temperature is significantly higher than that caused by only Joule heating, due to the addition of the reversible heat. The temperature variation obtained is the superposition of Joule heating and reversible heat, as illustrated in Fig. 4.13.

Although coupled physics-basedmodels are accurate, they bring high computational cost. Such models can be simplified by applying scaling laws to non-dimensionalize parameters. For instance, Entremont and Pilon [116] non-dimensionalized the governing equations and boundary conditions and thereby reduced the twelve independent design parameters to seven non-dimensional parameters. These non-dimensional parameters can be used as a framework to develop thermal management strategies for electric double-layer capacitors.

Most physics-based models to date have been applied to symmetric electrolytes. However, in practical applications, asymmetric electrolytes are often used. A recent study by Entremont and Pilon [117] on asymmetric electrolytes with multiple ion species shows that the irreversible heat component decreases with increasing valency or increasing diffusion coefficient of the ion species due to the resulting increase in electrical conductivity of the electrolyte. On the other hand, the reversible heat generation rate increased with increasing counter-ion valency and/or decreasing counter-ion diameter. As a result, the electrode with the counter-ion of smaller diameter and/or larger valency experienced significantly larger temperature oscillations during galvanostatic cycling than the opposite electrode. Consequently, electrolytes consisting of ions with small diameter and valency produce large capacitance but suffer from large reversible and irreversible heating. All these studies indicate that physics-based thermal models capture the physics of heat generation effectively. However, signifi-

cant work remains to include the thermophysical properties of the other components such as the electrode and separator to make them more realistic.

4.2 Continuum Modeling of Heat Generation in Electrical Double-Layer Capacitors

4.2.1 Introduction

Electrical double-layer capacitors (EDLCs) are popular in applications requiring rapid response and long cycle life such as regenerative braking in electric vehicles [118, 119]. They exhibit higher energy density than conventional dielectric capacitors but offer higher power density than batteries. The electric charge in such devices is stored physically by electrostatic attraction forces in the electric double-layer formed at the boundary of mesoporous electrodes.

During EDLC charge/discharge processes, a significant fraction of the input electrical energy is dissipated as heat. The heat generation rate is closely coupled to ion transport behavior [114] and is thus influenced by numerous factors such as operating conditions, cell design and constituent material properties. Sustained high temperature is known to cause accelerated aging [120–122], high self-discharge rate, electrolyte evaporation [103], and increased cell pressure. The capacitance degrades and internal resistance rises as it ages. Typically, the lifetime is halved for every 10 K rise in operating temperature [123]. Furthermore, temperature difference among individual cells in stacked systems causes voltage imbalances resulting in accelerated aging [120, 124]. Mitigation of such harmful effects requires a thorough understanding of the thermal behavior and its dependence on the various system parameters.

Experiments have been conducted in the past to estimate heat generation rate in commercial EDLCs [101, 102, 110, 121]. Gualous et al. [121] investigated temperature evolution of a commercial BCAP350 F supercapacitor subjected to galvanostatic charge/discharge operation between 1.25 and 2.5 V, with natural convection cooling at the outer surface. Temperatures were recorded with the help of thermocouples attached to its outer surface. The recorded temperature showed an initial rise followed by saturation after a particular time. However, the curve was smooth and did not contain any oscillations. Temperature oscillations were observed in the following

study by Gualous [102] under same operating conditions. However, this time, thermocouples were placed inside the device at different positions along the radial axis, instead of only on the surface. The average temperature and oscillation amplitude were found to decline along the radial direction owing to natural convection at the outer surface.

Thermal characterization using thermocouples, although useful, lack accuracy due to added thermal mass of the themocouples during measurement [125]. Calorimetric techniques were first used by Pascot [126] and then by Dandeville [127] to measure heat generation rates in custom-made symmetric and asymmetric capacitors. Heat generation rate was estimated from the measured temperature evolution of the cell using deconvolution analysis. The symmetric device consisted of activated carbon electrodes while the asymmetric device consisted of activated carbon and MnO_2 electrodes. The reversible heat generation rate was found to be of opposite sign for the carbon and the MnO_2 electrode indicating that it is primarily influenced by enthalpy of ion adsorption onto the electrode surface. Recently, Munsteshari et al. [125] designed an isothermal calorimeter to measure heat generation rates at each individual electrode accurately to gain insights into the contributing factors of the reversible heat generation rate.

The time-dependent temperature profile obtained duing continuous galvanostatic cycling can in general, be mathematically expressed as superposition of a constant linear temperature rise along with temperature oscillations repeating at cycle frequency. The linear temperature rise corresponds to Joule or irreversible heating, which is proportional to square of the current and is always positive, while the temperature oscillations correspond to entropic heating, which varies linearly with current.

Schiffer et al. [101] was the first to associate the temperature oscillations to the entropic effect. The reversible phenomenon occurs because the net entropy of the ions (a) decreases during charging, as the ions form an electric double-layer and (b)

increases during discharging as the ions return to their original random orientation. A simple model expressing the reversible heat generation rate as

$$\dot{Q}_{rev} = -T\frac{dS}{dt} = -2\frac{Tk_b}{e}ln(\frac{V_H}{V_0})I(t) \tag{4.34}$$

was used to explain the exothermic and endothermic nature of the charging and discharging processes. Recent models [114, 116] based on first principles suggest that the reversible heat generation rate has contributions from ion diffusion, entropy of mixing, steric effects and possibly redox reactions.

Thermal modeling is an effective technique to predict temperature evolution of EDLCs. The models can be broadly categorized into: (a) equivalent circuit, (b) lumped, (c) finite element and (d) first principles model [1]. The heat generation rate calculation in most of these models has typically been oversimplified; it is considered spatially uniform and is estimated as Joule heating from the imposed current and the experimentally measured device electrical resistance. In equivalent circuit models, the heat generation rate is estimated by summing up Joule heating terms from all resistor elements in the equivalent circuit representing the device [128]. In lumped models, an energy balance is solved for the time varying average temperature while neglecting spatial temperature variations inside the cell [103, 129, 130]. Finite-element models represent an improvement over the lumped model and solve for the spatio-temporal temperature variation assuming a constant heat generation rate [121]. Recently, d'Entremont and Pilon [114, 116] developed a spatio-temporal physical model based on first principles which accounted for coupled ion transport, heat generation rates and thermal transport in an EDLC. The model was successful in developing a deep understanding of physical phenomena underlying the experimentally observed temperature oscillations. However, although the simulated temperature profile was in qualitative agreement with experimental results, they differed by orders of magnitude quantitatively due to the reason that they make the rarely accurate assumption of considering electrodes as flat plates while neglecting electrode morphology completely.

In the present study, we develop a one-dimensional model to simulate the spatio-temporal temperature evolution in a sandwich EDLC structure comprised of two
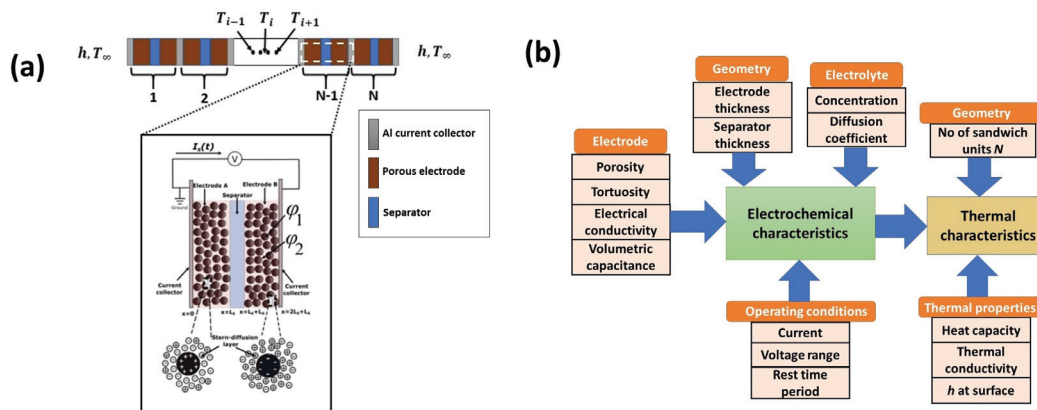
Fig. 4.14. (a) Schematic of a complete supercapacitor cell consisting of N sandwich units. The zoomed up view of a single unit shows its major components: (1) aluminum current collector (2) two porous electrodes each length L_e, composed of activated carbon and (3)a separator of length L_s. The magnified view shows a cross-section of the cell structure. Dark spheres correspond to activated carbon that constitute the two electrodes. The electrolyte residing in the porous regions of the carbon electrodes is electrically neutral except for the thin Stern diffusion layer forming around the walls of the activated carbon spheres. (b) An overview of the numerous factors influencing heat generation in an EDLC cell.

porous electrodes and a separator impregnated with a binary symmetric electrolyte. Drawing from porous electrode theory, we derive expressions for the total heat generation rate as a function of the current flowing in the solid and liquid phases of the electrodes. Such model is an improvement over the flat plate electrode model and takes into consideration factors such as electrode porosity, volumetric surface area and electrode and electrolyte conductivity. In addition, we present a scaling analysis of the model which led to simplification of the problem. Eleven independent design parameters were simplified to seven dimensionless similarity parameters which govern the spatio-temporal evolution of electrode and electrolyte phase potentials, ion concentration, heat generation rates and temperature evolution.

4.2.2 Analysis

Schematics and Assumptions

Fig. 4.14 illustrates a one-dimensional cell of thickness L_{dev} composed of N elemental sandwich EDLC units in series. Each unit consists of two electrodes with thickness L_e (left denoted electrode A and right denoted electrode B) sandwiching a separator of thickness L_s. A symmetric, binary electrolyte resides within the porous structure of the electrodes and separator. Ions present in the completely dissociated electrolyte accumulate at the electrode interface forming a Stern-diffusion layer. The electrolyte residing in the electrode pores away from the Stern-diffusion layer is electrically neutral. Ion accumulation in the Stern-diffusion layer induces an equal and opposite charge on the electrode surface.

Each EDLC unit is charged/discharged at a constant current density $I_{im}(t)$ imposed at the boundary of the right electrode. In galvanostatic charge/discharge measurements, the imposed current density is allowed to vary periodically with time as,

$$I_{im}(t) = \begin{cases} -I_0, & \text{for } 2(n-1)t_0 \leq x \leq (2n-1)t_0. \\ +I_0, & \text{for } (2n-1)t_0 \leq x \leq 2nt_0. \end{cases} \quad (4.35)$$

where I_0 is the applied current density in A m^{-2}, n $(=1,2,3,...)$ is the cycle number, and t_0 is half the cycle period. The cell voltage is allowed to vary periodically from V_{min} to V_{max} and vice-versa. Here, $\Delta V = V_{max} - V_{min}$ is referred to as the potential window.

The following assumptions were made (1) The electrolyte completely dissociates into its constituent ions. (2) The electrolyte is binary and symmetric (z_+=-z_-=1 and $c_{1,\infty}$=$c_{2,\infty}$=c_b); also the bulk diffusion coefficient is equal for both types of ions (D_+=D_-=D). (3) Chemical reactions and ion adsorption due to non-electrostatic forces are absent inside the electrode. (4) Bulk movement of the electrolyte *i.e.*, advection, is negligible. (5) Steric effects due to ion-ion repulsion are neglected. (6) All electrolyte properties are independent of temperature. (7) The ambient temperature

is constant at T_∞. (8) The heat transfer coefficient h is constant and independent of surface temperature. (9) Porous electrode theory is sufficient to represent the electrochemical and thermal behavior of the EDLC.

In the past, porous electrode theory has been employed to solve transport problems for a wide variety of energy storage systems such as batteries [131], fuel cells [132], EDLCs [133, 134] and hybrid pseudocapacitors [135, 136]. This approach is applicable only when the microscopic features are uniform and much smaller than the system dimension to justify volume averaging liquid and solid phase properties in the form of a continuum set of equations. This condition is applicable to activated carbon electrodes, which are typically around on hundred microns thick and consist of agglomerate carbon particles with sizes on the order of a micron.

Electrochemical Transport

Conservation of charge requires that the input current density $I_{im}(t)$ is equal to the sum of currents flowing through the solid and liquid phases of the electrode,

$$I_{im}(t) = I_1 + I_2. \tag{4.36}$$

The current density in the solid phase and in the liquid phase of the electrode can be expressed by Ohm's law as

$$\begin{aligned} I_1 &= -\sigma \frac{\partial \phi_1}{\partial x}, \\ I_2 &= -\kappa \frac{\partial \phi_2}{\partial x} \end{aligned} \tag{4.37}$$

where the electrical conductivity of the solid phase σ is a constant and the electrolyte ionic conductivity κ is a function of the local ion concentration c and is given by

$$\kappa = \frac{2F^2 Dc}{R_u T_0}. \tag{4.38}$$

The positive and negative ion concentrations differ only in a narrow region around the electrode/electrolyte interface called the Stern-diffusion layer. Because the pores occupy a much larger volume, it is safe to assume that the average concentrations of

positive and negative ions are equal in the binary symmetric electrolyte, $c_+ = c_- = c$. The diffusion coefficient is assumed to be equal for the positive and negative ions and incorporates the effects of porosity and tortuosity: $D = D_\infty \epsilon / \tau$ [137, 138]. In the past, self-consistent effective medium theories have been used to show that when the porosity ( ) is uniform over a length scale that is small relative to the system dimension, as assumed in the present study, the tortuosity (τ) can be approximated by the Bruggeman relation [139, 140] $\tau = ^{-1/2}$. Thus, the diffusion coefficient in the electrode region (D_e) and in the separator region (D_s) is expressed as

$$
\begin{aligned}
D_e &= D_\infty \,_e^{3/2}, \\
D_s &= D_\infty \,_s^{3/2}
\end{aligned}
\tag{4.39}
$$

The electrolyte concentration is considered spatially uniform initially,

Table 4.1.
Field equations

Left Electrode $(0 < x < L_e)$	Separator region $(L_e < x < L_e + L_s)$	Right Electrode $(L_e + L_s < x < 2L_e + L_s)$
$\frac{\partial \phi_1}{\partial x} = -\frac{I_{im}(t) - I_2}{\sigma}$	-	$\frac{\partial \phi_1}{\partial x} = -\frac{I_{im}(t) - I_2}{\sigma}$
$\frac{\partial \phi_2}{\partial x} = -\frac{I_2}{\kappa}$	$\frac{\partial \phi_2}{\partial x} = -\frac{I_2}{\kappa}$	$\frac{\partial \phi_2}{\partial x} = -\frac{I_2}{\kappa}$
$\frac{\partial I_2}{\partial x} = aC\frac{\partial(\phi_1 - \phi_2)}{\partial t}$	$I_2 = I_{im}(t)$	$\frac{\partial I_2}{\partial x} = aC\frac{\partial(\phi_1 - \phi_2)}{\partial t}$
$e\frac{\partial c}{\partial t} = D_e\frac{\partial^2 c}{\partial x^2} + \frac{aC}{2F}\frac{\partial(\phi_1 - \phi_2)}{\partial t}$	$s\frac{\partial c}{\partial t} = D_s\frac{\partial^2 c}{\partial x^2}$	$e\frac{\partial c}{\partial t} = D_e\frac{\partial^2 c}{\partial x^2} + \frac{aC}{2F}\frac{\partial(\phi_1 - \phi_2)}{\partial t}$

$$
c(x,0) = c_\infty \qquad \text{for} \quad 0 \le x \le 2L_e + L_s.
\tag{4.40}
$$

The boundary conditions at the current collector and electrode/separator boundaries are listed in Table 4.2. At the current collector, the solid phase transports the imposed current density entirely while at the electrode/separator boundaries, the liquid phase carries the imposed current density. The potential at the left collector is set to zero; hence, the cell voltage is given by ϕ_1 at the right collector.

Table 4.2.
Boundary conditions

Current Collector $(x=0)$	Electrode-separator boundary $(x=L_e)$	Electrode-separator boundary $(x=L_e + L_s)$	Current collector $(x=2L_e + L_s)$
$\phi_1 = 0$	$\frac{\partial \phi_1}{\partial x}\big|_L = -\frac{I_{im}(t)-I_2}{\sigma}$	$\frac{\partial \phi_1}{\partial x}\big|_R = -\frac{I_{im}(t)-I_2}{\sigma}$	$\frac{\partial \phi_1}{\partial x}\big|_R = -\frac{I_{im}(t)-I_2}{\sigma}$
$\frac{\partial \phi_2}{\partial x} = -\frac{I_2}{\kappa}$	$[\kappa \frac{\partial \phi_2}{\partial x}]_L = [\kappa \frac{\partial \phi_2}{\partial x}]_R$	$[\kappa \frac{\partial \phi_2}{\partial x}]_L = [\kappa \frac{\partial \phi_2}{\partial x}]_R$	$\frac{\partial \phi_2}{\partial x} = -\frac{I_2}{\kappa}$
$I_2 = 0$	$I_2 = I_{im}(t)$	$I_2 = I_{im}(t)$	$I_2 = 0$
$\frac{\partial c}{\partial x} = 0$	$D\frac{\partial c}{\partial x}\big|_L = D\frac{\partial c}{\partial x}\big|_R$	$D\frac{\partial c}{\partial x}\big|_L = D\frac{\partial c}{\partial x}\big|_R$	$\frac{\partial c}{\partial x} = 0$

The capacitance per unit projected area of the electrodes, C_A (F m^{-2}) is evaluated as

$$C_A = \frac{I_0 t_{dc}}{\Delta V_d} \tag{4.41}$$

where t_{dc} represents the discharge phase duration and ΔV_d represents the potential change during discharge ($\Delta V_d = V_{d,st} - V_{min}$). The device equivalent series resistance (ESR) is obtained by

$$ESR = \frac{IR_{drop}}{2I_0}, \tag{4.42}$$

where IR_{drop} represents the voltage drop at the beginning of discharge ($IR_{drop} = V_{max} - V_{d,st}$).

Thermal Transport

In the absence of chemical reactions and convection heat transfer, the energy conservation equation can be expressed as

$$\rho c_p \frac{\partial T}{\partial t} = k \frac{\partial^2 T}{\partial x^2} + \dot{q}_{tot}, \tag{4.43}$$

where $\dot{q}_{tot}$ is the volumetric heat generation rate. It can be interpreted as the summation of an irreversible component $\dot{q}_{irr}$, which is positive during both charge and

discharge; and a reversible component $\dot{q}_{rev}$ which is positive during charge and negative during discharge [101]:

$$\dot{q}_{tot} = \dot{q}_{irr} + \dot{q}_{rev}. \tag{4.44}$$

The irreversible component is the sum of Joule heating in the solid electrode phase and in the liquid electrolyte phase $\dot{q}_{irr} = \dot{q}_{irr,elc} + \dot{q}_{irr,ely}$. Hence, in the electrode regions ($0{\leq}x{\leq}L_e$ and $L_e + L_s{\leq}x{\leq}2L_e + L_s$),

$$\dot{q}_{irr,elc} = \frac{I_1^2}{\sigma}; \qquad \dot{q}_{irr,ely} = \frac{I_2^2}{\kappa}. \tag{4.45}$$

The imposed current density $I_{im}(t)$ is transported entirely through the liquid phase in the separator region. Thus, in the separator region ($L_e{\leq}x{\leq}L_e + L_s$),

$$\dot{q}_{irr} = \dot{q}_{irr,ely} = \frac{I_0^2}{\kappa}. \tag{4.46}$$

The reversible heat generation rate caused by entropy change during double-layer formation is predicted to hold a linear relation with the double-layer current according to the model proposed by Schiffer et al. [101]

$$\dot{q}_{rev} = -2\frac{T_0 k_b}{e} ln(\frac{V_H}{V_0})i(t). \tag{4.47}$$

In the present study, an entropy constant β is used to relate the $\dot{q}_{rev}$ to the rate of charge formation at the electrode/electrolyte interface. Reversible heat generation rate in the electrode domains ($0{\leq}x{\leq}L_e$ and $L_e + L_s{\leq}x{\leq}2L_e + L_s$) is expressed as

$$\dot{q}_{rev} = \beta(aC\frac{\partial(\phi_1 - \phi_2)}{\partial t}). \tag{4.48}$$

whereas it is zero in the separator domain. The reversible heat generation rate in the electrode domains can also be expressed as

$$\dot{q}_{rev} = \beta\frac{\partial I_2}{\partial x}. \tag{4.49}$$

β formulated in this fashion was determined by Schiffer et al. [101] and d'Entremont et al. [114] as 0.101 J C^{-1} and 0.06 ± 0.012 J C^{-1} respectively by comparing analytical

models to experimental measurements. In summary, the heat generation rate $\dot{q}_{tot}$ is expressed as

$$\dot{q}_{tot} = \begin{cases} \frac{I_1^2}{\sigma} + \frac{I_2^2}{\kappa} + \beta\frac{\partial I_2}{\partial x}, & 0 \leq x \leq L_e \\ \frac{I_0^2}{\kappa}, & L_e \leq x \leq L_e + L_s \\ \frac{I_1^2}{\sigma} + \frac{I_2^2}{\kappa} + \beta\frac{\partial I_2}{\partial x}, & L_e + L_s \leq x \leq 2L_e + L_s. \end{cases} \tag{4.50}$$

Energy conservation over a complete charge/discharge cycle requires that the electrical energy supplied in the charge phase is the sum of energy output in the discharge phase and the total dissipated energy. The dissipated energy can, in principle, be transformed into various forms of energy by different physical and chemical processes. Pascot et al. [126] verified that the dissipated energy calculated from the difference of the input and output energy is equal to the total heat generation. In other words,

$$\begin{aligned} \int_0^{t_c} I_0.Vdt &= \int_{t_c}^{t_c+t_{dc}} I_0.Vdt + \int_{t_c}^{t_c+t_{dc}}\int_0^{2L_e+L_s} \dot{q}_{tot}dxdt \\ &= \int_{t_c}^{t_c+t_{dc}} I_0.Vdt + \int_{t_c}^{t_c+t_{dc}}\int_0^{2L_e+L_s} \dot{q}_{irr}dxdt. \end{aligned} \tag{4.51}$$

A portion of the energy input during charging is lost in the form of heat which is dissipated to the ambient while the rest is stored in the device and available during discharge. Note that although the reversible component of heat generation rate contributes to the instantaneous value of total heat generation rate, its net contribution over the duration of the entire cycle is zero due to opposite signs in the charge and the discharge phase. The physical properties in the electrode and separator domains are calculated using a weighted average,

$$\begin{aligned} M_{elc,av} &= \epsilon_e M_{ely} + (1 - \epsilon_e)M_{elc} \\ M_{sep,av} &= \epsilon_s M_{ely} + (1 - \epsilon_s)M_{sep} \end{aligned} \tag{4.52}$$

where M represents density ρ, thermal conductivity k or thermal diffusivity α. In a typical commercial supercapacitor, the electrode and separator assembly is wound into several layers either in the form of a stack or in the form of a cylinder. The number of layers vary with device size. Schiffer et al. [101] estimated the number of layers

for a 5000 F Nesscap supercapacitor device to be 80. The heat generated during continuous charge/discharge cycling leads to non-uniform temperature distribution inside the device. Due to convection heat loss, the temperature at the center of the device may exceed the surface temperature by as much as 3 °C as estimated by Gualous et al. [102]. The temperature distribution inside the device and its variation with time is expected to influence device aging significantly and hence needs to be thoroughly investigated.

In this study, 50 sandwich units are stacked in series to construct a device (schematic shown in Fig. 4.14a) and its temperature evolution is studied. Eq. 4.43 was solved for the entire device to evaluate the spatio-temporal evolution of temperature. The electrochemical response of each unit was assumed to be identical. The initial temperature was assumed to be uniform,

$$T(x, 0) = T_0 \qquad 0 < x < L_{dev}. \tag{4.53}$$

The left end boundary condition is

$$-k_{Al} \frac{\partial T}{\partial x}(0, t) = h(T_\infty - T(0, t)). \tag{4.54}$$

Similarly, the boundary condition at the right end is

$$-k_{Al} \frac{\partial T}{\partial x}(L_{dev}, t) = h(T(L_{dev}, t) - T_\infty). \tag{4.55}$$

Here, the ambient temperature T_∞ is considered equal to the initial temperature of the device T_0.

Dimensional Analysis

The following scaling parameters were defined to make the formulation dimensionless,

$$
\begin{aligned}
x^* &= \frac{x}{L_e}, \phi^* = \frac{\phi}{R_u T_0 / F}, t^* = \frac{t}{L_e^2 / D_e}, \\
I^* &= \frac{I}{I_0}, c^* = \frac{c}{c_\infty}, T^* = \frac{T(x, t) - T_0}{T_0}.
\end{aligned}
\tag{4.56}
$$

Table 4.3.
Normalized field equations

Left electrode $(0 < x^* < 1)$	Separator region $(1 < x^* < 1+L_1^*)$	Right Electrode $(1+L_1^* < x^* < 2+L_1^*)$
$\frac{\partial \phi_1^*}{\partial x^*} = -\Pi_1\left(\frac{I_{im}(t)}{I_0} - I_2^*\right)$	-	$\frac{\partial \phi_1^*}{\partial x^*} = -\Pi_1\left(\frac{I_{im}(t)}{I_0} - I_2^*\right)$
$\frac{\partial \phi_2^*}{\partial x^*} = -\Pi_2\frac{I_2^*}{c^*}$	$\frac{\partial \phi_2^*}{\partial x^*} = -\Pi_2\left(\frac{e}{s}\right)^{3/2}\frac{I_2^*}{c^*}$	$\frac{\partial \phi_2^*}{\partial x^*} = -\Pi_2\frac{I_2^*}{c^*}$
$\frac{\partial I_2^*}{\partial x^*} = \frac{\Pi_3}{\Pi_1}\frac{\partial(\phi_1^*-\phi_2^*)}{\partial t^*}$	$I_2^* = \frac{I_{im}(t)}{I_0}$	$\frac{\partial I_2^*}{\partial x^*} = \frac{\Pi_3}{\Pi_1}\frac{\partial(\phi_1^*-\phi_2^*)}{\partial t^*}$
$e\frac{\partial c^*}{\partial t^*} = \frac{\partial^2 c^*}{\partial x^{*2}} + \frac{\Pi_2\Pi_3}{\Pi_1}\frac{\partial(\phi_1^*-\phi_2^*)}{\partial t^*}$	$\frac{\partial c^*}{\partial t^*} = \left(\frac{s}{e}\right)^{1/2}\frac{1}{e}\frac{\partial^2 c^*}{\partial x^{*2}}$	$e\frac{\partial c^*}{\partial t^*} = \frac{\partial^2 c^*}{\partial x^{*2}} + \frac{\Pi_2\Pi_3}{\Pi_1}\frac{\partial(\phi_1^*-\phi_2^*)}{\partial t^*}$

Table 4.4.
Normalized boundary conditions

Current Collector $(x^*=0)$	Electrode-separator boundary $(x^*=1)$	Electrode-separator boundary $(x^*=1+L_1^*)$	Current Collector $(x^*=2+L_1^*)$
$\phi_1^* = 0$	$\frac{\partial \phi_1^*}{\partial x^*}\big|_L = -\Pi_1\left(\frac{I_{im}(t)}{I_0} - I_2^*\right)$	$\frac{\partial \phi_1^*}{\partial x^*}\big|_R = -\Pi_1\left(\frac{I_{im}(t)}{I_0} - I_2^*\right)$	$\frac{\partial \phi_1^*}{\partial x^*}\big|_R = -\Pi_1\left(\frac{I_{im}(t)}{I_0} - I_2^*\right)$
$\frac{\partial \phi_2^*}{\partial x^*} = -\Pi_2\frac{I_2^*}{c^*}$	$c^*\frac{\partial \phi_2^*}{\partial x^*}\big|_L = \left(\frac{s}{e}\right)^{3/2} c^*\frac{\partial \phi_2^*}{\partial x^*}\big|_R$	$\left(\frac{s}{e}\right)^{3/2} c^*\frac{\partial \phi_2^*}{\partial x^*}\big|_L = c^*\frac{\partial \phi_2^*}{\partial x^*}\big|_R$	$\frac{\partial \phi_2^*}{\partial x^*} = -\Pi_2\frac{I_2^*}{c^*}$
$I_2^* = 0$	$I_2^* = \frac{I_{im}(t)}{I_0}$	$I_2^* = \frac{I_{im}(t)}{I_0}$	$I_2^* = 0$
$\frac{\partial c^*}{\partial x^*} = 0$	$\frac{\partial c^*}{\partial x^*}\big|_L = \left(\frac{s}{e}\right)^{3/2}\frac{\partial c^*}{\partial x^*}\big|_R$	$\left(\frac{s}{e}\right)^{3/2}\frac{\partial c^*}{\partial x^*}\big|_L = \frac{\partial c^*}{\partial x^*}\big|_R$	$\frac{\partial c^*}{\partial x^*} = 0$

Here, the position vector x was scaled by the electrode length L_e while the solid phase and liquid phase potentials were scaled by the thermal voltage $R_u T_0/F$ which represents the voltage equivalent to the thermal energy for an ion of valency 1 at ambient temperature T_0. The time t was scaled by the characteristic time for ion diffusion across the length of the electrode estimated as $\tau_d = L_e^2/D_e$, while the solid phase and liquid phase current densities I_1 and I_2 were scaled by the applied current density I_0. Finally, the ion concentration $c(x,t)$ and temperature change $T(x,t) - T_0$ were scaled by the bulk ion concentration c_∞ and initial temperature T_0 respectively. The resulting dimensionless governing equations are shown in Table 4.3 and the associated dimensionless boundary conditions are documented in Table 4.4. Using scaling analysis, the 11 dimensional quantities I_0, L_e, σ, D_e, c_∞, aC, α, k, β, h and T_0 are simplified to the following 7 non-dimensional paramters:

$$\Pi_1 = \frac{I_0 F L_e}{\sigma R_u T_0}$$
$$\Pi_2 = \frac{I_0 L_e}{2 F D_e c_\infty}$$
$$\Pi_3 = \frac{aC D_e}{\sigma}$$
$$Le = \frac{\alpha_{ely}}{D_e} \tag{4.57}$$
$$\Pi_5 = \frac{I_0 L_e R_u}{F D_e (\rho c_p)_{ely}}$$
$$\Pi_6 = \frac{\beta F}{R_u T_0}$$
$$\Pi_7 = \frac{h L_e}{k_{Al}}.$$

The non-dimensional number Π_1 scales the voltage across the length of the electrode in the solid phase $I_0 L_e/\sigma$ by the thermal voltage $R_u T_0/F$. Similarly, the dimensionless number Π_2 scales the voltage across the length of the electrode in the liquid phase $I_0 L_e/\kappa_e$ by the thermal voltage $R_u T_0/F$. The Lewis number Le is given by the ratio of the characteristic time for ion diffusion $\tau_d = L_e^2/D_e$ to that for heat diffusion $\tau_{th} = L_e^2/\alpha_{ely}$ in the electrolyte. The non-dimensional number Π_5 is the ratio of the characteristic volumetric heat capacity $C_d = I_0 L_e R_u/F D_e$ to that of the elec-

trolyte $(\rho c_p)_{ely}$. Similarly, Π_6 scales the reversible heat coefficient β to the thermal voltage and Π_7 is the effective Biot number considering the characteristic length to be the electrode thickness L_e. The non-dimensional energy conservation equation is expressed as:

$$\frac{\partial T^*}{\partial t^*} = \begin{cases} \frac{\alpha_{Al}}{\alpha_{ely}} Le \frac{\partial^2 T^*}{\partial x^{*2}} + \frac{\sigma}{\sigma_{Al}} \frac{(\rho c_p)_{ely}}{(\rho c_p)_{Al}} \Pi_1 \Pi_5, & x^* \quad collector \\ \frac{\alpha_{elc,av}}{\alpha_{ely}} Le \frac{\partial^2 T^*}{\partial x^{*2}} + \frac{(\rho c_p)_{ely}}{(\rho c_p)_{elc,av}} \left(\Pi_1 \Pi_5 \left(\frac{I_s(t)}{I_0} - I_2^* \right)^2 + \Pi_2 \Pi_5 \frac{I_2^{*2}}{c^*} + \Pi_5 \Pi_6 \frac{\partial I_2^*}{\partial x^*} \right), & x^* \epsilon \, electrode \\ \frac{\alpha_{sep,av}}{\alpha_{ely}} Le \frac{\partial^2 T^*}{\partial x^{*2}} + \frac{(\rho c_p)_{ely}}{(\rho c_p)_{sep,av}} \frac{\Pi_2 \Pi_5}{c^*}, & x^* \quad separator \end{cases}$$

$$(4.58)$$

The boundary condition at the left end boundary is given by,

$$\frac{\partial T^*}{\partial x^*} \Big|_{x^*=0} = \Pi_7 T^* \big|_{x^*=0}. \tag{4.59}$$

Similarly, the boundary condition at the right end boundary is given by,

$$\frac{\partial T^*}{\partial x^*} \Big|_{x^*=\frac{L_{dev}}{L_e}} = -\Pi_7 T^* \big|_{x^*=\frac{L_{dev}}{L_e}}. \tag{4.60}$$

4.2.3 Method of Solution

The set of governing equations (Table 4.1) and associated boundary and initial conditions (Table 4.2 and Eq. 4.40) were used to solve for electrochemical transport variables ϕ_1, ϕ_2, I_2 and c. The electrochemical transport equations were solved for a single unit with uniform mesh size in both electrode and separator regions. On the other hand, for the thermal model, the computational domain consisted of N number of stacked units. The energy conservation equation, Eq. 4.43 along with the associated boundary and initial conditions (Eq. 4.53-55) was solved to determine the spatio-temporal variation of temperature. The electrochemical performance of each unit in the stack was assumed to be identical and thus the results obtained by solving the electrochemical problem were used repetitively to estimate the local

heat generation rate at each grid point. The mesh size for the thermal model was chosen to be p times larger than that for the electrochemical model, and hence only the pth multiples of the evaluated electrochemical transport variables were used to compute the local heat generation rate. The expansion factor p was introduced to reduce the computation time while maintaining accuracy. Refinement was performed on mesh size, time step and expansion factor p to determine their appropriate values. Numerical convergence was assessed on the basis of computed energy, power density, spatially averaged heat generation rate during charge phase ($\dot{Q}_{av,ch}$) and discharge phase ($\dot{Q}_{av,dc}$).
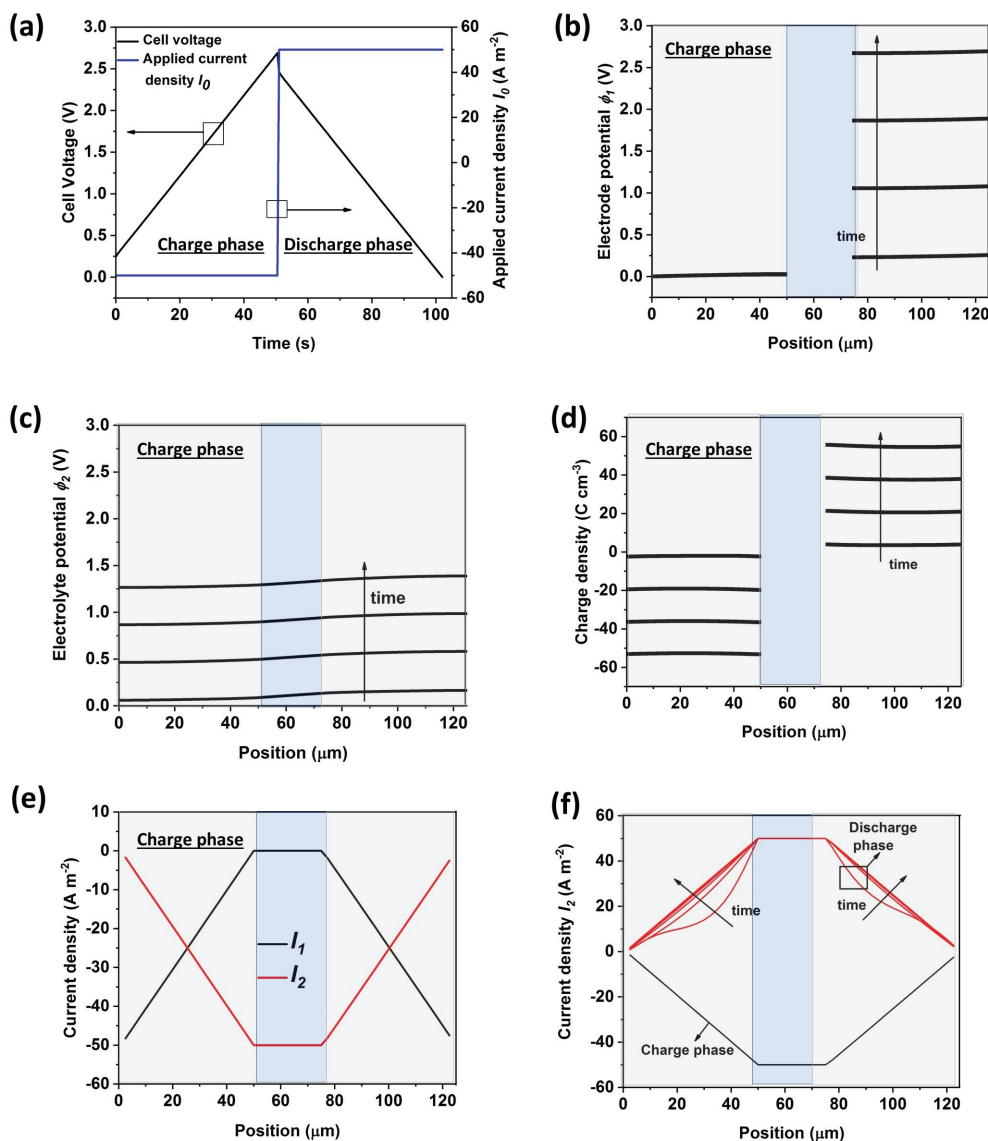
Fig. 4.15. (a) Cell voltage as a function of time during a single charge/discharge cycle for an operating current density I_0=50 A m^{-2}. The device operates in the voltage range of 0 and 2.7 V. Spatial variation of solid phase potential ϕ_1, liquid phase potential ϕ_2 and stored charge density $Q_{ch} = aC(\phi_1 - \phi_2)$ at equi-spaced time intervals from the beginning to end of discharge (t/t_c =0.0, 0.17, 0.34, 0.51) are shown in (b), (c) and (d) respectively. Spatial variation of the solid phase current density I_1 and liquid phase current density I_2 during the charge phase (t/t_c=0.25) are shown in (e), while the spatial variation of I_2 during transition from charge to discharge phase is shown in (f). The grey and blue regions in the plots represent the electrode and separator regions in the device.

4.3   Results and Discussion

Simulations were performed for the set of parameters shown in Table 4.9. Refinement studies were performed for mesh size, time step and expansion factor p. The results of refinement study are displayed in Tables A1, A2 and A3. Upon inspection, less than 1% change exists in the computed values upon refinement beyond a mesh size value of 0.5 μm, a time step of 0.05 s and a division factor p of 5. Therefore, these parameters are used in all subsequent calculations. Electrochemical performance and heat generation rates were evaluated during constant-current cycling at a current density I_0=50 A m^{-2} in the voltage range 0-2.7 V. Detailed numerical simulations were performed to investigate the influence of operating current density I_0, imposed rest period, convection heat transfer coefficient h, set voltage range of operation ΔV and the number of sandwich units N on spatio-temporal temperature evolution in the device during galvanostatic charge/discharge cycling.

4.3.1   Electrochemical Behavior

The variation of cell voltage with time is studied for continuous cycling at I_0= 50 A m^{-2}. The cycle time is modulated in order to cycle the device over the prescribed voltage range of 0-2.7 V. Fig. 4.15(a) shows that the cell voltage rises linearly from 0 to 2.7 V during charging, while in the discharge phase, first it undergoes a drop of 0.23 V and then declines linearly to 0 V. The cycle period t_c of 102 s is comparable to that observed for a commercial EDLC composed of porous electrodes. Note that unlike past EDLC simulations [114,116] in which flat and planar electrodes were considered, here a porous electrode EDLC of realistic dimensions is simulated. As expected, the porous electrodes charge slowly relative to planar EDLCs, and hence the cycle period t_c is similar to that measured experimentally. Fig. 4.15(b) and (c) display the time evolution of electrode phase potential, ϕ_1 and electrolyte phase potential, ϕ_2 at equally spaced time intervals from beginning to end of charge phase, for I_0=50 A m^{-2}. The grey and blue zones denote the electrode and separator domains respectively. During

charging, the positive electrode potential rises at a constant rate, while the negative electrode potential stays invariant. A mild slope in ϕ_1 can be observed across the length of the electrodes at all times. This slope is expected to rise with operating current density and decrease in solid phase electrical conductivity σ. Similar to ϕ_1, the electrolyte phase potential ϕ_2 can be observed to vary spatially. The variation is larger in the separator region than in the electrodes, which can be attributed to I_2 being larger in the separator region. The volumetric charge density in the electrodes Q_{ch} which is equal to product of the volumetric capacitance (aC) and the difference between solid phase and liquid phase potentials (ϕ_1 - ϕ_2) is shown in Fig. 4.15(d) at equi-spaced time instants during a single charge phase. The charge density rises as a function of time during the charge phase and decreases during the discharge phase. Furthermore, the distribution is non-uniform, indicating insufficient electrode utilization.

Fig. 4.15(e) shows the spatial variation of solid phase current density I_1 and liquid phase current density I_2 during a single charge phase. Both I_1 and I_2 are symmetric about the centerline, which is representative of pure double-layer behavior. At the current collector interface, the operating current density is transported entirely through the solid phase. Also, the charging phase corresponds to a negative value of the operating current density, I_0. Thus, during the charge phase, I_1 increases linearly from $-I_0$ at the current collector interface to 0 at the separator interface while I_2 declines linearly from 0 at the current collector interface to a value of $-I_0$ at the separator interface. In the separator region, the liquid phase solely transports the operating current. The charging process continues until the cell potential reaches the upper set value. During the discharge phase, a reversal of sign of both the solid phase current density, I_1 and liquid phase current density, I_2 occurs. The corresponding transition of the liquid phase current density I_2 is displayed in Fig. 4.15f. Clearly, at the beginning of the discharge phase, I_2 follows a non-linear profile which corresponds to non-equillibrium conditions. However, it gradually attains a linear profile, about 3 s into the discharge phase.

Fig. A1 shows the electrolyte concentration $c(x,t)$ as a function of position x at several time instants during a charge/discharge step. At the beginning of the charge phase, salt concentration $c(x,t)$ can be observed to be larger at the negative electrode compared to that at the positive electrode. However, as the cell voltage continues to rise, the salt concentration at the negative electrode reduces while it rises at the positive electrode, similar to past simulations [141]. Notably, the concentration variation is steeper in the separator region compared to the electrodes, which may be attributed to the lower diffusion coefficient in the separator region. The cell voltage profiles at different operating current densities I_0=30, 50 and 70 A m^{-2} are displayed in Fig. A2. All the profiles exhibit similar shape. The voltage rises linearly from a positive value to the upper limit during charge phase. At the beginning of discharge, a sharp voltage drop occurs followed by a linear decline.

Conservation of charge in the neutral liquid phase requires the spatial derivative of electrolyte phase current to be equal to the rate of charge accumulation at the electrode/electrolyte interface

$$\frac{\partial I_2}{\partial x} = aC\frac{\partial(\phi_1 - \phi_2)}{\partial t}. \tag{4.61}$$

Performing mass conservation for the electrolyte bulk concentration in the electrode domain yields

$$e\frac{\partial c}{\partial t} = D_e\frac{\partial^2 c}{\partial x^2} + \frac{aC}{2F}\frac{\partial(\phi_1 - \phi_2)}{\partial t}. \tag{4.62}$$

where the first and second terms on the right side represent ion flux corresponding to diffusion and corresponding to migration in an electric field respectively. Ion flux in the separator domain is caused only by diffusion, and thus the mass conservation equation is

$$s\frac{\partial c}{\partial t} = D_s\frac{\partial^2 c}{\partial x^2}. \tag{4.63}$$

The complete set of transport equations governing the electrode phase potential ϕ_1, the electrolyte phase potential ϕ_2, the electrolyte phase current density I_2 and the bulk electrolyte concentration c is listed in Table 4.1.
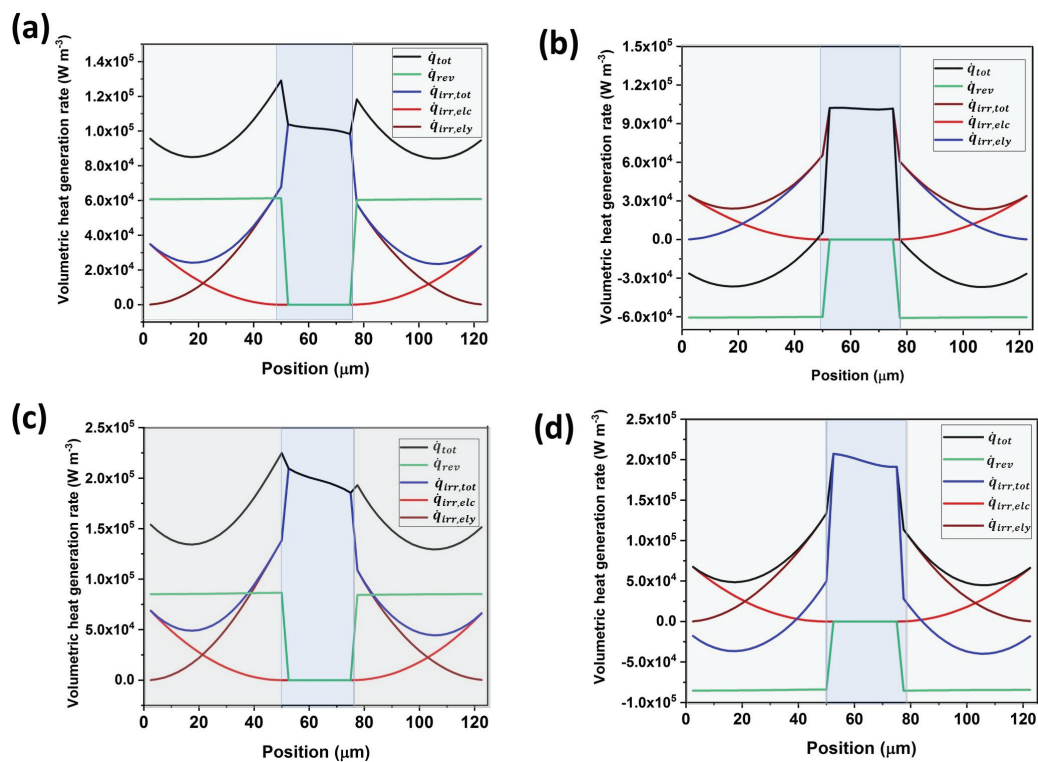
Fig. 4.16. Predicted heat generation rates $\dot{q}_{irr,elc}$, $\dot{q}_{irr,ely}$, $\dot{q}_{irr,tot}$, $\dot{q}_{rev}$ and $\dot{q}_{tot}$ as functions of location x at non-dimensional time (a) t/t_c=0.25 and (b) t/t_c=0.75 for I_0= 50 A m^{-2}. Predicted heat generation rates $\dot{q}_{irr,elc}$, $\dot{q}_{irr,ely}$, $\dot{q}_{irr,tot}$, $\dot{q}_{rev}$ and $\dot{q}_{tot}$ as functions of location x at non-dimensional time (a)t/t_c=0.25 and (b)t/t_c=0.75 for I_0=70 A m^{-2}.

4.3.2 Thermal Behavior

Local Heat Generation Rates

Fig. 4.16 shows the predicted value of volumetric heat generation rates $\dot{q}_{irr,elc}$, $\dot{q}_{irr,ely}$, $\dot{q}_{irr,tot}$, $\dot{q}_{rev}$ and $\dot{q}_{tot}$ as functions of location x during the charge phase (non-dimensional time $t/t_c=0.25$) and during the discharge phase (non-dimensional time $t/t_c=0.75$). The results for $I_0=$ 50 A m^{-2} are shown in Fig. 4.16(a) and (b) while results for $I_0=70$ A m^{-2} are displayed in Fig. 4.16(c) and (d). The grey and blue regions in the plots represent electrode and separator, respectively. Fig. 4.16(a) indicates that the total heat generation rates is more uniform in the separator compared to in the electrodes. Such observation can be attributed to the fact that in the separator the reversible heat generation rate $\dot{q}_{rev}$ is zero, and the liquid phase current density I_2 is uniform. The slight variation in $\dot{q}_{tot}$ within the separator is due to varying local electrolyte concentration c. On the other hand, the irreversible heat generation rate variation within the electrodes can be attributed to changing solid phase current density I_1 and liquid phase current I_2 as shown in Fig. 4.16(b) and (c). Such spatial variation in irreversible heat generation rate was neglected in the first principles model developed by d'Entremont et al. [114] in which the computational domain consisted of only the electrolyte. The reversible heat generation rate $\dot{q}_{rev}$ does not vary spatially within the electrodes, which implies that the total reversible heat generation rate within a cell is linearly proportional to the electrode thickness.

Comparing Fig. 4.16(a) and (b), the total heat generation rate $\dot{q}_{tot}$ is larger within the electrodes in the charge phase compared to the discharge phase because the reversible heat generation rate $\dot{q}_{rev}$ is positive during charge and negative during discharge. On the other hand, in the separator, the total heat generation rate is almost the same. A comparison of Fig. 4.16(a) and (c) establishes that a change in the operating current density I_0 leads to a substantial change in the magnitude and spatial variation of the volumetric heat generation rates. Both the reversible heat generation rate $\dot{q}_{rev}$ and the irreversible heat generation rate $\dot{q}_{irr,tot}$ are higher
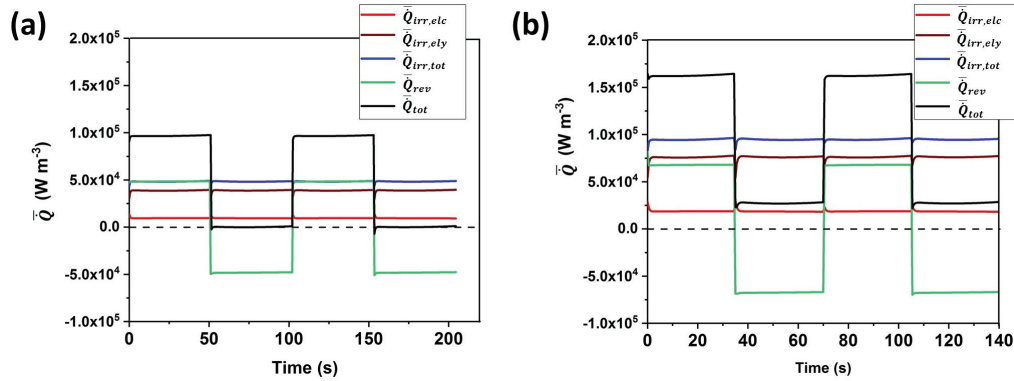
Fig. 4.17. Spatially averaged irreversible heat generation rate in the solid phase $\dot{\bar{Q}}_{irr,elc}$, irreversible heat generation rate in the liquid phase $\dot{\bar{Q}}_{irr,ely}$, total irreversible heat generation rate $\dot{\bar{Q}}_{irr,tot}$, reversible heat generation rate $\dot{\bar{Q}}_{rev}$ and total heat generation rate $\dot{\bar{Q}}_{tot}$ plotted as a function of time t for two consecutive charge/discharge cycles at operating current density (a) I_0=50 A m^{-2} and (b) I_0=70 A m^{-2}.

at I_0=70 A m^{-2} compared to I_0=50 A m^{-2}. Furthermore, in the separator region, $\dot{q}_{tot}$ has a larger slope at I_0=70 A m^{-2} which can be attributed to the larger gradient in electrolyte concentration c at high current densities. In summary, the total heat generation rate varies considerably in space during both charge and discharge, which was neglected entirely in past equivalent circuit electro-thermal models [103, 126].

Overall Heat Generation Rates

In order to assess the relative significance of the different components of the total heat generation rate, spatial and temporal integration needs to be performed on the evaluated volumetric heat generation rate $\dot{q}_i(x,t)$. In this context, four new terms are defined: spatially integrated instantaneous heat generation rate $\dot{Q}_i(t)$ [W m^{-2}]= $\int_0^{2L_e+L_s} \dot{q}_i dx$, spatially averaged instantaneous heat generation rate $\dot{\bar{Q}}_i(t)$[W m^{-3}]= $\int_0^{2L_e+L_s} \dot{q}_i dx/(2L_e + L_s)$, the total heat generation in a charge/discharge cycle Q_i [J m^{-2}]= $\int_0^{t_c+t_{dc}} \int_0^{2L_e+L_s} \dot{q}_i dx$, and the spatially and temporally averaged heat generation rate $\hat{\bar{Q}}_i$ [W m^{-3}]= $\int_0^{t_c+t_{dc}} \int_0^{2L_e+L_s} \dot{q}_i dx/[(2L_e+L_s)(t_c+t_{dc})]$. Fig. A3 compares

the breakdown of the net energy input during the charge phase ($\int_0^{t_c} I_0.V\,dt$) into its various components. According to Eq.(19), the components are: total energy dissipated as Joule heat in the solid electrode phase ($Q_{irr,elc}$), total energy dissipated as Joule heat in the liquid electrolyte phase ($Q_{irr,ely}$), and total energy output during discharge ($\int_{t_c}^{t_c+t_{dc}} I_0.V\,dt$). The results are shown for two operating current densities I_0=50 and 70 A m^{-2}. As observed in Fig. A3, for the higher operating current density, the net energy dissipated due to Joule heat is much larger, and consequently, the energy output is lower.

Fig. 4.17 shows the net spatially averaged total heat generation rate, $\overline{\dot{Q}}$ and its various components, $\overline{\dot{Q}}_{irr,elc}$, $\overline{\dot{Q}}_{irr,ely}$ and $\overline{\dot{Q}}_{rev}$ as functions of time. Two cases are considered: (a) I_0=50 A m^{-2} and (b) I_0=70 A m^{-2}. First, in both cases the irreversible Joule heating rates $\overline{\dot{Q}}_{irr,elc}$, $\overline{\dot{Q}}_{irr,ely}$ and $\overline{\dot{Q}}_{irr,tot}$ are always positive and constant. In addition, they are proportional to square of the operating current density I_0. The spatially averaged reversible heat generation rate $\overline{\dot{Q}}_{rev}$ on the other hand, is positive during the charge phase and negative during discharge but equal in magnitude, as observed experimentally. Furthermore, an inspection of Fig. 4.17(a) and (b) demonstrates that it is a linear function of I_0.

The spatially integrated instantaneous heat generation rate, $\dot{Q}_{rev}(t)$ is evaluated as 6.06 and 8.49 W m^{-2} at I_0=50 and 70 A m^{-2} respectively. These results are similar to the reversible heat generation rates of 5.03 and 7.05 W m^{-2} calculated using Eq. 4.34 as proposed by Schiffer [101]. Another noteworthy point is that $\dot{Q}_{rev}(t)$ is independent of the separator length because the separator has no contribution, in contrast with the model proposed by Schiffer et al. [101] which predicted increasing values of $\dot{Q}_{tot,rev}$ with increasing inter-electrode distance.

The spatially integrated total heat generation rate $\dot{Q}_{tot}(t)$ alternates between two constant values during charge and discharge. For I_0=50 A m^{-2}, it is 96.5 and -0.1 kW m^{-3} in the charge and in the discharge phases respectively. Thus, in the discharge phase, there is no net heat generation rate, because the Joule heating rate is completely offset by the reversible heat generation rate. Similarly, for I_0=70 A
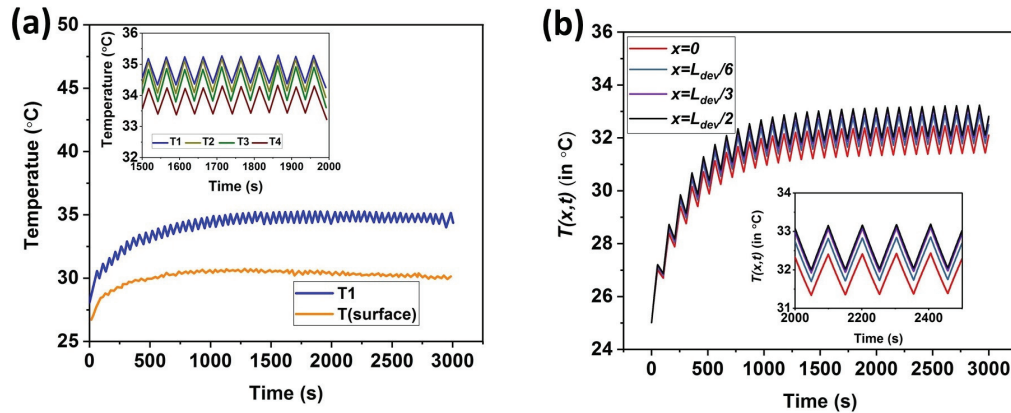
Fig. 4.18. (a) Thermocouple temperature measurements at different positions of a BCAP350 F EDLC cycled at $\pm$ 15 A plotted as a function of time t (reproduced from Fig. 10(a) of Ref. [102]). The inset shows a magnified view of the temperature profiles (reproduced from Fig. 10(b) of Ref. [102]). In the figure, T(surface) represents the temperature measured on the outer surface, while T1, T2, T3 and T4 represent temperature measurements corresponding to positions moving away from the center of the device. (b) Numerically predicted temperature evolution with time at positions $x = 0$, $x = L_{dev}/6$, $x = L_{dev}/3$ and $x = L_{dev}/2$ for imposed current density $I_0 = 50$ A m^{-2} and outer convection heat transfer coefficient $h = 20$ W m^{-2} K^{-1}. The inset shows a magnified view of the temperature profiles in the time range of 2000 and 2500 s.

m^{-2}, the total heat generation rate $\dot{Q}_{tot}(t)$ alternates between 163 and 27 kW m^{-3}. Thus at large currents, the Joule heat generation rate exceeds the reversible heat generation rate in the discharge phase leading to a net positive total heat generation rate.

Fig. 4.20(a) shows the predicted device centerline temperature as a function of time t for continuous charge/discharge cycling at three values of operating current density $I_0 = 30$, 50 and 70 A m^{-2}. The cycle time was adjusted in order to maintain the device in a voltage window of 0-2.7 V. In all cases, the average temperature rises initially, followed by saturation after a certain time. The temperature oscillates over a longer time period at low operating current densities which correspond to longer cycle

Table 4.5.

Input parameters for Cases 1 to 3 used to illustrate the scaling analysis. The dimensionless parameters $\Pi_1 = 1.453$, $\Pi_2 = 2.540$, $\Pi_3 = 0.0034$, $Le = 1.16 \times 10^4$, $\Pi_5 = 0.0172$, $\Pi_6 = 2.337$ and $\Pi_7 = 2.44 \times 10^{-6}$ are same in all three cases.

-	I_0 (A m^{-2})	σ (S m^{-1})	D_∞ (m^2 s^{-1})	k_{Al} (W/(m.K))	k_{elc} (W/(m.K))	k_{ely} (W/(m.K))	k_{sep} (W/(m.K))	h (W/(m^2.K))
Case 1	50	0.067	1×10^{-11}	205	0.649	0.164	0.334	10
Case 2	100	0.134	2×10^{-11}	410	1.298	0.328	0.668	20
Case 3	25	0.033	5×10^{-11}	103	0.325	0.082	0.167	5
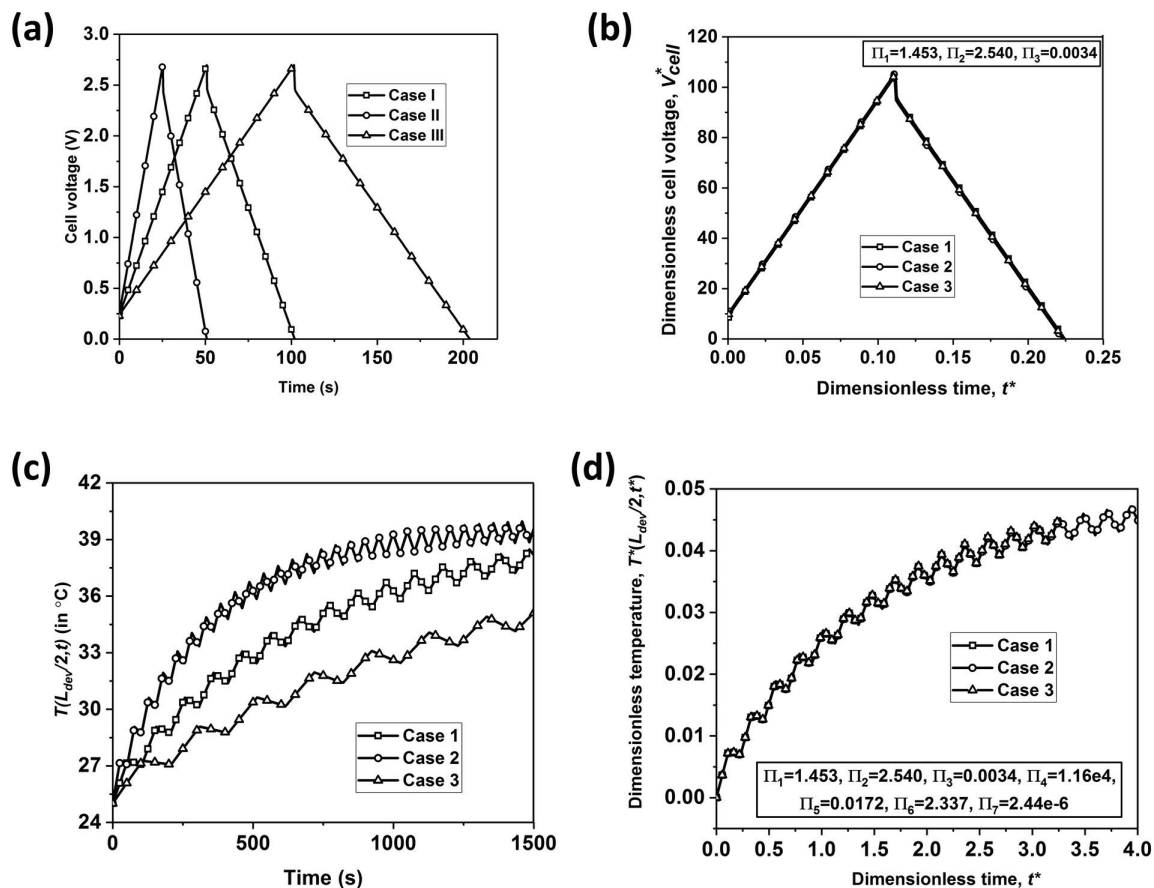
Fig. 4.19. Computed (a) cell voltage V_{cell} as a function of time t, (b) dimensionless cell voltage V^*_{cell} as function of dimensionless time t^* during a single galvanostatic charge/discharge cycle for cases 1 to 3 (Table 4.5). Computed (c) device centerline temperature $T(L_{dev}/2, t)$ as a function of time t and (d) dimensionless centerline temperature $T^*(L_{dev}/2, t^*)$ as a function of dimensionless time t^* for cases 1 to 3 (Table 4.5).

time periods. The trend is similar to measured temperature profiles on the surface of a commercial EDLC reported by Gualous et al. [121]. The steady-state temperature value obtained from experiments [102] (after 3000 s of cycling) is plotted as a function of operating current in Fig. 4.20(d). The quadratic function shown in the plot can be observed to fit the results very well, thus confirming the hypothesis that at steady state, Joule heating solely defines the average temperature of the device. Similarly, the numerically predicted device centerline temperature follows a quadratic variation with operating current density as shown in Fig. 4.20(b).

The numerically predicted spatial variation of temperature inside the device at the end of 3000s is shown in Fig. 4.21(a), (b) and (c) for the three operating current densities. As expected, the temperature profile is parabolic in all cases with the maximum temperature occurring at the device center and the minimum temperature at the device surface. Both the center temperature as well as the surface temperature rise as a function of operating current density. The temperature difference between center and surface was predicted to be 0.24, 0.40 and 1.42 °C at operating current densities I_0=30, 50 and 70 A m^{-2}. Such a non-linear variation is because the Joule heating varies with square of operating current density. This difference in temperature between the center and surface was measured to be in between 1-3 °C for a BCAP 350 F EDLC by Gualous et al. [102].

Temperature Evolution

Fig. 4.18 compares the numerical predictions of the present model with experimental temperature measurements on commercial supercapacitors reported in the literature [102]. Parameters for the simulations are presented in Table 4.9. Fig. 4.18a displays the temperature response measured by Gualous et al. [102] in a 350 F EDLC subjected to galvanostatic charge/discharge at an operating current of 15 A and cooled by natural convection on the external surface. T_{sur} represents the temperature measured on the external surface of the device while T_1, T_2, T_3 and T_4 represent
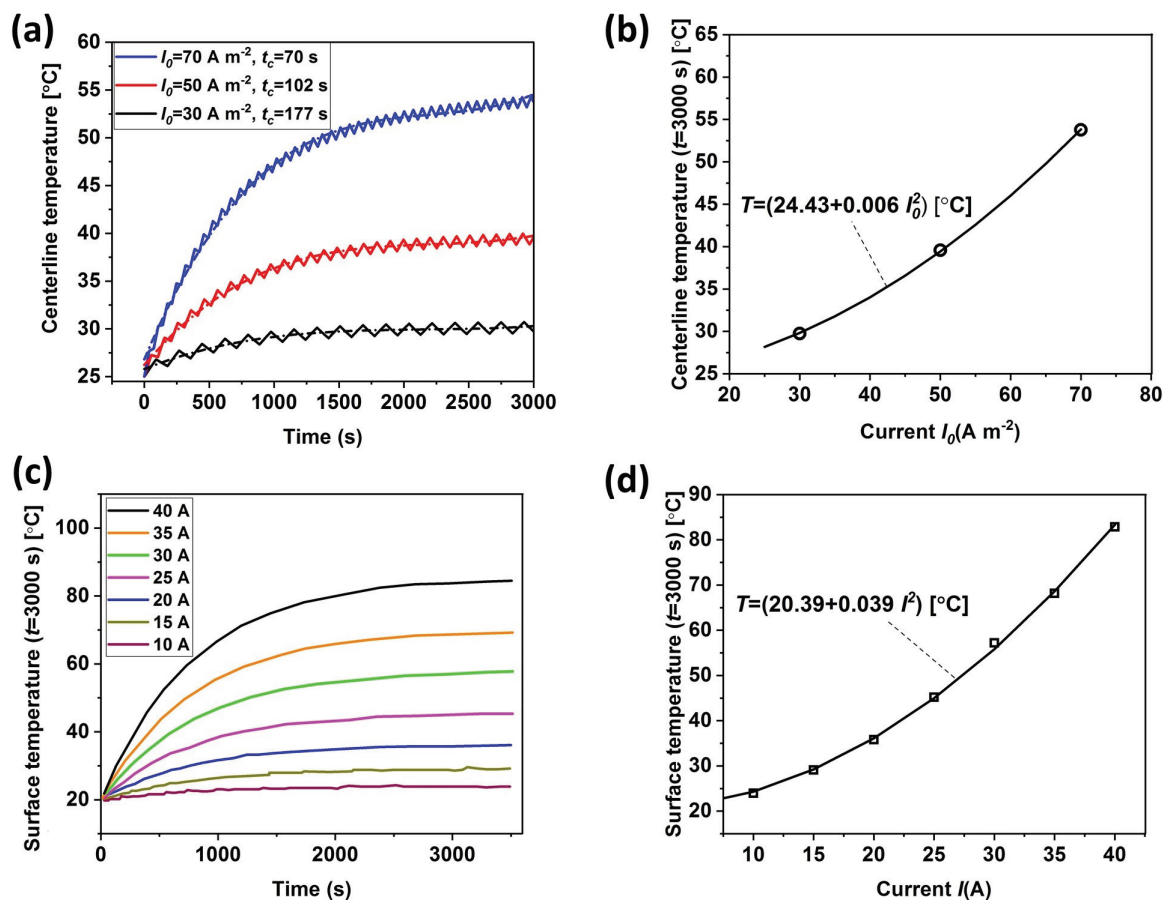
Fig. 4.20. (a) Predicted device centerline temperature $T(L_{dev}/2, t)$ as a function of time t for galvanostatic cycling at three different operating current densities, I_0=30, 50 and 70 A m^{-2}. The dotted lines represent the cycle-averaged temperature profiles. The convection heat transfer coefficient h on the outer surface of the device is assumed to be 20 W m^{-2} K^{-1}. (b) Numerically predicted device cycle averaged centerline temperature after 3000 s of cycling plotted as a function of cycling current density. (c) Measured surface temperature of a Maxwell BCAP350 F supercapacitor as a function of time, reported by Gualous et al. [121] for cycling currents 10, 15, 20, 25, 30, 35 and 40 A (reproduced from Fig. 13). (d) Plot of measured surface temperature after 3000 s of galvanostatic cycling as a function of operating current.

temperature measurements at different radial positions inside the device from the center to a point closest to the outer surface. The results indicate that temperature decreases along the radius due to dissipated convective heat flux on the outer surface. Furthermore, the external surface temperature profile T_{sur} does not exhibit the oscillations apparent in measurements taken inside the device.

Fig. 4.18(b) shows the numerical results obtained from the present model for a cycling current density of I_0=50 A m^{-2} and a fixed value of convection heat transfer coefficient, h= 20 W m^{-2} K^{-1} at the outer device surface. The inset illustrates a comparison of the temperature profiles computed at different locations along the length of the device. Our physical model results resemble the experimental response of commercial EDLCs during galvanostatic cycling quite well. The predicted thermal behavior is similar to experimental results both qualitatively as well as quantitatively. At all locations, the cycle-averaged temperature rises rapidly initially, followed by gradual saturation. Furthermore, temperature oscillations are superimposed onto the average temperature profile as a consequence of reversible heat generation. At saturation, the total heat generation rate inside the device equals the heat dissipation rate to the ambient. The temperature oscillations occur due to reversible heat generation which is opposite in sign during the charge and discharge phase. The predicted amplitude of the oscillations is around 1.15 °C, which is close to 0.9 °C measured by Schiffer [101].for a voltage range of 0.5 and 2.5 V. Importantly, the agreement in temperature results contrasts with recent simulations based on planar electrodes [114,116] which predicted temperature profiles that were similar in shape to measurements, but whose oscillation amplitudes magnitude were smaller by several orders of magnitude because of the assumption of flat and metallic electrodes instead of porous electrodes.

4.3.3   Dimensional Analysis

Table 4.5 summarizes the three sets of input parameters used for scaling analysis. Case 1 was based on realistic system parameters described by Verbrugge et al. [133].

The electrolyte ionic conductivity was assumed to be that of 0.93 M TEABF$_4$ salt in acetonitrile solvent at 25 °C. The input parameters for case 2 and 3 were varied in a way such that the dimensionless numbers remained constant. The dimensionless numbers corresponding to each case was Π_1=1.453, Π_2=2.540, Π_3=0.0034, Le=1.16 × 10^4, Π_5=0.0172, Π_6=2.337 and Π_7=2.44× 10^{-6}. The dimensionless governing equations along with associated boundary conditions represented in Table 4.3 and 4.4 respectively were solved to compute ϕ_1^*, ϕ_2^*, I_2^* and c^*, while Eqs. (26)-(28) were used to determine T^*. The results depend only on the seven dimensionless numbers defined in Eq. 4.57 and a few property ratios ($\frac{L_e}{L_s}$, $\frac{\epsilon_e}{\epsilon_s}$, $\frac{\sigma}{\sigma_{Al}}$, $\frac{\alpha_{elc}}{\alpha_{Al}}$, $\frac{\alpha_{sep}}{\alpha_{Al}}$, $\frac{(\rho c_p)_{Al}}{(\rho c_p)_{elc}}$ and $\frac{(\rho c_p)_{Al}}{(\rho c_p)_{sep}}$). Fig. 4.19(a) illustrates the cell voltage as a function of time t during a single galvonostatic charge/discharge cycle for all three cases. The cell voltage profiles featured different cycle periods due to different values of operating current density I_0. Fig. 4.19(b) plots the dimensionless cell voltage V_{cell}^* versus dimensionless time t^*, and the dimensionless voltage profiles can be observed to collapse onto a single curve.

Similarly, Fig. 4.19(c) and (d) illustrate the dimensional analysis for temperature profiles. The device centerline temperature is shown as a function of time t for all three cases in Fig. 4.19(c). As expected, higher operating current density I_0 is observed to lead to higher temperature. However, when the results are plotted in terms of dimensionless temperature versus dimensionless time, they all collapse onto a single curve as shown in Fig. 4.19(d).

4.3.4 Influence of Convection Heat Transfer Coefficient

The convection heat transfer coefficient h governs the heat transfer rate from the external boundary of the device to the ambient. A previous study by Sakka et al. [103] has compared the temperature evolution in supercapacitor modules during cycling while being subjected to natural and forced convection. In general, the convection heat transfer coefficient is a function of the flow conditions on the outer surface of the device. In a few studies, the device is modeled as a horizontal cylinder, and

the convection heat transfer coefficient is estimated using Nusselt number- Rayleigh number relations [121]. In the case of laminar convection ($10^3 \leq$ Ra $\leq 10^9$)

$$Nu = 0.53Ra^{1/4}, \tag{4.64}$$

while in case of turbulent convection ($10^9 \leq$ Ra $\leq 10^{13}$)

$$Nu = 0.10Ra^{1/3}. \tag{4.65}$$

In case of forced convection, the total heat transfer coefficient (including convection and radiation) is estimated from empirical relations such as [142, 143]

$$h = 5 + 17.(v + 0.1)^{0.66} \tag{4.66}$$

where h is in W m^{-2} K^{-1} and v is in m s^{-1}. Fig. 4.22 displays the influence of h on the temperature evolution in the device upon continuous charge/discharge cycling at an operating current density of 50 A m^{-2}. As shown in Fig. 4.22(a), the numerically predicted device centerline temperature undergoes a rapid rise initially, followed by gradual saturation or a slow rise. For h=20 W m^{-2}K^{-1}, the average temperature saturates at 33 °C, while for h=10 W m^{-2}K^{-1}, it saturates at 39 °C. However, for h=5 W m^{-2}K^{-1}, the average temperature continues to rise at a slow pace even at the end of 3000 s. As expected, a large heat transfer coefficient improves device cooling resulting in lower average temperature at the end of 3000 s. As shown in the inset of Fig. 4.22(a), the device centerline temperature decreases from a value of 51 °C at h=5 W m^{-2}K^{-1} to 33 °C at h=20 W m^{-2}K^{-1}. The spatial variation of temperature inside the device at the end of 3000 s is shown in Fig. 4.22(b). Such parametric analysis could prove useful in sizing of a cooling system required to prevent the maximum temperature to rise above the rated temperature which is typically 65 °C for commercial EDLCs [103].

4.3.5 Influence of Number of Sandwich Units

Commercial EDLCs are packaged by stacking several layers of the sandwich units in a casing. The number of layers is expected to depend on the shape of the casing
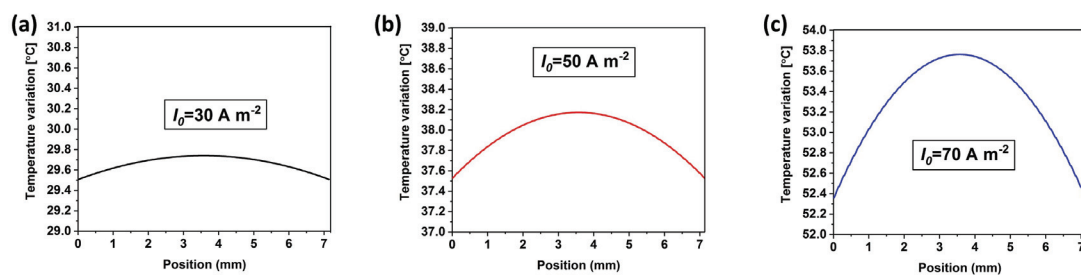
Fig. 4.21. Numerically predicted spatial variation of temperature in the device after 3000 s of galvanostatic cycling ($T(x,\ t{=}3000$ s) - $T(x{=}0,\ t{=}3000$ s)) at operating current density values of $I_0{=}$ (a) 30 A m^{-2}, (b) 50 A m^{-2} and (c) 70 A m^{-2}. The convection heat transfer coefficient h on the outer surface of the device is assumed to be 20 W m^{-2} K^{-1}.

and desired capacitance of the device. Schiffer et al. [101] estimated the number of layers for a commercial Nesscap 5000F EDLC device to be 80. Here, we consider the 1D model shown in Fig. 4.14(a), consisting of a linear stack of elementary units. The total number of layers in the device defines its size and is expected to influence the temperature evolution in the device. Fig. 4.23(a) shows the numerically predicted device centerline temperature evolution profiles for different numbers of layers. The device centerline temperature for N=30 saturates at a temperature of 33 °C after about 1000 s, while the device with N=50 saturates at 38 °C at the end of 1400 s. However, for N=80, the temperature does not saturate but continues to rise gradually even after 3000 s. Thus, the average device temperature increases with the number of constituent sandwich units. The average temperature plotted as a function of N shown in the inset of Fig. 4.23(a) demonstrates a linear relationship. This observation may be attributed to the fact that as the number of units rises, the total heat generation rate in the device increases accordingly. However, the outer surface area remains invariant due to its rectangular cross-section. In addition to the device centerline temperature, the spatial variation in temperature from the center to the edge is found to rise with the number of units. The temperature difference is evaluated to be 0.26, 0.70 and 1.70 °C for N=30, 50 and 80 respectively.

4.3.6 Influence of Rest Time Period

In practical applications, the operation of EDLCs involves rest times imposed between charge and discharge processes, instead of continuous charge/discharge. This stems from the fact that in hybrid vehicles, EDLCs are charged by regenerative braking which is stored for some time and then released during rapid acceleration. The Scania and BMW driving cycles that were tested on commercial EDLCs by Sakka et al. [103] featured charging/discharging currents of the order of 100-300A separated by rest periods of 20-100s. Thus, in order to make realistic predictions of temperature evolution, it is essential to study the impact of rest time duration on thermal
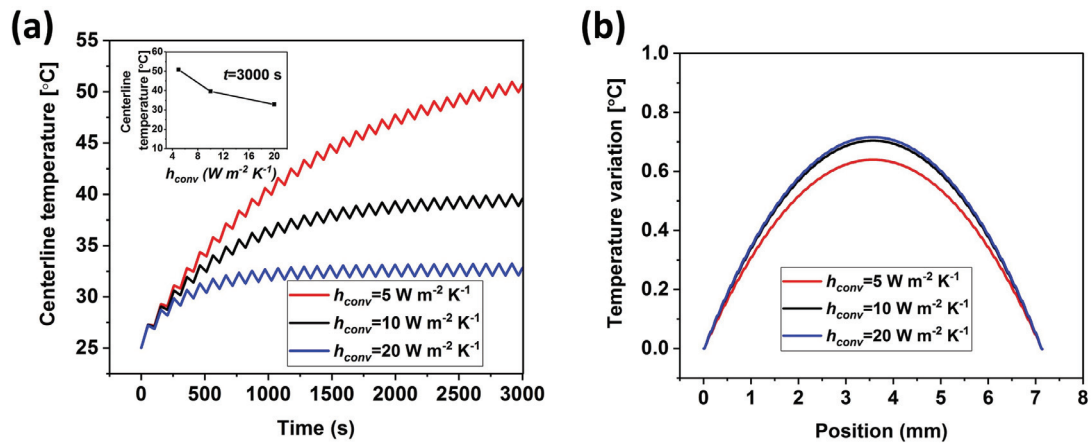
Fig. 4.22. (a) Predicted device centerline temperature $T(L_{dev}/2, t)$ as a function of time t and (b) spatial variation of temperature inside the device at the end of 3000s of cycling ($T(x,$ 3000 s) - $T(0,$3000 s)) at an operating current density I_0=50A m^{-2}, plotted for three different values of convection heat transfer coefficient, h=5, 10 and 20 W m^{-2} K^{-1}. The inset of (a) shows the variation of the device centerline temperature at the end of 3000 s, ($T(L_{dev}/2, 3000s)$) as a function of the convection heat transfer coefficient h.

behavior. The results shown in Fig. 4.24 compare the effect of including rest periods in the charge/discharge cycle at operating current density I_0=50 A m^{-2} and I_0=100 A m^{-2}. In the case of continuous charge/discharge operation at an operating current density I_0=50 Am^{-2}, the average device centerline temperature experiences an initial rise followed by saturation at 39 °C. In the absence of a rest period, the temperature oscillations exhibit a symmetric shape.

The introduction of a rest period before and after every discharge step leads to two effects: (a) reduction in the steady state temperature value and (b)asymmetry in shape of the temperature ripple. The first observation can be attributed to the extra time during which the device is idle and heat generation rate is zero. The second observation, i.e. a loss in symmetry at steady state needs to be investigated. The temperature drop occurring during the discharge phase is because the negative reversible heat exceeds the positive Joule heating, leading to a negative net heat generation rate. Because the device loses heat to the ambient during the rest periods before and after the discharge phase, the temperature drop in the profile is continuous over the three consecutive phases. However, the same is not true for I_0=100 Am^{-2}, the results of which are displayed in Fig. 4.24(b). A sudden kink can be observed in the profiles with pause durations of 20 s and 50 s. In this case, because of the high cycling current, the Joule heating rate exceeds the reversible heat in the discharge phase, leading to a positive net heat generation rate. In addition to the kink, the average temperature rises at a much faster rate than the profiles shown in Fig. 4.24(a).

4.3.7 Influence of Operating Voltage Window

Fig. 4.25 shows the device centerline temperature as a function of time t for continuous cycling at a current density of 50 A m^{-2} in case of different operating potential window 0-2.7 V and 1.35-2.7 V. The average temperature profile is similar in both cases. However, the oscillation amplitude is higher for cycling at 0-2.7 V compared to cycling at 1.35-2.7 V due to larger reversible heat generation rate. This
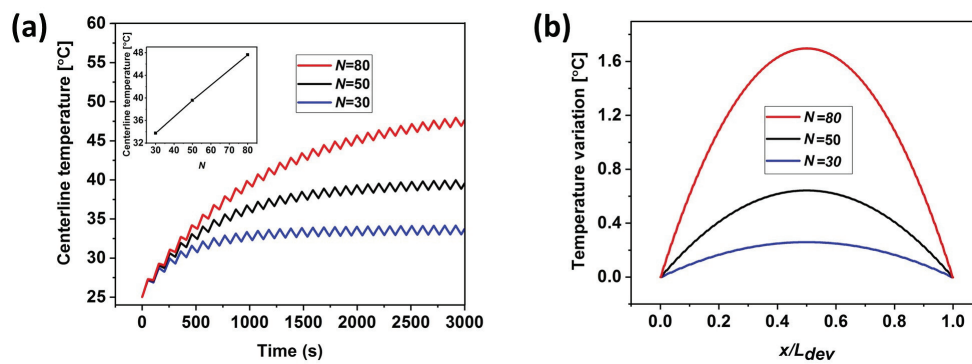
Fig. 4.23. (a) Predicted device centerline temperature $T(L_{dev}/2, t)$ as a function of time t and (b) spatial temperature variation inside the device at 3000 s ($T(x, 3000 \text{ s}) - T(0, 3000 \text{ s})$) as a function of dimensionless length x/L_{dev}, plotted for different number of sandwich units N. The inset of (a) shows the variation of the device centerline temperature at the end of 3000 s, as a function of N. The convection heat transfer coefficient h on the outer surface of the device is assumed to be 20 W m^{-2} K^{-1}.

observation is in agreement with the experimental results reported by Schiffer et al. [101] who found the temperature oscillation amplitude to vary linearly with the voltage window size.

4.3.8   Influence of Electrode Volumetric Capacitance

In the previous sections, we investigated the influence of various operating conditions and geometric characteristics of the device while assuming the electrode/electrolyte properties in each sandwich unit to remain constant. However, beginning from this section, we consider the effect of variation of characteristics of each individual building block of the device. The volumetric capacitance parameter aC of the electrode material is product of the specific surface area per unit volume a (m^2 m^{-3}) and the area-normalized specific surface area C (F m^{-2}). In past studies, it has been found that this parameter is dependent on both the type of electrode material and the type of ions present in the electrolyte. In general, activated carbon electrodes exhibit large values of volumetric capacitance, around 80 F cm^{-3} in aqueous electrolytes [144] and around 50 F cm^{-3} in organic electrolytes [145].

The influence of the volumetric capacitance aC on the electrochemical and thermal behavior of the device at an operating current density of I_0=50 A m^{-2} is displayed in Fig. 4.26 and Table 4.6. Three values of aC are selected for demonstration: 30, 42 and 70 F cm^{-3}. Other parameters are maintained at their base values. Fig. 13a shows that the cycle duration is longer for a larger aC value which indicates a higher area-normalized capacitance value C_A for the device. Table 4.6 shows that C_A increases proportionately with aC, while the device ESR remains the same.

Furthermore, Table 4.6 demonstrates that all components of the net heat generation rate remain invariant with change in aC, except the reversible heat generation rate $\hat{Q}_{rev}$. The time variance of the $\hat{Q}_{rev}$ establishes that it is invariant of aC which is expected from Eq. 4.49. The kink observed at the beginning of discharge can be attributed to the non-equillibrium current density values I_2 during transition as
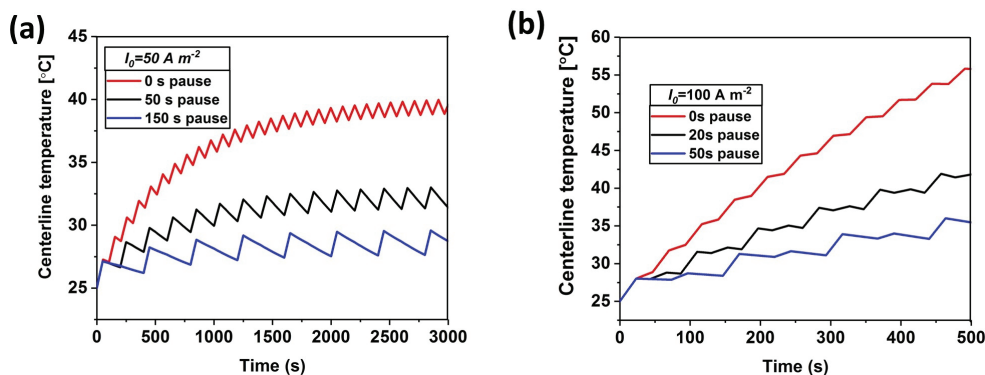
Fig. 4.24. Influence of imposed rest time duration on the temperature evolution characteristics. Predicted device centerline temperature $T(L_{dev}/2, t)$ as a function of time t for (a) cycling current density I_0=50 A m^{-2} and rest periods of duration 0 s, 50 s and 150 s applied before every charge and discharge step and (b) cycling current density I_0=100 A m^{-2} and rest periods of duration 0 s, 20 s and 50 s applied before every charge and discharge step. In all cases, the charge and discharge time durations are adjusted in order to cycle the device in a voltage range of 0 and 2.7 V. The convection heat transfer coefficient h on the outer surface of the device is assumed to be 20 W m^{-2} K^{-1}.

shown in Fig. 4.15f. Because the cycle duration increases as a function of aC, both the temperature oscillation amplitude and the oscillation period is larger for higher aC values as shown in Fig. 4.26c. Nevertheless, the cycle-averaged centerline temperature follows a similar profile for all three cases.

4.3.9   Influence of Bulk Diffusion Coefficient

The ionic conductivity of the electrolyte influences both the electrochemical and thermal behavior of the device significantly, and is governed by the diffusion coefficient and the concentration of the electrolyte. In general, the ionic conductivity is higher for aqueous electrolytes compared to organic electrolytes. The influence of the bulk diffusion coefficient D_∞ on the electrochemical and thermal behavior of the device at an operating current density of I_0=50 A m^{-2} is displayed in Fig. 4.27 and Table 4.7. Three values of D_∞ are selected for demonstration: 10^{-11}, 5×10^{-11} and 10^{-10}

m^2 s^{-1}. As shown in Table 4.7, the area-normalized capacitance improves fairly with change in D_∞ from 10^{-11} to 5×10^{-11} m^2 s^{-1}, but varies hardly upon further rise in D_∞. The GCD curves shown in Fig. 4.27a point to a similar result. In contrast, the device ESR decreases significantly upon increase in D_∞ which leads to a low value of irreversible heat generation rate in the electrolyte. Table 4.7 shows that the spatially and temporally averaged irreversible heat generation rate in electrolyte $\hat{Q}_{irr,ely}$ decreases significantly upon improvement in D_∞ from a value of 10^{-11} to 5×10^{-11} m^2 s^{-1}, while the rest of the terms change marginally. The time dependent temperature profiles plotted in Fig. 4.27c display a much lower temperature rise for electrolyte with high diffusion coefficient. However, the change is quite insignificant for change in value of diffusion coefficient from 5×10^{-11} to 10^{-10} m^2 s^{-1}

4.3.10 Influence of Electrode Thickness

The influence of the electrode thickness on the electrochemical and thermal characteristics of the device is explained in Fig. 4.28 and Table 4.8. Three values of L_e are chosen for comparison: 40, 50 and 60 μm. Table 4.8 demonstrates that both area-normalized capacitance C_A and internal resistance vary significantly with change in L_e. A thick electrode provides larger surface area for double-layer formation and hence C_A improves from a value of 832 to 1241 F m^{-2} upon raising the thickness from 40 to 60 μm. On the other hand, a thick electrode also presents a more tortuous path for the ions to flow through, which leads to high ESR value. However, despite a high ESR value, the thicker electrode exhibits almost same value of $\hat{Q}_{tot}$ because the length of the electrode is normalized for its computation. The device centerline temperature profiles shown for the three cases in Fig. 4.28c demonstrates that the average temperature rise is larger for a device with thick electrodes. Such observation can be exaplained by the fact that although the average heat generation rate $\hat{Q}_{tot}$ is same in all three cases, the total thickness of the device (sum of N number of sandwich units) is larger in case of thick electrodes which causes a large spatially
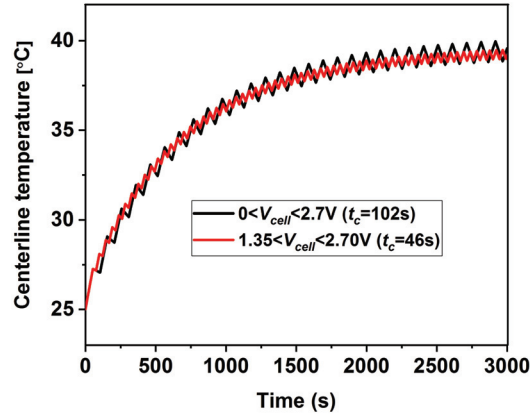
Fig. 4.25. Predicted device centerline temperature $T(L_{dev}/2, t)$ as a function of time t for cycling at operating current density $I_0{=}50$ A m^{-2} over different operating voltage windows. The convection heat transfer coefficient h on the outer surface of the device is assumed to be 20 W m^{-2} K^{-1}.

integrated total heat generation rate $\overline{\dot{Q}}_{tot}(t)$. Because the outer surface area available for convection heat transfer to the ambient remains invariant, the temperature rises at the center of the device is more pronounced in case of thick electrodes.

Table 4.6.

Influence of the electrode volumetric capacitance parameter aC on the electrochemical performance and average heat generation rate values $\hat{\dot{Q}}_i$ at an operating current density of 50 A m^{-2}.

aC (F cm^{-3})	Cycle duration (s)	C_A (F m^{-2})	ESR (mΩ.m^2)	$\hat{\dot{Q}}_{irr,elc}$ (W m^{-3})	$\hat{\dot{Q}}_{irr,ely}$ (W m^{-3})	$\hat{\dot{Q}}_{irr,tot}$ (W m^{-3})	$\hat{\dot{Q}}_{rev}$ (W m^{-3})	$\hat{\dot{Q}}_{tot}$ (W m^{-3})
30	72.5	742	2.54	9525	38694	48219	48313	47926
42	102	1037	2.52	9537	38721	48258	47277	48050
70	169.5	1730	2.54	9515	39245	48760	47736	48594
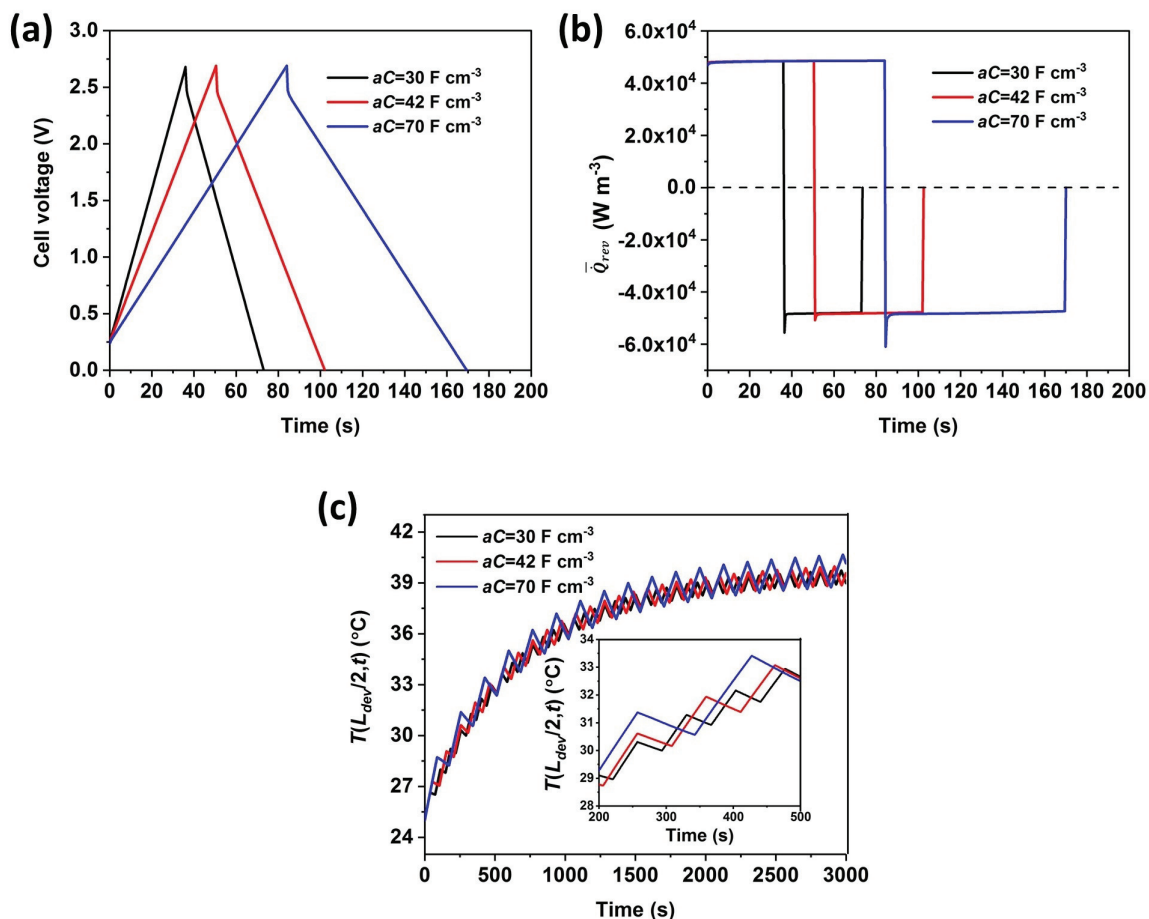
Fig. 4.26. Influence of the electrode volumetric capacitance parameter aC on the electrochemical and thermal characteristics of the device. (a) Cell voltage $V_{cell}(t)$ plotted as a function of time, (b) spatially averaged time-dependent reversible heat generation rate $\bar{\dot{Q}}_{rev}$ plotted as a function of time for a single charge/discharge corresponding to an operating current density of 50 A m^{-2} and aC values of 30, 42 and 70 F cm^{-3}. Plot (c) shows the predicted device centerline temperature $T(L_{dev}/2, t)$ as a function of time upon continuous galvanostatic cycling over a duration of 3000 s. The inset of plot (c) shows a magnified view of the temperature profiles.

Table 4.7.

Influence of bulk diffusion coefficient D_∞ on the electrochemical performance and average heat generation rate values $\hat{\dot{Q}}_i$ at an operating current density of 50 A m^{-2}.

D_∞ (m^2 s^{-1})	Cycle duration (s)	C_A (F m^{-2})	ESR (mΩ.m^2)	$\hat{\dot{Q}}_{irr,elc}$ (W m^{-3})	$\hat{\dot{Q}}_{irr,ely}$ (W m^{-3})	$\hat{\dot{Q}}_{irr,tot}$ (W m^{-3})	$\hat{\dot{Q}}_{rev}$ (W m^{-3})	$\hat{\dot{Q}}_{tot}$ (W m^{-3})
10^{-11}	101.5	1039	2.54	9487	38948	48435	48330	48540
5×10^{-11}	108	1048	1.08	9402	7799	17200	48277	17060
10^{-10}	109	1050	0.81	9384	3891	13275	48291	13137
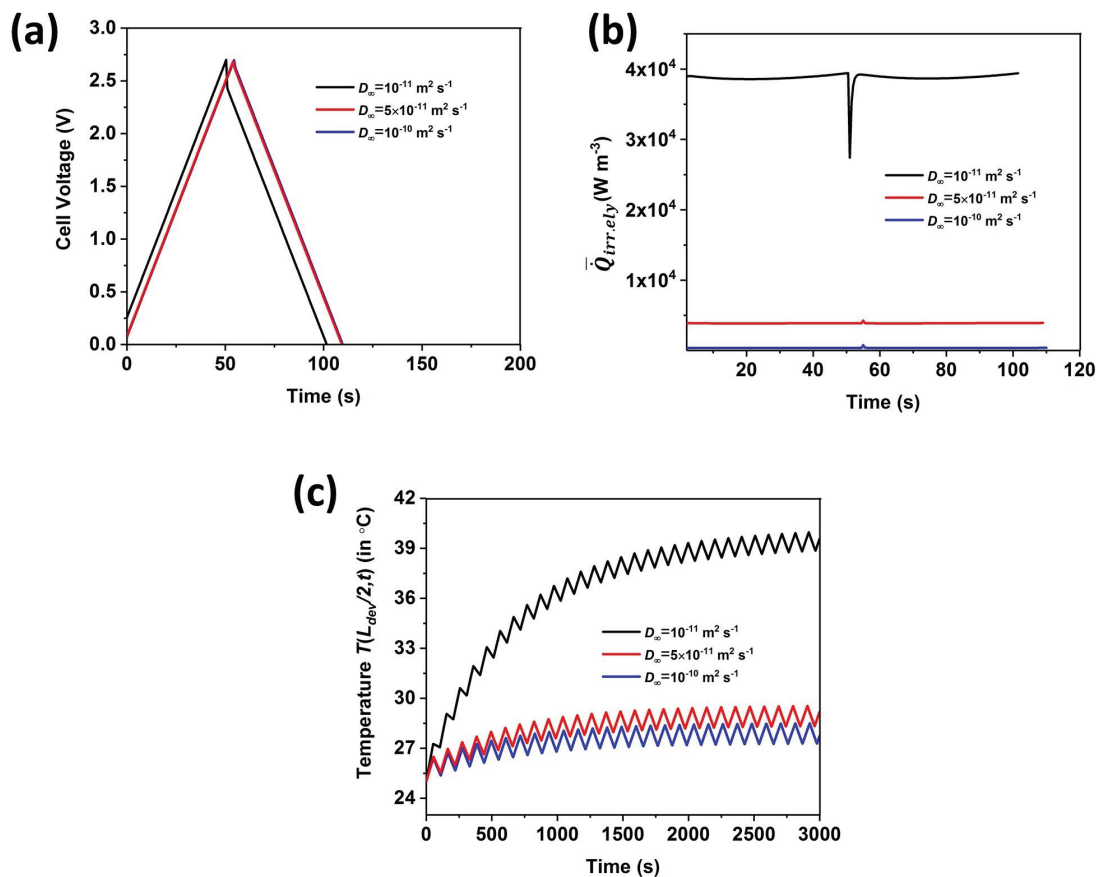
Fig. 4.27. Influence of electrolyte bulk diffusion coefficient D_∞ on the electrochemical and thermal characteristics of the device. (a) Cell voltage $V_{cell}(t)$ plotted as a function of time, (b) spatially averaged time-dependent irreversible heat generation rate in electrolyte $\bar{\dot{Q}}_{irr,ely}$ plotted as a function of time for a single charge/discharge corresponding to an operating current density of 50 A m^{-2} and D_∞ values of 10^{-11}, 5×10^{-11} and 10^{-10} m^2 s^{-1}. Plot (c) shows the predicted device centerline temperature $T(L_{dev}/2, t)$ as a function of time upon continuous galvanostatic cycling over a duration of 3000 s.

Table 4.8.

Influence of electrode thickness L_e on the electrochemical performance and average heat generation rate values $\hat{\dot{Q}}_i$ at an operating current density of 50 A m^{-2}.

L_e (μm)	Cycle duration (s)	C_A (F m^{-2})	ESR (mΩ.m^2)	$\hat{\dot{Q}}_{irr,elc}$ (W m^{-3})	$\hat{\dot{Q}}_{irr,ely}$ (W m^{-3})	$\hat{\dot{Q}}_{irr,tot}$ (W m^{-3})	$\hat{\dot{Q}}_{rev}$ (W m^{-3})	$\hat{\dot{Q}}_{tot}$ (W m^{-3})
40	83	832	2.05	9485	38833	48318	60388	48794
50	102	1039	2.55	9519	38766	48285	48400	48386
60	120	1241	2.88	9577	38694	48271	39650	48176
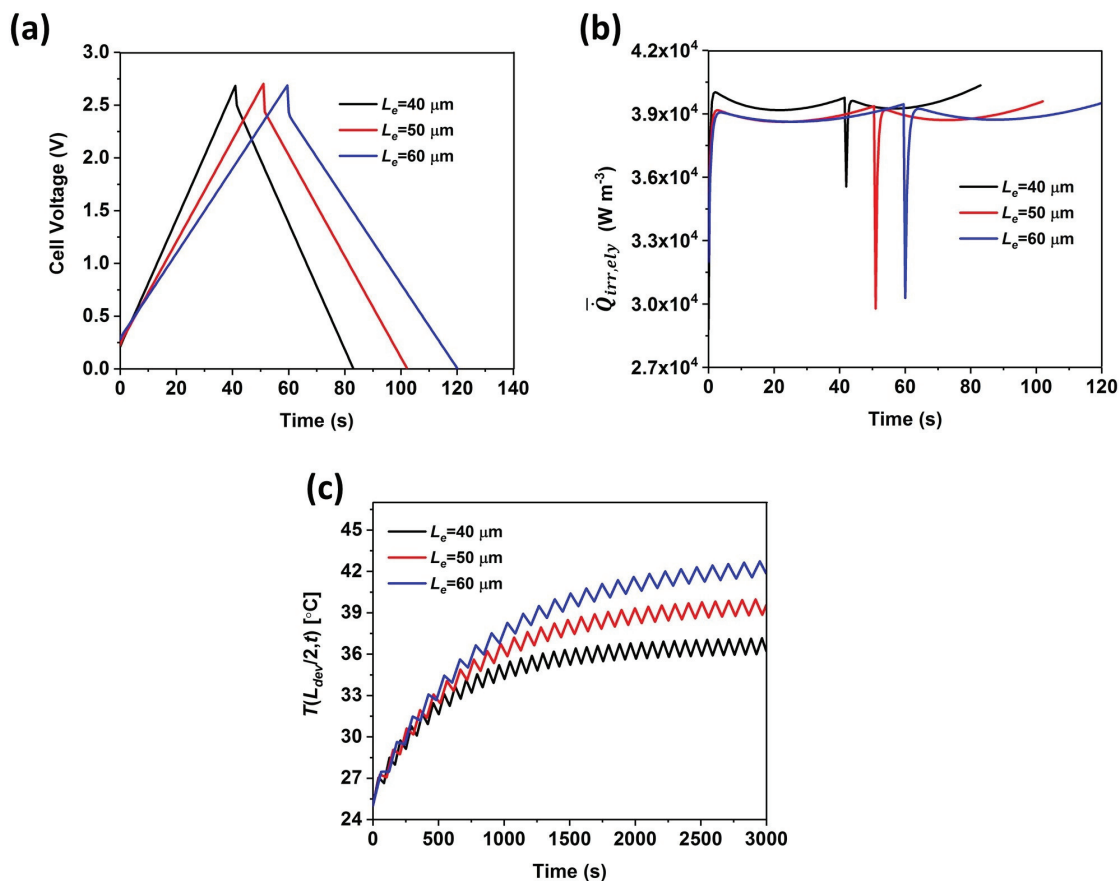
Fig. 4.28. Influence of electrode thickness L_e on the electrochemical and thermal characteristics of the device. (a) Cell voltage $V_{cell}(t)$ plotted as a function of time, (b) spatially averaged time-dependent irreversible heat generation rate in electrolyte $\bar{\dot{Q}}_{irr,ely}$ plotted as a function of time for a single charge/discharge corresponding to an operating current density of 50 A m^{-2} and L_e values of 40, 50 and 60 μm. Plot (c) shows the predicted device centerline temperature $T(L_{dev}/2, t)$ as a function of time upon continuous galvanostatic cycling over a duration of 3000 s.

Conclusions

Here, we present a new continuum model based on porous electrode theory for simulating coupled electrochemical and thermal transport during constant-current charging and discharging of EDLCs. Expressions for irreversible and reversible heat generation rates have been rigorously derived. Non-dimensionalization of the thermal and electrochemical model equations simplifies the problem from eleven independent parameters to seven dimensionless similarity parameters. The temperature evolution is computed for a commercial EDLC consisting of multiple units of an elementary sandwich assembly. The results compare favorably with past measurements [101, 102] both in qualitative and quantitative senses. According to the authors' knowledge, the present study is the first to relate the heat generation rate to the average physical properties of electrode, electrolyte and separator in EDLCs. Using the model, valuable insights have been obtained regarding the dependence of the thermal behavior of EDLCs on the various system and operating parameters.

Table 4.9.
Parameters used in the simulations.

Quantity	Value	Units	Ref.
Carbon electrode thickness L_e	50	μm	[133]
Separator thickness L_s	25	μm	[133]
Volumetric capacitance aC	42	F cm^{-3}	[133]
Initial bulk salt concentration c_∞	0.93	M	[133]
Void volume of carbon electrodes $_e$	0.67	-	[146]
Void volume of separator $_s$	0.5	-	[146]
Bulk ionic conductivity κ_∞ at c$_\infty$	0.67	mS cm^{-1}	[133]
Solid phase conductivity σ	0.521	mS cm^{-1}	[133]
Base temperature T_0	298	K	-
Upper voltage limit V_{up}	2.7	V	[114]
Lower voltage limit V_{low}	0	V	[114]
Aluminum density ρ_{Al}	2700	kg m^{-3}	-
Bulk electrolyte density ρ_{ely}	1205	kg m^{-3}	[114]
Electrode density ρ_{elc}	600	kg m^{-3}	[147]
Separator density ρ_{sep}	492	kg m^{-3}	[147]
Specific heat capacity of aluminum $c_{p,Al}$	900	J kg^{-1}K^{-1}	[147]
Bulk specific heat capacity of electrolyte $c_{p,ely}$	2141	J kg^{-1}K^{-1}	[114]
Specific heat capacity of electrode $c_{p,elc}$	700	J kg^{-1}K^{-1}	[147]
Specific heat capacity of separator $c_{p,sep}$	1978	J kg^{-1}K^{-1}	[147]
Thermal conductivity of aluminum k_{Al}	205	W m^{-1}K^{-1}	[147]
Bulk thermal conductivity of electrolyte k_{ely}	0.164	W m^{-1}K^{-1}	[147]
Thermal conductivity of electrode k_{elc}	0.649	W m^{-1}K^{-1}	[147]
Thermal conductivity of separator k_{sep}	0.334	W m^{-1}K^{-1}	[147]

Table 4.10.
List of Symbols

Symbol	Description	Units
a	interfacial area per unit volume	cm^2 cm^{-3}
A	cross-sectional area of the electrode	cm^2
c_∞	Bulk electrolyte concentration	mol m^{-3}
C_s	capacitance per unit interfacial area	F cm^{-2}
D_∞	Bulk electrolyte diffusion coefficient	m^2 s^{-1}
D_e	Electrolyte diffusion coefficient in electrode domain	m^{2}s^{-1}
D_s	Electrolyte diffusion coefficient in separator domain	m^{2}s^{-1}
E_{sp}	Area-specific energy density	J m^{-2}
e	Electrode porosity	-
s	Separator porosity	-
F	Faraday constant	C
h	Convection heat transfer coefficient at the outer boundary of the device	W m^{-2} K^{-1}
$I_s(t)$	Time-variant applied current density	A m^{-2}
I_0	Magnitude of applied current density	A m^{-2}
I_1	Current density in the electrode phase	A m^{-2}
I_1	Current density in the electrolyte phase	A m^{-2}
k_{Al}	Thermal conductivity of aluminum	W m^{-1} K^{-1}
κ_∞	Bulk electrolyte ionic conductivity	Sm^{-1}
κ_e	Electrolyte ionic conductivity in electrode region	S m^{-1}
κ_s	Electrolyte ionic conductivity in separator region	S m^{-1}
L_e	Electrode length	m
L_s	Separator length	m
L_{dev}	Length of the full device consisting of multiple sandwich units	-
m	Cell body mass	kg
N	Number of sandwich units in a device	-
Nu	Nusselt number $\left(\frac{hD}{k_{air}}\right)$	-
Ra	Rayleigh Number $\left(\frac{c_{p,air}\rho_{air}^2 g\beta(T-T_{amb})D^3}{\lambda_{air}\mu_{air}}\right)$	-

Table 4.11.
List of Symbols (contd.)

Symbol	Description	Units
ϕ_1	Solid phase electrical potential	V
ϕ_2	Electrolyte phase electrical potential	V
P_{sp}	Area-specific power density	W m^{-2}
$\dot{q}_{irr,elc}$	Irreversible heat generation rate in solid phase of electrode	W m^{-3}
$\dot{q}_{irr,ely}$	Irreversible heat generation rate in liquid phase of electrode	W m^{-3}
$\dot{q}_{irr,tot}$	Total heat generation rate in liquid and solid phase of electrode	W m^{-3}
R_u	Universal gas constant	J mol^{-1} K^{-1}
R_s	Specific equivalent series resistance	Ω.m^2
ρ_{elc}	Bulk density of electrode solid phase	kg m^{-3}
ρ_{ely}	Bulk density of electrolyte liquid phase	kg m^{-3}
ρ_{sep}	Bulk density of separator solid phase	kg m^{-3}
σ	Electrode electrical conductivity	Sm^{-1}
t	time	s
t_{ch}	Charging phase duration	s
t_{dc}	Discharge phase duration	s
t_c	Total cycle time duration	s
T_0	Initial temperature of the device	K
T_∞	Ambient temperature	K
V_{min}	Lower voltage limit of operation	V
V_{max}	Upper voltage limit of operation	V
x	Position	μ m
z_i	Valency	-
σ	Electrical conductivity of solid phase in electrode	S m^{-1}
σ_{Al}	Electrical conductivity of aluminum	S m^{-1}
σ_{elc}	Phase-averaged electrical conductivity in the electrode region	S m^{-1}
$(\rho c_p)_{Al}$	Volumetric heat capacity of aluminum	J m^{-3} K^{-1}
$(\rho c_p)_{elc}$	Phase-averaged volumetric heat capacity in electrode region	J m^{-3} K^{-1}
$(\rho c_p)_{sep}$	Phase-averaged volumetric heat capacity in separator region	J m^{-3} K^{-1}
β	Entropy constant	J C^{-1}

4.4   Calorimetric measurements of heat generation in pseudocapacitors

In this study, an isothermal calorimeter is used to measure heat generation rates in fabricated all-solid-state sandwich supercapacitor devices. This work was done in collaboration with Prof. Laurent Pilon's group at University of California, Los Angeles. The isothermal calorimeter used in this study was designed, fabricated, and validated to measure time-dependent heat generation rates in EDLC cells upon galvanostatic cycling in a previous study [125]. The EDLC cells used in the previous study consisted of activated carbon electrodes and separator immersed in an aqueous electrolyte. However, in this study, the calorimeter has been employed to probe the difference in transient heat generation rate characteristics of all-solid-state EDLCs and pseudocapacitors during galvanostatic charge/discharge operation.

Heat generation rate measured for pseudocapacitors operate quite differently from pure EDLCs due to additional heating or cooling caused by exothermic/endothermic reactions. Very few studies have investigated the temperature evolution of pseudo-capacitors. Pascot et al. [126] and Dandeville et al. [127] assembled a non-adiabatic calorimetric setup to measure transient heat generation rates in EDLCs and hybrid pseudocapacitors. The setup consisted of (i) a sandwich cell with activated carbon and MnO_2 pseudocapacitive electrodes immersed in (ii) aqueous electrolyte, (iii) a heat flux sensor, and (iv) two isothermal cold plates. Each heat flux sensor was composed of 16 thermocouples connected in series and enclosed in a polyphenylene sulfide plate. The heat generation rate was computed for the complete device by deconvolving the temperature difference between the test cell and the cold plates as a function of time. In contrast, in the present setup, the instantaneous heat generation rate is acquired accurately for each individual electrode. Thus, this setup is capable of comparing the heat generation rate in two identical electrodes with different polarity and also the influence of electrolyte. Two types of devices have been studied here, (i) a pure EDLC composed of BP/GP electrodes and PVA-H_3PO_4 gel electrolyte, and (ii) a pseudocapacitor that is composed of BP/GP electrodes and re-

dox gel electrolyte, PVA-$K_3Fe(CN)_6$/-$K_4Fe(CN)_6$. The construction of the isothermal calorimeter is described below:

Fig. 4.29 shows (a) an exploded view of the apparatus and (b) an enlarged view of the sensing area. The two heat flux sensor plates were placed firmly in thermal contact in between the cold plate and the electrode surface with the help of a vertical clamp. The copper rod helps in conducting heat generated in the electrode through the heat flux sensr to the cold plate. The 10×10 mm thermoelectric heat flux sensors (gSKIN-XP, greenTEG) had a sensitivity of 0.161 μV/K. Further information about the experimental setup is detailed in Ref. [125].

Fig. 4.30 and 4.31 show the schematic of the all-solid-state supercapacitor device assembly. The buckypaper/graphene petal (BP/GP) electrodes have a footprint area of 0.77 cm^2 and a thickness of 100 μm. Two identical electrodes are sandwiched with a gel electrolyte film leading to an overall thickness of 300 μm for the entire device. The composition of the PVA-H_3PO_4 and the PVA-PFC gel electrolyte films are prepared following the same technique as Section 2.2.1. Sample devices (S1 and S2) are fabricated by sandwiching the PVA-H_3PO_4 gel electrolyte film in between 2 BP/GP electrodes, while sample devices (S3 and S4) are fabricated by sandwiching the PVA-PFC gel electrolyte film in between 2 BP/GP electrodes. Fig. 4.30 includes an enlarged view of the transparent PVA-H_3PO_4 gel electrolyte film used to compose samples S1 and S2, while Fig. 4.31 consists of an enlarged view of the yellowish-green colored gel electrolyte film used to compose samples S3 and S4.

4.4.1 Electrochemical Performance

Fig. 4.32 displays cyclic voltammetry (CV) curves measured on the samples S1 and S2 which are composed of PVA-H_3PO_4 gel electrolyte film and on the samples S3 and S4 which are composed of PVA-PFC gel electrolyte film. For samples S1 and S2, the measurements were performed in the potential window of 0 and 1.0 V at scan rates ranging from 5 to 30 mV s^{-1}, while for samples S3 and S4 the measurements
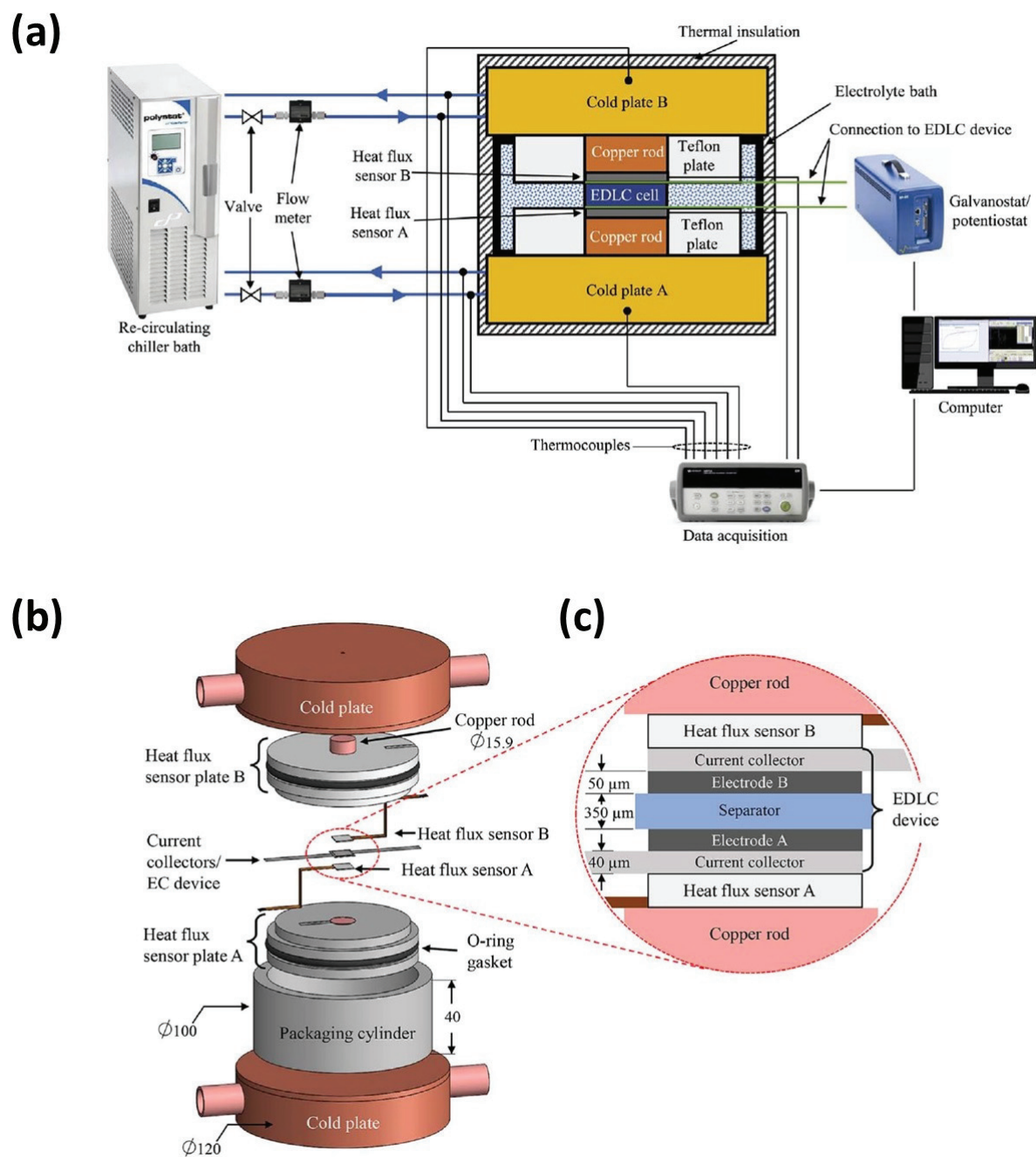
Fig. 4.29. (a) Schematic of the isothermal calorimeter used for measuring heat generation rates. (b)Exploded and enlarged view of the test area, adopted from Ref. [125]
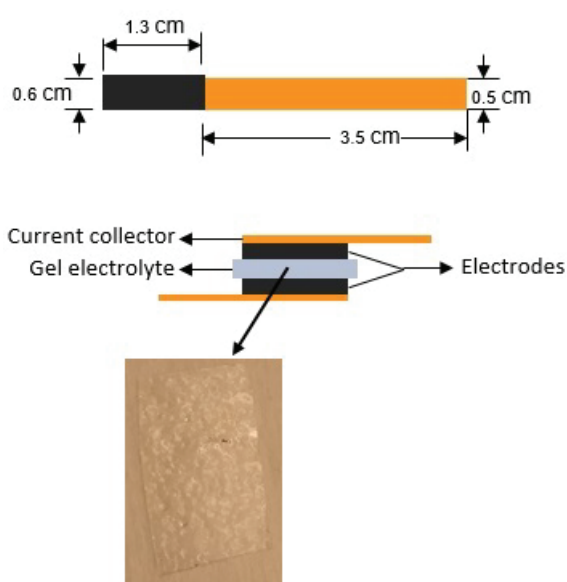
Fig. 4.30. Schematic of the two-electrode sandwich symmetric device with BP/GP electrodes and PVA-H$_3$PO$_4$ gel electrolyte.

were performed in the potential window of 0 and 1.2 V at scan rates ranging from 5 to 30 mV s^{-1} .

The quasi-rectangular nature of the CV curves for samples S1 and S2 indicate only electrical double-layer contribution in energy storage. Furthemore, it is noteworthy that the curves are quite similar for the two samples indicating good repeatability. The CV curves for samples S3 and S4 exhibit a noticeable peak at a potential of 0.4 V which is indicative of the redox reaction corresponding to the ferrocyanide/ferricyanide redox couple.

The cell's integral capacitance C_{int} can be evaluated by integrating the area enclosed by the CV curves for a given scan rate ν as,

$$C_{int}(\nu) = \frac{1}{\psi_{max} - \psi_{min}} \quad \frac{I}{2\nu} d\psi \qquad (4.67)$$

Fig. 4.33 shows the variation of device capacitance derived from the CV curves as a function of operating scan rate for the 4 samples. The device capacitance for samples S3 and S4 is much higher than that for samples S1 and S2 at all scan rates due to the contribution of the redox reactions in charge storage. However, the capacitance decays at a faster rate with increase in scan rate for samples S3 and S4 indicating lower rate capability. Furthermore, the variation is found to be similar for samples S1 and S2 and for samples S3 and S4 indicating good repeatability in electrochemical performance of the devices.

Fig. 4.34 shows the galvanostatic charge/discharge profiles meaured on the samples at operating current values ranging from 1 to 6 mA. The operating voltage window was kept at 0-1.0 V for samples S1 and S2, while it was maintained in the range of 0-1.2 V for samples S3 and S4. The internal resistance of the device is calculated from the potential drop at the beginning of the discharge phase using

$$R_S = \frac{\psi_s(t_c^+) - \psi_s(t_c^-)}{2I} \qquad (4.68)$$

where $\psi_s(t_c^+)$ and $\psi_s(t_c^-)$ are the potentials across the EDLC cell at the end of charging step and immediately after the beginning of the discharge phase respectively. For
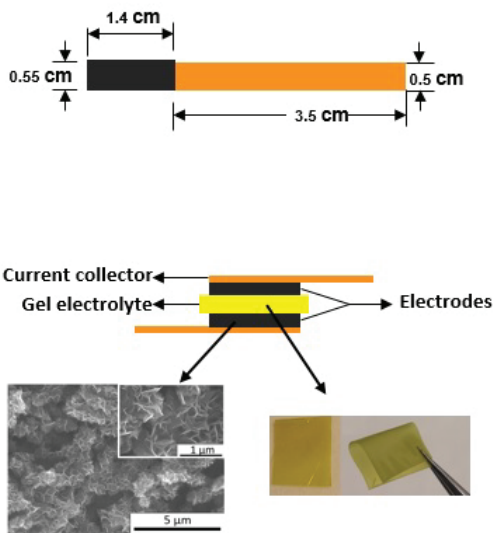
Fig. 4.31. Schematic of the two-electrode sandwich symmetric device with BP/GP electrodes and PVA-PFC gel electrolyte.

the devices composed of PVA-H_3PO_4 gel electrolyte (S1 and S2), the cell voltage rises linearly with time during charge and declines linearly during discharge at all operating current densities. The internal resistance is calculated to be 15 Ω and 8 Ω for the samples S1 and S2. On the other hand, for the samples S3 and S4, the charge/discharge profiles deviate from linear behavior. At the beginning of charge phase, the slope is small which is indicative of pseudocapacitive processes. Furthermore, the internal resistance is much higher, 65 Ω and 70 Ω for the samples S3 and S4 respectively. The higher internal resistance compared to the PVA-H_3PO_4 electrolyte devices is indicative of the lower ionic conductivity of the PVA-PFC gel electrolyte.

4.4.2 Time-Dependent Heat Generation Rate at Individual Electrodes

The transient heat generation rate measured at individual electrodes of the devices during galvanostatic cycling at a constant current of 3 mA is shown in Fig. 4.35. Results for the PVA-H_3PO_4 electrolyte devices, S1 and S2 are shown in (a) and (b),
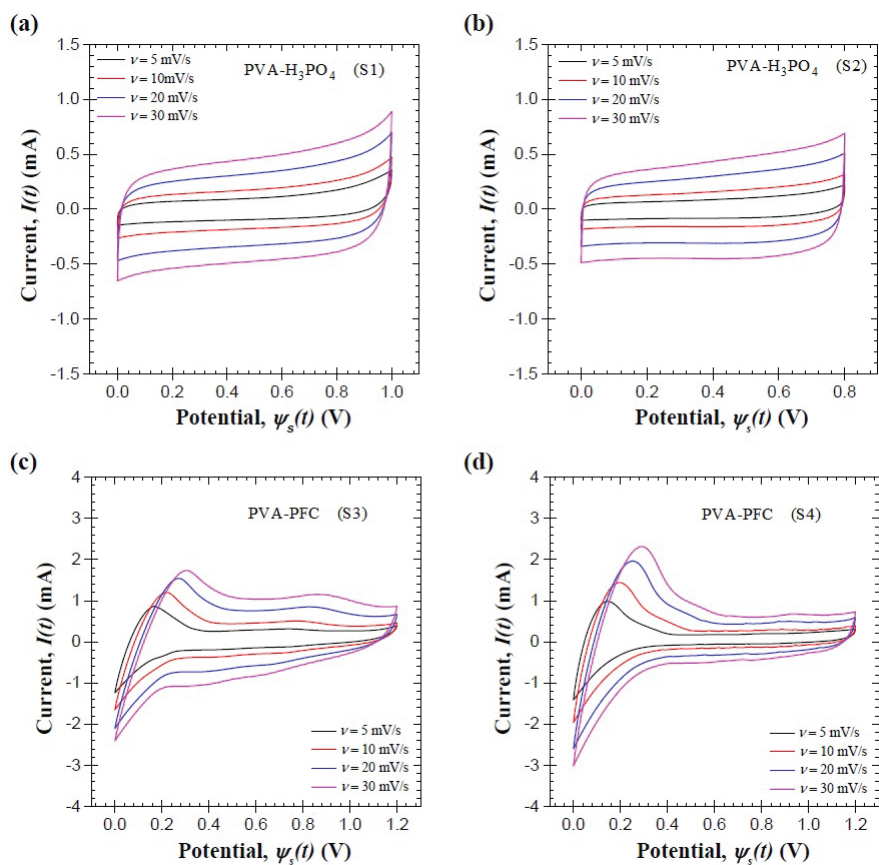
Fig. 4.32. Cyclic voltammetry curves for the two PVA/H3PO4 gel electrolyte devices (S1 and S2) and the two PVA/PFC gel electrolyte devices (S3 and S4) for scan rates ranging from 5 to 50 mV s^{-1}.
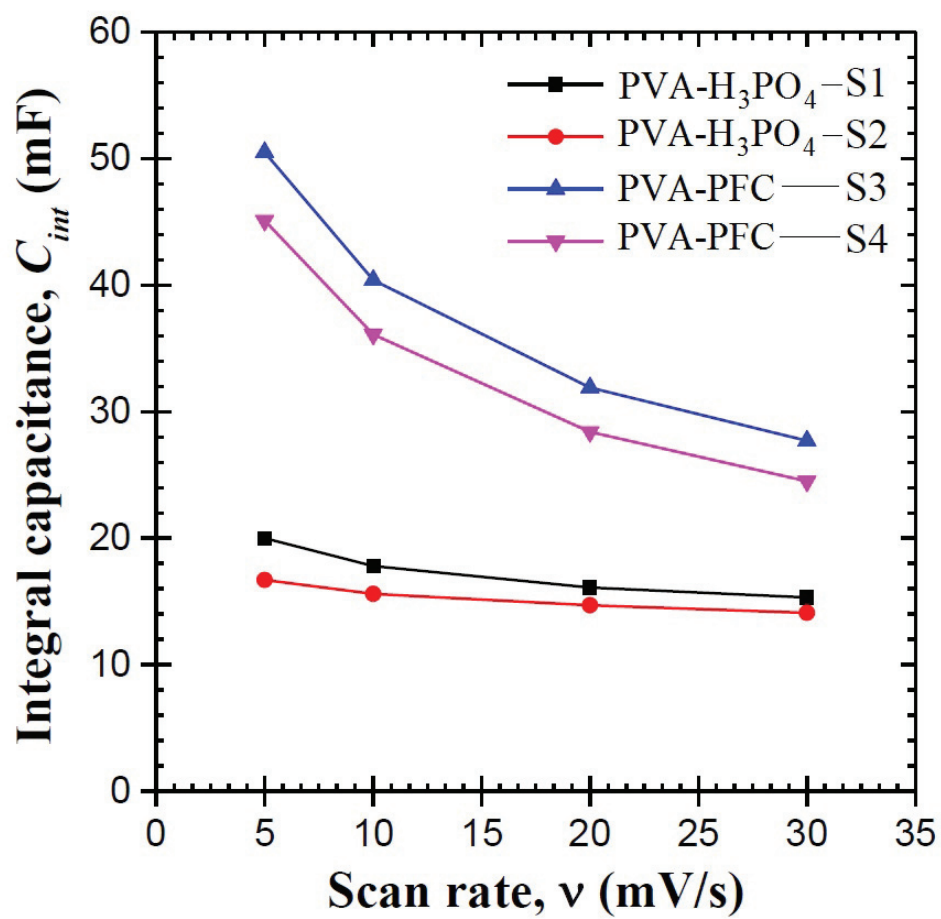
Fig. 4.33. Variation of integral capacitance with scan rate for the PVA-H$_3$PO$_4$ gel electrolyte and the PVA-PFC gel electrolyte devices.
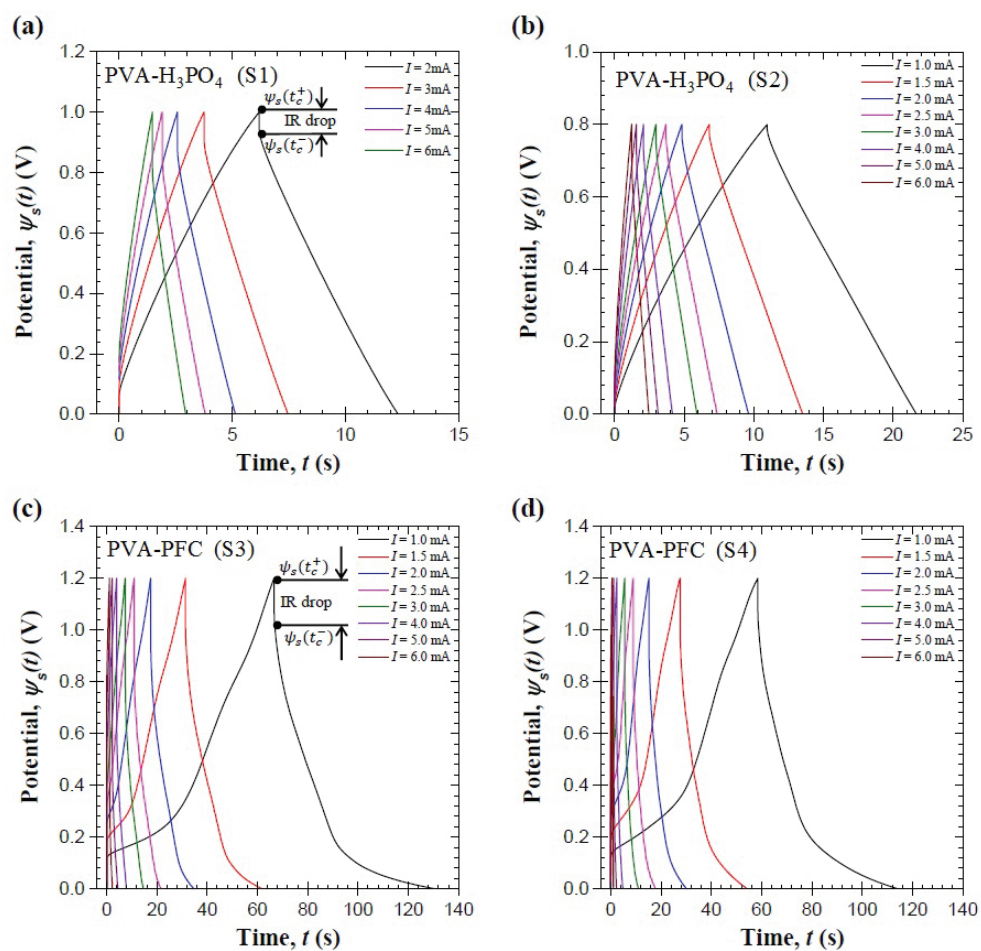
Fig. 4.34. Galvanostatic charge discharge curves for the two PVA/H3PO4 gel electrolyte devices (S1 and S2) and the two PVA/PFC gel electrolyte devices (S3 and S4) for constant current values ranging from 2 to 6 mA.

while results for the PVA-PFC devices, S3 and S4 are shown in (c) and (d). The heat generation rate oscillates with time in all cases. Fig. 4.35a demonstrates that the heat generation rate in the charge phase is greater than that in the discharge phase at both the electrodes. Such observation can be attributed to positive reversible heat in the charge phase and negative reversible heat in the discharge phase at both the electrodes. The instantaneous value of heat generation rate at the negative electrode is slighltly lower than that in the positive electrode which indicates smaller reversible heat generation corresponding to ion adsorption at the negative electrode.

The heat generation rate at both the positive and negative electrodes of the PVA-PFC sample shown in (c) exhibits a similar oscillatory behavior. The heat generation rate in the charge phase is higher than that in the discharge phase. However, the oscillation amplitude is higher than sample S1. The peak value of the total heat generation rate during the charge phase is arounf 0.9 mW which is much higher than that for the PVA-H_3PO_4 sample (S1) shown in (a). Furthermore, the cycle-averaged value of heat generation rate is much higher compared to sample S1, which can be attributed to its higher internal resistance caused by the low ionic conductivity of the PVA-PFC gel electrolyte.

Fig. 4.36 displays the cycle averaged heat generation rates as a function of the operating current for all the samples. Fig. 4.36a shows the sum of the cycle-averaged heat generation rate at the two electrodes of the PVA-H_3PO_4 electrolyte devices (Samples S1 and S2), while Fig. 4.36b shows the results for the PVA-PFC gel electrolyte devices (Samples S3 and S4). For both S1 and S2, it can be observed that the cycle-averaged total heat generation rate has almost same value as the Joule heat $I^2 R_S$. This is quite expected because in the cycle-averaged heat generation expression, the reversible heat generation rate terms in the charge and discharge phase nullify each other and only the Joule heat term remains. However, interestingly for the PVA-PFC electrolyte samples, S3 and S4, the cycle averaged heat generation rate exhibits a slight deviation from $I^2 R_S$ especially at high operating currents. Such
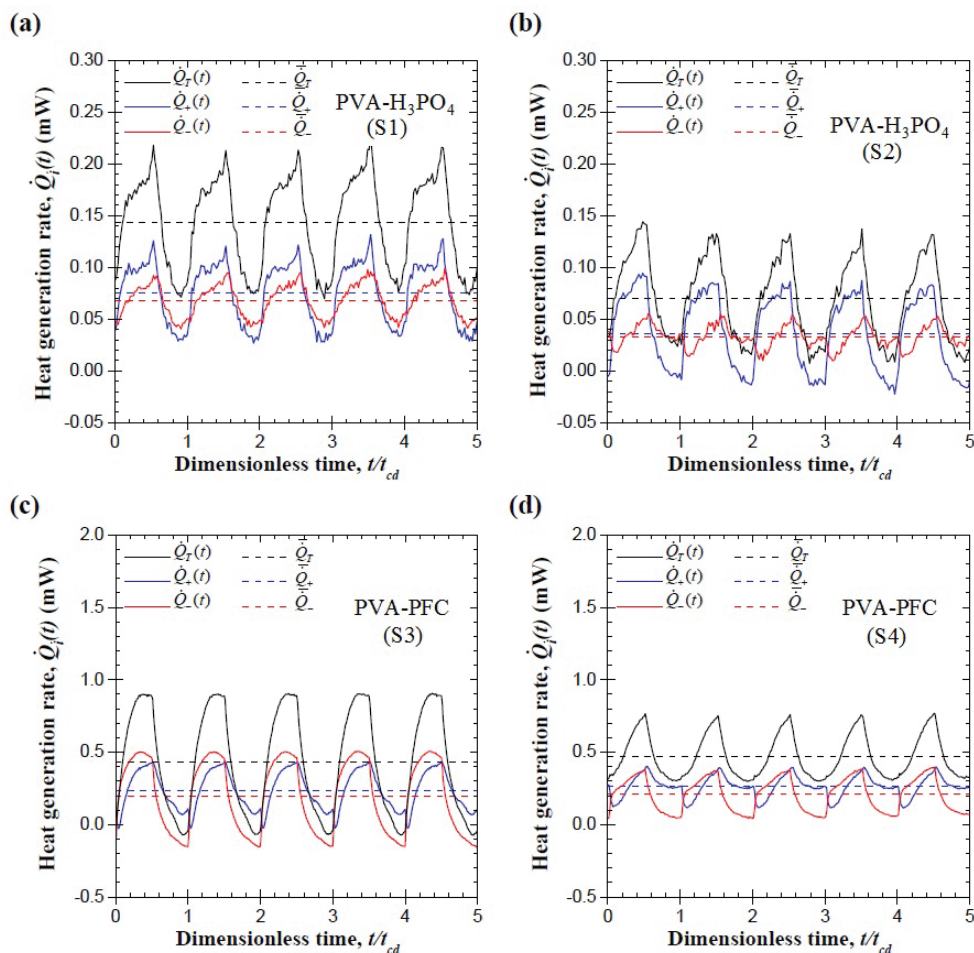
Fig. 4.35. Heat generation rates $\dot{Q}_+$ at the positive electrode (blue), $\dot{Q}_-$ at the negative electrode (red), and $\dot{Q}_T$ in the entire cell (black) as functions of the dimensionless time t/t_{cd} for current $I=3$ mA for all-solid-state supercapacitor devices composed of PVA-H$_3$PO$_4$ gel electrolyte(samples S1 and S2) for five galvanostatic cycles. Time-averaged heat generation rates $\bar{\dot{Q}}_+$, $\bar{\dot{Q}}_-$ and $\bar{\dot{Q}}_T$ under galvanostatic cycling are also displayed in the same plot. Heat generation rates $\dot{Q}_+$ at the positive electrode (blue), $\dot{Q}_-$ at the negative electrode (red), and $\dot{Q}_T$ in the entire cell (black) as functions of the dimensionless time t/t_{cd} for current $I=3$ mA for the all-solid-state supercapacitor devices composed of PVA-PFC gel electrolyte (samples S3 and S4) for five galvanostatic cycles. Time-averaged heat generation rates $\bar{\dot{Q}}_+$, $\bar{\dot{Q}}_-$ and $\bar{\dot{Q}}_T$ under galvanostatic cycling are also displayed in the same plot.
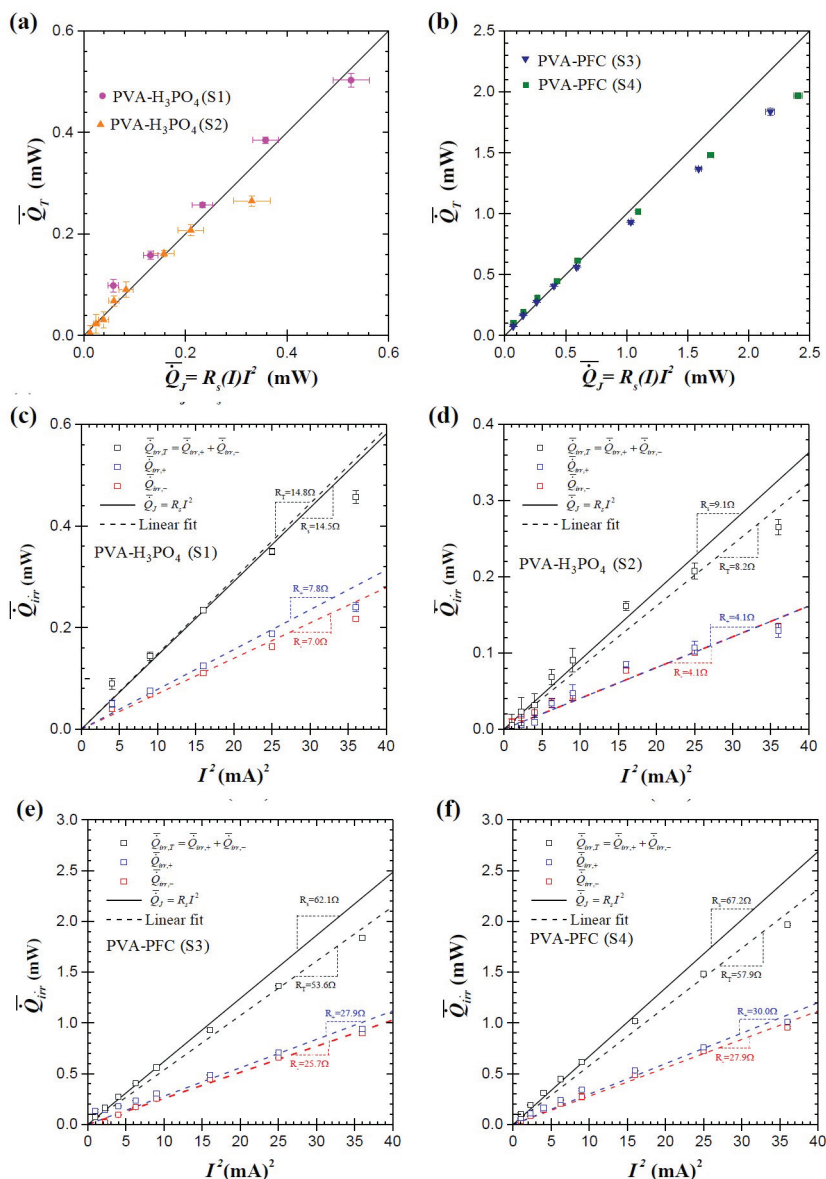
Fig. 4.36. Time-averaged total heat generation rate in the entire cell $\bar{\dot{Q}}_T$ plotted as a function of the time-averaged Joule heating rate for (a) all-solid-state supercapacitor devices composed of PVA-H_3PO_4 gel electrolyte(samples S1 and S2) and (b) all-solid-state supercapacitor devices composed of PVA-PFC gel electrolyte(samples S3 and S4) for five galvanostatic cycles. Time-avaraged heat generation rates $\bar{\dot{Q}}_+$, $\bar{\dot{Q}}_-$ and $\bar{\dot{Q}}_T$ under galvanostatic cycling as functions of I^2 for current I ranging from 1 to 6 mA for all-solid-state supercapacitor devices composed of PVA-H_3PO_4 gel electrolyte(samples S1 and S2) shown in (c) and (d) respectively. Time-avaraged heat generation rates $\bar{\dot{Q}}_+$, $\bar{\dot{Q}}_-$ and $\bar{\dot{Q}}_T$ under galvanostatic cycling as functions of I^2 for current I ranging from 1 to 6 mA for all-solid-state supercapacitor devices composed of PVA-PFC gel electrolyte(samples S3 and S4) shown in (e) and (f) respectively.
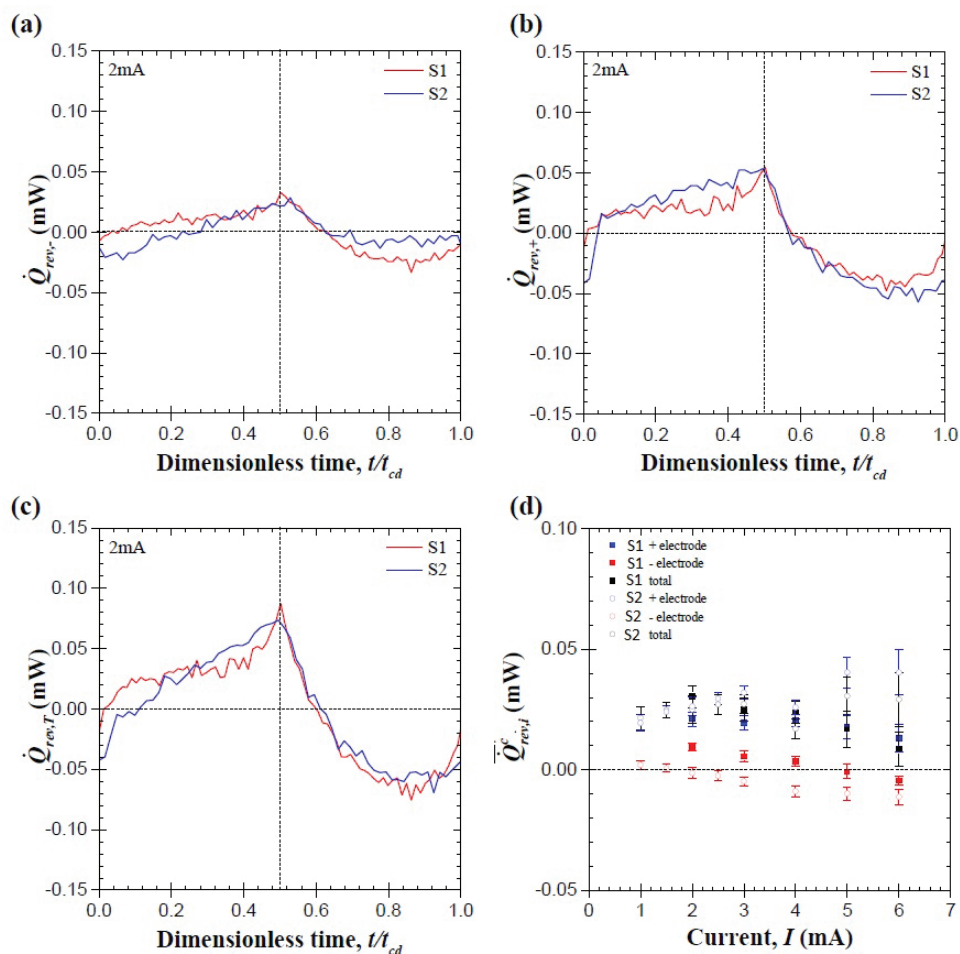
Fig. 4.37. Reversible heat generation rates at the (a) negative electrode $\dot{Q}_{rev,-}$, (b) positive electrode, $\dot{Q}_{rev,+}$ and (c) in the entire cell, $\dot{Q}_{rev,T}$ measured as a function of the dimensionless time t/t_{cd} on all-solid-state supercapacitor devices composed of PVA-H_3PO_4 gel electrolyte at an operating current $I=2$ mA. The red curves represent results for sample S1 while the blue curves represent results for sample S2. Time-averaged reversible heat generation rate measured in the charge phase for the positive electrode, negative electrode and entire cell is shown as a function of the operating current I for samples S1 and S2 in (d)
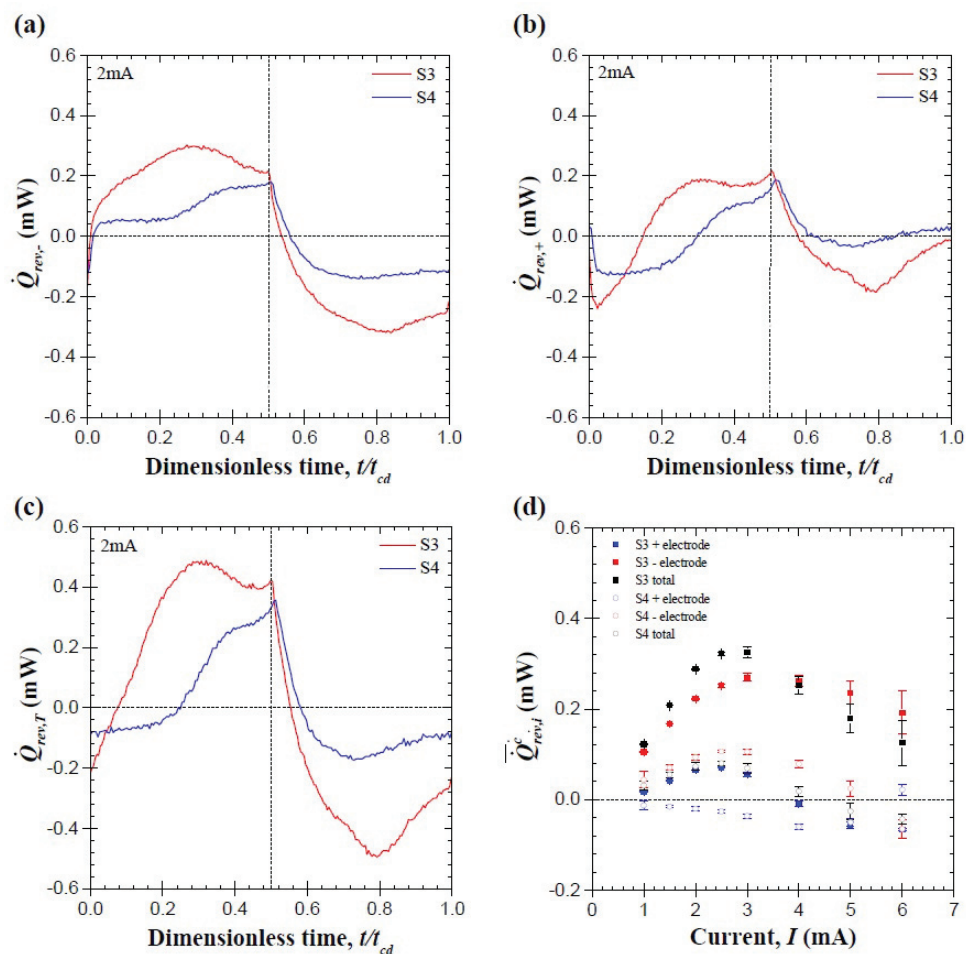
Fig. 4.38. Reversible heat generation rates at the (a) negative electrode $\dot{Q}_{rev,-}$, (b) positive electrode, $\dot{Q}_{rev,+}$ and (c) in the entire cell, $\dot{Q}_{rev,T}$ measured as a function of the dimensionless time t/t_{cd} on all-solid-state supercapacitor devices composed of PVA-PFC gel electrolyte at an operating current I=2 mA. The red curves represent results for sample S3 while the blue curves represent results for sample S4. Time-averaged reversible heat generation rate measured in the charge phase for the positive electrode, negative electrode and entire cell is shown as a function of the operating current I for samples S3 and S4 in (d).

an observation can be attributed to additional contributions to Joule heat from the exothermic/endothermic reactions occuring in the redox electrolyte.

Fig. 4.36c and d show the cycle-averaged heat generation rate at the individual electrodes of the samples S1 and S2 as a function of square of the operating current. A linear relationship is observed for both the electrodes. The slope of the curves produce the internal resistance corresponding to each electrode. The internal resistance values are found to be 7.9 Ω and 7.0 Ω for the positive and negative electrodes respectively in sample S1. Similarly, the internal resistance is 4.1 Ω for each electrode in sample S2.

Fig. 4.36(e) and (f) display the cycle-averaged heat generation rate at the individual electrodes of the samples S3 and S4 as a function of square of the operating current. At high operating currents, the results deviate from a linear behavior. However, the internal resitance inferred from linear fitting is found to be similar for the two electrodes (27.9 Ω and 25.7 Ω for the positive and negative electrodes respectively in sample S3).

4.4.3 Reversible Heat Generation Rates

Fig. 4.37 shows the reversible heat generation rate during a single charge/discharge cycle for the PVA-H_3PO_4 gel electrolyte devices (S1 and S2). Results are shown for the positive electrode, the negative electrode and the entire device in (a), (b) and (c) respectively. The average reversible heat generation rate during the charge phase is plotted as a function of the operating current in (d). The reversible heat generation rate is positive in the charge phase and negative during the discharge phase at both the electrodes. However, the transition from positive to negative value at the beginning of the discharge phase occurs smoothly instead of a rapid change. Fig. 4.38 reveals the time-dependent reversible heat generation rate in a single charge/discharge cycle for the PVA-PFC gel electrolyte device. Similar to PVA-H_3PO_4 gel electrolyte device, the reversible heat generation rate is positive in the charge phase and negative during

the discharge phase. However, its peak value during the charge phase exceeds that measured for the PVA-H_3PO_4 gel electrolyte devices by almost 4 times, which is indicative of the higher adsorption heat corresponding to the ferrocyanide/ferricyanide ions during charge/discharge.

5. ELECTROREFLECTANCE IMAGING OF GOLD ELECTRODE MICRO-SUPERCAPACITORS: EXPERIMENT METHODOLOGY AND AGING CHARACTERIZATION

Some of the material in this chapter has been published in *RSC Analyst* [24, 25]

5.1 Introduction

The ability to integrate power supplies 'on-chip' has enabled a broad range of microelectronic applications. Integrated power permits autonomous or semi-autonomous microdevices to operate with minimal or no direct interface to an external power supply. Implantable electrophysiology [148, 149] and remote sensing and analysis [150] are compelling demonstrations of autonomous microelectronics. Towards this goal many electrochemical capacitor designs, consisting primarily of integrated electrode-electrolyte interfaces, have been implemented as versatile power components that can be integrated on rigid or flexible substrates. In particular, 'microsupercapacitors' show great potential in complementing or even replacing microbatteries and conventional (electrolytic) capacitors on-chip. [151, 152] Measuring behavior and performance of integrated electrochemical structures has traditionally relied on electrical characterization methods such as cyclic voltammetry, constant charge/discharge, and electrochemical impedance spectroscopy. These methods are useful for assessing the electrical performance of the full electrochemical structure as a single unit. However, these methods measure an 'average' of the structure's internal performance, providing little or no information about microscopic details inside the device. This study demonstrates an electroreflectance imaging method to measure spatial variation of charge distribution in planar integrated electrochemical structures during

charge/discharge cycling. The imaging method is demonstrated here with submicron spatial resolution and one millisecond time resolution, though time resolution faster than one microsecond is possible. Because the method is fully optical and camera-based, the sample is not disturbed during measurements, and there is no need to scan a measurement probe across the surface of the sample. Electroreflectance describes the change in a material's optical reflectance in the presence of a changing electric field. Measurements of material electroreflectance at single point locations have been used extensively to characterize semiconductor band structure. [153, 154] In material electroreflectance characterization the sample is typically immersed in a liquid electrolyte with a controllable potential applied between the test electrode and a reference electrode. Electrode potential is modulated, and the resulting change in intensity of laser illumination reflected by the sample is measured by a photodetector. Reflectance measured from the spot location of incident illumination is considered representative of the whole sample if it is homogeneous. For metals, Feinleib [155] was the first to report the observation of significant electroreflectance modulation for gold immersed in salt water. He also reported electroreflectance spectra in other metals such as silver, copper and sodium tungsten bronze (Na_xWO_3). The electroreflectance phenomenon obtained from such a setup was initially attributed partially to the modulation of the optical properties of the metal and partially to that of the electrolyte. Calculations from Prostak et al. [156] concluded that the experimentally observed reflectance change for a gold-KCL system cannot be explained by electric field modulation of the electrolyte's optical constants. On the other hand, considering only electrical modulation of the optical properties of the metal in the calculations leads to a close match with experiment. Several factors can contribute to electromodulation of a metal's optical properties. Anderson et al. [157] considered contributions from modulation of the free electron concentration, core electron polarization, and interband transitions from the inner bands to the Fermi level, in their analysis. The contribution of core electron polarization was found to be independent of incident illumination wavelength while the other contributions were found to vary with wave-

length. Hansen et al. [158] argued that bound electrons remain essentially unaffected during the charging process, and the contribution from interband transitions varies in a similar way to the contribution of the free electrons. Hence they used free electron theory to calculate the change in optical constants. Calculations based on this simple model indicate that the variation in free electron concentration in the first $50\,\text{Å}$ to $100\,\text{Å}$ of the gold electrode caused by the application of an electric field produces the observed change in reflectance. In our study, we consider only free electron contributions to model the time dependent reflectance change in a microsupercapacitor. Gold has long been considered to be a noble and catalytically inactive material. However in the last three decades, the catalytic activity of gold has been heavily scrutinized. The most significant factors influencing the reactivity of gold are the surface structure and electrolyte pH. [159] Although bulk gold is unreactive in alkaline and acidic media [159], gold nanoparticles [160] and nanorods [161] supported on different metal oxides are reactive and have found applications in plasmon-enhanced spectroscopy and optical and optoelectronic devices. New strategies have been proposed to map the catalytic activity of gold in different electrochemical environments, using different imaging techniques. Munteanu et al. [162] studied the electrografting of nitrophenyl (NP) radicals to gold electrode surfaces using a combination of electrochemical actuation and optical detection techniques. Reflectivity microscopy imaging, allowing for spatio-temporal imaging with sub-micrometer lateral resolution was used to map the reacting fluxes of the NP radicals triggered by the electrochemical reduction of the precursor. Abanulo et al. [163] used surface plasmon resonance (SPR) spectroscopy to study the electrochemical response of gold-coated graded index channel waveguide sensors in sulphuric acid solution. Kakkassery et al. [164] studied the absorption spectra of gold nanocrystal assemblies formed from polyelectrolyte modified gold electrodes and used it to infer the dipole moment induced due to the interaction of the polyelectrolyte and the nanocrystals. Electroreflectance imaging exploits the change in reflectance of the metal electrode in an electrochemical system during charge and discharge cycles. The optical reflectance of most metals depends strongly on the

concentration of free electrons near its surface. In an electrochemical capacitor, electron concentrations near the surface of the metal electrode (at the interface with the electrolyte) change significantly while charging and discharging. A camera-coupled microscope using lock-in amplification synchronized to device excitation can measure the resulting change in metal electrode reflectance. The resulting image shows the magnitude and two-dimensional distribution of free charge in the device near the electrode-electrolyte interface. In this paper, part one of a two-part series on electroreflectance imaging of supercapacitors, the experimental method is described in detail with fundamental test results demonstrated for a gold-H_3PO_4 polymer electrolyte microsupercapacitor. A full model of the electroreflectance response based on the device equivalent electrical circuit will be presented. Electroreflectance image measurements are cross validated with this equivalent circuit model. This study considers a supercapacitor with gold electrodes, but in principle the method can be used to characterize active charge characteristics in any integrated electrochemical device where the metal electrode can be seen under an optical microscope and electrode material has sufficient electroreflectance response. Example materials with electroreflectance spectra suitable for imaging using the method described include, but are not limited to, Au, Ag [155,156,158,165] Pt, Ni [166], Hg [167], Pb [168], and Sn [169] among metals and Ge [170], Si, GaAs, GaSb, InP, ZnTe, CdTe, HgSe [169], MoS2, and MoSe2 [171,172] among semiconductors.In part two [173] of the series, electroreflectance imaging is used in a case study to assess ageing phenomenon in supercapacitors under extended cycling.

5.2 Device and Methods

5.2.1 Device Description

Microsupercapacitors have received attention for their ability to combine the high energy density of batteries with the high peak power of conventional capacitors. [152] Microsupercapacitors also exhibit long cycle life and can be integrated into a small
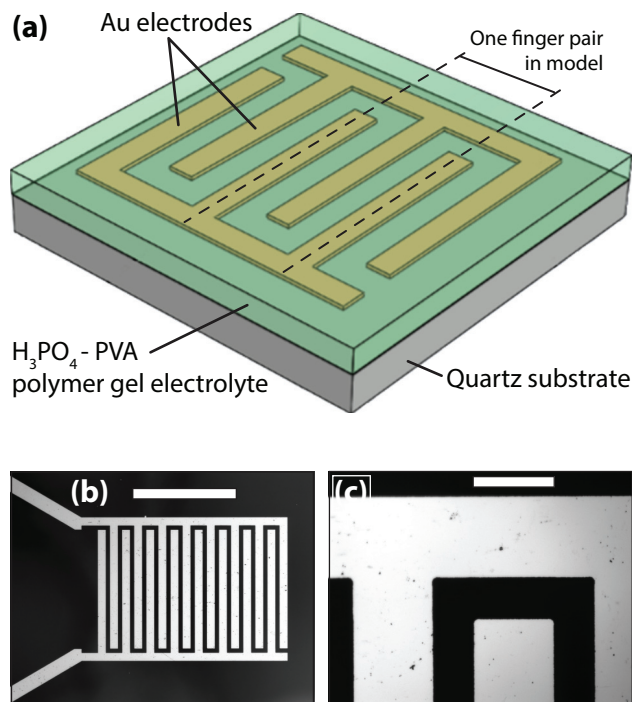
Fig. 5.1. (a) Schematic representation of the microsupercapacitor studied, based on gold electrode-H_3PO_4 polymer gel electrolyte. (b) Optical image of full microsupercapacitor with H_3PO_4 polymer gel electrolyte applied. The electrolyte is highly transparent in the narrowband 530 nm wavelength LED illumination used, allowing the patterned gold electrodes to be visible through the applied electrolyte. The gold electrodes appear light in the image. Dark regions indicate electrolyte on top of quartz substrate. Scale bar is 500 µm. (c) Optical image detail of Au electrode trace and gap between electrodes. Scale bar is 40 µm.

chip footprint. [174] Many designs, materials, and fabrication methods have been proposed for high-performance microsupercapacitors. A broad overview of this research is provided in a survey by Xiong et al. [151]

Electroreflectance imaging was performed on a planar integrated microsupercapacitor consisting of interdigitated gold fingers covered by an H_3PO_4 electrolyte in polymer solution. A schematic of the microsupercapacitor sample is shown in Fig.5.1a. Electrodes were fabricated by electron beam deposition of 200 nm gold, with a titanium buffer layer (50 nm) between the gold and electrically insulating quartz sub-

strate. The polymer gel electrolyte was made from $6\,g$ H_3PO_4 mixed with $60\,mL$ deionized water and $6\,g$ polyvinyl alcohol (PVA) powder. Detailed fabrication information is provided in the supplemental information. Fig.5.1b,c show topside optical microscope images of the full microsupercapacitor layout including anode/cathode leads and magnified detail of the gold electrodes. Total sample capacitance as measured by cyclic voltammetry was $33\,nF$.

5.2.2 Microsupercapacitor Electroreflectance Imaging

Images revealing spatial charge distribution in a metal/polymer electrolyte microsupercapacitor were achieved by measuring the small electroreflectance change on device electrodes during continuous bias cycling. Images were acquired with a high sensitivity charge coupled device camera attached to a reflectance microscope using narrowband visible wavelength illumination. Microsupercapacitor reflectance is proportional to free electron concentration in the metal, which varies with potential applied across the microsupercapacitor anode and cathode. The reflectance change in the microsupercapacitor for charge accumulation under typical bias is on the order of 10^{-4}. This change in light intensity is too small to be measured directly by a camera for a single microsupercapacitor modulation cycle. Consequently a lock-in amplification method was used to extract the small electroreflectance change by averaging over many identical microsupercapacitor excitation cycles. The method was adapted from thermoreflectance temperature imaging microscopy. [175–179] Thermoreflectance extracts the small temperature dependent change in reflectance ($10^{-5}\,K^{-1}$ to $10^{-3}\,K^{-1}$) from background noise by averaging over many device excitation cycles. Lock-in reflectance imaging is equally capable of measuring reflectance change at the electrode-electrolyte interface of a microsupercapacitor cell. In this case, however, the small reflectance change is primarily caused by modulating free electron concentration in the electrode rather than modulating temperature.
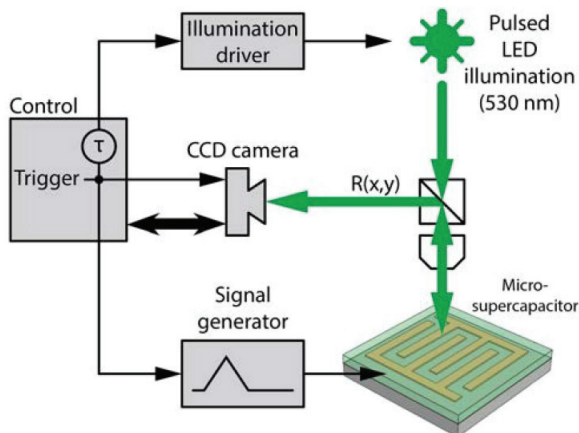
Fig. 5.2. Experiment configuration for electroreflectance imaging using lock-in modulation.

Measurement system configuration

Fig.5.2 shows the experimental configuration used for lock-in electroreflectance imaging of the microsupercapacitor. The device is placed under a reflectance microscope and illuminated by a monochromatic light-emitting diode (LED). An LED centered 530 nm was chosen because gold exhibits optimal modulation amplitude near this wavelength. [176] The microsupercapacitor is electrically excited by a periodic sawtooth voltage signal. The resulting modulation in charge density at the microsupercapacitor electrode-electrolyte interface produces a corresponding modulation in reflectance (electroreflectance) at this interface. A high sensitivity charge coupled device (CCD) camera synchronized to the microsupercapacitor excitation signal measures device reflectance continuously and extracts the small amplitude of electroreflectance change either by frequency domain [180, 181] or time domain [177, 179, 182] analysis. The result is an image map of microsupercapacitor electroreflectance amplitude over the microscope's full field of view. The signal-to-noise ratio improves by averaging over many device excitation cycles. Results in this study were acquired using a time domain signaling scheme described below. Hardware triggering, synchronization, and camera acquisition are controlled by a commercial Microsanj thermore-

flectance imaging system, with excitation waveforms customized for electroreflectance measurements. The microsupercapacitor's excitation signal is provided by an arbitrary waveform generator. Reflectance images were recorded using a scientific grade 512 x 512 pixel Andor Ixon II CCD camera with 14-bit grayscale intensity levels. The microsupercapacitor sample was fixed to a copper heat sink positioned under the microscope objective. All measurements were conducted at room temperature. Electrical contact to microsupercapacitor anode and cathode was achieved by soldering copper wires to gold portions of the electrodes extending outside the polymer gel electrolyte region of the cell. There was no contact between the electrolyte and the copper segments of the leads.

Microsupercapacitor modulation bias for electroreflectance imaging

Fig.5.3a shows the bias circuit used during electroreflectance imaging of the microsupercapacitor. The negative electrode of the microsupercapacitor and the sample substrate are held at ground. The arbitrary waveform generator applies signal $v_M(t)$ to the microsupercapacitor in series with a resistor R_M that is included to provide an independent element for measuring time varying current through the microsupercapacitor. Fig.5.3b illustrates the electrical response of an ideal capacitor when the continuous periodic voltage signal v_M is applied to the circuit during electroreflectance imaging. For the hypothetical case of an ideal microsupercapacitor with no internal parasitic resistance or current leakage and with $R_M = 0$, the voltage across the microsupercapacitor, $v_C(t)$, equals the applied voltage $v_M(t)$. The microsupercapacitor is electrically active during a 30 ms triangular voltage 'pulse.' The microsupercapacitor charges during the positive slope of the pulse ($v_M = 0\,\text{V}$ to $v_{M,max}$) and discharges during the negative slope ($v_M = v_{M,max}$ to $0\,\text{V}$). With $v_{M,max} = 1\,\text{V}$, the waveform produces a charge-discharge cycle equivalent to cyclic voltammetry at a scan rate of $66\,\text{V}\,\text{s}^{-1}$. For an ideal capacitor the triangular voltage pulse would produce a corresponding bipolar step current response as shown with positive current during

the positive voltage slope and negative current during negative voltage slope. The magnitude of excess charge in the electrodes as a function of time (not shown in the figure) follows the same triangular shape as the voltage pulse. Because micro-supercapacitor reflectance is a function of charge density at the electrode-electrolyte interface, reflectance modulation also follows the triangular shape of the applied voltage pulse. The waveforms illustrated in Fig.5.3b assume only ideal characteristics in the microsupercapacitor and no resistance in the bias circuit ($R_M = 0$). For the real experiment, both current through the microsupercapacitor and excess charge are skewed by the presence of parasitic electrical effects including circuit series resistance R_M and internal resistance and current leakage in the microsupercapacitor.
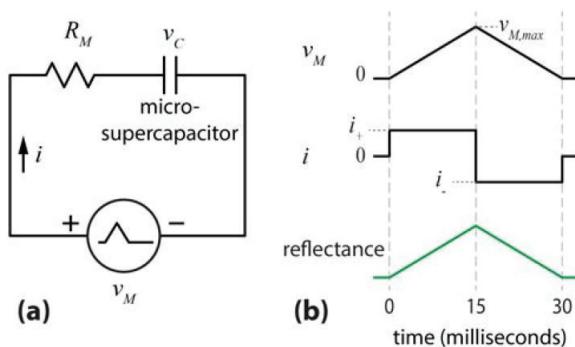
Fig. 5.3. (a) Bias circuit for electroreflectance imaging of the microsu-percapacitor. Applied signal v_M is a periodic low duty cycle triangle voltage 'pulse'. Series resistor R_M is used to measure current through the microsupercapacitor. (b) Electroreflectance imaging excitation for an ideal microsupercapacitor using a periodic 30 ms triangle voltage pulse. For the hypothetical ideal case shown, $R_M = 0$, $v_C = v_M$, and the microsupercapacitor has no parasitic electrical characteristics (internal resistance or current leakage). With $v_{M,max} = 1\,\mathrm{V}$, the applied waveform produces a charge and discharge cycle equivalent to cyclic voltammetry at a scan rate of $66\,\mathrm{V\,s^{-1}}$. Electrode excess charge (not shown) and reflectance follow the shape of applied voltage v_M. Electrical and reflectance response in the real microsupercapacitor is skewed from the ideal case shown due to parasitic effects.

Electroreflectance images of the microsupercapacitor were acquired using the box-car averaging method illustrated in Fig.5.4 in which the microsupercapacitor modu-

lation signal is synchronized to a pulsed probe illumination signal. Electroreflectance amplitude is calculated from two separately acquired images corresponding to the active and passive states of the microsupercapacitor. The camera records microsupercapacitor reflectance only during the probe illumination pulse. By controlling the phase delay (τ) of the illumination pulse relative to the modulation signal, sample reflectance can be measured at any time in the microsupercapacitor modulation cycle. Microsupercapacitor reflectance during the electrically active state (Fig.5.4a) is recorded by positioning the illumination pulse to occur during the charge/discharge time window of the modulation cycle (time = 0 ms to 30 ms) when $dv_C/dt = 0\,\mathrm{V}$. Then, reflectance during the electrically passive state (Fig.5.4b) is recorded by positioning the illumination pulse late in the cycle when $dv_C/dt = 0\,\mathrm{V}$ and both electrodes are electrically at ground. The active and passive reflectance images are acquired during separate averaging intervals. Images of electroreflectance changes are calculated from the difference between the two reflectance images acquired in the active and passive stages. Although the amplitude of electroreflectance modulation is small (10^{-4} to 10^{-3}), images with good signal to noise can be extracted in five minutes of cumulative averaging during continuous microsupercapacitor modulation. Modulation was intentionally performed at low duty cycle (20%) to ensure the microsupercapacitor returns to electrical and reflectance equilibrium during acquisition of the passive reflectance image. For the 30 ms triangle voltage pulse at 20% duty the corresponding system modulation was 6.67 Hz and 150 ms per cycle. Time resolution is determined by the duration of the illumination pulse, which was selected to be one millisecond for this study.
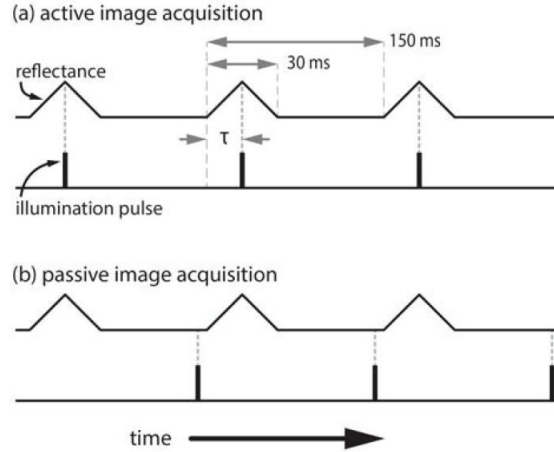
Fig. 5.4. 'Boxcar' averaging scheme for acquisition of microsupercapacitor electroreflectance image. The camera records reflectance only during the illumination pulse. Images of electroreflectance change are calculated from the difference of microsupercapacitor reflectance images acquired during the (a) active and (b) passive electrical states of the modulation cycle.

5.2.3 Model of Microsupercapacitor Electroreflectance

Electrode reflectance dependence on charge accumulation

The relation between complex refractive index of gold ($\tilde{n} = n_1 + i n_2$) and its complex dielectric constant ($\tilde{\epsilon} = \epsilon_1 + i\epsilon_2$) derived from Maxwell's equations is expressed as: [183]

$$\tilde{n} = \sqrt{\tilde{\epsilon}}. \tag{5.1}$$

The dielectric constant contains additive contributions from free electrons and bound electrons:

$$\tilde{\epsilon} = \tilde{\epsilon}_f + \tilde{\epsilon}_b. \tag{5.2}$$

Here we assume that the contribution of bound electrons remains unchanged with charging/discharging of the microsupercapacitor. [158] The contribution of free electrons to the dielectric constant is related to the incident light frequency by the expression

$$\tilde{\epsilon}_f(\omega) = 1 - \frac{\omega_p^2}{\omega^2 + i\omega/\tau}, \tag{5.3}$$

where τ is the frequency-dependent relaxation time of electrons in the conduction band [158,184] and ω is the frequency of incident light given by $\omega = \frac{2\pi c}{\lambda}$. c is the speed of light in vacuum and λ the wavelength of incident light. ω_p, the plasma frequency at which the electron gas oscillates in electrically neutral conducting media such as plasma and metals, is given by [157]

$$\omega_p = ((\eta e^2)/(_0 m))^{1/2}, \tag{5.4}$$

where η is charge density, e is the electron charge, $_0$ is vacuum permittivity, and m is the electron effective mass. On applying a voltage bias to the microcapacitor electrodes, an electric field is formed that causes charge to drift and hence alters the free electron concentration in the top surface layer of the gold electrode. This change in free electron concentration, or excess charge density $\Delta\eta$, leads to a change in the plasma frequency given by

$$\frac{\Delta\omega_p}{\omega_p} = (1 + \frac{\Delta\eta}{\eta_0})^{1/2} - 1, \tag{5.5}$$

where η_0 is the intrinsic electron concentration in gold ($5.9 \times 10^{28}/m^3$). This process alters the complex dielectric constant and the refractive index of gold. In order to simplify the calculations, the refractive index is considered to be shifted on the frequency (ω) axis by the same fraction that ω_p is shifted such that [158]

$$\frac{\Delta\omega}{\omega} = \frac{\Delta\omega_p}{\omega_p}. \tag{5.6}$$

Table 5.1 [157] shows refractive indices of gold for a range of wavelengths (λ) near green in the visible part of the spectrum. n_{1f} and n_{1b} represent the real part of the refractive index for thin film gold ($60\,\text{Å}$) and bulk gold respectively, while n_{2f} and n_{2b} represent the imaginary part of the refractive index for gold film and bulk gold respectively. The wavelength used in the experiment (530 nm) corresponds to $n_1 = 0.82$ and $n_2 = 2.29$ for uncharged gold. The gold electrode used in the experiment is approximately 80 nm thick, so the optical constants of thin film of gold have been used. The reflectance change is calculated considering a single positively charged or

Table 5.1.
Gold refractive index at selected illumination wavelengths near green in the visible spectrum. Real (n_1) and imaginary (n_2) part is given for both thin film (60 Å) and bulk.

λ (nm)	n_{1f}	n_{1b}	n_{2f}	n_{2b}
500	1.21	0.90	1.94	1.82
520	0.91	0.60	2.16	2.00
540	0.72	0.38	2.41	2.23
560	0.60	0.28	2.69	2.57

negatively charged gold finger electrode. The electric double layer is formed at the interface between the gold electrode and polymer electrolyte. Charge density due to excess or deficient electrons on the gold side is equal and opposite in sign to the excess charge density of the ions on the electrolyte side (σ_{ion}) as given by

$$\Delta \eta e = -\sigma_{ion}. \tag{5.7}$$

Excess charge on the gold surface during the charge/discharge pulse is given by

$$\Delta \eta = \frac{q}{Aed}, \tag{5.8}$$

where q is the total charge in a single gold finger electrode, A is the area of the top surface of a finger electrode, e is the electron charge and d is the unknown skin layer thickness. Although the charge is modeled to accumulate only in the fingers, in reality, it also transfers further into the terminals because they are in contact with the polymer electrolyte. The total surface area of finger electrodes of a particular polarity (including the terminal portion) is 346200 μm^2. A is $1/8^{th}$ of this value, which is 43275 μm^2. q as a function of time is expressed as

$$q(t) = \begin{cases} \int_0^t i_1 \, dt & 0\,\text{ms} < t \le 15\,\text{ms} \\ \int_0^{t-15} i_1 \, dt + q_0 & 15\,\text{ms} < t \le 30\,\text{ms} \\ \int_0^{t-30} i_1 \, dt + q_1 & 30\,\text{ms} < t \le 40\,\text{ms}. \end{cases} \tag{5.9}$$
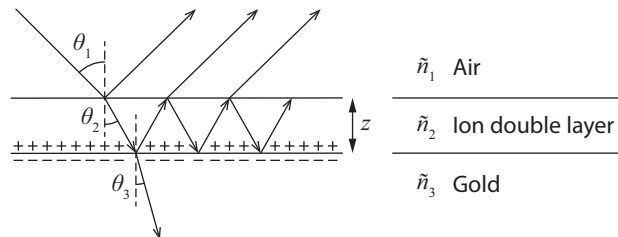
Fig. 5.5. Three-media reflectance model for the microsupercapacitor.

where q_0 is the value of q at the end of 15 ms, q_1 is the value of q at the end of 30 ms, and i_1 is the current charging the finger electrode. The definition of current i_1 is in (5.20).

The Fresnel laws of reflection have been used to determine the differential reflectance change $\frac{\Delta R}{R}$ for the three-medium model shown in Figure 5.5. The three media in the model are air (refractive index $\tilde{n}_1$ is 1), ion double layer whose thickness, z, is considered to be 100 Å (refractive index $\tilde{n}_2$ is 1.34) [156] and gold (refractive index $\tilde{n}_3$ is $0.82 + 2.29i$ in the uncharged state corresponding to $\lambda = 530nm$). Prostak et al. [156] found that for the gold-KCL system, variation in the electrolyte layer thickness or electric field modulation of the electrolyte refractive index does not reproduce the peak observed in electroreflectance experiments. Consequently the influence of change in the thickness parameter z has not been studied here. The reflectance as a function of the reflection coefficient is given by

$$R = r_{123}^2, \tag{5.10}$$

where r_{123} is given by [165, 183]

$$r_{123} = \frac{r_{12} + r_{23}e^{-2i\beta}}{1 + r_{12}r_{23}e^{-2i\beta}}, \tag{5.11}$$

and r_{12} is the reflection coefficient from medium 1 to medium 2 given by

$$r_{12} = \frac{\tilde{n}_1 cos\theta_1 - \tilde{n}_2 cos\theta_2}{\tilde{n}_1 cos\theta_1 + \tilde{n}_2 cos\theta_2}. \tag{5.12}$$

Similarly, r_{23} is the reflection coefficient from medium 2 to medium 3 given by

$$r_{23} = \frac{\tilde{n}_2 cos\theta_2 - \tilde{n}_3 cos\theta_3}{\tilde{n}_2 cos\theta_2 + \tilde{n}_3 cos\theta_3}, \qquad (5.13)$$

where $\beta = \frac{2\pi\tilde{n}_2 z}{\lambda}$ is the phase factor, and the ion double layer thickness, z, is 100 Å. Because near normal reflectance has been studied, $\theta_1 = \theta_2 = \theta_3 = 0$. For the present analysis, the reflectance of the system with uncharged gold ($R_{uncharged}$) and that of the system with charged gold ($R_{charged}$) have been evaluated at every time step. Finally, the differential reflectance change $\frac{\Delta R}{R}$ has been calculated at every time step from the expression

$$\left(\frac{\Delta R}{R}\right)_{model} = \frac{R_{charged} - R_{uncharged}}{R_{uncharged}}. \qquad (5.14)$$

The unknown value of the skin layer thickness is obtained by fitting the model reflectance change values with the experimentally obtained values. The mean square error defined by

$$MSE_{ref} = \frac{1}{n} \sum_{i=1}^{n'} \left(\left(\frac{\Delta R}{R}\right)_{model} - \left(\frac{\Delta R}{R}\right)_{exp}\right)^2 \qquad (5.15)$$

is minimized for this purpose. n is the number of data points used for the study. Here, we have used 41 points each at an interval of 1 ms.

Equivalent circuit model

The in-plane microsupercapacitor device shown in Fig.5.1 consists of two sets of eight interdigitated electrode fingers connected to the positive and negative device terminals. On charging, mobile ions in the electrolyte accumulate in the double layer region atop of the electrodes. The microsupercapacitor electrodes do not contain any pseudocapacitive material [185]; therefore the electrode-electrolyte interface is expected to behave as a pure electric double layer capacitor (EDLC) with negligible charge transfer directly between electrode and electrolyte.

The electrical equivalent circuit for the full microsupercapacitor sample and applied thermoreflectance imaging modulation is illustrated in Fig.5.6. If we consider each adjacent positive and negative electrode finger pair in the microsupercapacitor
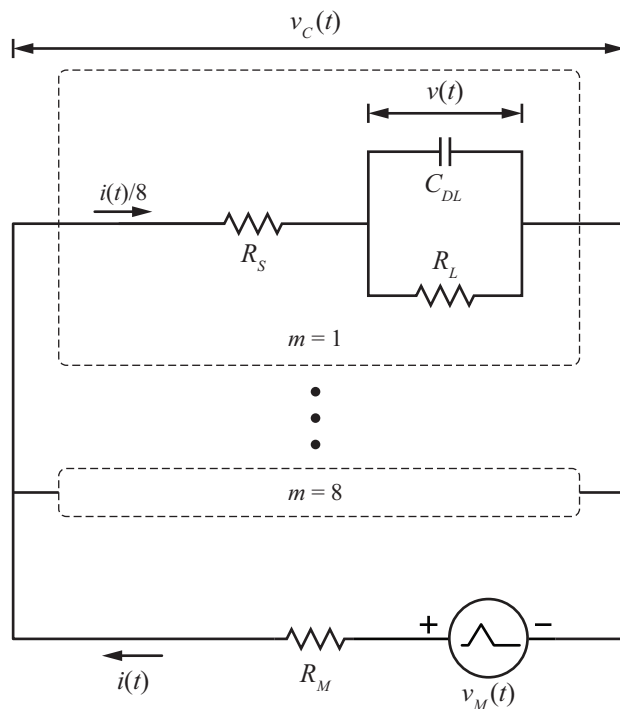
Fig. 5.6. Equivalent circuit for the full microsupercapacitor sample and applied thermoreflectance imaging modulation bias. Each adjacent positive and negative electrode finger pair is modeled by a Randles equivalent circuit. The Randles circuit for the $m = 1$ finger pair is shown in detail. The full microsupercapacitor is modeled as eight identical Randles circuits connected in parallel.

as a single electrical unit, the full device can be modeled as eight of these finger pair units connected in parallel, all at potential v_C. Each individual finger pair can be modeled as a Randles [186] equivalent circuit, consisting of the capacitance created at the electrode-electrolyte interface along with parasitic components. The Randles circuit for the $m = 1$ finger pair is highlighted in Fig.5.6. R_S represents series electrical resistance to charge transport both in the electrode metal and in the electrolyte. C_{DL} represents an ideal capacitor at the electrode-electrolyte interface which stores charge during charging and releases charge during discharging. Leakage resistance, R_L, represents the self-discharge characteristics of the capacitor due to parasitic shunt current paths to ground. Current leakage can explain the nonideal current waveform

observed during operation. For example measured total current through the circuit as a function of time, plotted in Fig.5.10a, shows that current amplitude is greater during charging than discharging. Conservation of charge (area under the current curve) implies that the additional current is lost through parasitic leakage. Because the eight finger pairs are assumed equivalent, only one finger pair is considered for analysis. The cumulative parallel contribution of each finger pair is then factored into the full device model.

The time period from $0\,\mathrm{ms}$ to $40\,\mathrm{ms}$ is considered in 3 parts: (a) charging from approximately $0\,\mathrm{ms}$ to $15\,\mathrm{ms}$, (b) discharging from approximately $15\,\mathrm{ms}$ to $30\,\mathrm{ms}$, and (c) idle from $30\,\mathrm{ms}$ to $40\,\mathrm{ms}$. The externally applied electroreflectance modulation voltage, $v_M(t)$, is,

$$
v_M(t) = \begin{cases} 66.7t & 0\,\mathrm{ms} < t \le 15\,\mathrm{ms} \\ 1 - 66.7t & 15\,\mathrm{ms} < t \le 30\,\mathrm{ms} \\ 0 & 30\,\mathrm{ms} < t \le 40\,\mathrm{ms}. \end{cases}
\tag{5.16}
$$

An analytical expression for the double layer voltage $v(t)$, the voltage across C_{DL} in the Randles circuit of Fig.5.6, is obtained through

$$
(8R_M + R_S)C_{DL}\frac{dv}{dt} + \frac{(8R_M + R_S + R_L)}{R_L}v = v_M.
\tag{5.17}
$$

Thereafter, the current $i(t)$ is obtained from the equation,

$$
i(t) = 8(C_{DL}\frac{dv}{dt} + \frac{v}{R_L})
\tag{5.18}
$$

The unknown parameters in the model, namely R_S, R_L and C_{DL} are obtained by fitting the current obtained from the model to the experimentally measured current shown in Fig.5.10a. The combination of the parameters that results in the minimum mean square error (MSE) given by

$$
MSE_{curr} = \frac{1}{n}\sum_{i=1}^{n'}(i_{model} - i_{exp})^2
\tag{5.19}
$$
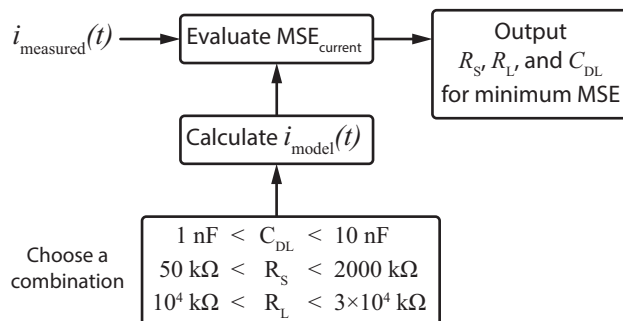
Fig. 5.7. Flowchart for calculating Randles parameters for the microsupercapacitor.

is selected to represent the circuit elements. A detailed flowchart of the adopted method is shown in Fig.5.7. The current charging the capacitor C_{DL} in one finger pair, is evaluated from

$$i_1(t) = C_{DL}\frac{dv}{dt} = \frac{i(t)}{8} - \frac{v}{R_L}. \tag{5.20}$$

5.3 Results and discussion

5.3.1 Electroreflectance Spectral Response

The electroreflectance response for the gold-H_3PO_4 microsupercapacitor was measured at several probe illumination wavelengths. This allowed selection of optimum wavelength for electroreflectance imaging response. Fig.5.8 shows electroreflectance amplitude as a function of probe illumination wavelength. Measurements are compared for narrowband LED sources with wavelengths centered at $405\,\mathrm{nm}$, $455\,\mathrm{nm}$, $470\,\mathrm{nm}$, $530\,\mathrm{nm}$ and $940\,\mathrm{nm}$. The plot suggests a peak in electroreflectance response for the gold-H_3PO_4 microsupercapacitor near $500\,\mathrm{nm}$ wavelength probe illumination. This spectrum is consistent with previous electroreflectance measurement of gold-electrolyte interfaces. Feinlab observed a similar peak in measured electroreflectance for gold in a KCL solution. [155] The gold-KCL spectrum is plotted (blue curve) with the microsupercapacitor data in Fig.5.8. The agreement between gold electroreflectance spectra despite differing electrolytes suggests reflectance change in the metal

(gold) is the dominant cause of the electroreflectance response, as postulated by our open circuit model of excess charge in the electrodes.
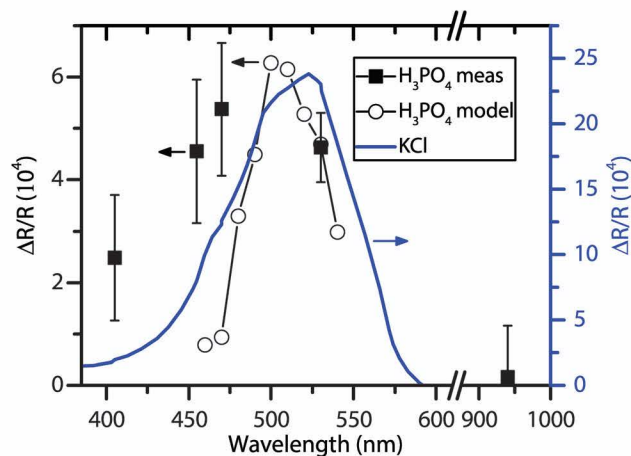
Fig. 5.8. Measured and modeled electroreflectance amplitude as a function of incident illumination wavelength. Microsupercapacitor (gold-H_3PO_4) electroreflectance was measured for incident narrow-band LED sources centered at wavelengths 405 nm, 455 nm, 470 nm, 530 nm and 940 nm. Values shown were measured on the microsupercapacitor positive electrode at time = 16 ms into the triangle voltage pulse. Modeled spectral response for the microsupercapacitor is also plotted. The peak in electroreflectance for gold-H_3PO_4 near 500 nm is similar to the peak measured for gold-KCl (solid blue curve), per Feinlab [155], copyright (1966) by The American Physical Society.

The variation of reflectance change with wavelength has also been evaluated from the model. The charge obtained from the current fitting model at 16 ms and the fitted skin layer thickness (90 Å) have been used for the analysis. The $R_{uncharged}$ in Eq.(5.14) has been obtained by using the gold refractive index at the particular wavelength for an uncharged gold electrode. $R_{charged}$ has been calculated for the charged gold electrode at the same wavelength value. Calculated electroreflectance spectral parameters for three incident wavelengths are summarized in Table 5.2 and compared to measured values in Fig.5.8. The peak in the reflectance change is obtained at 500 nm wavelength which corresponds to 2.49 eV. This is similar to the peak at 2.5 eV obtained by Prostak et al [156], which supports the assertion that the

Table 5.2.
Calculated electroreflectance spectral parameters based on $\Delta\eta/\eta = 1.63 \times 10^{-4}$, $\Delta\omega/\omega = 8.13 \times 10^{-5}$, and $\Delta E = 1.91 \times 10^{-4}\,\text{eV}$.

λ (nm)	n_{old}	k_{old}	n_{new}	k_{new}	$\Delta R/R$
460	1.36	1.75	1.36	1.75	0.79×10^{-4}
500	0.90	1.82	0.90	1.82	6.28×10^{-4}
530	0.49	2.12	0.49	2.12	4.69×10^{-4}

metal is the dominant factor in the electroreflectance response for both gold-KCL and gold-H_3PO_4 systems.

5.3.2 Microsupercapacitor Transient Electrical Response and Transient Electroreflectance Distribution

Fig.5.9b-f shows transient electroreflectance microscope images of the microsupercapacitor at selected times during one typical cycle of voltage excitation. Fig.5.9a shows the optical microscope image of the microsupercapacitor with positive and negative electrodes indicated. Voltage bias matched the waveform described in Fig.5.3b with triangular pulse duration of 30 milliseconds and pulse repetition every 150 milliseconds. External applied voltage amplitude, v_M, ranged from $0\,\text{V}$ to $1\,\text{V}$. This modulation bias produced a voltage ramp during the 30 millisecond triangle pulse that was effectively equivalent to cyclic voltammetry using a scan rate of $66\,\text{V}\,\text{s}^{-1}$. It should be noted that in conventional cyclic voltammetry measurements, the sample typically undergoes voltage ramping (dV/dt) continuously without interruption. In comparison, the electroreflectance modulation signal is periodic with a duty cycle of $20\,\%$. Consequently, the voltage ramp occurs only for one fifth of each cycle and the device is passive for the remainder of the cycle. (See Fig.5.4.) Time varying voltage across the microsupercapacitor v_C and total current i were measured by oscilloscope. Choosing series resistance R_M to be $40\,\text{k}\Omega$ produced the most accurate measurement

of total current in the circuit. Each image data point was averaged for 10 min (4000 continuous cycles).
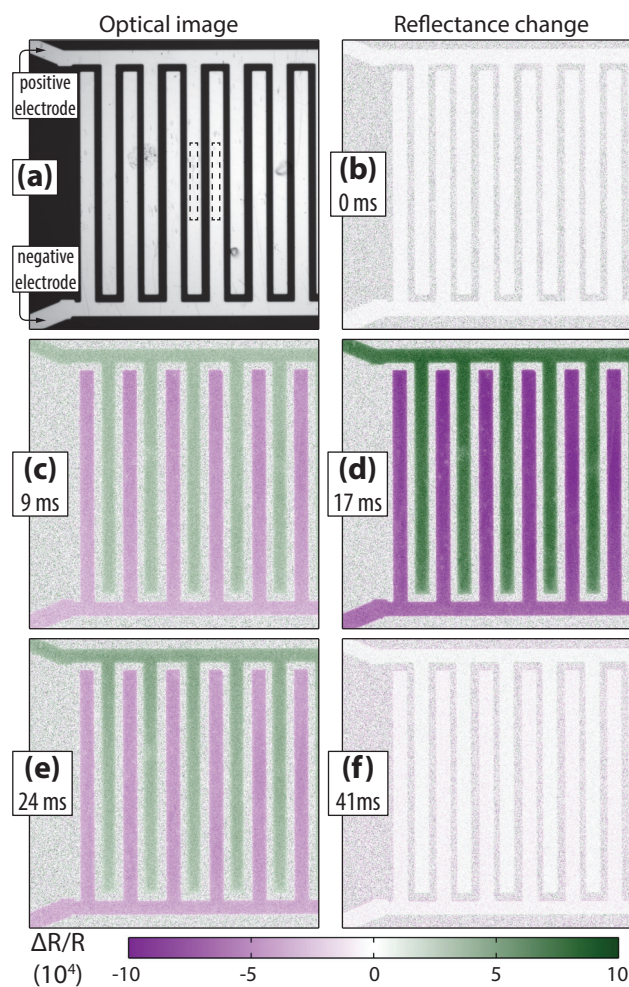
Fig. 5.9. Transient electroreflectance images of the microsupercapacitor in response to 30 ms triangle charge/discharge voltage pulse excitation. (a) Optical image of the microsupercapacitor with positive and negative electrodes indicated. (b-f) Reflectance change images at selected times during one voltage excitation cycle. Each image was averaged for 10 min (4000 continuous cycles).

Fig.5.10 plots measured and modeled microsupercapacitor electrical parameters and corresponding electrode reflectance as a function of time for one 30 ms charge/discharge cycle. Fig.5.10a plots applied voltage modulation v_M and resulting measured voltage across the full sample v_C and measured total current in the circuit i. Fig.5.10c

plots corresponding measured electrode reflectance change $\Delta R/R$. Plotted reflectance change was extracted from electroreflectance images at corresponding times in the cycle. Each reflectance change data point was calculated from the mean of all pixels within sampling regions on the positive and negative electrodes in the image. Location of image sampling rectangles are indicated in the optical image of the microsupercapacitor in Fig.5.9a.

The transient plot reveals electrode reflectance change closely follows voltage with respect to time. This is true for both positive and negative electrodes. Maximums for both v_C and $\Delta R/R$ occur at the charge/discharge inflection point approximately 16 ms into the triangle waveform. Maximum $\Delta R/R$ is 8.5×10^{-4} on the positive electrode and -9.0×10^{-4} on the negative electrode. It is expected that reflectance change is opposite in sign on the positive and negative electrodes because excess charge is opposite on the respective electrodes.

Both v_C and $\Delta R/R$ are symmetric with respect to time during the charge and discharge stages of the triangle waveform. That is, amplitude of v_C and $\Delta R/R$ are nearly identical at equal times before and after the charge/discharge inflection point (≈ 16 ms). However, it is notable that total current through the microsupercapacitor does not display the same time symmetry. Maximum current amplitude while charging ($i_{+,max} = 2.6\,\mu\text{A}$ at time $= 15$ ms) is twice the maximum amplitude while discharging ($i_{-,max} = 1.3\,\mu\text{A}$ at time $= 30$ ms). This behavior is not surprising because electrical response of the real microsupercapacitor diverges from the case of an ideal capacitor due to parasitic effects, which manifest in the asymmetric current waveform. These parasitic effects are included in the microsupercapacitor equivalent circuit model discussed later in this section. It will be argued that the different behavior observed for i during charge and discharge portions of the cycle is due to device internal current (shunt) leakage in parallel with its capacitance. This leakage has a small effect on magnitude of both v_C and $\Delta R/R$, but negligible effect on symmetry with respect to the time axis at their respective charge/discharge inflection points.

Because microsupercapacitor electrode reflectance varies with temperature as well as with charge density in the metal, it should be considered whether the measured reflectance change is influenced significantly by temperature change due to electrical self-heating (Joule heating) in the electrodes during cycling. The fraction of reflectance change caused by electrical self-heating is assumed to be very small because power density in the electrodes for the applied bias (i^2R/cm^2) is extremely small. Based on measured maximum current during cycling, temperature change in the electrodes is estimated to be less than $10\,\mathrm{mK}$. However, if the measured reflectance change was caused exclusively by electrical self-heating in the electrode it would imply that the electrode heats up and cools down by more than $3\,\mathrm{K}$ during each cycle. Because the estimated temperature change of $10\,\mathrm{mK}$ during cycling accounts for only a 0.03 fraction of the measured reflectance change we can conclude that device reflectance change is primarily caused by changes in the electrode free electron concentration during cycling. The preceding calculation is based on the electrode temperature dependence of reflectance, using a thermoreflectance coefficient for bare gold [176] of $2.34 \times 10^{-4}\,\mathrm{K}^{-1}$. Thermal transport in the microsupercapacitor due to ion movement during cyclic excitation is an acknowledged possibility, though its effect on reflectance change for the device studied is expected to be smaller than the effect from electrode charge density. An alternate imaging experiment is under consideration that would separate electrical and thermal contributions to reflectance change on the microsupercapacitor.

Fig.5.10a also shows fitted total current through the sample, i, and modeled voltage across the double layer, v. Modeled electrical parameters are based on the full equivalent circuit of Fig.5.6. Current fitting was done by iterating over combinations of the free parameters in the Randles equivalent circuit, consisting of double layer capacitance C_{DL} and parasitic resistances R_S and R_L. These free Randles parameters are illustrated for the $m = 1$ finger pair in Fig.5.6. Values of the Randles parameters that resulted in optimal current fit are: $C_{DL} = 3.5\,\mathrm{nF}$, $R_S = 101.2\,\mathrm{k\Omega}$, and

$R_L \approx 6\,\mathrm{M\Omega}$. Fitting also yields a model the voltage across the double layer, v, and this critical waveform is included for reference in all three panels of Fig.5.10.

Because all the capacitors are connected in parallel, the net capacitance is approximately 8 times C_{DL}, or 28 nF total. This compares well to the 33 nF measured for the sample using cyclic voltammetry. The series resistance of the device, on the other hand is $1/8^{th}$ times R_S, i.e. 12.7 $k\Omega$. The series resistance of microsupercapacitors with in-plane configuration are generally higher than those built with sandwich configuration. For example, Gao et al. [187] reported microsupercapacitors with graphite oxide (GO) electrodes to have series resistance of 6.5 $k\Omega$ in the in-plane configuration compared to 126 Ω in the sandwich configuration. Sensitivity of the modeled current, $i(t)$, in Fig.5.10 has been evaluated for each of the relevant parameters in the Randles equivalent circuit representation of the microsupercapacitor. For R_S, R_L, and C_{DL},

$$\frac{\partial i_{avg}}{\partial R_S} = \frac{\Delta i_{avg}}{\Delta R_S} = -3.15 \times 10^{-4} \mu A/k\Omega, \tag{5.21}$$

$$\frac{\partial i_{avg}}{\partial R_L} = \frac{\Delta i_{avg}}{\Delta R_L} = 2.37 \times 10^{-6} \mu A/k\Omega, \tag{5.22}$$

$$\frac{\partial i_{avg}}{\partial C_{DL}} = \frac{\Delta i_{avg}}{\Delta C_{DL}} = 2.70 \times 10^{-1} \mu A/nF, \tag{5.23}$$

where i_{avg} is the time averaged current calculated by $i_{avg} = \sum_{n=1}^{n=41} |i(t_n)|/41$ and the change in parameters corresponds to 10% of their base values.

Current leakage produces the different peak magnitudes of i_{measured} observed during charge and discharge. A detailed parametric variation is shown in Fig. 5.11. Modeled current is shown for several different values of the three Randles circuit parameters C_{DL}, R_s and R_L. As $R_L \to \infty$, current leakage becomes negligible, and the circuit resembles an ideal capacitor C_{DL} in series with R_S. In this case the positive and negative maximums of i are equal. Both the positive and negative maximums increase on increasing C_{DL} individually, while they decrease on increasing R_s individually.

With the fitted Randles parameters, leakage current can be subtracted from total current. The remaining current causes the microsupercapacitor electrodes to charge

and discharge. We designate i_1 as the current needed to charge and discharge one finger pair of the microsupercapacitor. Integrating i_1 with respect to time gives the excess charge, Δq, in one electrode finger pair. Fig.5.10b shows waveforms of the modeled excess charge Δq on the positive and negative electrode for one electrode finger pair. As expected, the waveform for double layer voltage, v, closely follows the waveform for excess charge. However, calculated double layer voltage is skewed from voltage measured across the full sample, v_C, shown in Fig.5.10a. This is due to the parasitic Randles parameters (R_S, R_L, and C_{DL}), which cause a slight attenuation in the amplitude of the double layer voltage v, and also introduce a time delay of approximately $1\,\mathrm{ms}$.

Fig.5.10c shows electrode reflectance change (measured and modeled) for the same charge/discharge portion of the modulation cycle. Modeled reflectance change was calculated from excess charge shown in Fig.5.10b. Because electrode reflectance is proportional to excess charge in the electrode and also therefore proportional to the double layer voltage, the waveforms for $\Delta R/R$ and v should display good correspondence. This correspondence is confirmed by the observation that both $\Delta R/R$ and v waveforms are delayed in time by $\approx 1\,\mathrm{ms}$ from the applied modulation v_M shown in Fig.5.10a. The measured reflectance change waveform can be reconciled with the observed asymmetry in the measured current waveform by including current leakage in the equivalent circuit model, represented by the Randles parameter R_L. Current leakage explains why excess charge in the electrode returns to equilibrium between each modulation cycle, despite the asymmetric magnitudes of current during charge/discharge.

The skin layer thickness parameter d in equation 5.8 is unknown and hence a fitting analysis has been used to determine its appropriate value. The mean square error defined as,

$$MSE_{ref} = \frac{1}{n} \sum_{i=1}^{n'} ((\frac{\Delta R}{R})_{model} - (\frac{\Delta R}{R})_{exp})^2 \tag{5.24}$$

is minimized by selecting the appropriate value of d. The MSE_{ref} is shown as a function of the assumed d in Fig.5.12. The minimum is achieved at $90\,\text{Å}$. This value

is quite reasonable because Hansen et al. [158] assumed the electron density to change for the entire $50\,\text{Å}$ thin gold film, in their model and got a good match with their experimentally measured reflectance change values.

Sample calculations of reflectance change at time $= 15\,\text{ms}$ are shown in Table 5.3 assuming a skin layer thickness of 90 Å.

Table 5.3.
Microsupercapacitor parameters calculated at time $= 15\,\text{ms}$ into the v_M bias pulse

Electrode polarity	Positive	Negative
q (nC)	2.21	-2.21
$\Delta\eta$ (/m^3)	-1.91×10^{25}	1.91×10^{25}
$\Delta\eta/\eta_0$	-3.24×10^{-4}	3.24×10^{-4}
$\Delta\omega_p/\omega_p$	-1.62×10^{-4}	1.62×10^{-4}
$\Delta\omega/\omega$	-1.62×10^{-4}	1.62×10^{-4}
λ(nm)	530	530
$\Delta\lambda$	0.086 nm	-0.086 nm
n_1	1.00	1.00
n_2	1.33	1.33
r_{12}	-0.1427	-0.1427
$n_{3,uncharged}$	$0.8180 + 2.2850i$	$0.8180 + 2.2850i$
$r_{23,uncharged}$	$-0.4177 - 0.6186i$	$-0.4177 - 0.6186i$
$n_{3,charged}$	$0.8172 + 2.2861i$	$0.8188 + 2.2839i$
$r_{23,charged}$	$-0.4180 - 0.6188i$	$-0.4174 - 0.6184i$
$r_{123,uncharged}$	$-0.4032 - 0.6572i$	$-0.4032 - 0.6572i$
$r_{123,charged}$	$-0.4035 - 0.6574i$	$-0.4030 - 0.6570i$
$R_{uncharged}$	0.5945	0.5945
$R_{charged}$	0.5949	0.5940
$\frac{\Delta R}{R}$	0.000833	-0.000835

Linear time-dependent model

Calculated excess charge can be used to quantify reflectance dependence on charge density in the Au electrode for the incident illumination wavelength. Fig.5.10 shows that applying a linearly changing external voltage (v_M) across the full circuit produces approximately linear changes in the microsupercapacitor internal voltage v, excess charge Δq, and mean reflectance change $\Delta R/R$. All three waveforms can be approximated as linear over the voltage range inspected ($v_M = 0\,\mathrm{V}$ to $1\,\mathrm{V}$) and described by:

$$Y = \begin{cases} At & 0\,\mathrm{ms} < t \leq 18\,\mathrm{ms} \\ B - A(t - 18) & 18\,\mathrm{ms} < t \leq 36\,\mathrm{ms} \\ 0 & 36\,\mathrm{ms} < t \leq 40\,\mathrm{ms}. \end{cases} \tag{5.25}$$

The coefficients are shown in table 5.4. From these relations, the reflectance

Table 5.4.
Estimated values of constants for the linear time-dependent model of
voltage, charge and reflectance change expressed by (5.25)

Variable	A	B	RMS error
$v(t)$	0.038 (V/s)	0.71 V	0.050 $\sqrt{V}$
$q(t)$	0.131 (nC/s)	2.43 nC	0.175 $\sqrt{nC}$
$\frac{\Delta R}{R}$ ($\times\ 10^4$)	0.50	8.11	0.79

change $\frac{\Delta R}{R}$ can be expressed as a linear functions of charge and voltage by

$$\frac{\Delta R}{R} = 3.45 \times 10^{-4} q \tag{5.26}$$

and

$$\frac{\Delta R}{R} = 13.2 \times 10^{-4} v, \tag{5.27}$$

where q is charge in nanoCoulombs and v is the voltage across C_{DL} in volts. Using the relation $q(t) = C_{DL} \times v(t)$ and (5.26) and (5.27), $\frac{\Delta R}{R}$ can also be expressed as a function of the capacitance. At $t = 15ms$,

$$\frac{\Delta R}{R} = 1.97 \times 10^{-4} C_{DL}. \tag{5.28}$$

Minimum resolution

Dividing (5.26) by area of the electrode gives an expression for reflectance dependence on charge per unit area in the microsupercapacitor. Approximating this dependence as linear over the range inspected, we define a scalar electroreflectance coefficient, C_{ER}, for the electrochemical system at a given incident illumination wavelength. For the gold-H_3PO_4 microsupercapacitor at 530 nm illumination,

$$C_{ER} = \frac{\Delta(\Delta R/R)}{\Delta q/A} = 1.49 \times 10^{-7} \, \text{cm}^2 \, \text{nC}^{-1}. \tag{5.29}$$

This dependence can be used to estimate minimum experiment measurement resolution. We define minimum resolution as the amount of excess charge per unit area of the electrode sufficient to produce magnitude of reflectance change equal to one standard deviation in the measured reflectance change for all pixels in a region of interest. From the electroreflectance image in Fig.5.9 (any time window), one standard deviation measured reflectance change for all pixels within a sampling rectangle covering the full area of one electrode finger is $\sigma = 7 \times 10^{-5}$. For 530 nm incident illumination and 10 min averaging (4000 coninuous cycles), estimated minimum resolution of the electroreflectance imaging technique for the gold-H_3PO_4 microsupercapacitor is $\sigma / C_{ER} \approx 500 \, \text{nC} \, \text{cm}^{-2}$, equivalent to modulation of one charge per 32 nm^2 electrode surface area. To date, the high sensitivity of the electroreflectance response has been used primarily to characterize material properties. However, these studies typically require averaging the response over macroscopic regions of a uniform sample and consequently provide no spatial information. The imaging method presented here demonstrates this excellent sensitivity can be extended to precise spatial characterization of microscale integrated electrochemical devices.

5.3.3 Electroreflectance Spatial Uniformity Across Microsupercapacitor

Electroreflectance imaging can reveal subtle variations in charge distribution with submicron spatial resolution. Fig.5.13 compares electroreflectance amplitudes and spatial distributions for two similar gold-H_3PO_4 microsupercapacitors. Optical images of the two samples are shown in Fig.5.13a,c. Both samples have identical fabrication, electrode and electrolyte composition, and active area layout. Both samples were measured under identical modulation bias at time $= 15\,ms$ into the applied voltage pulse v_M. Corresponding electroreflectance images of the two samples are shown in Fig.5.13b,e. A cursory visual inspection reveals distinct differences in both amplitude and spatial distribution of reflectance change under modulation bias. Profiles of electroreflectance change along five electrode finger pairs, positive and negative, are plotted in Fig.5.13c,f for sample 1 and sample 2 respectively. Locations of sampled reflectance change profiles are indicated by the vertical dashed lines in the optical images, measured top to bottom. The profiles show magnitude of reflectance change on sample 1 is approximately double the magnitude of peak reflectance change on sample 2. Also, sample 2 exhibits a clear radial shaped feature in the center of the electroreflectance image (Fig.5.13e). There is no evidence of this feature in the corresponding optical image of sample 2. Reflectance change profiles along sample 2 electrodes show attenuation by as much as a factor of four. Conversely, no similar spatial anomaly exists in sample 1, which displays much more uniform reflectance change distribution. Reflectance change profiles along sample 1 electrodes vary only by about $20\,\%$ across the finger. Additionally, a quantitative correlation was observed between total device capacitance and mean electroreflectance of samples 1 and 2. The ratio of total capacitance for samples 1 and 2 (obtained from CV measurement) is $C_1/C_2 = 3.7 \pm 1.0$. The ratio of mean reflectance change for samples 1 and 2 is $(\Delta R/R)_{mean1}/(\Delta R/R)_{mean2} = 2.8 \pm 0.5$. This observation supports the need for further investigation into the relationship between microsupercapacitor spatial defects, average electrical performance, and reflectance. Quantitative analysis would likely

require a full model of the microscopic polarization dynamics between electrodes during cycling. We note the cause of the spatial anomaly in sample 2 has not yet been determined. The defect was observed to be a permanent feature of the sample, not changing in location or electroreflectance amplitude over the course of several days and hundreds of thousands of electric modulation cycles.

5.3.4 Aging Characterization

Nominal microsupercapacitor

The ageing experiment was first performed with a nominal microsupercapacitor with close-to-ideal behavior as a control for further samples. CV curves and capacitance values are shown in Fig. 5.14. The maximum scan rate of the capacitance measurements was 25 V s^{-1}, whereas the electroreflectance cycling scan rate was 66.7 V s^{-1}. These two scan rates were chosen to be as close as possible within the constraints of the measurement systems. There are no pseudocapacitance reactions present, and the microsupercapacitor is close to ideal. The capacitance remains at a fairly constant value throughout the cycling period, indicating that no significant changes occurred to degrade the device performance at these cycling conditions.

The reflectance change associated with the nominal microsupercapacitor is shown in Fig. 5.15. The magnitude of reflectance change was relatively constant throughout the testing period, as expected given the constant trend of capacitance. The positive electrode exhibited a slight increasing trend, which is considered small in this case. Reflectance images throughout the study indicated that charge accumulated uniformly on both electrodes during charge/discharge processes.

The time-series of reflectance change during each individual voltage pulse were very consistent in shape throughout the ageing period (not shown here for brevity; see Fig. 5.21 for an example). The shape of each series closely followed that of the voltage pulse applied to the device, while the reflectance change was positive on the positive electrode and was negative on the ground electrode. However, in general,

the positive electrode reflectance change was slightly larger in magnitude than that of the negative reflectance change.

Microsupercapacitor with burn-in behavior

A repeat measurement was performed on a sample exhibiting non-uniform charge accumulation on the negative electrode. Microsupercapacitor CV curves at various cycling times, capacitance values, and the mean reflectance of each electrode are displayed in Fig. 5.16. The CV curves were again relatively rectangular in shape, which is indicative of ideal electrochemical behavior.

A summary of the mean reflectance throughout the study is shown in Fig. 5.17. It is clear that a discontinuity in measured capacitance occurred between 1.2 and 1.5 million cycles. The CV curve shape indicates the device behaved more ideally at and beyond 1.5 million cycles. While no known external factor occurred to cause the sudden increase in capacitance, it provided an interesting feature to study the corresponding charge distribution. The relation between capacitance and reflectance along with several reflectance series associated with this device are presented in the electroreflectance modeling section below (Fig. 5.21).

Reflectance images before and after the sudden increase in capacitance are shown in Fig. 5.18 during charging, maximum charge, and discharging phases of operation. At 1.2 million cycles, an area on the negative electrode exhibited less charge accumulation than its complement area. The unactivated area became progressively smaller from 0.0 to 1.2 million cycles until a sudden activation occurred. Therefore, at 1.5 million cycles, the area appeared to be fully activated.

Between 1.5 and 4.1 million cycles, the reflectance of each electrode decreased uniformly. These two distinct phases of ageing behavior suggested a change in dominance of two underlying physical mechanisms. We hypothesize that the first phase was dominated by decreased wetting of the electrolyte to the electrode, and the sec-

ond phase was dominated by breakdown of the electrolyte. This point is supported further by the equivalent circuit model results presented below.

During the discharge phase when the electrodes were fully activated, as shown in Fig. 5.18(f), the charge dissipated away first from the area furthest from the electrode lead (bottomleft on the negative electrode). This effect was consistently observed throughout every discharge cycle recorded, and visually represents electrons funnelling out of the negative electrode during diffusive-dominated discharge. This pattern may be more subtle during the charging phase as the dominating mechanism is electrostatic force, which is more likely to cause uniform charge accumulation.

Model results

The microsupercapacitor with burn-in behavior was chosen for model analysis in order to understand its discontinuous behavior. The experimental and fitted model current profiles for various ageing conditions are shown in Fig. 5.19. For the experimentally measured current profiles, the magnitude of the maximum current was larger than the magnitude of the minimum current. For example, for the ageing condition of 1.5 million cycles, the maximum was 6.7 μA while the magnitude of the minimum was 5.9 μA. This difference occurs because a fraction of the accumulated charge was dissipated by self-discharge. The fitted circuit parameters of the electrical model are represented in Table 1 for various cycling conditions. The capacitance of the model device was obtained by multiplying C_{dl} by 8, because there were 8 electrode fingers each with capacitance C_{dl} in parallel. The device capacitance is compared with the experimentally-measured capacitance from CV measurements in Fig.5.16.

We hypothesize that two different phenomenoa dominate the device performance at two different ageing phases. From 0.0 to 1.5 million cycles, the device increased in capacitance. Similarly, RL increased and reached its highest value at 1.5 million cycles. In a comparable inverse trend, Rs experienced a significant decrease during this period. In other words, both values moved closer toward an ideal double layer

capacitor ($R_L = \infty$ and $R_S = 0$). The trend in ESR supports the previously stated hypothesis that the initial capacitance trend occurs due to poor initial wetting of the electrolyte to the electrode, as also evidenced by the nonuniformity in the reflectance images (Fig.5.18). By definition, as the electrolyte wets the electrode more effectively, ESR decreases.

In the second phase, from 1.5 to 4.1 million cycles, the device gradually decreased in capacitance. In this phase, the ESR fluctated and no significant degradation of the electrode was visible in the reflectance images. However, R_L gradually declined during this phase, and therefore was the dominant cause of ageing. This is likely to be a result from increasing ohmic leakage through conduction paths between the electrodes.

The fitted circuit parameters were used to quantify the charge accumulation in a single finger electrode capacitor C_{dl}, resulting in the values shown in Fig. 5.20. The external resistor in the measurement circuit induced an RC time constant, therefore causing the charge to reach maximum after the peak voltage (15 ms) and to reach zero after the end of discharge (30 ms). Throughout ageing, the peak charge increased from its lowest value of 2.1 nC (0.6 million cycles) to a value of 4.7 nC (1.5 million cycles) and thereafter reduced to 3.8 nC (4.0 million cycles). As expected, this trend follows the trend of capacitance Cdl with ageing.

The reflectance change obtained from the model and the experiment are plotted in Fig. 5.21. The shape of the reflectance change with time followed closely that of the calculated charge variation with time. Also, the magnitudes of the positive and negative experimentally-observed reflectance change were approximately equal, agreeing well with the assumption that charge formation only perturbs the refractive index of gold. Overall, the reflectance change varies linearly with charge accumulation and thus capacitance.26

The skin layer thickness d was unknown for the reflectance calculations, and hence a parametric variation was performed to minimize the mean square error MSE_{ref} as shown in Fig. 5.22 for several ageing conditions. The final value for d was assumed

to be 80 A for all reflectance calculations. Because this thickness is a fraction of the actual thickness of gold (80 nm), the underlying titanium layer was not considered in the model. Similarly, Hansen et al.21 reported that a change in reflectance is caused by a change in electron concentration in the first 50 A of bulk gold.

High voltage cycling

An increased-voltage study was completed in order to simulate accelerated ageing. The nominal microsupercapacitor was used subsequent to the previously described study. Increasingly higher voltages were applied to the device circuit: 1.4 V, 1.6 V, and 1.8 V. The voltage pulse length remained at 30 ms, which corresponded to increased scan rates for each voltage level. In this case, the reflectance change signal was only recorded at 16 ms into the voltage pulse because it was greatest in magnitude. As previously, each image was averaged over 2000 cycles (5 minutes). This modified scheme has the advantage of enabling the record of data points more frequently in terms of number of cycles. On the other hand, the disadvantage is that reflectance change is not recorded at any other time steps during the voltage pulse.

CV curves were recorded between each voltage step, as shown in Fig. 5.23. The results indicate that the capacitance slightly increased throughout this measurement despite the decreasing trend during the last phase in reflectance measurements. This effect was likely due to the fact that the capacitance was measured at 25 V s $^{-1}$, while the reflectance measurements were recorded at greater scan rates that slightly varied due to the external resistor.

The mean reflectance change and standard deviation results are shown in Fig. 5.24. The device reflectance did not change significantly during the first phase (1.4 V), then began to change during the second phase (1.6 V), and clearly degraded during the third phase (1.8 V). Because of the presence of the resistor in the circuit, the measured maximum voltages applied to the device were 1.19 V, 1.31 V, and 1.46 V, respectively. We note that PVA electrolyte requires some moisture to function

correctly. Electrolysis of water occurs at 1.23 V; therefore degradation in performance was expected.

A change in standard deviation of the reflectance images was also observed. During the second phase (1.6 V), the standard deviation trend is similar for both electrodes. Therefore, the physical source of this effect was likely the electrolyte. However, a detailed understanding of this trend remains unclear. For the third phase (1.8 V), a change in standard deviation occurred only on the negative electrode. The results indicate that the mean did not change significantly, but the reflectance distribution became more varied.

This trend was likely related to the visibly-degrading negative electrode in the CCD image. In contrast, the mean for the positive electrode decreased significantly, while the standard deviation remained relatively constant, indicating that the entire electrode was degrading, yet more uniformly.

As shown in Fig. 5.25, the negative electrode clearly underwent visible ageing during the third phase (1.8 V). The effect is consistent with previous references claiming that the negative electrode is subject to more degradation (Sec. 1). However, it seemed that this degradation did not strongly affect the reflectance change. Recall that this electrode primarily interacted with the H+ ions. Because the degradation was limited to a single electrode, we conclude that the bulk electrolyte was not the cause of the ageing, but rather the electrode surface changed. An edge effect along the outline of each electrode finger is also evident in the CCD image. The degradation is less apparent toward the lead-side of the device (toward the right in the image), as the electric field may be weaker in that area. Further, individual defect spots emerged on the CCD image and became visible on the reflectance image, as highlighted in Fig. 5.25.
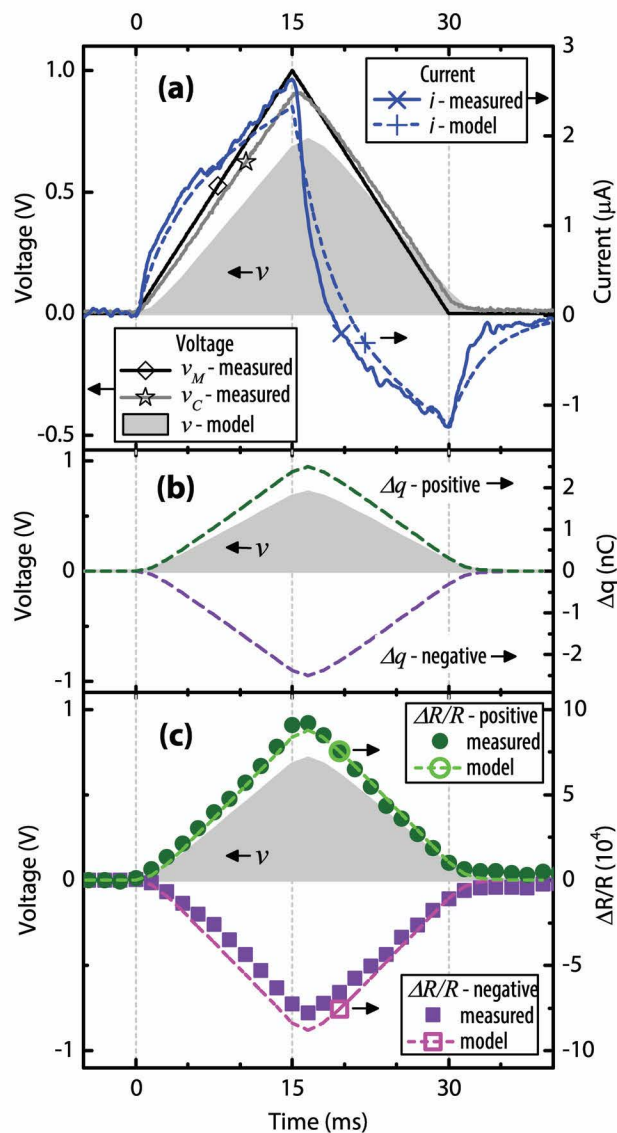
Fig. 5.10. Measured and modeled microsupercapacitor transient electrical response and electrode reflectance change during one 30 ms charge/discharge cycle. (a) Applied triangular voltage modulation, v_M, measured voltage across full sample, v_C, measured and modeled total current, i, and modeled voltage across the double layer, v, for one cycle. (See Fig.5.6 for equivalent circuit.) Fitting measured total current extracts the Randles parameters: double layer capacitance, C_{DL}, and parasitic resistances, R_S, and R_L. These parasitics cause the double layer voltage, v, to lag in time and attenuate in amplitude slightly from voltage measured across the full sample, v_C. (b) Modeled excess charge, Δq, on the positive and negative electrodes. (c) Reflectance change (measured and modeled) for the positive and negative electrodes. $\Delta R/R$ values were sampled from the mean of all pixels corresponding to the location of the rectangles indicated in the optical image of Fig.5.9a. Measured reflectance change closely follows the modeled double layer voltage. Standard deviation for measured $\Delta R/R$, v_C, and i was 7×10^{-5}, 0.09 V, and 0.1 μA respectively.
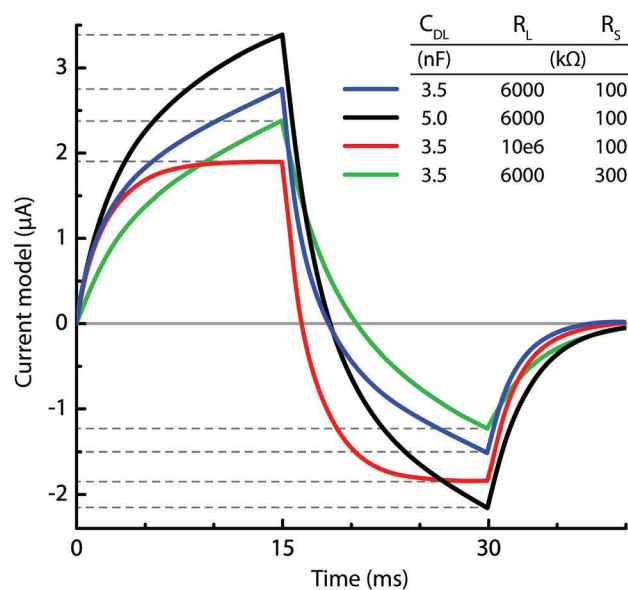
Fig. 5.11. Influence of Randles parameters on modeled current $i(t)$. Optimal fitting of the experimentally measured total current yielded: $C_{DL} = 3.5\,\mathrm{nF}$, $R_L \approx 6\,\mathrm{M\Omega}$, and $R_S = 101.2\,\mathrm{k\Omega}$.
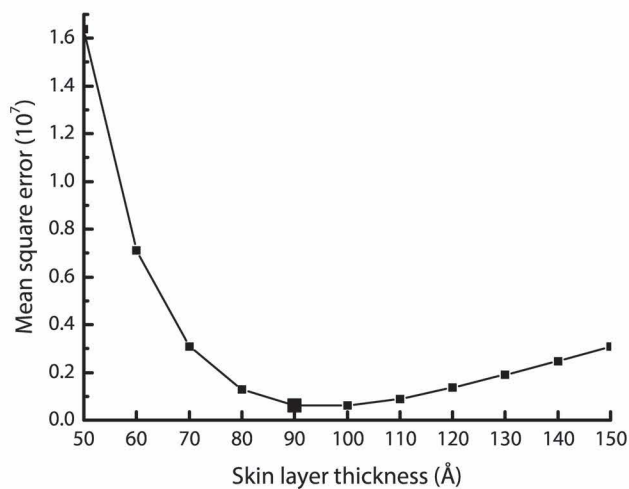
Fig. 5.12. Estimated gold electrode skin layer thickness based on fit of measured reflectance change. Estimate of 90 Å shows good agreement with Hansen et al. [158]
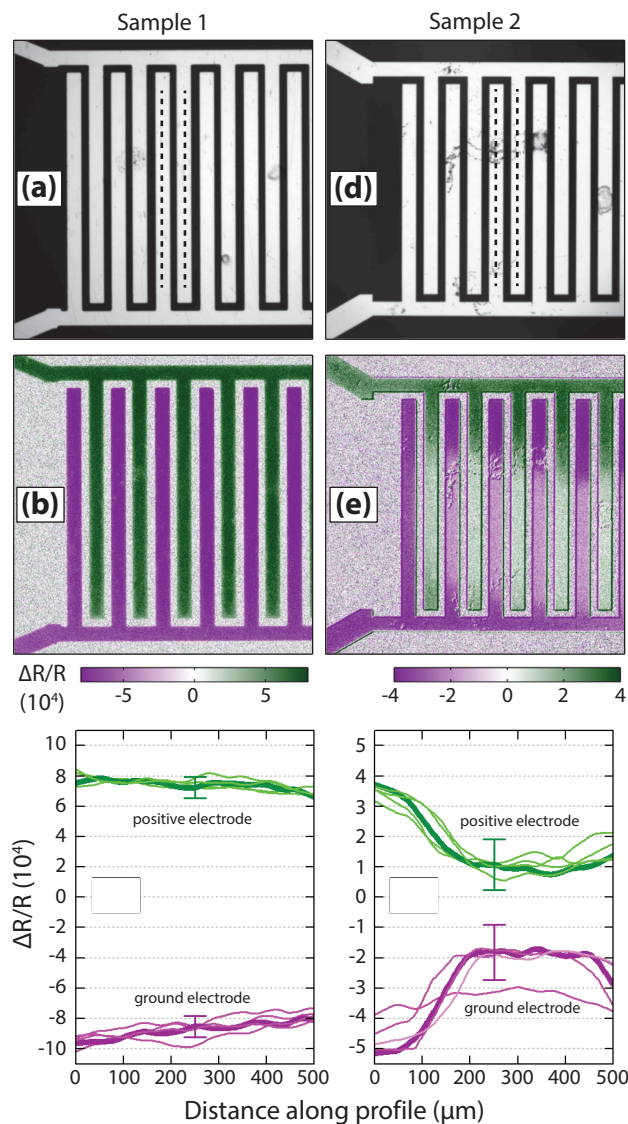
Fig. 5.13. Spatial conformity of electroreflectance distribution for two similar gold-H_3PO_4 microsupercapacitor devices under identical bias. Optical images of sample 1 and sample 2 are shown in (a) and (d). Fabrication, active area layout, and electrolyte composition are identical for both samples. Corresponding electroreflectance images at the peak of the applied voltage pulse v_M, time $= 15\,\mathrm{ms}$, are shown in (b) and (e). Reflectance change profiles for five electrode finger pairs (positive and negative) are plotted in (c) for sample 1 and (f) for sample 2. Dashed lines in the optical images show location of sampled reflectance change profiles, measured top to bottom. Third finger pair from left for each sample is emphasized in the plot. Profiles show moving average of a 10 pixel window. Error bars show maximum and minimum reflectance change in the averaging window centered at $250\,\mathrm{\mu m}$.
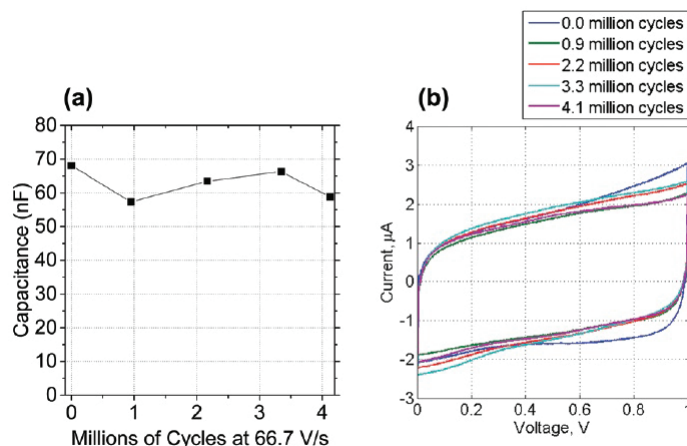
Fig. 5.14. (a) Measured capacitance and (b) CV curves at a scan rate of 25 V s^{-1} for the nominal microsupercapacitor
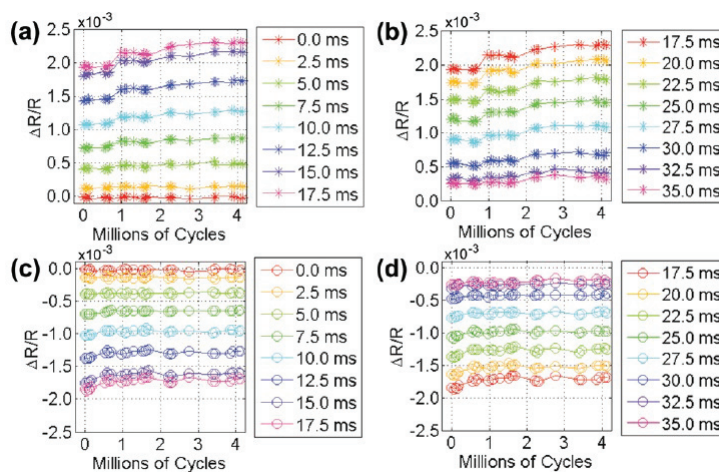
Fig. 5.15. (Mean reflectance change for positive (star) and negative (circle) electrodes during charge (left) and discharge (right) phases for the nominal microsupercapacitor. (a) Positive electrode during charge phase, (b) positive electrode during discharge phase, (c) negative electrode during charge phase, and (d) negative electrode during discharge phase. Each data point was averaged over 2000 cycles.
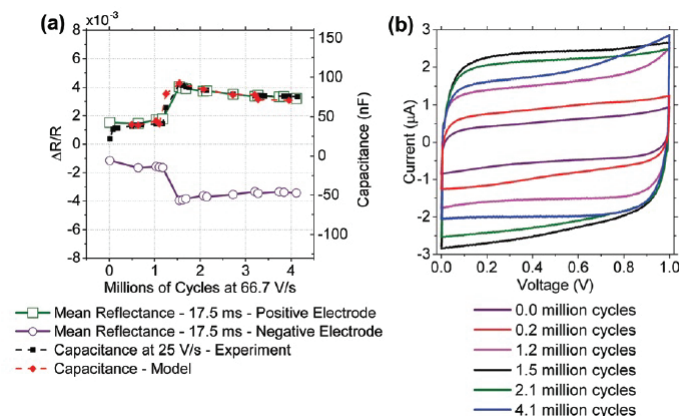
Fig. 5.16. (a) Mean reflectance change of each electrode at 17.5 ms into the voltage plse and capacitance calculated from the equivalent circuit model. The corresponding capacitance at 25 V s^{-1} is shown for comparison, measured separately with CV curves shown in (b). Data corresponds to the microsupercapacitor with burn-in behavior.
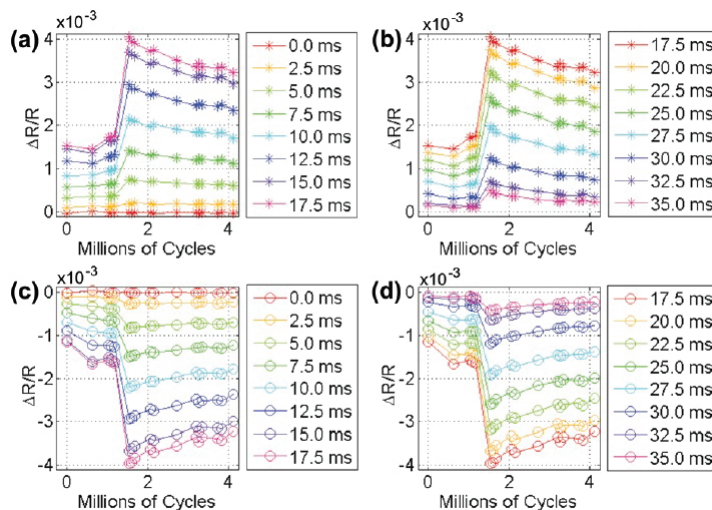
Fig. 5.17. Mean reflectance change for positive (star) and negative (circle) electrodes during charge (left) and discharge (right) phases for the microsupercapacitor with burn-in behavior. The graphs correspond to the (a) positive eelctrode during charge phase, (b) positive electrode during discharge phase, (c) negative electrode during charge phase, and (d) negative electrode during discharge phase. Each data pointis averaged over 2000 cycles.
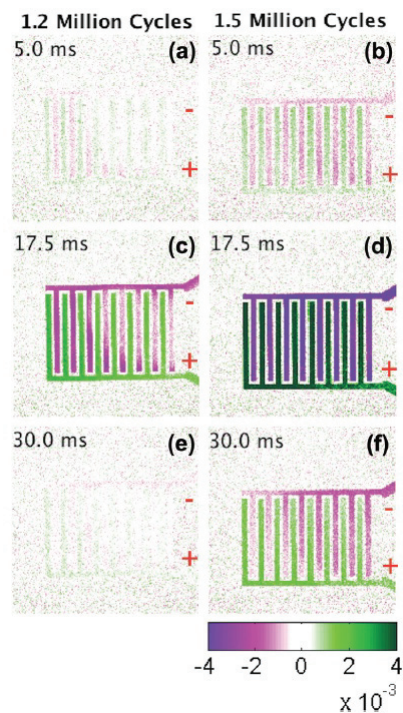
Fig. 5.18. For the microsupercapacitor with burn-in behavior, electroreflectance images before ((a,c,e)) and after ((b,d,f)) the discontinuous capacitance increase at time steps during charging (5.0 ms), charged (17.5 ms), and discharging (30.0 ms).
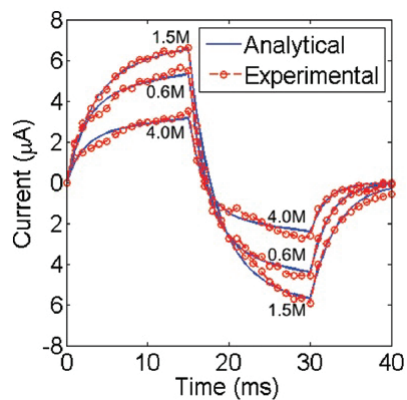
Fig. 5.19. Current and voltage profiles for various ageing conditions for the microsupercapacitor with burn-in behavior. Reported for various ageing conditions in millions of cycles.
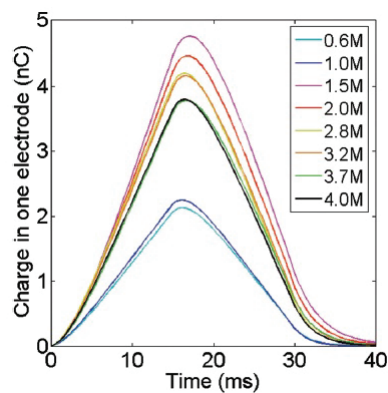
Fig. 5.20. Calculated charge accumulation in one positively charged finger electrode for the microsupercapacitor with burn-in behavior. Reported for various ageing conditions in millions of cycles.
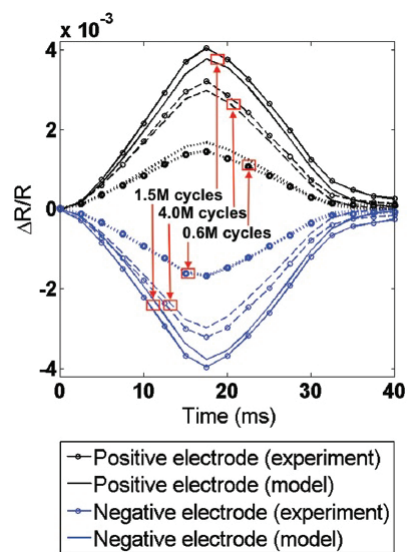
Fig. 5.21. Reflectance cahnge obtained from model and experiment for various cycling conditions of the device with burn-in behavior
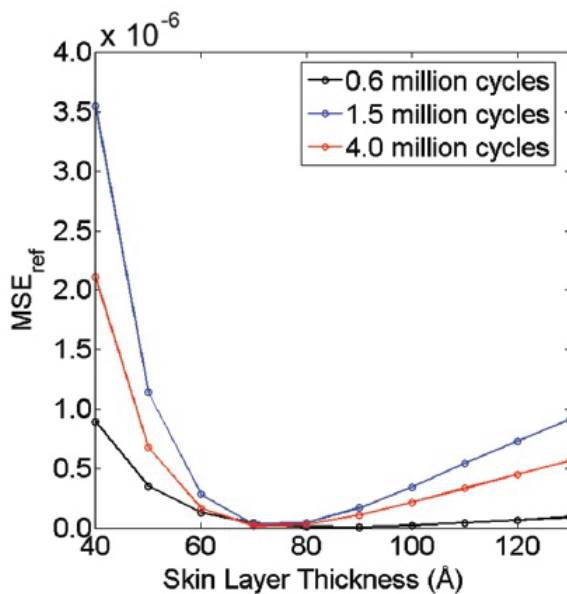
Fig. 5.22. MSE_{ref} as a function of the assumed skin layer thickness at various aging conditions.
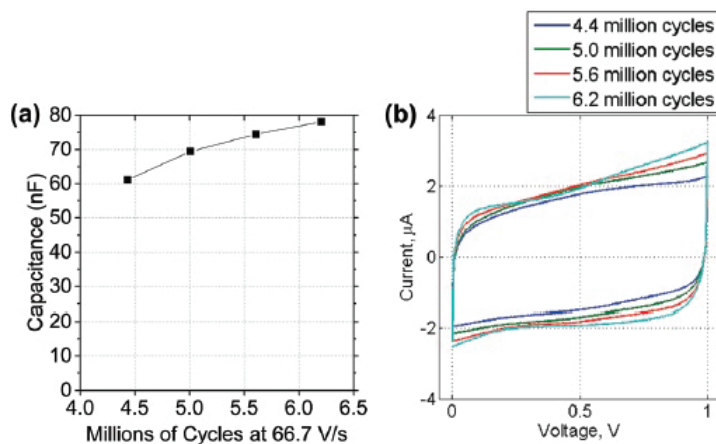
Fig. 5.23. (a) Capacitance and (b) CV curves of the nominal micro-supercapacitor durng increased-voltage cycling, all measured at 25 V s^{-1}. The applied voltage was increased after each capacitance measurement. Each sucessive data point refers to capacitance measurements after cycling at v_M=1.0 V, 1.4 V, 1.6 V and 1.8 V.
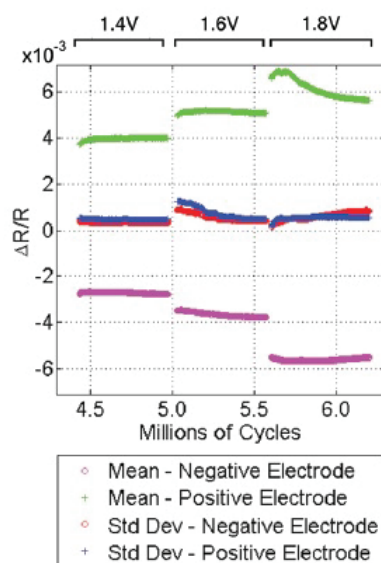
Fig. 5.24. Mean reflectance change at 16 ms into the voltage pulse during increased voltage cycling. Data were recorded for applied voltages of v_M= 1.4 V, 1.6 V and 1.8 V.
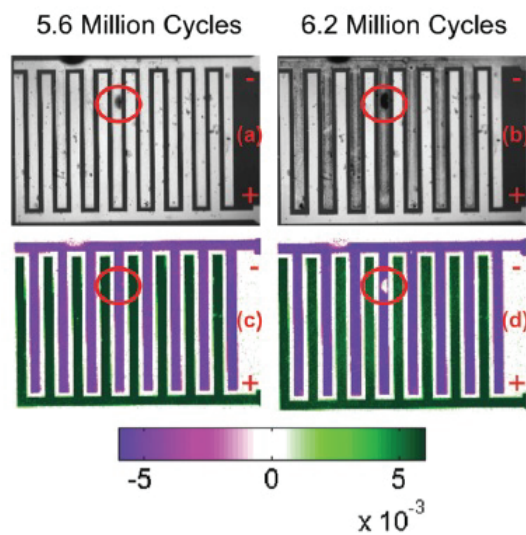
Fig. 5.25. (a,b) CCD and (c,d) relectance images (a,c) before and (b,d) after cycling with an applied voltage of 1.8 V to the test circuit during the increased-voltage experiment. Annotation highlights individual defect areas.

5.4 Conclusions

Camera-based electroreflectance imaging microscopy has been demonstrated as a highly sensitive, non-contact method for characterizing dynamic charge accumulation and distribution in active integrated electrochemical devices. Electroreflectance imaging of an interdigitated gold electrode-H_3PO_4 polymer electrolyte microsupercapacitor during active charge/discharge cycling was demonstrated with submicron spatial resolution and millisecond time resolution. The high sensitivity of the method enables electroreflectance resolution on the order of $500\,\mathrm{nC\,cm^{-2}}$, equivalent to modulation of one charge per $32\,\mathrm{nm^2}$ electrode surface area. A model relating device reflectance change to excess charge in the gold electrode, based on the microsupercapacitor equivalent circuit including parasitic electrical effects, shows good agreement with measured device electroreflectance. Results demonstrate that electroreflectance imaging can be used for rapid, high-sensitivity characterization of real time performance and spatial charge distribution in microscale integrated electrochemical devices. This paper examined effects caused primarliy by double layer capacitance at the supercapacitor gold-electrolyte interface. The method might also be used to investigate pseudocapacitance in supercapacitors and Faradaic processes in integrated batteries such as lithium ion systems. Future studies will apply the method to non-intrusive spatial analysis of electrochemical based biosensors and other systems involving nanoscale charge-dipole characteristics.

In the aging study, reflectance and CCD images were recorded over a period of 4.1 million cycles for a nominal device and a device with initial nonuniform charge behavior. The performance of the nominal device had insignificant changes in reflectance and capacitance. In contrast, the capacitor with burn-in behavior exhibited two phases of ageing behavior. The reflectance images and equivalent circuit model supported the hypothesis that the device behavior was first dominated by wetting of the electrolyte followed by ohmic leakage through the electrolyte. Next, an accelerated ageing test demonstrated that the negative electrode is impacted more greatly in

response to increased voltage, as visualized from CCD images. To complete the study, a numerical model included the relationship between electrode charge accumulation and reflectance change to predict the observed reflectance signal.

6. MAGNETOTHERMOELECTRIC EFFECTS IN GRAPHENE AND THEIR DEPENDENCE ON SCATTERER CONCENTRATION, MAGNETIC FIELD AND BAND GAP

Some of the chapter has been published in *Journal of Applied Physics* [72]

6.1 Introduction

Thermoelectric materials are capable of continuous generation of electrical energy in response to a temperature gradient without involvement of moving parts. Many prior research efforts have focused on developing new materials for practical power generation applications based on thermoelectrics since the discovery of Bi_2Te_3 in the 1950s [188]. In comparison to thermoelectric effects, thermomagnetic effects have been less studied. The Nernst (Ettingshausen) effect involves the generation of electric (heat) current in the cross product direction between a temperature gradient (electric field) and an applied magnetic field. The advantages of building a thermomagnetic conversion module have been highlighted by Sakuraba et al. [189]. Their module consisting of series-connected ferromagnetic wires has a much simpler design than the conventional thermoelectric modules consisting of alternatively aligned n- and p-type semiconductor pillars. Apart from devices, these effects have also been used as sensitive probes for studying the electronic structure of various materials [190].

Graphene is a 2D material with high electron mobility and mechanical strength [191]. These attributes make it a good candidate for thermoelectric and thermomagnetic applications. However, it has two major disadvantages in this regard. First, it is gapless and has a symmetric electronic bandstructure. Consequently, the electrons (above Dirac point) and holes (below Dirac point) have opposite group velocities and

hence they thermodiffuse in counter directions. This leads to a zero value of the Seebeck coefficient at the Dirac point. Second, it is an excellent thermal conductor, resulting in a low value of ZT [192].

However, several studies [193, 194] have demonstrated that appropriate nanostructuring and introduction of a band gap around the Dirac point can enhance the in-plane Seebeck coefficient of graphene many-fold without diminishing electrical conductivity. Xiao et al. [193] demonstrated an enhancement of Seebeck coefficient in few-layer graphene (FLG) films up to 700 μV/K upon oxygen plasma treatment, which was attributed to disorder-induced band gap opening. Furthermore Wang et al. [194] obtained a Seebeck coefficient of 180 μV/K upon introducing a band gap by applying a vertical electric field between two gates in dual-gated bilayer graphene.

Experimentally, thermoelectric and thermomagnetic measurements are performed as functions of Fermi energy E_F. The Fermi energy is tuned by varying the gate voltage and thereby controlling the charge carrier density. Depending on whether E_F is above or below the Dirac point, the system behaves either electron-like or hole-like. Most experimental studies have used single-layer graphene sheets mechanically exfoliated from highly oriented pyrolytic graphite (HOPG) [195–198]. However, a few reports exist for graphene sheets grown using chemical vapor deposition (CVD) [193, 198–201] that are then transferred onto Si/SiO$_2$ substrates.

Table1 lists the experimental parameters for Seebeck and Nernst effect measurements in the literature. In most cases, a microfabricated heater is used to create a temperature gradient in the longitudinal (in-plane) direction. Typically, a temperature difference of 80-300 mK is applied across a length of 5-10μm (Ref. [198]). The thermovoltage signal generated in the longitudinal and transverse directions is detected using a four-point method in a Hall bar geometry. Checkelsky and Ong [197] studied the thermoelectric properties of exfoliated graphene on SiO$_2$ in the presence of strong magnetic fields (5-14 T). Both Seebeck and Nernst coefficients were found to oscillate at high magnetic fields implying the formation of discrete Landau levels. An increase in magnetic field from 5 to 14 T led to a rise in the peak value of the

transverse Seebeck coefficient S_{xy} from 20 to 40 μV/K and a fall in the number of oscillations. Liu et al. [198] measured the longitudinal Seebeck coefficient S_{xx} and the transverse Seebeck coefficient S_{xy} for samples with different mobilities in magnetic fields up to 8 T. The peak in S_{xy} increased almost linearly from 22 μV/K at 1 T to 160 μV/K at 8 T, while the peak in S_{xx} rose from 70 to 100 μV/K upon increasing the magnetic field from 2 to 8 T.

Theoretical modeling of Seebeck and Nernst effects has been primarily performed using either the analytical Mott relation or the non-equilibrium Green's function (NEGF) approach. The Mott relation [195, 199, 202] predicts a linear rise in S_{xx} with temperature. Zuev et al. [195] found experimental results to follow the Mott relation in the temperature range of 10-300 K. They attributed this observation to the dominance of impurity scattering over phonon scattering. The Mott relation has been thus found to hold true only when $\frac{\gamma}{k_b T} >> 1$ [196] where γ is the impurity bandwidth proportional to the square root of impurity concentration $\gamma \propto \sqrt{n_{imp}}$ [203]. In order to avoid inaccuracies at high temperatures, many authors have used NEGF methods to model thermoelectric and magnetothermoelectric effects [204–207]. Ugarte et al. [205] included effects of unitary and charged impurities and presented results for both low and high temperatures. Although the NEGF method is more rigorous than the Mott relation, it cannot treat scattering of charged impurities at high magnetic fields.

A thorough understanding of the energy dependence of various scattering mechanisms is crucial in elucidating thermoelectric and magnetothermoelectric transport properties [198]. Different scattering mechanisms have been identified and experimentally validated for both suspended and supported graphene films. These include long range Coulomb scattering due to impurities in the SiO_2 substrate and electron-phonon scattering. Stauber et al. [208] proposed an additional scattering mechanism that may originate from vacancies, cracks or defects in the sample. They showed that incorporating this additional mechanism into the Boltzmann transport equation dramatically improved agreement between theoretical and experimental values of mobility.

In this work, we investigate the thermomagnetic and thermoelectric properties of single-layer graphene. The Boltzmann formalism has proven useful in understanding transport in graphene [209] as well as its three-dimensional counterpart, Weyl semimetals [210], and shows good agreement with other theoretical approaches such as the Kubo formalism [211]. The analytical solution to the BTE, which is valid for a 1D system within the relaxation time approximation (RTA) and near equilibrium conditions, is used to derive analytical expressions for the various transport coefficients. The mean relaxation times accounting for various scattering mechanisms have been used in the derivations. The Seebeck coefficient S_{xx} and Nernst coefficient N are thoroughly characterized as functions of impurity concentrations, temperature, carrier concentration and magnetic field, and valuable insights emerge in comparing model results with previously published experimental data. Although this technique of evaluatng thermoelectric and thermomagnetic properties has been applied to single layer periodic graphene in this paper, it can be used to study other materials in the future, given their bandstructure and scattering rate information.

The paper is organized as follows. In Sec. II, detailed formulations of the transport coefficients from the BTE solution are provided. The solution methodology and final form of the transport coefficients are presented in Sec. III. Model results are presented in Sec. IV, including parametric variations of impurity density, temperature, band gap and magnetic field.

6.2   Theory

The Nernst coefficient N is defined as [212, 213]

$$N = \frac{E_y}{-B\nabla_x T}\big|_{J_x=J_y=0},\tag{6.1}$$

where E_y is the electric field in the y direction, B is the magnetic field in the z direction, and $\nabla_x T$ is the temperature gradient in the x direction. Thus, E, B and $\Delta_x T$ are mutually perpendicular. J_x and J_y are electrical current densities in the x and y directions respectively. The transverse Seebeck coefficient S_{xy} is obtained

by multiplying the Nernst coefficient N with the magnetic field B. The longitudinal Seebeck coefficient S_{xx} is

$$S_{xx} = \frac{E_x}{-\nabla_x T}\Big|_{J_x=J_y=B=0}.\qquad(6.2)$$

In linear response theory, J_x and J_y are related to the electric field and temperature gradient as

$$J_x = \sigma_{xx}E_x + \sigma_{xy}E_y + \alpha_{xx}\nabla_x T,$$
$$J_y = \sigma_{yy}E_y + \sigma_{yx}E_x + \alpha_{yx}\nabla_x T,\qquad(6.3)$$

where σ_{xx} and σ_{xy} are the longitudinal and transverse electrical conductivities respectively, and α_{xx} and α_{xy} represent the longitudinal and transverse thermoelectric coefficients respectively. Under isotropic conditions $\sigma_{xx} = \sigma_{yy}$, $\alpha_{xx} = \alpha_{yy}$, $\sigma_{yx} = -\sigma_{xy}$ and $\alpha_{yx} = -\alpha_{xy}$. Setting the current densities to zero and using Eqs. 6.1 and 6.2, we obtain the expressions for Nernst and Seebeck coefficients as

$$N = \frac{\sigma_{xy}\alpha_{xx} - \sigma_{xx}\alpha_{xy}}{B(\sigma_{xx}^2 + \sigma_{xy}^2)},\qquad(6.4)$$

and

$$S_{xx} = \frac{\sigma_{xx}\alpha_{xx} + \sigma_{xy}\alpha_{xy}}{\sigma_{xx}^2 + \alpha_{xy}^2}.\qquad(6.5)$$

The electronic states in periodic graphene at the six corners K and K of the first Brillouin zone have a linear dispersion relation $(k) = \pm\hbar v_F|k| = \pm\hbar v_F \sqrt{k_x^2 + k_y^2}$, where v_F is the Fermi velocity (assumed to be 1×10^6 m/s [214, 215]). The density of states is

$$D(\ ) = \frac{2|\ |}{\pi\hbar^2 v_F^2}.\qquad(6.6)$$

The semiclassical Boltzmann transport equation (BTE) with the relaxation time approximation is

$$\frac{\partial f_{\mathbf{k}}}{\partial t} + v_{\mathbf{k}}\cdot\nabla_{\mathbf{r}}f_{\mathbf{k}} + F_e\cdot\nabla_{\mathbf{p}}f_{\mathbf{k}} = -\frac{f_{\mathbf{k}} - f_{eq}}{\tau_m},\qquad(6.7)$$

where $f_{\mathbf{k}}$ is the probability density function of carriers with wave vector $\mathbf{k}$, f_{eq} is the equilibrium Fermi-Dirac distribution, τ_m is the mean relaxation time, $v_{\mathbf{k}}$ is the

group velocity $v_{\mathbf{k}}=\hbar^{-1}\partial\epsilon/\partial\mathbf{k}$, and F_e is the force field. In the presence of electric and magnetic fields, the force field is

$$F_e = eE + e\vec{v} \times B. \tag{6.8}$$

The 1D steady state linearized solution of the BTE in the absence of magnetic field $(B = 0)$ is [216]

$$f_{\mathbf{k}} = f_{eq} + \tau_m(-\frac{\partial f_{eq}}{\partial\epsilon})v_{\mathbf{k}}.(-e\mathbf{E} + \frac{-\mu}{T}(-\nabla\mathbf{T})) \tag{6.9}$$

at near-equilibrium conditions. The resulting current density (J_x) assuming spin degeneracy is

$$J_x = 2 \sum_p \sum_k ev_x.f_{\mathbf{k}}, \tag{6.10}$$

where the factor of 2 represents spin degeneracy and p represents summation over all branches. From Eqs. 6.3, 6.9 and 6.10 we obtain

$$\sigma_{xx} = 4e^2 \int [\mathbf{dk}]v_x^2\tau_m(-\frac{\partial f_{eq}}{\partial\epsilon}), \tag{6.11}$$

$$\alpha_{xx} = -\frac{4e}{T} \int [\mathbf{dk}]v_x^2\tau_m(\ -\mu)(-\frac{\partial f_{eq}}{\partial\epsilon}), \tag{6.12}$$

where $[\mathbf{dk}] = \frac{d^2k}{(2\pi)^2} = \frac{kdk}{2\pi}$.

We now discuss the case of a perpendicular magnetic field $B\hat{z}$ in the presence of a londitudinal thermal gradient $\nabla_x T\hat{x}$. The Boltzmann equation is modified in the following form to account for the influence of the magnetic field [210]

$$f_{\mathbf{k}} = f_{eq} + (-\frac{\partial f_{eq}}{\partial\epsilon})(\tau_m v_x \frac{-\mu}{T}(-\nabla_x T) + v_x\Lambda_x + v_y\Lambda_y). \tag{6.13}$$

The correction factors Λ_x and Λ_y have been derived [210] by satisfying the steady state form of Eq. 6.7 while using the force field from Eq. 6.8

$$\Lambda_x = eB\tau_m\nabla_x T\frac{-\mu}{T}\frac{[\frac{v_x}{m_{xy}} - \frac{v_y}{m}][-\frac{eBv_y}{m} + \frac{eBv_x}{m_{xy}} - \frac{v_x}{\tau_m}] + [\frac{v_x}{m} + \frac{v_y}{m_{xy}}][\frac{eBv_x}{m} - \frac{eBv_y}{m_{xy}} - \frac{v_y}{\tau_m}]}{[-\frac{eBv_y}{m} + \frac{eBv_x}{m_{xy}} - \frac{v_x}{\tau_m}]^2 + [\frac{eBv_x}{m} - \frac{eBv_y}{m_{xy}} - \frac{v_y}{\tau_m}]^2}, \tag{6.14}$$

$$\Lambda_y = eB\tau_m \nabla_x T \frac{-\mu}{T} \frac{[\frac{v_x}{m_{xy}} - \frac{v_y}{m}][-\frac{eBv_y}{m_{xy}} + \frac{eBv_x}{m} - \frac{v_y}{\tau_m}] - [\frac{v_x}{m} + \frac{v_y}{m_{xy}}][-\frac{eBv_y}{m} + \frac{eBv_x}{m_{xy}} - \frac{v_x}{\tau_m}]}{[-\frac{eBv_y}{m} + \frac{eBv_x}{m_{xy}} - \frac{v_x}{\tau_m}]^2 + [\frac{eBv_x}{m} - \frac{eBv_y}{m_{xy}} - \frac{v_y}{\tau_m}]^2}.$$

$$(6.15)$$

Considering only linear terms in B

$$\Lambda_i = \tau_m \nabla_x T \frac{-\mu}{T} c_i, \qquad (6.16)$$

where $c_x = -\frac{eB\tau_m}{m_{xy}}$ and $c_y = \frac{eB\tau_m}{m}$. The band mass m_{ij} is defined as $m_{ij}^{-1} = \hbar^{-2}\partial^2 (k)/\partial k_i \partial k_j$. Using Eqs.6.3, 6.10 and 6.13, the thermoelectric coefficients (longitudinal and transverse) are

$$\alpha_{xx} = -\frac{4e}{T} \quad [\mathbf{dk}] v_x^2 \tau_m (-\mu)(-\frac{\partial f_{eq}}{\partial \epsilon})(1 + \frac{eB\tau_m}{m_{xy}}), \qquad (6.17)$$

$$\alpha_{xy} = -\frac{4e}{T} \quad [\mathbf{dk}](-\mu)\tau_m(-\frac{\partial f_{eq}}{\partial \epsilon})eB\tau_m(\frac{v_y^2}{m} - \frac{v_x v_y}{m_{xy}}), \qquad (6.18)$$

Similarly, the electrical conductivity coefficients (longitudinal and transverse) can be shown to be

$$\sigma_{xx} = 4e^2 \quad [\mathbf{dk}] v_x^2 \tau_m(-\frac{\partial f_{eq}}{\partial \epsilon})(1 + \frac{eB\tau_m}{m_{xy}}), \qquad (6.19)$$

$$\sigma_{xy} = 4e^2 \quad [\mathbf{dk}] \tau_m(-\frac{\partial f_{eq}}{\partial \epsilon})eB\tau_m(\frac{v_y^2}{m} - \frac{v_x v_y}{m_{xy}}), \qquad (6.20)$$

under the isotropic approximation $v_x = v_y = v_F/\sqrt{2}$ and $k_x = k_y = k/\sqrt{2}$.

We now discuss the various scattering mechanisms that have been considered in the analysis. Scattering due to long-range Coulomb scatterers in the Si/SiO$_2$ substrate exhibits a linear dependence with k [208]

$$\tau_{imp}(k) = \frac{16\hbar^2 v_F{}_0^2{}_r^2(1+\gamma)^2|k|}{n_{imp}Z^2 e^4}, \qquad (6.21)$$

where Z is the valency of the charged impurities considered to be 1, and n_{imp} is the charged impurity concentration. Acoustic phonon scattering time varies inversely with k [208]

$$\tau_{AP}(k) = \frac{8\hbar^2 \rho v_s^2 v_F}{D_A^2 k_b T |k|}, \qquad (6.22)$$

$\tau_{AP,LA}$ and $\tau_{AP,TA}$ correspond to scattering with acoustic phonons of LA and TA branches respectively. ρ is the mass per unit area $(7.6\times 10^{-7} \text{ kg/m}^2)$ and v_s is the

group velocity (7333 m/s and 2820 m/s) for the LA and TA phonon branches (respectively). D_A is the acoustic deformation potential, which generally varies with carrier concentration but is assumed constant for simplicity in many studies. Bolotin et al. [214] found D_A to be 29 eV for ultraclean suspended graphene compared to 17 eV reported for unsuspended graphene [217]. On the other hand, Stauber et al. [208] assumed D_A to be 9 eV. In this study, D_A has been assumed to be 17 eV because unsuspended graphene is considered. Electron scattering with optical phonons are expected to have negligible contribution to the net scattering rate because the usual energy of optical phonons is in the range of 0.1-0.2 eV for graphene-related materials [208], thus diminishing their interactions with low energy scatterers. Electron-electron scattering has been neglected considering Born approximation. Acoustic phonon scattering and substrate impurity scattering have only been considered in the mean relaxation time for comparison with experimental findings in a few studies [218, 219]. However, Stauber et al. [208] criticises this assumption because of the high density of charged impurities $n_{imp} > 10^{12}$ cm^{-2} needed in the Boltzmann formalism to obtain the experimentally observed mobilities, that are not likely to be present in an insulator like SiO$_2$. Based on this argument, they proposed an additional scattering mechanism due to midgap states that may be caused by vacancies present in the substrate. The scattering time of this mechanism is proportonal to k up to logarithmic corrections

$$\tau_{vac}(k) = \frac{|k|(ln(|k|R_0)^2}{\pi^2 v_F n_{vac}}, \tag{6.23}$$

where n_{vac} is the concentration of vacancies, cracks or boundaries in the sample [208], and R_0 is the average radius of vacancies assumed to be 1.4 Å. On consideration of the foregoing three scattering mechanisms, a low impurity density of $n_{imp} \approx 10^{11}$ cm^{-2} is able to justify the experimentally observed mobilities of $\mu \approx 5000$ cm^2/(V.s). The mean relaxation time τ_m is finally obtained using Matthiesen's rule

$$\frac{1}{\tau_m} = \frac{1}{\tau_{AP,LA}} + \frac{1}{\tau_{AP,TA}} + \frac{1}{\tau_{imp}} + \frac{1}{\tau_{vac}}. \tag{6.24}$$

Combining Eqs. 6.21-24, τ_m is expressed as

$$\frac{1}{\tau_m(k)} = \frac{a_1}{|k|} + a_2|k| + \frac{a_3}{|k|(ln(|k|R_0))^2}, \tag{6.25}$$

where a_1, a_2 and a_3 are independent of k. τ_m is used in the Boltzmann formalism to obtain new expressions for the transport coefficients. To demonstrate the effect of an introduced bandgap, the following dispersion relation is assumed [220]

$$(k) = \pm \overline{(\hbar^2 v_F^2 |k|^2 + \quad{}^2)}, \tag{6.26}$$

where   is the bandgap. Such a dispersion equation has been assumed to produce the bandstructure of Dirac systems possessing a band gap. In the above equation,   has a minimum value of   at zero Fermi energy (k=0), and it follows the dispersion relation of graphene at high k values, considering   to be quite small. The group velocity for such a dispersion relation has an energy dependence of

$$v(\ ) = v_F \ \overline{1 - \frac{{}^2}{{}^2}}. \tag{6.27}$$

For a non-zero band gap, the transport coefficients are obtained by energy integration from $-\infty$ to $+\infty$ while omitting the range from $-$ to $+$, because the density of states is zero in that zone. Eq. A-4 in the Appendix contains the final expression of the longitudinal conductivity σ_{xx} for such a system.

6.3   Solution Methodology

Eqs. 6.28-6.31 shown below represent the final form of the electrical conductivities and thermoelectric coefficients used throughout the subsequent sections of the paper.

$$
\begin{aligned}
\sigma_{xx} =& \frac{e^2}{\pi\hbar} \frac{E_F^2 |k_F|}{4\hbar k_b T} \int_0^\infty \frac{x^2 (cosh^{-2}(\frac{E_F}{2k_b T}(x-1)) + cosh^{-2}(\frac{E_F}{2k_b T}(x+1)))}{(a_1 + a_2 k_F^2 x^2 + \frac{a_3}{|ln(k_F x R_0)|^2})} dx \\
&- \frac{e^2}{\pi\hbar} \frac{eB v_F^3 k_F^3}{8k_b T} \int_0^\infty \frac{x^2 (cosh^{-2}(\frac{E_F}{2k_b T}(x-1)) - cosh^{-2}(\frac{E_F}{2k_b T}(x+1)))}{(a_1 + a_2 k_F^2 x^2 + \frac{a_3}{|ln(k_F x R_0)|^2})^2},
\end{aligned}
\tag{6.28}
$$

$$
\sigma_{xy} = \frac{e^2}{\pi\hbar} \frac{eB v_F^3 k_F^3}{4k_b T} \int_0^\infty \frac{x^2 (cosh^{-2}(\frac{E_F}{2k_b T}(x-1)) - cosh^{-2}(\frac{E_F}{2k_b T}(x+1)))}{(a_1 + a_2 k_F^2 x^2 + \frac{a_3}{(ln(k_F x R_0))^2})^2} dx, \tag{6.29}
$$

$$\alpha_{xx} = \frac{e^2}{\pi\hbar} \frac{v_F^2 h |k_F|^3 E_F}{8\pi e k_b T^2} \int_0^\infty \frac{x^2(x-1)cosh^{-2}(\frac{E_F}{2k_bT}(x-1)) - x^2(x+1)cosh^{-2}(\frac{E_F}{2k_bT}(x+1))}{(a_1 + a_2 k_F^2 x^2 + \frac{a_3}{(ln(k_F x R_0))^2})} dx$$

$$- \frac{e^2}{\pi\hbar} \frac{B v_F^3 |k_F|^3 E_F}{8 k_b T^2} \int_0^\infty \frac{x^2(x-1)cosh^{-2}(\frac{E_F}{2k_bT}(x-1)) + x^2(x+1)cosh^{-2}(\frac{E_F}{2k_bT}(x+1))}{(a_1 + a_2 k_F^2 x^2 + \frac{a_3}{(ln(k_F x R_0))^2})^2} dx,$$

$$(6.30)$$

$$\alpha_{xy} = \frac{e^2}{\pi\hbar} \frac{v_F^3 B E_F |k_F|^4}{4 k_b T^2 k_F} \int_0^\infty \frac{x^2(x-1)cosh^{-2}(\frac{E_F}{2k_bT}(x-1)) + x^2(x+1)cosh^{-2}(\frac{E_F}{2k_bT}(x+1))}{(a_1 + a_2 k_F^2 x^2 + \frac{a_3}{(ln(k_F x R_0))^2})^2} dx.$$

$$(6.31)$$

The constants a_1, a_2 and a_3 are given by

$$a_1 = \frac{n_{imp} Z^2 e^4}{16 \hbar^2 v_F^2 \epsilon_0^2 \epsilon_r^2 (1+\gamma)^2},$$

$$a_2 = \frac{D_A^2 k_b T (1/v_{s,LA}^2 + 1/v_{s,TA}^2)}{8 \hbar^2 \rho v_F}, \qquad\qquad (6.32)$$

$$a_3 = \pi^2 v_F n_{vac}.$$

A sample derivation of σ_{xx} is given in the Appendix. In these expressions, the integration variable x represents the normalized energy ϵ/E_F where E_F is the Fermi energy. The integrations are carried out using the trapezoidal rule. A step size of 10^{-4} is used for x after mesh refinement analysis. The upper limit of ∞ in the integrations is taken as 10 to make them computationally efficient without affecting the results.

Experimentally, the carrier concentration is controlled by varying the gate voltage (V_g) in a parallel plate geometry. For the experimental range of parameters used, it is generally assumed that the capacitance of the device is constant and the carrier density depends linearly on the gate voltage as $n = C_g V_g/e$, where the gate capacitance C_g is the capacitance per unit area generally in the range of 100-115 aF/μm^2 [196, 198, 199]. Here we assume C_g to have a value of 100 aF/μm^2. The Fermi energy E_F is related to the carrier density n by $E_F = \hbar v_F \sqrt{\pi n}$ [196].

6.4 Results and Discussions

We first consider the electrical conductivity coefficients at zero magnetic field. Fig. 6.1(a) shows the temperature dependence of the scattering rates. Fig. 6.1(b)

displays the temperature dependence of mobility μ calculated using the Drude relation $\sigma_{xx} = \mu n e$ near the Dirac point. The charged impurity scattering rate and vacancy scattering rate remain constant with temperature while the phonon scattering rate increases linearly with temperature, as indicated by Eqs. 6.21-6.23. Thus, at low temperature and high impurity concentrations, τ_m does not contain significant contributions from phonon scattering, and hence the conductivity and mobility are effectively independent of temperature. The mobility remains almost constant with temperature up to about 50 K, after which it decreases. This is consistent with experiments conducted by Chen et al. [217] and Zhu et al. [221] for single-layer graphene. Thus, for samples with high impurity concentrations, impurity scattering dominates the determination of conductivity at low temperatures while phonon scattering dominates at high temperatures. Conversely, for samples with low impurity concentrations such as highly oriented pyrolitic graphite studied by Sugihara et al. [222], the mobility decreases almost linearly with temperature even at temperatures below 50 K.

The room-temperature value of conductivity is important for many practical applications; therefore the conductivity at 300 K has been evaluated and is shown in Fig. S23 for Fermi energy 0.1 eV. The charged impurity and vacancy concentrations have been kept equal and varied along the x-axis. The room-temperature conductivity remains constant at $15e^2/(\pi\hbar)$ for charged impurity concentrations up to 10^{10} cm^{-2}, after which it decays. This result implies that the room-temperature conductivity is primarily influenced by phonon scattering and not by impurity scattering if the concentration of impurities is below a threshold value. Furthermore, the charged impurity and vacancy concentrations have been varied separately, and the results are tabulated in the inset of Fig. S23. An increase in the vacancy concentration at a fixed charged impurity concentration leads to a greater reduction in room-temperature conductivity compared to an equivalent increase in the value of charged impurity concentration at a fixed vacancy concentration, as can be inferred from Eqs. 6.21 and 6.23..

The Boltzmann transport formalism predicts the electrical conductivity to fall to zero at the Dirac point (E_F=0). Experimentally however, it is found to have a non-

zero σ_{min}. Tan et al. [219] reported that almost all measured σ_{min} lie in the range of $1\text{-}6e^2/(\pi\hbar)$. They justify this observation by the fact that in the low carrier density limit near the Dirac point where the carrier concentration becomes smaller than the charged impurity density, the system breaks up into puddles of electrons and holes in which a duality in two dimensions guarantees that, locally, transport occurs either through the hole channel or the electron channel. Most samples are reported to have $\sigma_{min} \approx 2e^2/(\pi\hbar)$ [218]. Because we have no way to include such physics in our model, the value of σ_{xx} is artificially raised by a value of $2e^2/(\pi\hbar)$ in the carrier density range $|n| < |n_{imp}|$.

Fig. 6.2 shows the variation of σ_{xx} with Fermi energy E_F for different impurity concentrations and compares it with the experimental results of Liu et al. [198]. σ_{xx} varies symmetrically around the Dirac point both in the model and experimental results, although unlike the experimental results, the model values deviate from parabolic behavior at high E_F.

Next, we evaluate the influence of magnetic field on the conductivity values. At non-zero magnetic field, the Lorentz force leads to bending trajectories of thermally diffusing carriers. At zero magnetic field, the Lorentz force is absent and both the Hall conductivity σ_{xy} and Nernst coefficient N are zero, while σ_{xx} varies symmetrically with Fermi energy E_F around the Dirac point. Eq. 6.29 shows that at non-zero magnetic field, σ_{xy} behaves as an odd function of E_F. Also, Eq. 6.28 shows that σ_{xx} loses its symmetry with E_F around the Dirac point. A similar trend is observed in experiments conducted by Cho et al. [223] , but the applied field is 8 T, which might lead to discrete Landau levels not considered in the present model.

The expressions for α_{xx} and α_{xy} shown in Eqs. (30) and (31) respectively explain certain characteristics about the variation of the Seebeck coefficient S_{xx} and the Nernst coefficient N. At zero magnetic field, σ_{xy} and α_{xy} are zero. Hence from Eqs. (4) and (5), N is zero and S_{xx} is simply α_{xx}/σ_{xx}. Also, α_{xx} and σ_{xx} are odd and even functions of E_F respectively which leads to S_{xx} being odd function of E_F.

Next, we compare the model results for S_{xx} and N obtained from Eqs.(4),(5), and (28)-(31) to available experimental results of Liu et al. [198]. The purpose of the fitting study is to make a qualitative comparison between model and experiment and determine the unknown values of scatterer concentrations through fitting. Fitting studies are done in the literature primarily by comparing only mobilities. Conversely, we chose to perform the fitting study for mobility as well as Nernst and Seebeck coefficients. It is noteworthy from the experiments that although the mobility of the tested graphene devices were all different, the scatterer concentrations in the devices were largely unknown. Hence a comparison with the model results may provide an approximate value of the scatterer concentration in the samples. The model results have been compared to measurements on one of the samples (mobility 12900 cm^2 V^{-1} s^{-1}) for validation in Fig. 6.3. In the experiment, S_{xx} was found to be positive below the Dirac point (holes as charge carriers), zero at the Dirac point, and negative above the Dirac point (electrons as charge carriers). Similar trends are observed in the model results plotted in the same figure. As the magnitude of E_F is raised from zero, the magnitude of S_{xx} increases, reaches a maximum, and then decreases. Comparing the model results to the experiments, impurity and vacancy concentrations of 10^{11} cm^{-2} provide the best match.

For both experiment and model, the Nernst coefficient N reaches its peak value near zero E_F and decays slowly with increasing Fermi energy E_F to a negative value before rising back to a positive value at very high E_F. Close to the Dirac point, the electrons and holes produce an additive effect on the Nernst coefficient as they are deflected in opposite directions under a magnetic field and thereby add to the transverse voltage. At high E_F, the asymptotic decay is predicted by Fermi liquid theory according to which N vanishes due to Sondheimer's cancellation [210, 224]. Comparing model with experiment, the decay in N upon moving away from zero E_F is observed to be steeper in the experiment than in the model. Impurity and vacancy densities of 2.5×10^{11} cm^{-2} provide the best match with experimental results.

To summarize, the variations of the Seebeck and Nernst coefficients with Fermi energy qualitatively match those obtained from past experiments. The impurity concentrations obtained from our fitting process (2.5×10^{11} cm^{-2} for the Nernst coefficient and 10^{11} cm^{-2} for the Seebeck coefficient) are close to the value of the Coulomb scatter density (4×10^{11} cm^{-2}) evaluated to fit the experimental value of mobility in Ref. [208].

6.4.1   Nernst Coefficient

In this section, the influence of impurity concentration and temperature on the Nernst coefficient is studied. The magnetic field is considered to be 1 T because we have neglected higher order terms in B in the transport coefficient calculations. Under high magnetic fields, the electronic band structure breaks down into discrete Landau levels, and such effects are not considered in our analysis. Fig. 6.4 shows variation of the Nernst coefficient N with Fermi energy for graphene samples with different impurity concentrations at 300 K. The peak value of N decreases with increasing impurity concentration. The peak values are 50, 20, 11 and 7 μV K^{-1}T^{-1}for impurity concentrations of 2.5×10^{11} cm^{-2}, 5×10^{11} cm^{-2}, 7.5×10^{11} cm^{-2} and 10^{12} cm^{-2} respectively. Moreover, as the impurity concentration decreases, the full width at half maximum (FWHM) decreases. The trends are consistent with the experimental results of Liu et al. [198] who found the Nernst signal S_{xy} to increase almost linearly with mobility. Mobility of devices decreases with increased impurity concentration as shown in Fig. 6.1b and 6.2.

The only related prior study on the temperature dependence of N is that of Wei et al. [196]. Their experiments on mechanically exfoliated graphene showed a reduction in oscillations of N and a rise in peak values with increasing temperature. A rigorous analysis of the influence of temperature needs to be conducted. Fig. 6.5 shows the variation in N from 10 to 400 K for samples with impurity concentrations of 2.5×10^{11} cm^{-2} and 5×10^{11} cm^{-2}. The shape of the curves change slightly with

increasing temperature. At low temperatures, the curve is quite flat, and N remains positive for almost all values of E_F. But as temperature increases, N attains higher positive peaks for low E_F values. In Fig. 6.5(a), the peak value rises from 5 to 54 μV K^{-1}T^{-1} upon varying temperature from 10 to 200 K and then slightly decreases to 40 μV K $^{-1}$T^{-1} at 400 K. On the other hand, in Fig. 6.5(b), N increases from 1 to 20 μV K^{-1}T^{-1} from 10 to 300 K and then declines to 19 μV K^{-1}T^{-1}at 400 K. The temperature dependence of N is shown for different values of impurity concentrations at a fixed E_F of 0.05 eV in Fig. 6.6(a). At the lowest impurity concentration, N increases rapidly from 4 to 37 μV K^{-1}T^{-1} after which it decreases slightly to 28 μV K^{-1}T^{-1} at 400 K. For higher impurity concentrations, N increases at a slower pace with temperature until 300 K, after which it saturates. The trends in Fig. 6.6(b) showing the variation of N with temperature for different values of Fermi energy at a fixed impurity concentration are similar.

The temperature dependence of the Nernst coefficient can be explained through analysis of the equations derived in the paper. From Eq. 6.4, the Nernst coefficient can be defined as $N = -\alpha_{xy}/B\sigma_{xx}$ neglecting the contribution of the other terms. From Eq. 6.18 and 6.19, N can be approximated as

$$N = constant \times \frac{[\mathbf{dk}](\epsilon - \mu)(-\frac{\partial f_{eq}}{\partial \epsilon})\tau_m}{T \ [\mathbf{dk}](-\frac{\partial f_{eq}}{\partial \epsilon})}. \tag{6.33}$$

From Eq. 6.24, τ_m can be approximated as,

$$\tau_m = 1/(k_2 n_{imp} + k_3 T + k_4) \tag{6.34}$$

where k_2, k_3 and k_4 are constants. At low temperatures, the Fermi-Dirac function f_{eq} has a sharp peak at $\epsilon = \mu$ which leads to almost zero value of N. As temperature increases, f_{eq} starts to spread out, causing the numerator of Eq. 6.33 to increase more rapidly than the temperature term in the denominator. At even higher temperature, the numerator term saturates while the scattering rate of acoustic phonons decreases rapidly leading to overall reduced scattering rate. This leads to a decline in the value of N at very high temperature. The temperature corresponding to peak value of N

can be evaluated by setting the temperature derivative of Eq. 6.33 to zero, yielding $T_{peak} = k_2 n_{imp}/2k_3$. Thus, T_{peak} is small for low impurity density whereas it is high for large impurity density.

Fig. 6.7 displays variations in N with Fermi energy for different values of band gap . Introducing a band gap leads to a decrease in the peak value of N, from 50 μV K^{-1}T^{-1} at =0 to 13 μV K^{-1}T^{-1}at =100 meV. Also, the Fermi energy values corresponding to the peak values are found to be near the bottom of the conduction band. This can be explained by the fact that for Fermi energy in the range of - to , the density of states of both electrons and holes is zero, which implies relatively few carriers undergoing deflection due to magnetic field.

6.4.2 Seebeck Coefficient

Fig. 6.8 shows the Seebeck coefficient S_{xx} as a function of Fermi Energy E_F for various charged impurity and vacancy concentrations. The peak values of S_{xx} are lower for higher concentrations. They decrease from 60 μV/K at 10^{11} cm^{-2} to 46 μV/K at 10^{12} cm^{-2}. Furthermore, at high impurity concentrations, the curves are found to exhibit a smoother transition (over a larger E_F) from positive to negative near the Dirac point. These trends are consistent with experimental results [198] as well as with tight binding model results [225]. Liu et al. [198] observed that S_{xx} increases from 50 to 75 μV/K with increased mobility from 4560 to 12900 cm^2 V^{-1} s^{-1} . Hao et al. [225] found that as the impurity density is raised from 0 to 5×10^{12} cm^{-2}, the peak Seebeck coefficient is found to occur at higher values of Fermi energy.

Fig 6.9 shows the Seebeck coefficient S_{xx} as a function of Fermi energy E_F for different operating temperatures. The impurity concentration is kept fixed at 2.5 $\times 10^{11}$ cm^{-2}. S_{xx} increases monotonically with temperature initially but decreases eventually. Such behavior can be inferred from an analysis of Eqs. (17) and (19). S_{xx} derived from these equations is

$$S_{xx} = constant \times \frac{[\mathbf{dk}](- \mu)(-\frac{\partial f_{eq}}{\partial \epsilon})}{T \ [\mathbf{dk}](-\frac{\partial f_{eq}}{\partial \epsilon})} \tag{6.35}$$

At near-zero temperature, the Fermi-Dirac function has a very sharp peak at $\epsilon = \mu$ which leads to almost zero S_{xx}. However with rise in temperature, the Fermi Dirac function spreads out and covers more number of energy levels which all contribute to the term ($\epsilon - \mu$). This increase dominates over the temperature term in the denominator and consequently, S_{xx} increases monotonically with temperature. However, S_{xx} peaks at 300 K (shown in the inset of Fig. 6.9), because the contribution of the Fermi-Dirac function saturates compared to the temperature term in the denominator.

The foregoing results suggest that the Seebeck coefficient is limited to around 60 μV/K at zero magnetic field, as has also been confirmed experimentally. We also consider the possibility of accentuating the Seebeck coefficient S_{xx} by applying a perpendicular magnetic field or introducing a band gap. Fig. 6.10 shows the variation of S_{xx} with Fermi energy E_F at different values of magnetic field, from -1 to +1 T. The curves become asymmetric upon applying a magnetic field although they all cross zero at the Dirac point. At negative magnetic field, the peak is $\sim$71 μV/K in the negative Fermi energy region and $\sim$-54 μV/K in the positive region. The trend reverses upon changing the direction of magnetic field. Thus applying a magnetic field of 1 T can accentuate the peak Seebeck coefficient from 60 to 71 μV/K.

Previous experimental [193] and theoretical [220] studies have shown that the introduction of a band gap accentuates the Seebeck coefficient S_{xx}. Fig. 6.11 and 6.12 show the effect of band gap from 0 to 100 meV at zero magnetic field. In Fig. 6.11, S_{xx} is observed to rise with increasing band gap at all E_F values. The inset shows similar trends obtained using a Green's function formalism for graphene nanoribbons in the positive Fermi energy regime [226]. The shape of the curves is similar to that of our study. Fig. 6.12 indicates that the peak value of S_{xx} increases linearly with band gap, following the trend of previous studies [220, 226]. This result is expected because upon introduction of a band gap, the electrons and holes no longer nullify each other near the band edge, thus producing a higher value of S_{xx}. The linear

relationship between the maximum Seebeck coefficient and band gap conforms with the theoretical prediction of Goldsmid et al. [227] for a general semiconductor.

6.5   Conclusions

In summary, an analytical solution to the BTE has been used to derive the electric and thermoelectric transport coefficients of single-layer periodic graphene both in the presence and absence of magnetic field. By incorporating phonon, charged impurity and vacancy scattering mechanisms into the analysis, we are able to replicate experimentally measured results qualitatively, and also quantitatively to some degree. Impurity concentration is found to be a critical factor in determining the thermoelectric and thermomagnetic transport coefficients. The results include specific predictions for the Seebeck and Nernst coefficients, some of which remain to be verified experimentlally. At high impurity concentrations, the Nernst coefficient has a lower peak around zero Fermi energy and shows less variation at high Fermi energy. Similarly, the Seebeck coefficient has a higher peak value for low impurity concentrations. Upon increasing temperature, the peak Nernst coefficent near the Dirac point increases monotonically to 300 K, after which it decreases slightly. Creating a band gap enhances the Seebeck coefficient but degrades the Nernst coefficient. Detailed knowledge of the variation of the thermoelectric and thermomagnetic properties of graphene shown in this work will prove helpful for improving the performance of magnetothermoelectric coolers and sensors.

APPENDIX

Sample derivation of longitudinal electrical conductivity: Eq. 6.11 for σ_{xx} in the absence of magnetic field becomes

$$
\begin{aligned}
\sigma_{xx} &= 4e^2 \int_{-\infty}^{\infty} \frac{|2\pi k dk|}{(2\pi)^2} \frac{v_F^2}{2} \tau_m \left(-\frac{\partial f_{eq}}{\partial \epsilon}\right) \\
&= 4e^2 \int_{-\infty}^{0} \frac{|2\pi k dk|}{(2\pi)^2} \frac{v_F^2}{2} \tau_m \left(-\frac{\partial f_{eq}}{\partial \epsilon}\right) \\
&+ 4e^2 \int_{0}^{\infty} \frac{|2\pi k dk|}{(2\pi)^2} \frac{v_F^2}{2} \tau_m \left(-\frac{\partial f_{eq}}{\partial \epsilon}\right) \\
&= \sigma_{xx,+} + \sigma_{xx,-}.
\end{aligned}
\tag{A-1}
$$

For $\sigma_{xx,+}$,

$$
\begin{aligned}
-\frac{\partial f_{eq}}{\partial \epsilon} &= \frac{\frac{1}{k_b T} exp(\frac{-\mu}{k_b T})}{(1 + exp(\frac{-\mu}{k_b T}))^2} \\
&= \frac{1}{k_b T (exp(\frac{-\mu}{k_b T}) + 2 + exp(-\frac{-\mu}{k_b T}))} \\
&= \frac{1}{k_b T (2 + 2cosh(\frac{-\mu}{k_b T}))} \\
&= \frac{1}{k_b T (4cosh^2(\frac{-\mu}{2k_b T}))}.
\end{aligned}
\tag{A-2}
$$

For $\sigma_{xx,-}$, performing the variable transform $\quad = - \quad$,

$$
-\frac{\partial f_{eq}}{\partial \epsilon} = \frac{1}{k_b T (4cosh^2(\frac{+\mu}{2k_b T}))}.
\tag{A-3}
$$

Considering the expression for τ_m in Eq. 6.25, and with the variable transform $x = \epsilon/E_F$, we obtain the final expression for σ_{xx} given by Eq. 6.28. For a band gap , the expression for σ_{xx} is modified using Eqs. (26), (27) to obtain

$$\sigma_{xx} = \frac{e^2}{\pi\hbar} \frac{E_F^2 |k_F|}{4\hbar k_b T} \int_{\overline{E_F}}^{\infty} (1 - \frac{2}{x^2 E_F^2}) \frac{x^2 (cosh^{-2}(\frac{E_F}{2k_b T}(x-1)) + cosh^{-2}(\frac{E_F}{2k_b T}(x+1)))}{a_1 + a_2 k_F^2 x^2 + \frac{a_3}{|ln(k_F x R_0)|^2}} dx$$
$$- \frac{e^2}{\pi\hbar} \frac{eBv_F^3 k_F^3}{8k_b T} \int_{\overline{E_F}}^{\infty} (1 - \frac{2}{x^2 E_F^2}) \frac{x^2 (cosh^{-2}(\frac{E_F}{2k_b T}(x-1)) - cosh^{-2}(\frac{E_F}{2k_b T}(x+1)))}{(a_1 + a_2 k_F^2 x^2 + \frac{a_3}{|ln(k_F x R_0)|^2})^2}.$$

$$(\text{A-4})$$
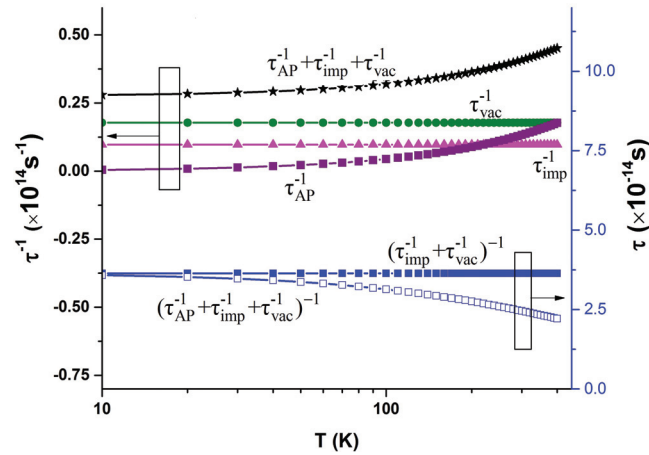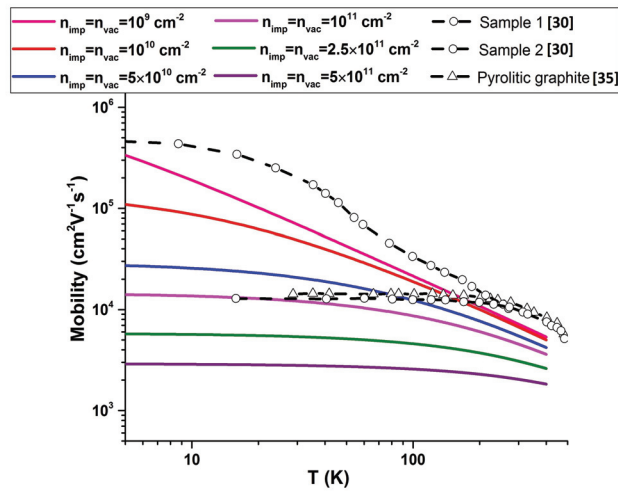
Fig. 6.1. (a) Variation of scattering time τ and scattering rate τ^{-1} for different scattering mechanisms, with temperature T, at charged impurity concentration n_{imp} and vacancy concentration n_{vac} both equal to 5×10^{11}cm^{-2}, and Fermi energy E_F=0.1 eV. (b) Mobility as a function of temperature T for different impurity and vacancy concentrations and comparison with experiments by Chen et al. [217] and Sugihara et al. [222] at Fermi energy E_F=0.1 eV.
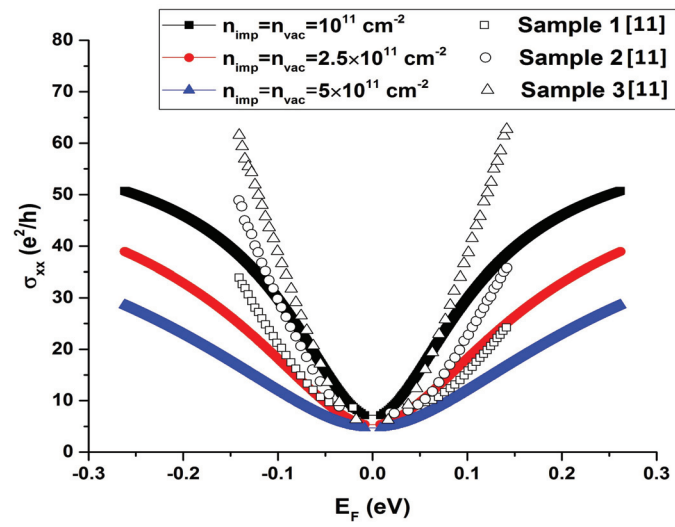
Fig. 6.2. Electrical conductivity σ_{xx} normalized by $e^2/(2\pi\hbar)$ at temperature T=150 K, magnetic field B=0 for various charged impurity and vacancy concentrations, and its comparison with experimental results of Liu et al. [198].
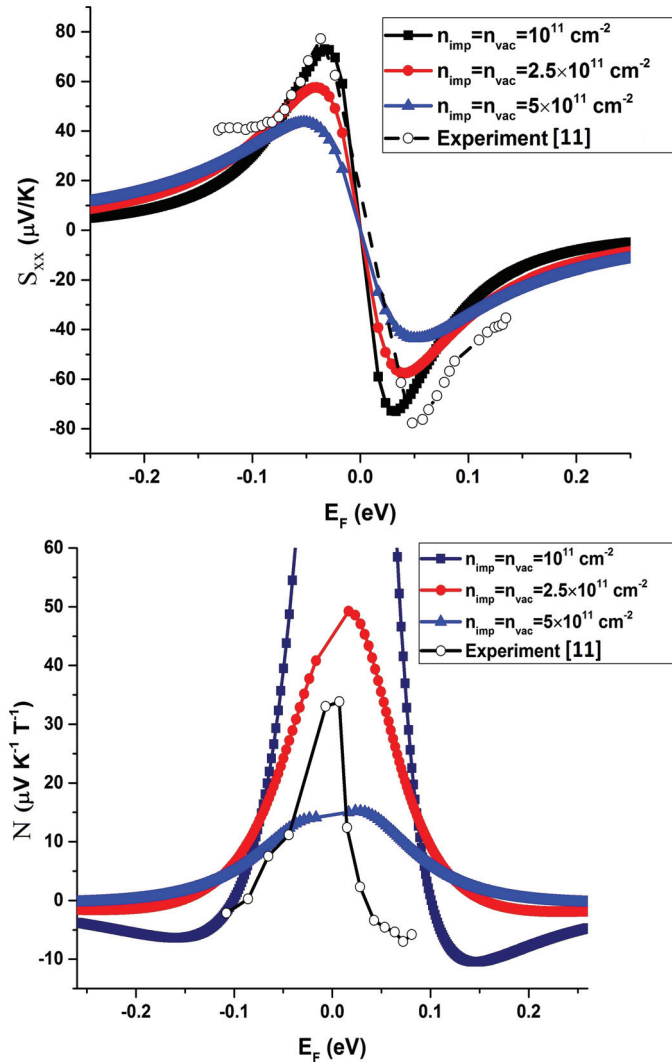
Fig. 6.3. Comparison of (a)model Seebeck coefficient S_{xx} and (b)model Nernst coefficient N with experimental results of Liu et al. [198]. Temperature T=150 K and magnetic field B=0 for (a). Temperature T=150 K and magnetic field B=1 T for (b).
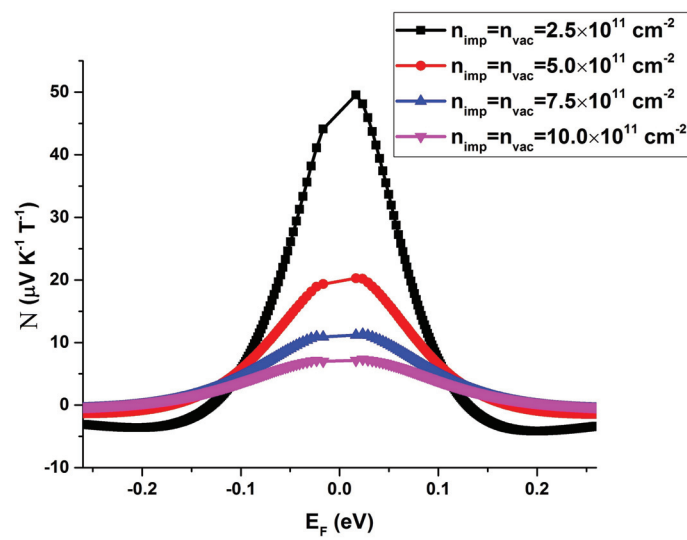
Fig. 6.4. Variation of Nernst coefficient N with charged impurity concentration n_{imp} and vacancy concentration n_{vac} at temperature $T=300$ K and magnetic field $B=1$ T.
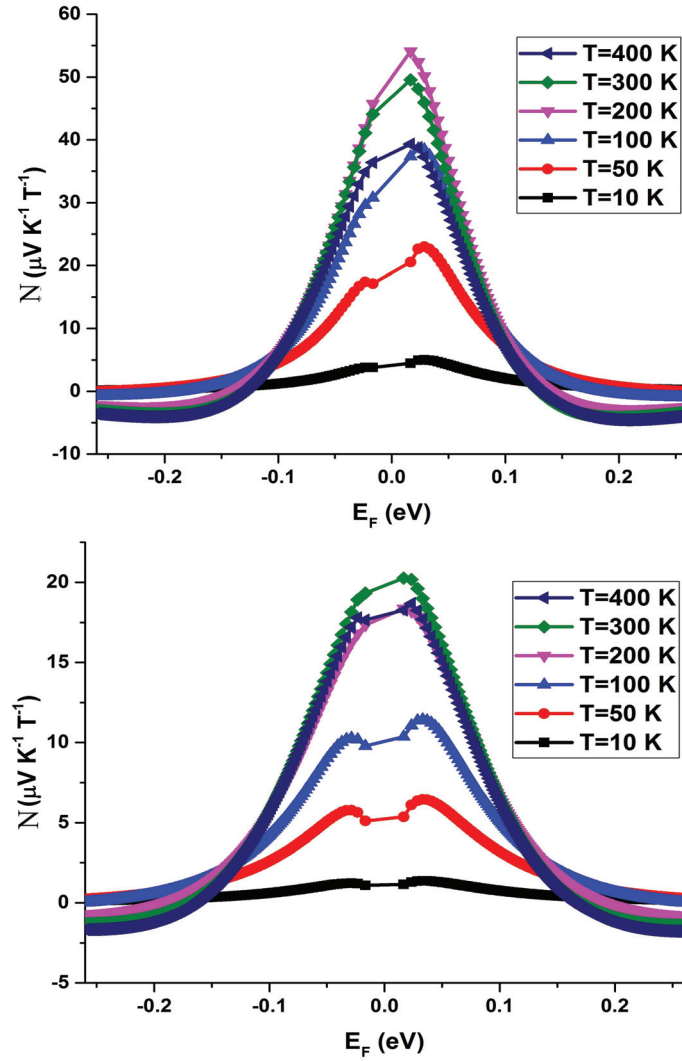
Fig. 6.5. Variation of Nernst coefficient N with Fermi energy E_F for temperature T varying from 10 K to 400 K. Magnetic field $B=1$ T, impurity concentration n_{imp} and vacancy concentration n_{vac} are both equal to (a) 2.5×10^{11} cm^{-2},(b)5×10^{11} cm^{-2}.
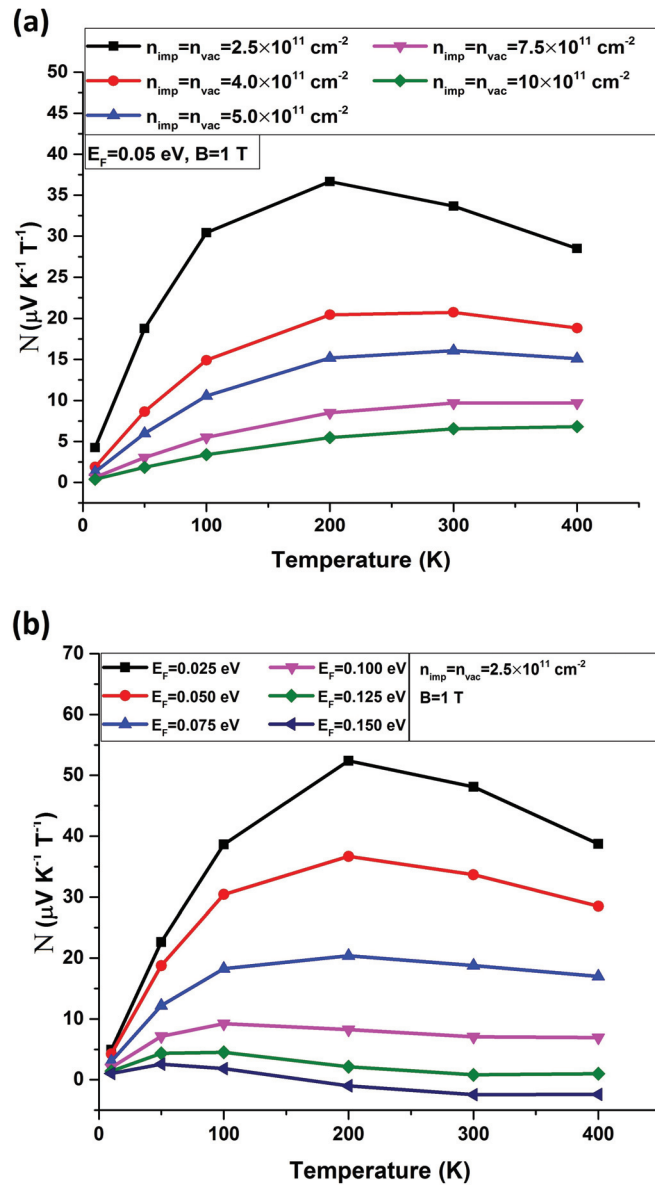
Fig. 6.6. (a) Variation of Nernst coefficient N with temperature T for different charged impurity concentration n_{imp} and vacancy concentration n_{vac} at fixed Fermi energy E_F= 0.05 eV and magnetic field B=1 T. (b) Variation of Nernst coefficient N with temperature T for different values of Fermi energy E_F at fixed charged impurity concentration n_{imp} and vacancy concentration n_{vac} of 2.5×10^{11} cm^{-2}, and magnetic field B=1 T.
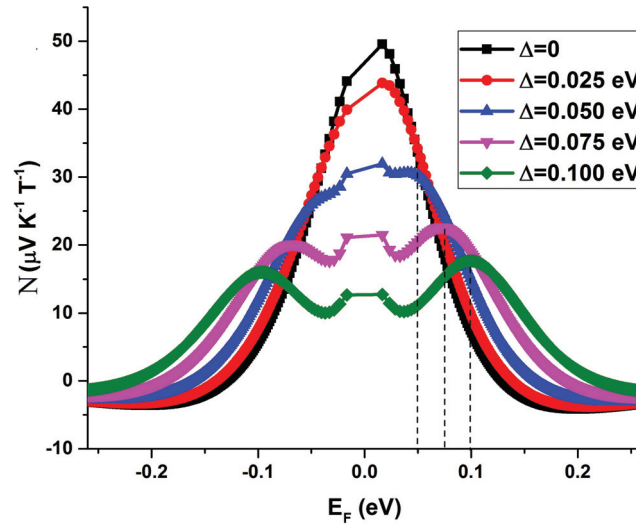
Fig. 6.7. Variation of Nernst coefficient N with Fermi energy E_F at magnetic field $B=1$ T, temperature $T=300$ K, charged impurity concentration n_{imp} and n_{vac} both equal to 2.5×10^{11} cm^{-2}.
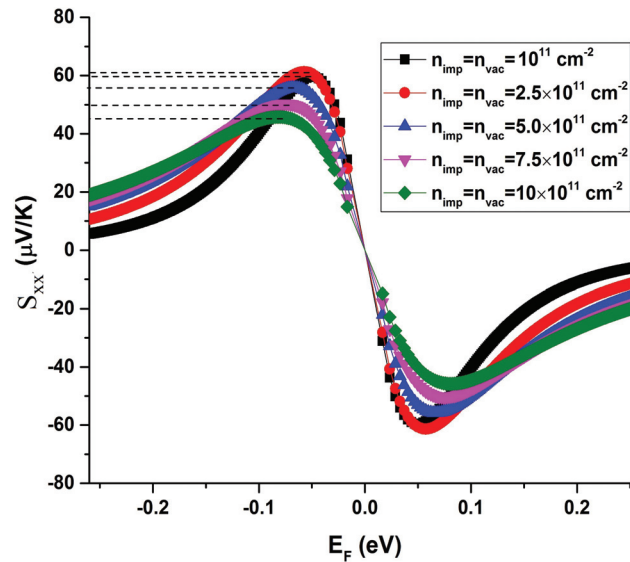
Fig. 6.8. Variation of Seebeck coefficient S_{xx} with Fermi energy E_F for different impurity concentrations at temperature $T=300$ K and magnetic field $B=0$.
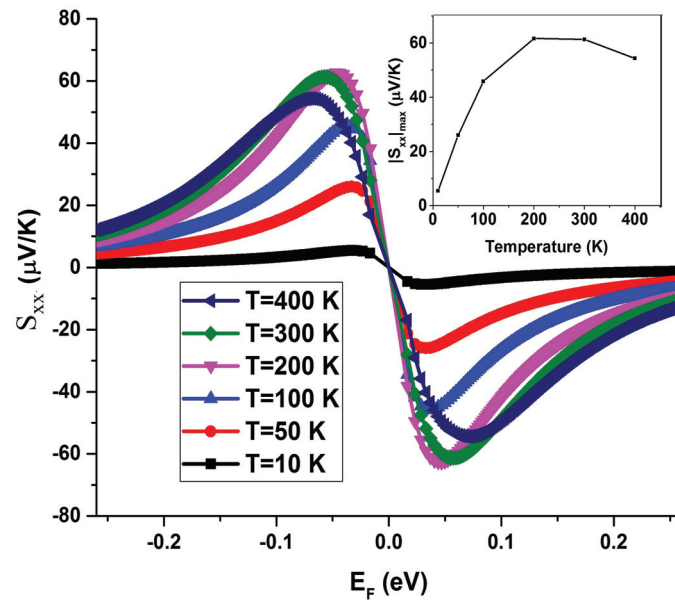
Fig. 6.9. Variation of Seebeck coefficient S_{xx} with Fermi energy E_F for different temperatures at $n_{imp} = n_{vac}$=2.5× 10^{11} cm^{-2} and magnetic field B=0.
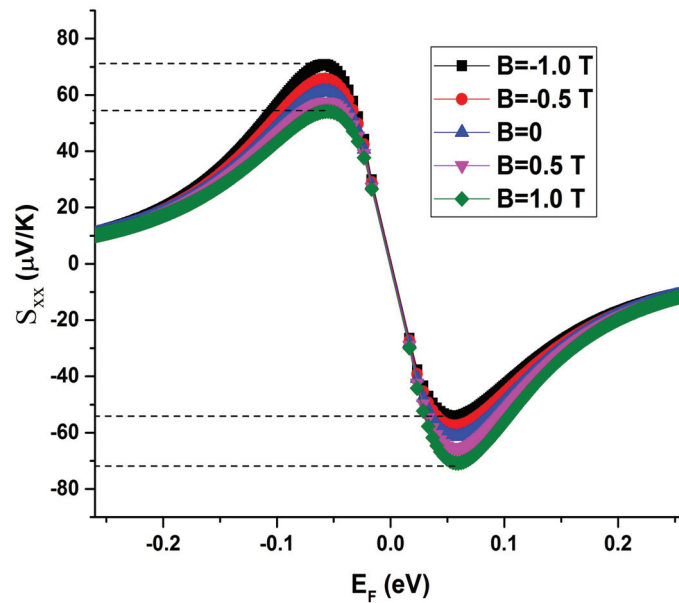
Fig. 6.10. Variation of Seebeck coefficient S_{xx} with magnetic field B from -1 T to 1 T at temperature T=300 K and $n_{imp} = n_{vac}$=2.5× 10^{11} cm^{-2}.
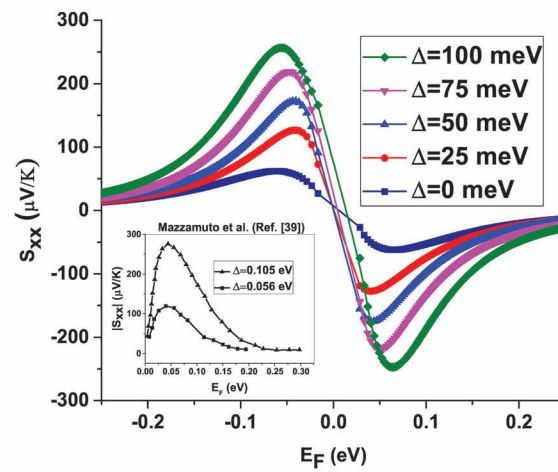
Fig. 6.11. Variation of Seebeck coefficient S_{xx} with Fermi energy E_F for band gap $\triangle$ varying from 0 to 100 meV at temperature T=300 K, magnetic field B=0 and charged impurity and vacancy concentrations $n_{imp} = n_{vac}$=2.5$\times$ 10^{11} cm^{-2}. The inset shows the results from the non-equilibrium Green's function model of Mazzamuto et al. [226] for band gap $\triangle$ value of 56 meV and 105 meV.
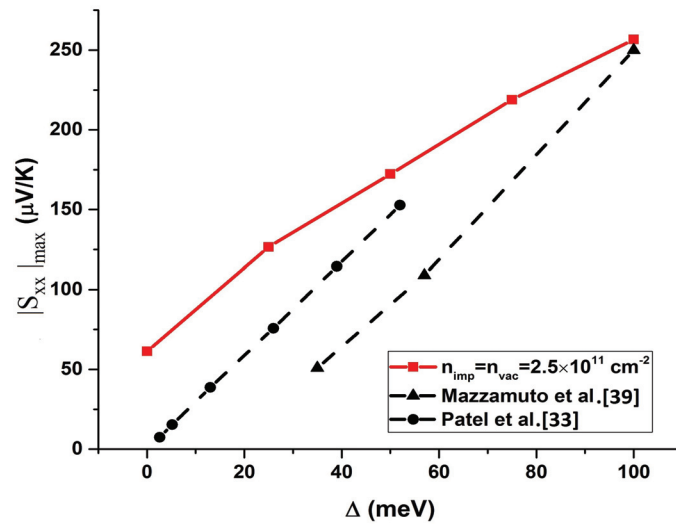
Fig. 6.12. Variation of peak value of Seebeck coefficient S_{xx} with band gap Δ ranging from 0 to 100 meV at temperature T=300 K, magnetic field B=0 and impurity concentrations n_{imp}=n_{vac}=2.5× 10^{11} cm^{-2}. The dotted lines show Green's function model results for graphene nanoribbons [226] and analytical model results for periodic single layer graphene [220]. The inset shows the Fermi energy E_F corresponding to the peak value of Seebeck coefficient S_{xx}.

7. SUMMARY

Broadly, this dissertation focuses on the interplay between electrochemical, thermal and optical effects in supercapacitors. Each new phenomenon has been investigated in depth with the aid of modeling and/or experimental techniques.

- The first part of this dissertation concerns the study of pseudocapacitive and thermogalvanic attributes of the ferrocyanide/ferricyanide redox couple. A novel high energy density thermally chargeable solid-state supercapacitor capable of converting waste heat directly into stored charge was conceptualized, designed and tested.

- The second part of this work focuses on the investigation of aging phenomena in supercapacitors during continuous cycling. A novel imaging technique is developed to spatially characterize charge accumulation in gold electrodes of a microsupercapacitor during charge/discharge. Furthermore, in order to study heat generation in commercial supercapacitors, which is the primary cause of aging, a continuum model based on porous electrode theory is developed and implemented to investigate the influence of various system parameters and operating conditions.

The contributions from the present work can be divided into five sections as discussed below. Additionally, in each section, directions for future research are prescribed.

7.1 Redox-active gel electrolyte based solid-state supercapacitor device

Major contributions:

- Performed electrochemical characterization of the electrodes in a three-electrode configuration cell with 3 different aqueous solutions: (i) $K_3Fe(CN)_6$-$K_4Fe(CN)_6$, (ii) 1 M H_3PO_4 and (iii) 1 M KOH.

- Fabricated a thin, lightweight, symmetric, all-solid-state supercapacitor device with BP/GP electrodes and redox-active gel electrolyte (PVA- $K_3Fe(CN)_6$-$K_4Fe(CN)_6$) film.

Key results:

- Sharp redox peaks were observed in the cyclic voltammetry curves for aqueous $K_3Fe(CN)_6$-$K_4Fe(CN)_6$ which are indicative of the pseudocapacitive contributions to charge storage. The area-normalized capacitance for this electrolyte exceeds that measured for H_3PO_4 by 4 times at a low scan rate of 10 mV s^{-1}.

- The all-solid-state symmetric device composed of the redox-active gel electrolyte exhibits a high electrode-specific capacitance of 0.95 F cm^{-2} and a high volumetric energy density of 7.4 mWh cm^{-3}; these values are compared to and considerably higher than devices with conventional gel electrolytes (PVA-H_3PO_4, PVA-KOH) due to the pseudocapacitive behavior of redox species in the electrolyte. Complementary to enhanced capacitance, the redox-active gel electrolyte device displays a large maximum voltage stability window up to 1.5 V. Furthermore, the device exhibits excellent long-term cyclic stability ($\geq$90% capacitance retention after 5000 cycles) and high coulombic efficiencies ($\geq$98%). However, on the flip side, the redox electrolyte device exhibited a large internal resistance and high self-discharge rate compared to the other devices.

7.2 Harnessing the thermogalvanic effect of the ferro/ferricyanide redox couple in a thermally chargeable supercapacitor

Major contributions:

- Fabricated and designed a supercapacitor device composed of carbon cloth electrodes and PVA-$K_3Fe(CN)_6$-$K_4Fe(CN)_6$ gel electrolyte that can convert an applied temperature gradient directly into stored charge.

- Built a test platform to test the thermoelectric properties of the device

- Measured the electrochemical performance of the fabricated device

- Developed an equivalent circuit model to illustrate the thermal' charging process

Key results:

- In addition to the characteristic Seebeck coefficient of -1.21 mV K^{-1}, the pseudocapacitive property of the ferrrocyanide/ferricyanide redox couple endows the device with a high area-specific capacitance of 13 F cm^{-2} which finally leads to high thermally induced energy storage density.

- The optimum thickness of the gel electrolyte film which leads to the largest value of thermally induced energy density in the device is determined to be around 1 mm.

- Experimentally obtained voltage and current measurements display a good match with the results obtained from the equivalent circuit model upon performing a fitting analysis.

7.3 Electroreflectance imaging of gold-H3PO4 micro-supercapacitors: Experiment methodology and aging characterization

Major contributions:

- Demonstrated electroreflectance microscopy as a high-resolution, imaging technique to map dynamic charge distribution in integrated microsupercapacitor structures during fast voltage cycling.

- Developed and validated a model describing changes in the metal electrodes optical constants as a function of free electron concentration.

Key results:

- Electroreflectance camera images of a gold-H_3PO_4 polymer electrolyte micro-supercapacitor reveal time varying charge distribution with submicron spatial resolution, millisecond time resolution, and electroreflectance resolution on the order of 500 nC cm^{-2}.

- In the aging characterization study, the developed model was successful in reproducing the reflectance signals and device capacitance values measured experimentally for devices subjected to over 4 million charge/discharge cycles.

7.4 Continuum modeling of heat generation in electrical double-layer capacitors

Major contributions:

- Built a continuum scale model describing electrochemical transport and heat generation in supercapacitors subjected to galvanostatic charge/discharge

- Formulated expressions for reversible and irreversible heat generation rates and thereby established the coupling between the governing energy equation and the electrochemical model based on porous electrode theory

- Performed numerical simulations based on this model to evaluate spatio-temporal evolution of temperature in a realistic EDLC device consisting of multiple sandwich units.

Key results:

- The temperature evolution results obtained from the model resemble past measurements both qualitatively and quantitatively under different operating conditions.

- Scaling analysis performed on the model simplifies eleven independent design parameters to seven dimensionless similarity parameters.

7.5 Magnetothermoelectric effects in graphene and their dependence on scatterer concentration, magnetic field, and band gap

- Derived analytical expressions for electric and thermoelectric transport coefficients of graphene in the presence and absence of a magnetic field, using a semiclassical Boltzmann transport equation.

- Evaluated Seebeck (S_{xx}) and Nernst (N) coefficients as functions of carrier density, temperature, scatterer concentration, magnetic field, and induced band gap, and compared the results to experimental data.

Key results:

- The peak values of both coefficients are found to increase with the decreasing scatterer concentration and increasing temperature. Furthermore, opening a band gap decreases N but increases S_{xx}.

- Applying a magnetic field introduces an asymmetry in the variation of S_{xx} with Fermi energy across the Dirac point.

8. APPENDIX

8.1   Appendix A. Supporting Information for Chapter 2: "Effect of redox-active gel electrolyte on graphitic petal based solid-state supercapacitors"

Supplementary Information includes:

- SEM images of bare buckypaper (BP) and buckypaper with graphene petals (BP/GPs)

- Comparison of the electrochemical performance of BP/GP electrodes in three-electrode configuration in 0.2 M $K_3Fe(CN)_6$/$K_4Fe(CN)_6$ and 1.0 M H_3PO_4 aqueous electrolytes

- Comparison of the electrochemical performance of fabricated two-terminal symmetric supercapacitor devices composed of PVA-PFC, PVA-H_3PO_4 and PVA-KOH gel electrolytes with respect to electrode-specific areal capacitance $C_{A,el}$, equivalent series resistance (ESR) and self-discharge characteristics

- Schematic description of microwave plasma chemical vapor deposition (MPCVD) system used to grow graphene petals (GPs) on bucky paper (BP) substrates

- Past demonstrations of enhancement in electrochemical performance (improvement in capacitance and reduction in ESR) achieved by addition of redox additives to gel electrolytes.

SEM images of bare buckypaper (BP) and buckypaper with graphene petals (BP/GPs)
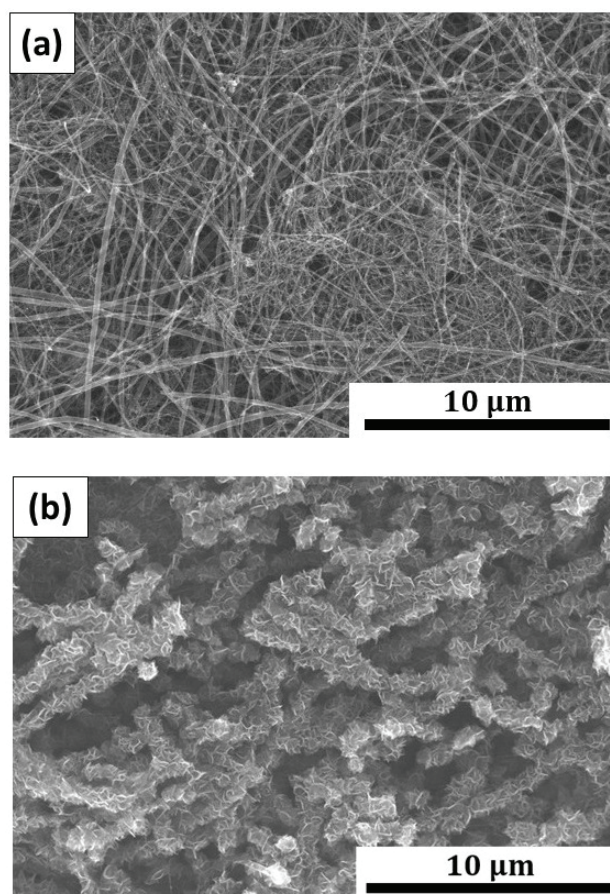
Fig. 8.1. SEM images of (a) bare commercial buckypaper (BP) and (b) BP/GP substrates at same magnification (5000x).
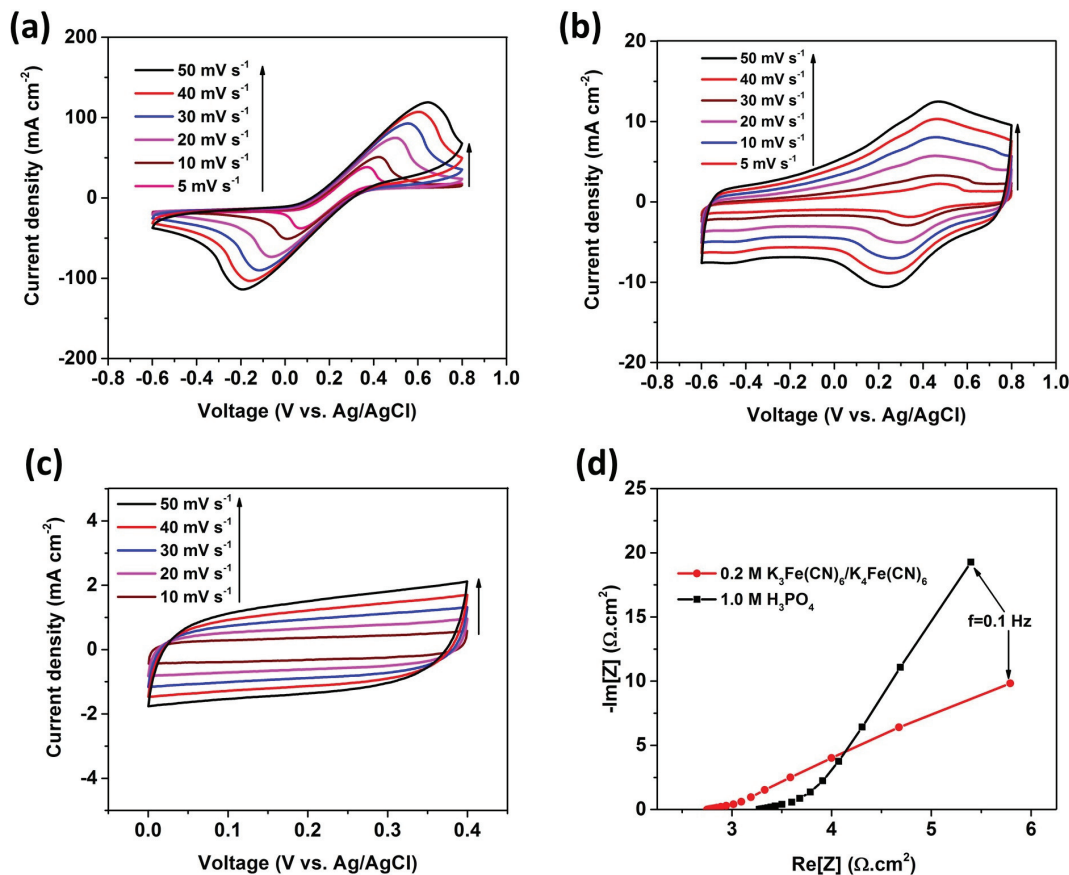
Fig. 8.2. Electrochemical performance of BP/GP electrodes in various electrolytes. (a) CV curves at scan rates ranging from 5 to 50 mVs^{-1} in a solution of 0.2 M K$_3$Fe(CN)$_6$ and 0.2 M K$_4$Fe(CN)$_6$. (b) CV curves at scan rates ranging from 5 to 50 mVs^{-1} in a potential window of 0 to 0.8 V vs. Ag/AgCl in 1.0 M H$_3$PO$_4$. (c) CV curves at scan rates ranging from 10 to 50 mVs^{-1} in a potential window of 0 to 0.4 V vs. Ag/AgCl in 1.0 M KOH and (d) Comparison of Nyquist plots obtained in electrolyte consisting of 0.2 M K$_3$Fe(CN)$_6$ and 0.2 M K$_4$Fe(CN)$_6$ solution and 1.0 M H$_3$PO$_4$ electrolyte. The frequency ranges from 100 kHz to 0.1 Hz.

Fabrication of GPs on buckypaper (BP)

Rectangular pieces of commercial buckypaper (Nanocomp Technologies, Inc., USA) with dimensions 1.5 cm × 1 cm, washed in 6 M HNO$_3$ for 15 min to eliminate
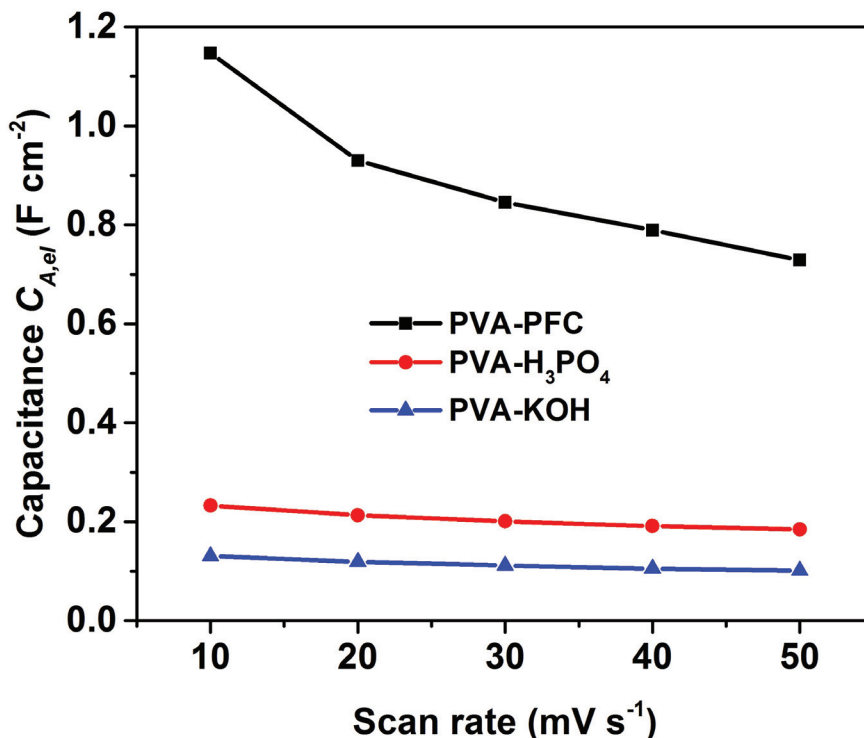
Fig. 8.3. Variation of electrode-specific areal capacitance derived from CV scans, with scan rate for PVA-PFC, PVA-H_3PO_4 and PVA-KOH based two-terminal symmetric devices.

surfactant and residuals before GP growth, were used as substrates to grow GPs. After drying overnight in a N_2 chamber, each sample was elevated 7 mm above a 55-mm-diameter Mo puck by ceramic spacers (see Figure S10), and then subjected to MPCVD conditions. A schematic diagram of the chamber is shown for the growth process in Figure S10. Unlike horizontal graphene growth by thermal CVD, GP growth is catalyst-free and requires a plasma environment. H_2 (50 sccm) and CH_4 (10 sccm) were used as the primary feed gases at 30 Torr total pressure and 650 W plasma power. The GP growth time was 20 min. This plasma is sufficient to heat the samples from room temperature up to approximately 1000°C, as measured by a dual-wavelength pyrometer (Williamson PRO 92).
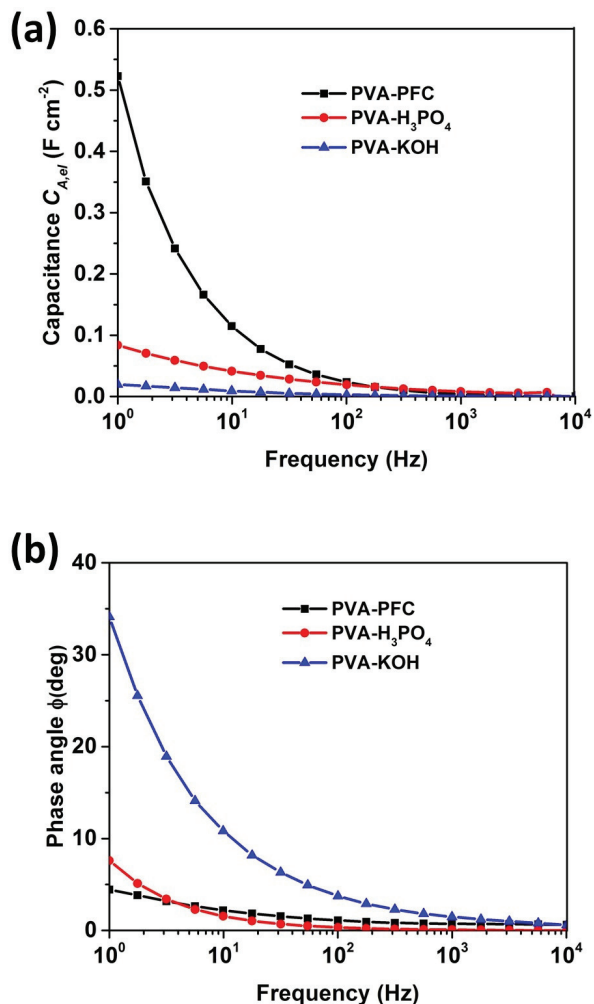
Fig. 8.4. (a) Electrode-specific areal capacitance derived from Nyquist plots drawn for PVA-PFC, PVA-H$_3$PO$_4$ and PVA-KOH based two-terminal symmetric devices (b) Bode plot for PVA-PFC, PVA-H$_3$PO$_4$ and PVA-KOH based two-terminal symmetric devices.

GP oxidation

GPs grown through MPCVD are hydrophobic by nature. Thus, before assembly process, the samples are activated to be hydrophilic. They are electrochemically oxidized to functionalize the GP surface with oxygen-containing functional groups. The
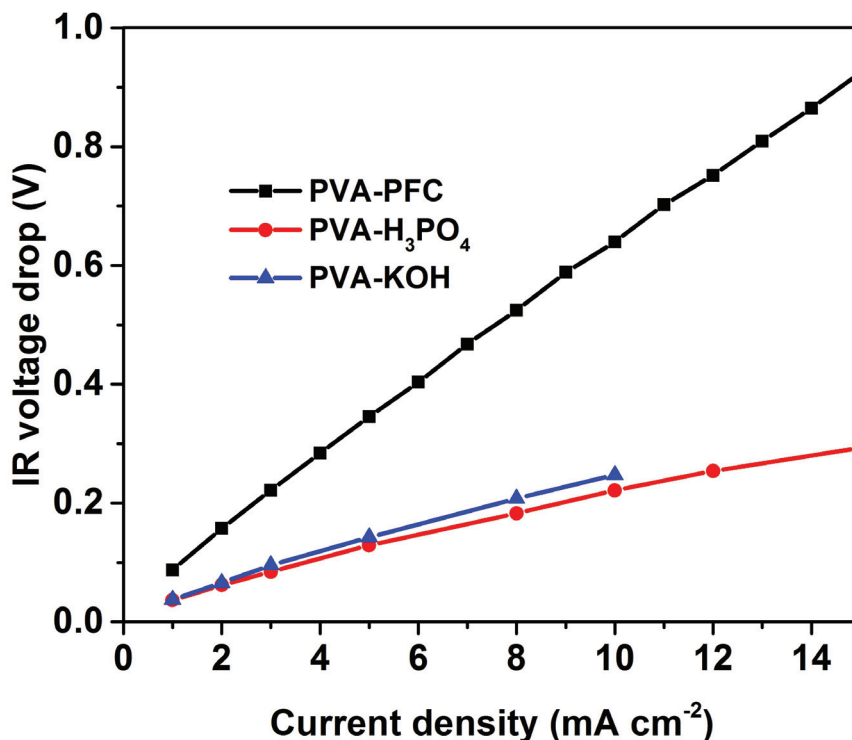
Fig. 8.5. Comparison of IR voltage drop measured at the beginning of discharge for GCD cycling of PVA-PFC, PVA-H$_3$PO$_4$ and PVA-KOH based two-terminal symmetric devices.

electrochemical oxidization (EO) process current and voltage transients are shown in Figure S11.

Calculations

Specific capacitance derived from cyclic voltammetry (CV) in three electrode configuration is calculated from:

$$C = \frac{1}{2sA(V_h - V_l)} \int_{V_s \to V_h \to V_l} I(V)dV \tag{A-1}$$

where C is the specific capacitance in F cm^{-2}, A is the geometric area of the electrodes, V_h and V_l are the high and low voltage limits of the CV tests, I is the instantaneous current measured during the CV test and V is the instantaneous applied voltage. The
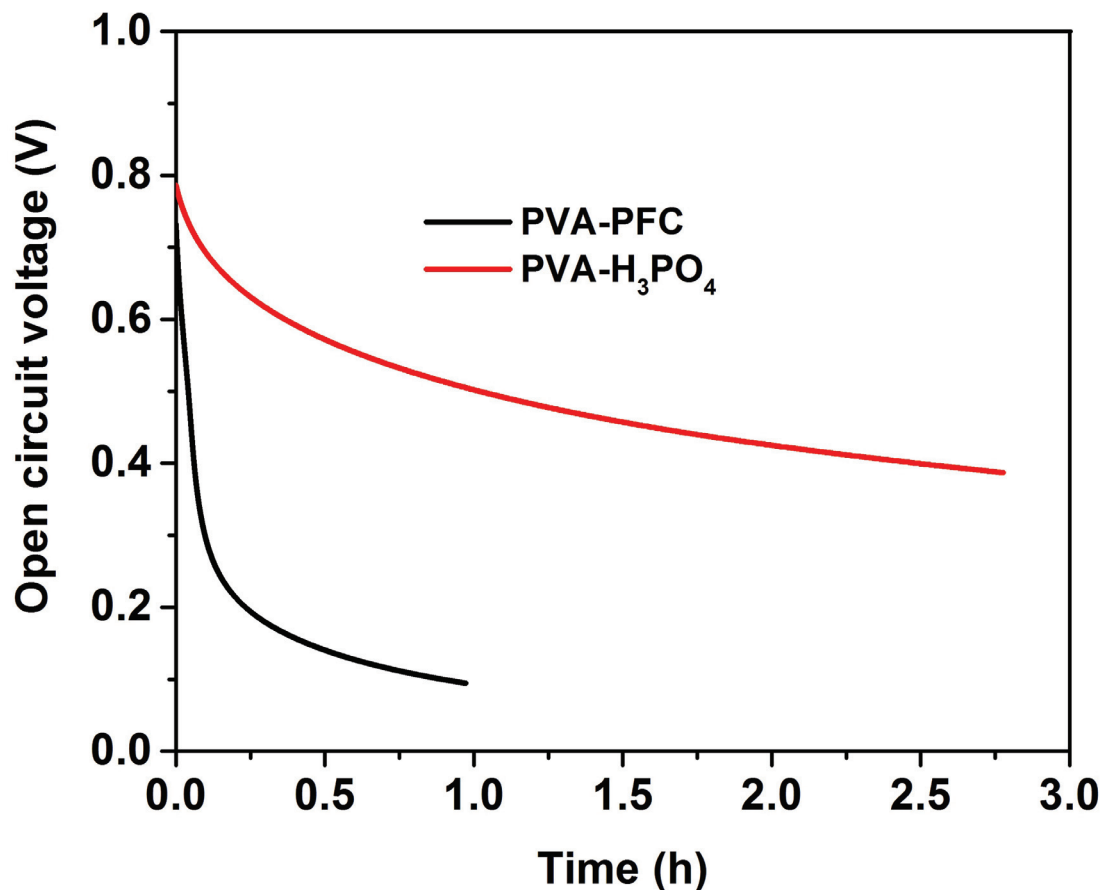
Fig. 8.6. Self-discharge characteristics of PVA-PFC and PVA-H$_3$PO$_4$ based two-terminal symmetric devices after maintaining at a constant voltage of 0.8 V for 5 min.

same expression is used to calculate the device capacitance C_{dev} from the obtained CV curves. The area-normalized internal resistance R (in $\Omega.cm^2$) is determined from the voltage drop occurring at the beginning of discharge process in the GCD curves and shown in Figure S5 for the fabricated two-terminal symmetric devices composed of PVA-PFC, PVA-H$_3$PO$_4$ and PVA-KOH gel electrolytes. R is evaulated using the expression:

$$R = \frac{V_{IR}A}{2I_d} \tag{A-2}$$

where V_{IR} is the voltage drop, I_d is the constant discharge current density and A is the electrode projected area. The values of R evaluated for the PVA-PFC, PVA-H$_3$PO$_4$
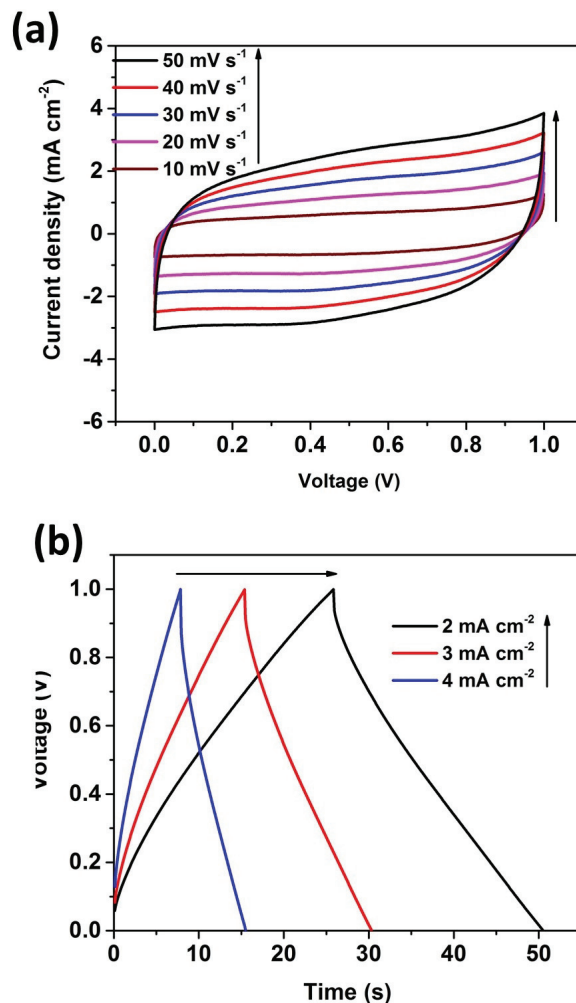
Fig. 8.7. (a) CV curves for scan rates ranging from 10 to 50 mVs^{-1} measured in a potential window of 0-1.0 V for the PVA-H$_3$PO$_4$ based two-terminal symmetric device. (b) GCD curves for constant current density ranging from 2 to 4 mA cm^{-2} measured in a potential window of 0-1.0 V for the PVA-H$_3$PO$_4$ based two-terminal symmetric device.

and PVA-KOH devices are evaluated to be 30.0, 8.8 and 12.2 Ω.cm^2 respectively. The capacitance retention during cyclic stability test is calculated using the expression:

$$\eta_{ret} = \frac{C}{C_0} \tag{A-3}$$
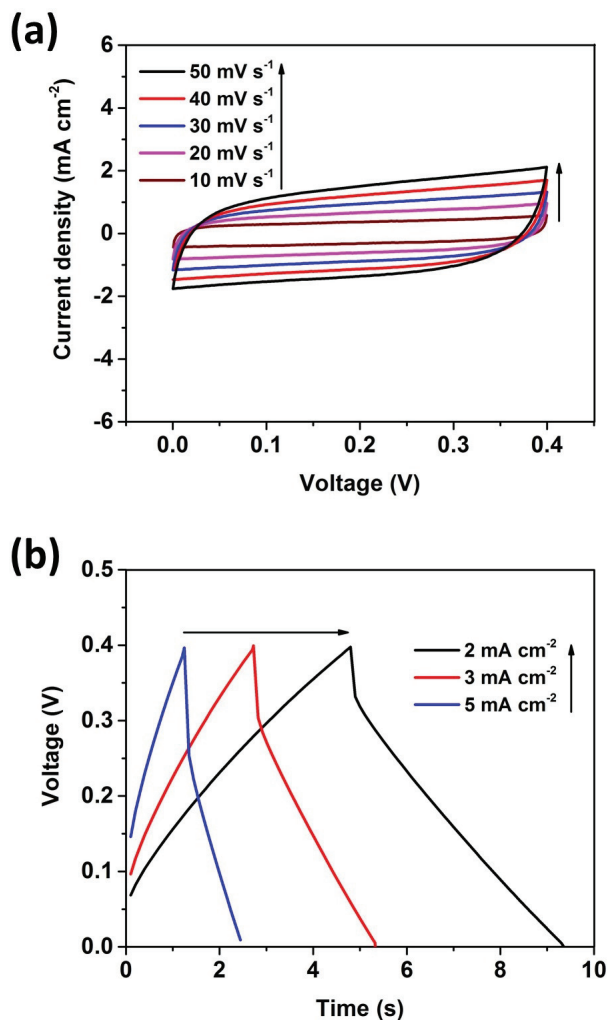
Fig. 8.8. (a) CV characteristics for scan rates ranging from 10 to 50 mVs^{-1} measured for the PVA-KOH based two-terminal symmetric device. (b) GCD curves for constant current density ranging from 2 to 5 mA cm^{-2} measured in the potential range of 0-1.0 V for the PVA-KOH based two-terminal symmetric device.

where C and C_0 are the areal capacitance derived from the GCD cycle at the end and beginning of the cyclic test respectively. The coulomic efficiency is calculated using the expression:

$$\eta_{coul} = \frac{Q_{dis}}{Q_{char}} = \frac{I.t_{dis}}{I.t_{char}} = \frac{t_{dis}}{t_{char}} \tag{A-4}$$
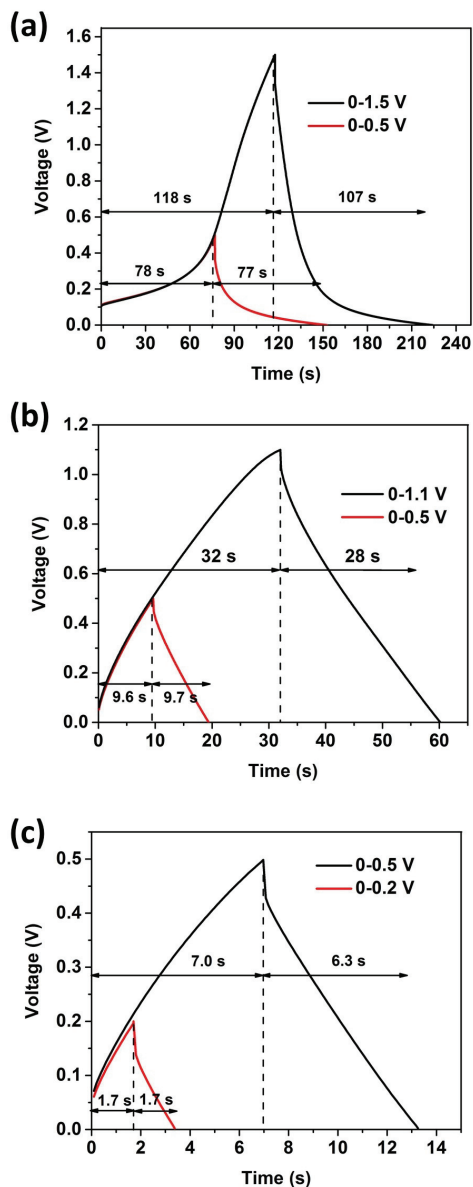
Fig. 8.9. (a) GCD characteristics in voltage range 0-0.5 V and 0-1.5 V acquired at a current density of 2 mA cm^{-2} for the PVA-PFC device. (b) GCD characteristics in voltage ranges of 0-0.5 V and 0-1.1 V acquired at a current density of 2 mA cm^{-2} for the PVA-H$_3$PO$_4$ device (c) GCD characteristics in voltage range 0-0.2 V and 0-0.5 V acquired at a current density of 2 mA cm^{-2} for the PVA-KOH device.

where Q_{char} and Q_{dis} are the charge stored and released during the charge and discharge phases of the GCD cycle. Similarly, t_{dis} and t_{char} are the durations of the charge and the discharge phase.
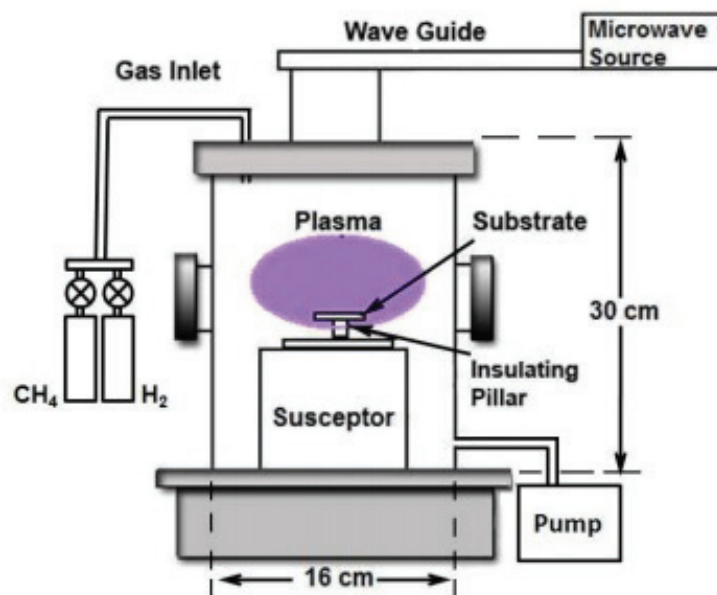
Fig. 8.10. Schematic diagram of the MPCVD chamber illustrating the approximate dimensions and positions of the substrate with respect to the plasma, reprinted with permission [44]
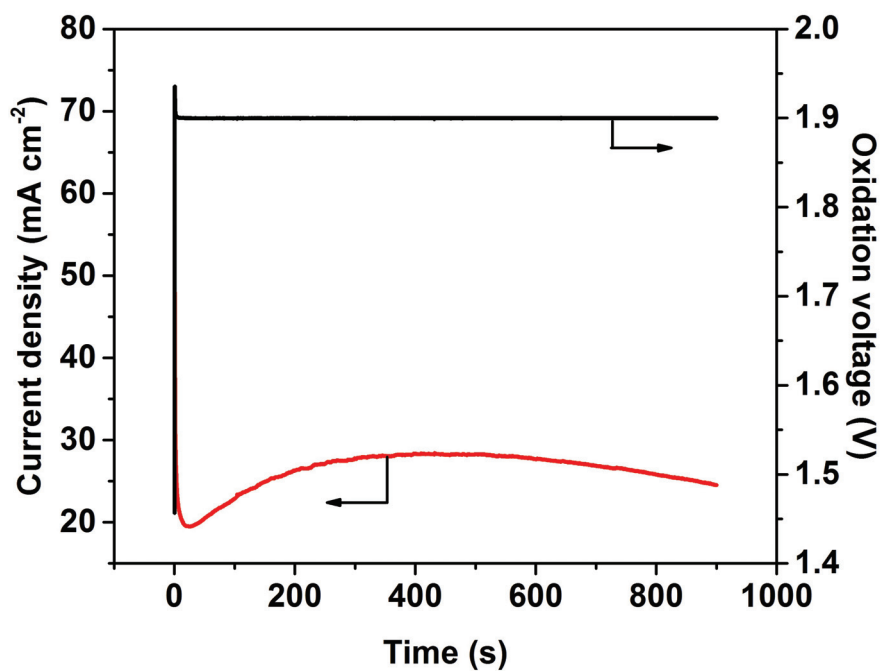
Fig. 8.11. Electrochemical oxidization process at 1.9 V in 1 M H_2SO_4 for 15 min
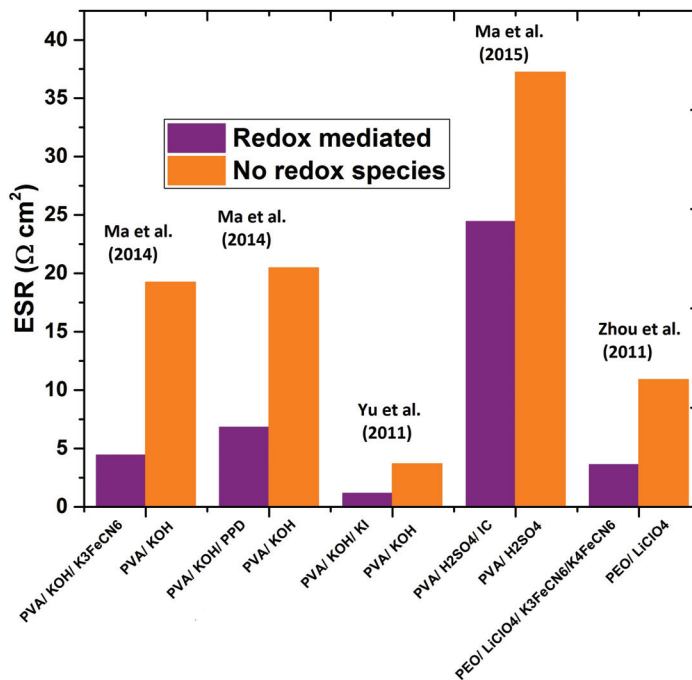
Fig. 8.12. Past demonstrations of reduction in equivalent series resistance achieved by adding redox additives [13, 16, 18, 228].
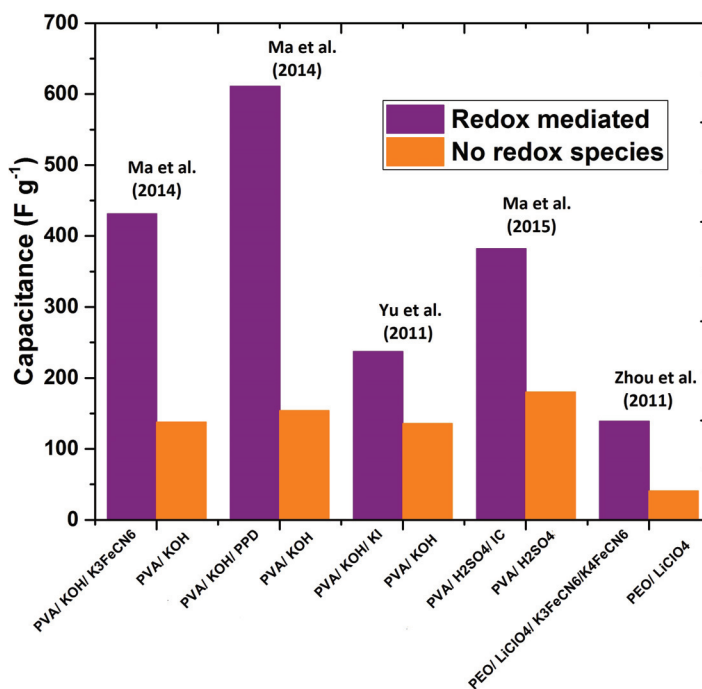
Fig. 8.13. Past demonstrations of enhancement in capacitance achieved by adding redox additives [13, 16, 18, 228].

8.2 Appendix B. Supporting Information for Chapter 3: "Harnessing the thermogalvanic effect of the ferro/ferricyanide redox couple in a thermally chargeable supercapacitor"

Supplementary Information includes:

- SEM images of bare carbon cloth (CC) and carbon cloth with graphene petals (CC/GP).

- Thermoelectric response of TCSC devices with different values of gel film thickness.

- Comparison of electrochemical performance of symmetric two-terminal TCSC devices composed of bare CC and CC/GP electrodes.

- Comparison of electrochemical performance of two-terminal symmetric supercapacitor devices composed of PVA-H_3PO_4 and PVA/$K_3Fe(CN)_6$/$K_4Fe(CN)_6$ gel electrolytes.

- Thermoelectric response of TCSC devices composed of PVA/$K_3Fe(CN)_6$/$K_4Fe(CN)_6$ gel electrolyte films with different values of thickness.

- Thermistor calibration.

- Model equations for different phases of the thermal charging experiment.

- Equations for deriving various performance parameters.

- Comparison of the performance of our TCSC device with a conventional system consisting of a Bi_2Te_3 thermoelectric connected in series to the same TCSC device (now playing the role of just supercapacitor).

SEM images of bare carbon cloth (CC) electrode:
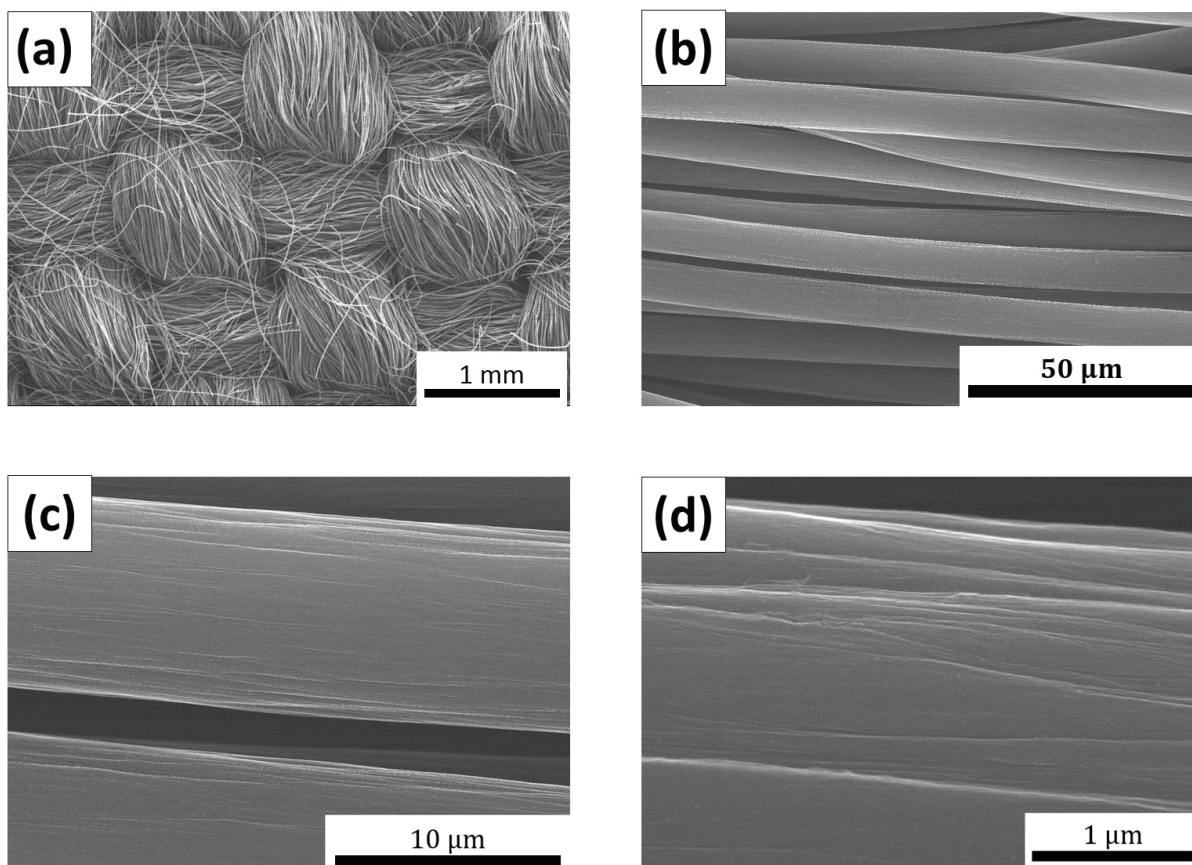
Fig. S14. SEM images of bare flexible carbon cloth at various magnifications.

SEM images of carbon cloth with graphene petal (CC/GP): In order to evaluate the effect of increased surface area of carbon cloth on electrode capacitance, graphene petals (GP) were grown in a microwave plasma chemical vapor deposition (MPCVD) system using growth conditions obtained from a previous study [9]. Figure S2 displays the uniform and large-area GP coverage on carbon cloth substrates at various magnifications. Fgure S2d shows nanopetal structures on carbon microfibers, in which GPs with sharp edges fully cover the outer surface of a microfiber.
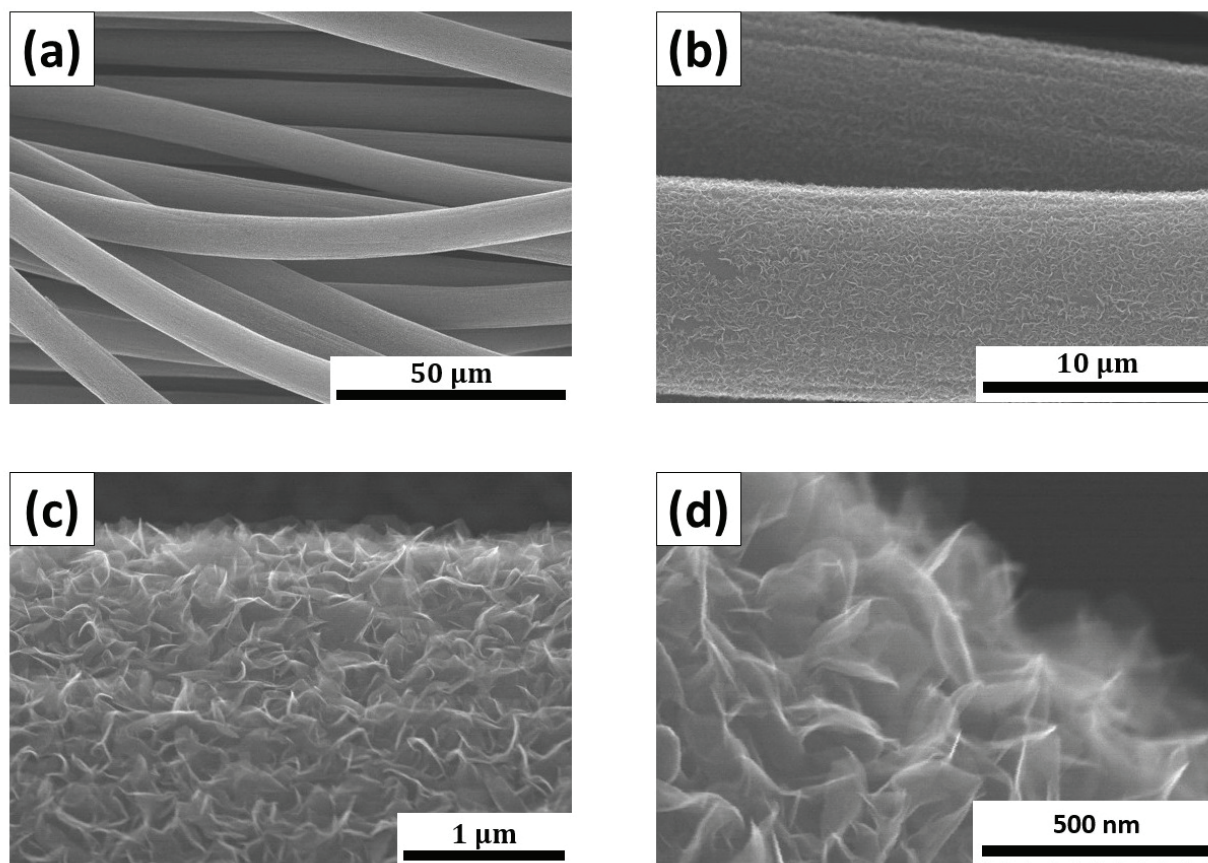
Fig. S15. SEM image of flexible carbon cloth embedded with graphene petals (CC/GP) at various magnifications.
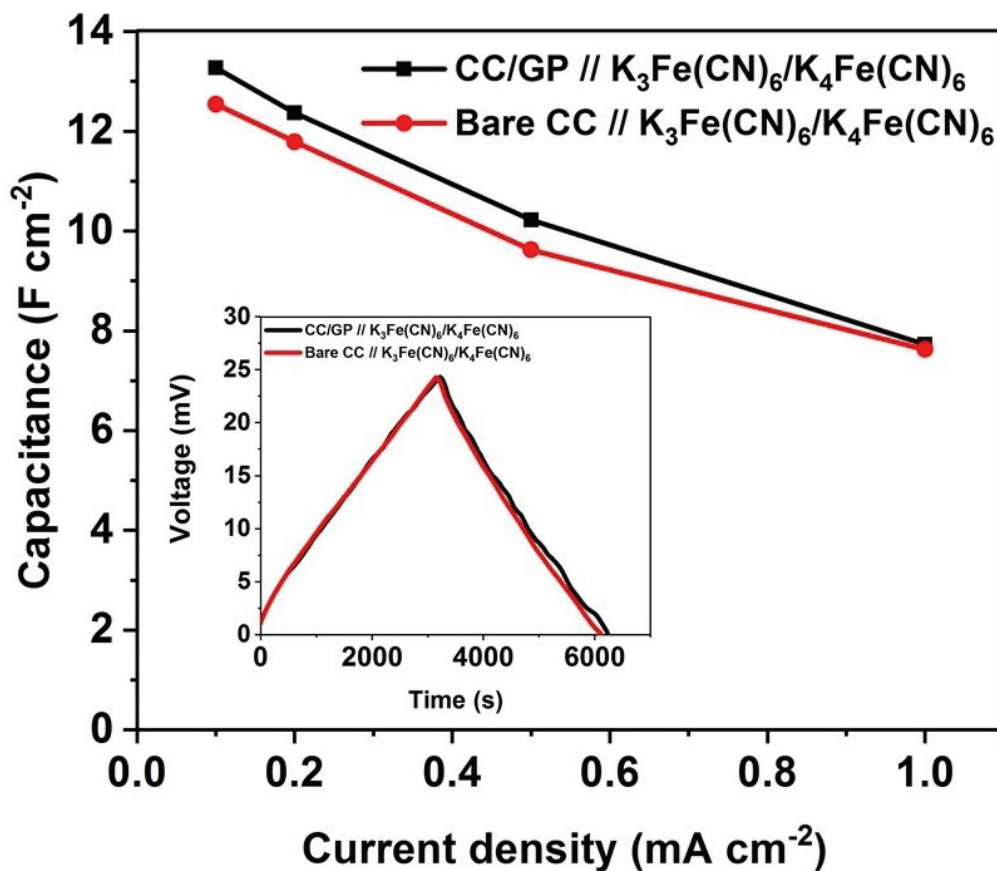
Fig. S16. Comparison of electrochemical performance of symmetric two-terminal TCSC devices composed of bare CC electrodes and CC/GP electrodes. A 1.5 mm thick film of $PVA/K_3Fe(CN)_6K_4Fe(CN)_6$ gel electrolyte is used to fabricate both the TCSC devices. The main plot compares the variation of area-specific capacitance as a function of current density for both devices, while the inset shows the GCD profiles corresponding to an operating current density of 0.1 mA cm^{-2}.
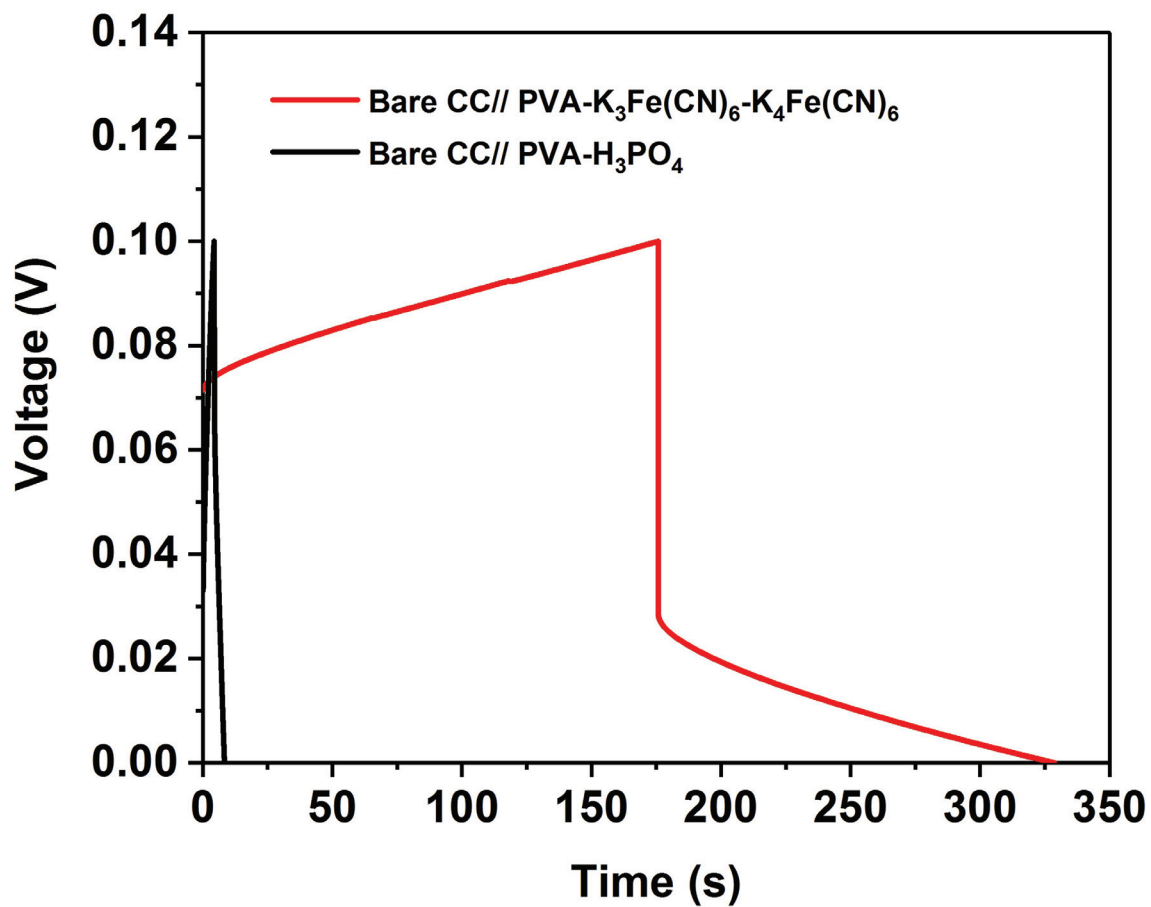
Fig. S17. Galvanostatic charge/discharge profiles at a constant current density of 1 mA cm^{-2} for symmetric two-terminal devices composed of 0.9 mm thick film of PVA-H$_3$PO$_4$ gel electrolyte and PVA-K$_3$Fe(CN)$_6$-K$_4$Fe(CN)$_6$ gel electrolyte. Bare CC electrodes are used to build both the devices.
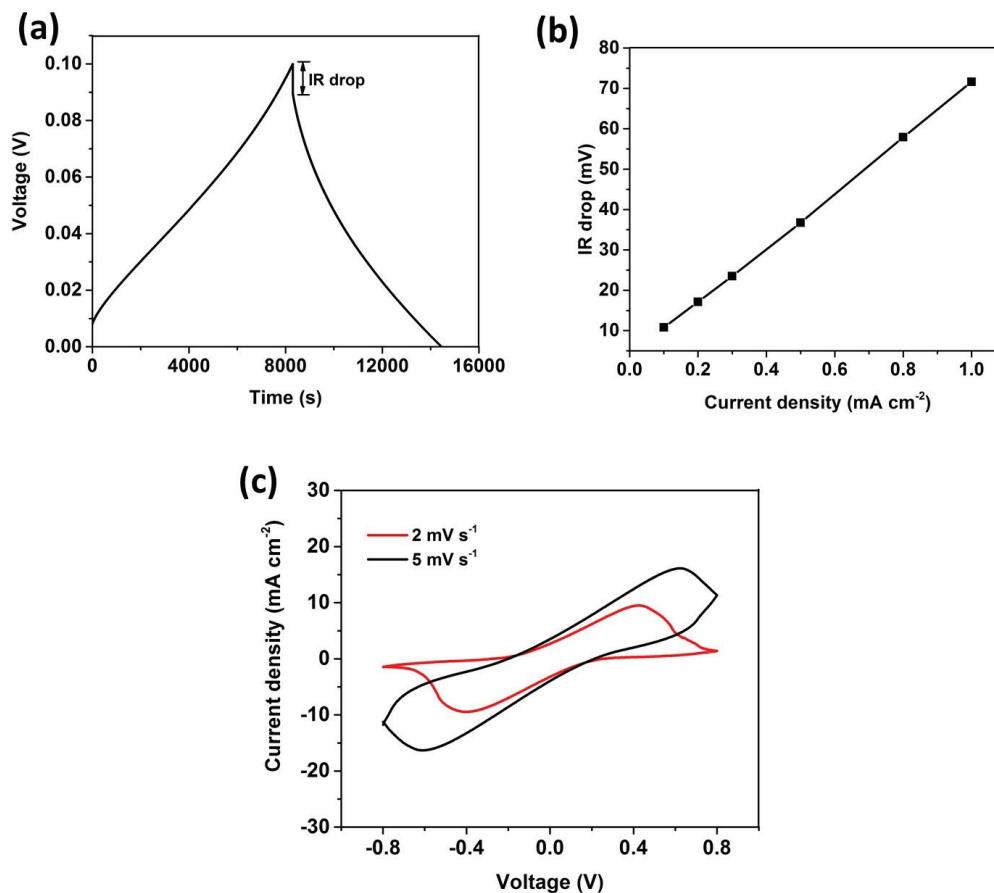
Fig. S18. Electrochemical performance of two-terminal symmetric supercapacitor device with carbon cloth electrodes and 1.5 mm thick gel film electrolyte. (a) Galvanostatic charge/discharge cycling at a constant current density of 0.1 mA cm^{-2} (b) Variation of the IR voltage drop observed at the beginning of discharge with current density (c) Cyclic voltammetry at scan rates of 2 and 5 mV s^{-1}.

Thermoelectric response of TCSC devices with different values of gel film thickness: Figure S6 shows the thermoelectric response of TCSC devices fabricated using 0.3 mm thick and 1.5 mm gel films. The external temperature gradient ΔT_{ext} is varied periodically in steps by changing the power input to the Peltier heater and cooler. The corresponding open circuit voltage values are recorded. As expected, the open circuit voltage recorded is highest for the 1.5 mm thick gel film due to its large

thermal resistance and consequently high effective temperature gradient occurring across the two faces of the film.
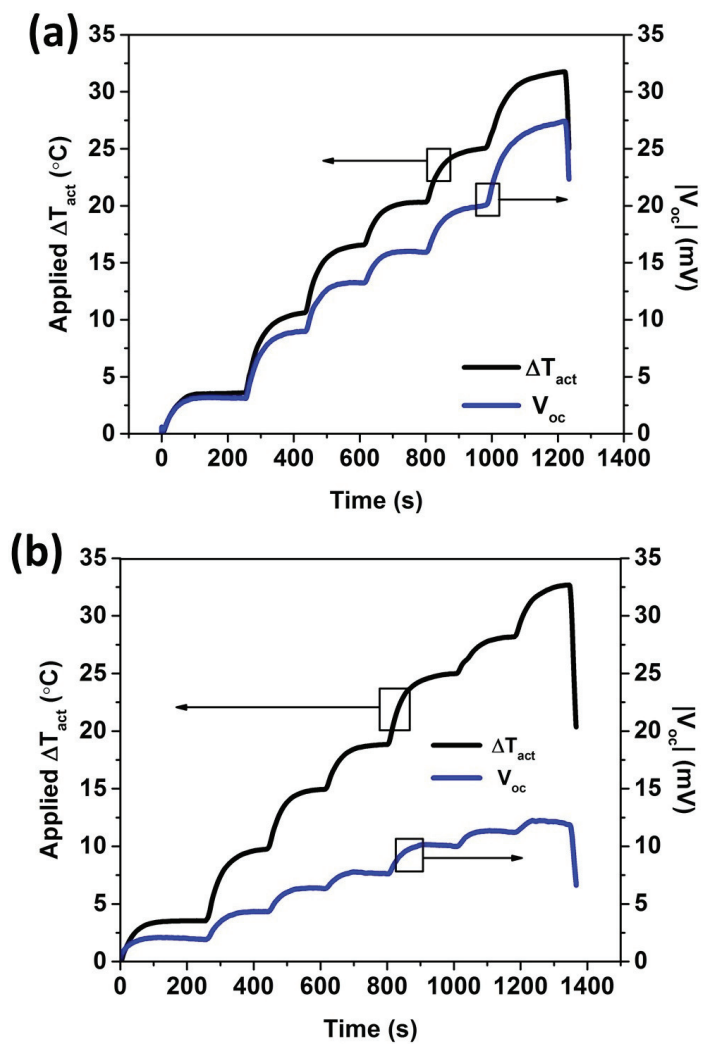
Fig. S19. Thermoelectric response to applied temperature gradients for TCSC device with film thickness (a) 1.5 mm and (b) 0.3 mm. The ΔT_{ext} was raised in steps of 5 $^\circ$ C. The V_{oc} was recorded after maintaining the corresponding value of ΔT_{ext} for 3 minutes.

Comparison of electrochemical performance of TCSC devices composed of bare CC and CC/GP electrodes
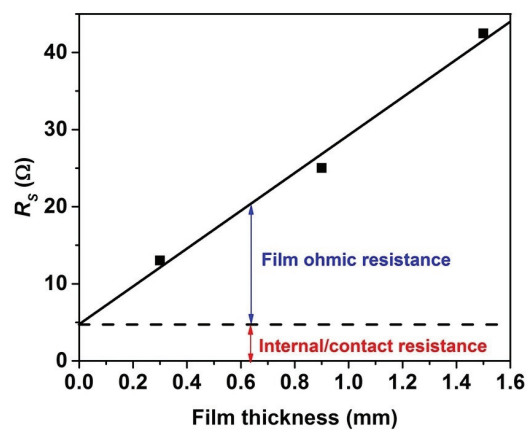
Fig. S20. Internal resistance of the TCSC device (obtained from x-intercept of the Nyquist plot shown in Figure 5c) plotted as a function of the gel film thickness.

Thermistor calibration: The thermistor used for temperature measurements at the hot and cold faces of the device was calibrated with a standard Parr 6775 digital thermometer. Both the probes were immersed in a beaker of water placed on a hot plate. The thermistor was placed in series with a resistor of fixed resistance 4.7 kΩ. The resistance of the thermistor was derived from the voltage reading across the thermistor. The temperature corresponding to the resistance value calculated was derived from the manufacturer's specifications databook. The results are shown in Table S1.

Table S1.
Calibration data for thermistor

Standard temperature	Thermistor resistance	Thermistor temperature	Error (%)
21.388	11.775	21.365	0.107
22.500	11.181	22.481	0.082
22.800	11.033	22.779	0.094
23.500	10.697	23.478	0.094
24.000	10.465	23.967	0.136
24.500	10.238	24.472	0.116
25.000	10.015	24.966	0.134

Model equations for different phases of the thermal charging experiment:

The analytical equations of voltage and current across the load terminals are listed below:

Phase 1:

$$V = \frac{S\Delta T R_{mc}}{R_S + R_L + R_{mc}}(1 - exp(-\frac{R_S + R_L + R_{mc}}{R_L C(R_S + R_{mc})}t_1)) + \frac{S.\Delta T R_{mc}}{R_S + R_{mc}}exp(-\frac{R_S + R_L + R_{mc}}{R_L C(R_S + R_{mc})}t_1)$$

$$V_1 = \frac{S\Delta T R_L}{R_S + R_L + R_{mc}}(1 - exp(-\frac{R_S + R_L + R_{mc}}{R_L C(R_S + R_{mc})}t_1))$$

$$I = \frac{V}{R_{mc}}$$

$$I_L = \frac{S\Delta T}{R_S + R_L + R_{mc}}(1 - exp(-\frac{R_S + R_L + R_{mc}}{R_L C(R_S + R_{mc})}t_1))$$

$$I_1 = I - I_L$$

$$(S1)$$

Phase 2:

$$V = S.\Delta T - \frac{S\Delta T R_L}{R_S + R_L + R_{mc}}(1 - exp(-\frac{R_S + R_L + R_{mc}}{R_L C(R_S + R_{mc})}t_1))exp(-\frac{t_2}{R_L C})$$

$$V_1 = \frac{S\Delta T R_L}{R_S + R_L + R_{mc}}(1 - exp(-\frac{R_S + R_L + R_{mc}}{R_L C(R_S + R_{mc})}t_1))exp(-\frac{t_2}{R_L C})$$

$$I = 0$$

$$I_1 = -I_L = \frac{-S.\Delta T}{R_S + R_L + R_{m,ch}}(1 - exp(-\frac{R_S + R_L + R_{m,ch}}{R_L C(R_S + R_{m,ch})}t_1))exp(-\frac{t_2}{R_L C})$$

$$(S2)$$

Phase 3:

$$V = -\frac{R_{md}}{(R_{md} + R_S)}\frac{S.\Delta T R_L}{(R_S + R_L + R_{mc})}(1 - exp(-\frac{R_S + R_L + R_{mc}}{R_L C(R_S + R_{mc})}t_1))exp(-\frac{t_2}{R_L C})exp(-\frac{R_S + R_L + }{R_L C(R_S + }$$

$$V_1 = \frac{S.\Delta T R_L}{R_S + R_L + R_{mc}}(1 - exp(-\frac{R_S + R_L + R_{mc}}{R_L C(R_S + R_{mc})}t_1))exp(-\frac{t_2}{R_L C})exp(-\frac{R_S + R_L + R_{md}}{R_L C(R_S + R_{md})}t_3)$$

$$I = \frac{V}{R_{md}}$$

$$I_L = \frac{S.\Delta T}{R_S + R_L + R_{mc}}(1 - exp(-\frac{R_S + R_L + R_{mc}}{R_L C(R_S + R_{mc})}t_1))exp(-\frac{t_2}{R_L C})exp(-\frac{R_S + R_L + R_{md}}{R_L C(R_S + R_{md})}t_3)$$

$$I_1 = I - I_L$$

$$(S3)$$

The corresponding quantities called $E_{Rm,ch}$, $E_{Rs,ch}$, $E_{C,ch}$ and $E_{Rl,ch}$ are given by,

$$E_{Rm,ch} = \int_0^{t_1} I^2 R_{mc} dt, \tag{S4}$$

$$E_{Rs,ch} = \int_0^{t_1} I^2 R_S dt, \tag{S5}$$

$$E_{C,ch} = \int_0^{t_1} I_1 V_1 dt, \tag{S6}$$

$$E_{Rl,ch} = \int_0^{t_1} I_L^2 R_L dt. \tag{S7}$$

$$E_{C,dc} = \int_{t_1+t_2}^{t_1+t_2+t_3} I_1 V_1 dt \tag{S8}$$

$$E_{Rm,dc} = \int_{t_1+t_2}^{t_1+t_2+t_3} I^2 R_{md} dt \tag{S9}$$

$$E_{Rs,dc} = \int_{t_1+t_2}^{t_1+t_2+t_3} I^2 R_S dt \tag{S10}$$

$$E_{Rl,dc} = \int_{t_1+t_2}^{t_1+t_2+t_3} I_L^2 R_L dt. \tag{S11}$$

Equations for deriving various performance parameters: Specific capacitance derived from cyclic voltammetry (CV) in three electrode configuration is calculated from:

$$C_{s1} = \frac{1}{2sA(V_h - V_l)} \int_{V_s \to V_h \to V_l} I(V)dV \qquad \text{(A-5)}$$

where C_{s1} is the specific capacitance in F cm^{-2}, A is the geometric area of the electrodes, V_h and V_l are the high and low voltage limits of the CV tests, I is the instantaneous current measured during the CV test and V is the instantaneous applied voltage. The same expression is used to calculate the device capacitance C_{dev} from the obtained CV curves. The area-specific capacitance of the device derived from the galvanostatic charge/discharge cycling is

$$C_{s2} = \frac{I.t_{dis}}{A\Delta V}, \qquad \text{(S12)}$$

whereas the internal resistance derived from the galvanostatic charge/discharge cycling is

$$R = \frac{IR_{drop}}{2I}. \qquad \text{(S13)}$$

The coulombic efficiency for a single charge/discharge cycle is

$$\eta_{coul} = \frac{q_{discharge}}{q_{charge}} = \frac{I.t_{discharge}}{I.t_{charge}} = \frac{t_{discharge}}{t_{charge}}. \qquad \text{(S14)}$$

Low coulombic efficiency is generally attributed to losses of charge due to self-discharge occurring from shuttling of mobile redox species. The capacitance retention percentage (η_{ret}) at the end of cyclic stability test conducted by cycling the device at the same current density for numerous cycles using

$$\eta_{ret} = \frac{C_{s1f}}{C_{s1i}} \times 100\% \qquad \text{(S15)}$$

where C_{s1f} and C_{s1i} are the device capacitance at the end and beginning of the cyclic stability test respectively.

Table S2.

Property comparison of the gel electrolyte used in this work with Bi_2Te_3 solid state thermoelectric.

Material	σ (S m^{-1})	κ (W m^{-1} K^{-1})	S_e (μ V K^{-1}))	Ref.
Bi_2Te_3	20000	0.216	190	[76]
$PVA/K_3Fe(CN)_6/K_4Fe(CN)_6$	0.6	1.85	1210	[83]

Table S3.

Comparison of various device combinations for energy capture from intermittent heat source with $\Delta T = 10°C$

Device	Efficiency (%)	Energy Density E_{ch} (μJ cm^{-2})	Flexibility	Cost
TCSC	4.78×10^{-5}	973	Yes	Low
Bi_2Te_3 and $PVA/K_3Fe(CN)_6/K_4Fe(CN)_6$ SC	0.55	24	No	High

The maximum charging efficiency of the TCSC device ($\eta = \frac{E_{ch}}{Q_{in}}$) is expressed as [66]

$$\eta = \frac{\Delta T}{2T_H + 10\frac{\lambda}{\sigma\alpha^2} - \frac{1}{2}\Delta T}. \tag{S16}$$

Influence of tunable parameters such as load resistance applied during thermal charging phase (Phase 1), and hold time applied on the energy storage characteristics, as evaluated from the equivalent circuit model

It can be observed from Figure S8 that as the load resistance value R_{mch} is raised for a fixed hold time duration, the charge and energy stored in the capacitor C decrease. This is because the small charging current is unable to charge the capacitor upto the thermoinduced voltage within the given charging time period. This also implies that if the device is allowed to thermally charge for a longer duration, the device can attain the maximum open circuit voltage value.
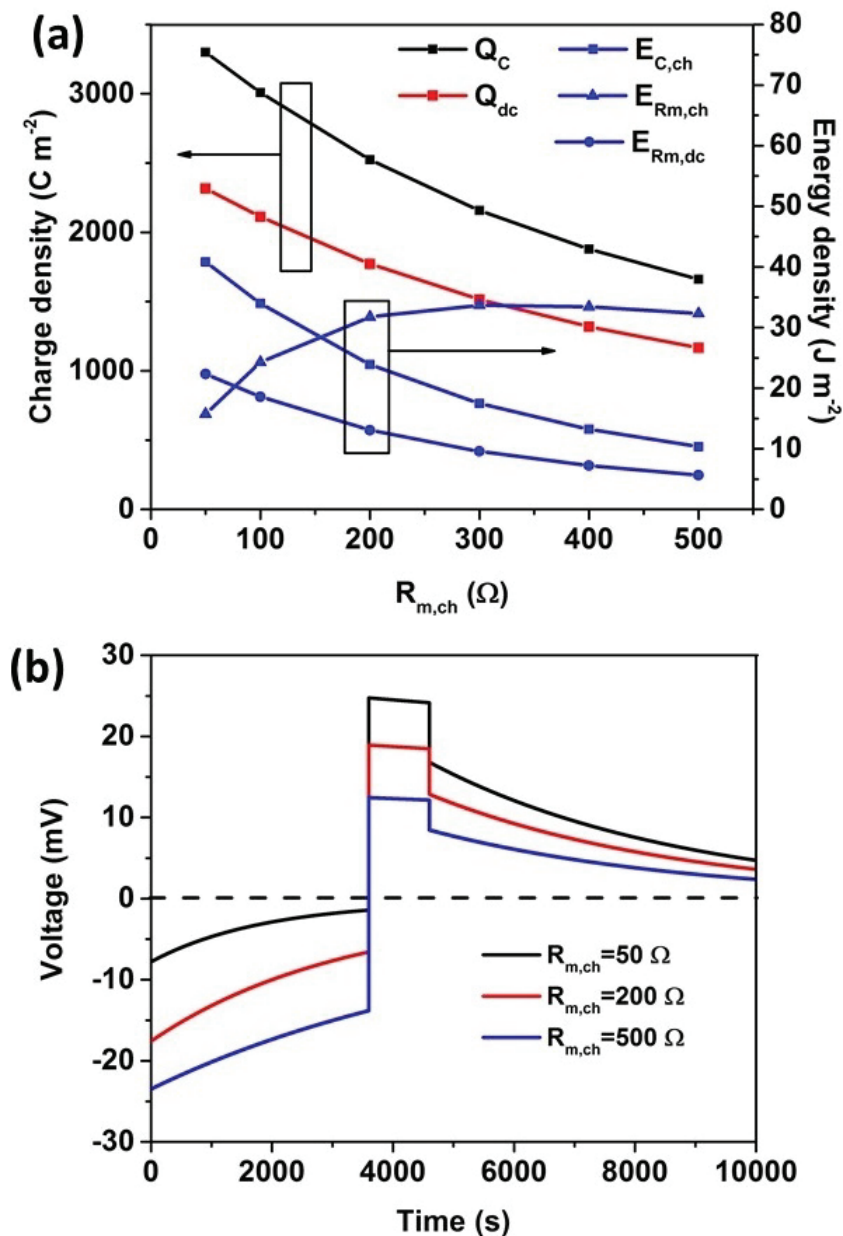
Fig. S21. Influence of load resistance $R_{m,ch}$ on the charge storage characteristics of the TCSC device, as obtained from the equivalent circuit model. (a) Variation of charge stored in capacitor C during the thermal charging phase Q_C, charge released by the capacitor during discharge Q_{dc}, energy output in the load resistor $R_{m,ch}$ during thermal charging $E_{Rm,ch}$, energy stored in the capacitor C during thermal charging $E_{C,ch}$ and energy output in the load resistor $R_{m,dc}$ during discharge. (b) Voltage profiles for different values of load resistance applied during thermal charging. The values of thermal charging time and actual temperature gradient ΔT_{act} have been kept fixed at 3600 s and 30 °C respectively.
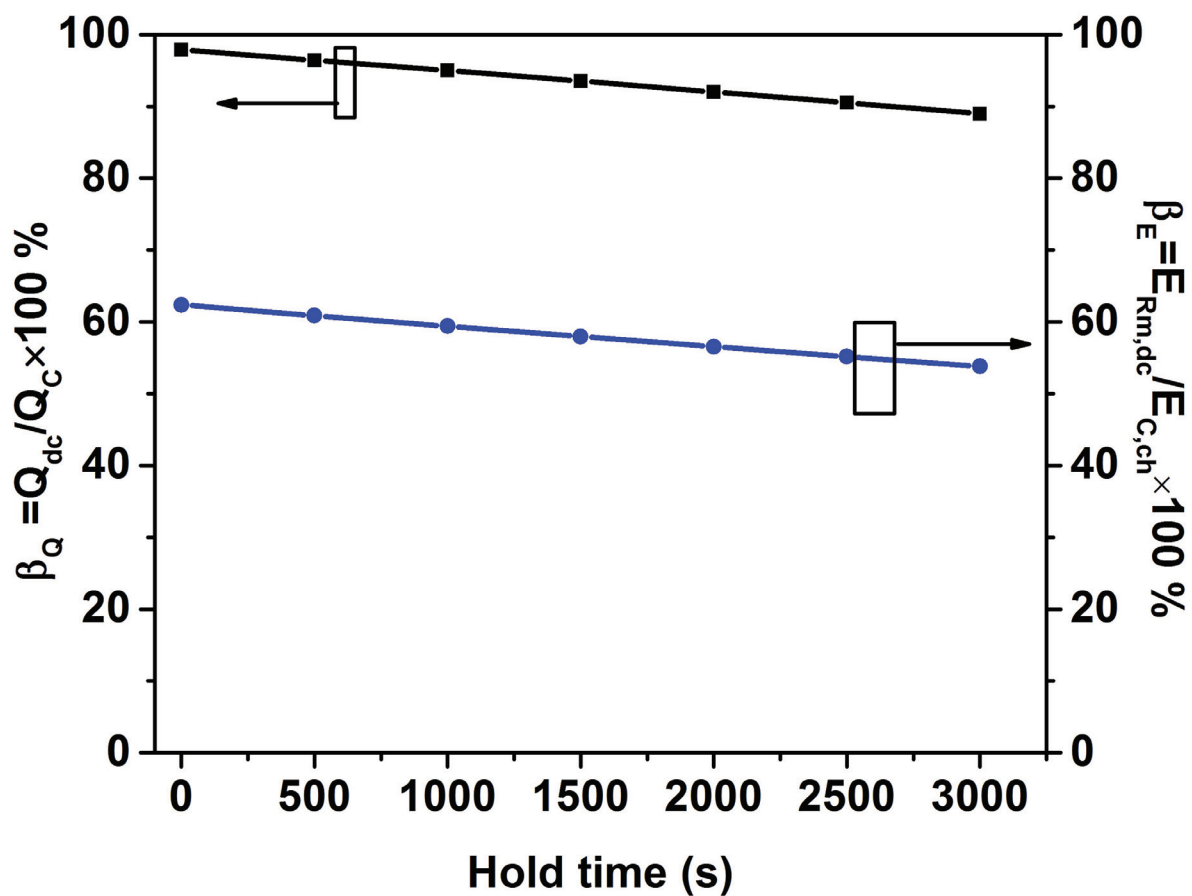
Fig. S22. Influence of hold time duration on the charge retention coefficient β_Q and the energy retention coefficient β_E.

CURRICULUM VITAE

Education

Purdue University

PhD in Mechancial Engineering   Aug. 2013 - present

- GPA: **3.97/4.0**

- Advisor: Prof. Timothy S. Fisher

Indian Institute of Technology, Kharagpur

Bachelor of Technology in Mechanical Engineering

Master of Technology in Thermal Engineering   July 2008 - May 2013

- GPA: **8.84/10**

Teaching experience

- Instructor for undergraduate course on Heat and Mass Transfer, ME315 at Purdue University for spring 2018 as a part of Ward A. Lambert fellowship

Publications

Journal Publications

- **<u>Kundu A.</u>**, Maize K., Xiong G., Saviers K., Fisher T.S., Ali S., Electroreflectance imaging of gold-H3PO4 supercapacitors. Part I: Experiment methodology, *RSC Analyst*, 2016, Vol.141, pp.1448-1461.

- Saviers K., **<u>Kundu A.</u>**, Maize K., Ali S., Fisher T.S., Electroreflectance imaging of gold-H3PO4 supercapacitors. Part II: microsupercapacitor ageing characterization, *RSC Analyst* 2016, Vol.141, pp.1462-1471.

- **<u>Kundu A.</u>**, Alrefae M., Fisher T.S., Magnetothermoelectric effects in graphene and its dependence on scatterer concentration, magnetic field and band gap *Journal of Applied Physics* 2017, Vol. 121, pp.125113.

- **<u>Kundu A.</u>**, Chowdhury K., Evaluating performance of mixed mode multistage helium plants for design and off-design conditions by exergy analysis, *International Journal of Refrigeration*, 2014, Vol.38, pp.46-57.

- **<u>Kundu A.</u>**, Fisher T.S., Harnessing the thermogalvanic effect of the ferro/ferricyanide redox couple in a thermally chargeable supercapacitor *(under review)*

- **<u>Kundu A.</u>**, Fisher T.S., A symmetric all-solid-state supercapacitor operating at 1.5 V using a redox-active gel electrolyte*(under review)*

- **<u>Kundu A.</u>**, Fisher T.S., Mathematical modeling of rate capability in electrical double layer capacitors *(draft)*

- **<u>Kundu A.</u>**, Fisher T.S., Mathematical modeling of temperature evolution in electrical double layer capacitors *(draft)*

Book

- Xiong G., **<u>Kundu A.</u>**, Fisher T.S., Thermal effects in supercapacitors, *Springer Briefs,* 2015.

Conference Proceedings

- **<u>Kundu A.</u>**, Fisher T.S., Novel redox gel electrolytes for all-solid-state supercapacitors, *232nd ECS Meeting, Oct 2017, National Harbor, MD, USA.*

- **<u>Kundu A.</u>**, Fisher T.S., Thermoelectric supercapacitor for waste heat recovery, *2nd Thermal and Fluid Engineering Conference, April 2017, Las Vegas, NV, USA.*

- **<u>Kundu A.</u>**, Thomas R.J., Ghosh P., Chowdhury K., Exergy Analysis to Determine Appropriate Design and Operating Parameters for Collins Refrigerator-Liquefier under Mixed Mode Operation, *12th Cryogenics Conference 2012, IIR International Conference, Dresden, Germany*, pp.233-239.

Skills

- Programming in Matlab, Python Comsol, Simulink, Fluent, Autocad

- Handling large datasets in Python using numpy and pandas libraries

- Data acquisition using Labview

- Fabricating graphene-based planar sandwich supercapacitor devices

- Using Gamry for electrochemical characterization of supercaapcitors by electrical impedance spectroscopy (EIS), cyclic voltammetry, constant current charge/discharge

- Chemical vapor deposition of graphene on carbon substrates

- SEM characterization

- Cleanroom trained to work with chemicals in hood

- Documentation in Word, Mathtype, Latex, Origin

PhD thesis

- Equivalent circuit modeling of an all-solid-state thermally chargeable supercapacitor

- Equivalent circuit modeling of electroreflectance phenomenon in gold electrode microsupercapacitors

- Continuum modeling of electrochemical performance and heat generation in EDLCs under galvanostatic charge/discharge operation

- Semiclassical BTE modeling of Nernst effect in single-layer graphene

Bachelors and Masters Thesis

- Dynamic modeling of helium pressurization systems in pump-fed liquid propellant rocket engines in Aspen Custom Modeler V.7.0 (modeling)

- Determination of optimum geometric and process parameters for Collins Refrigerator-Liquefier under mixed mode operation using Aspen Hysys V. 7.0 (modeling)

Awards

- Ward A. Lambert Teaching Fellow, Purdue University, 2017

- ECS Travel Grant 2017

- Department of Mechanical Engineering Travel Grant, Purdue University, 2017

- Best Poster Award at Indo-US workshop, 2017 held in Bangalore, India.

- Research Assistant (Aug. 2013-present)

- Merit-cum-means scholarship (2010-2012)

- NTSE scholarship (2009-2010)

REFERENCES

REFERENCES

[1] G. Xiong, A. Kundu, and T. S. Fisher, *Thermal effects in supercapacitors.* SpringerBriefs in Thermal Engineering and Applied Science, 2015.

[2] M. Winter and R. J. Brodd, "What are batteries, fuel cells, and supercapacitors?" *Chem Rev*, vol. 104, pp. 4245–4269, 2004.

[3] B. Zhang, F. Kang, J.-M. Tarascon, and J.-K. Kim, "Recent advances in electrospun carbon nanofibers and their application in electrochemical energy storage," *Progress in Materials Science*, vol. 76, pp. 319 – 380, 2016.

[4] A. Burke, "Ultracapacitors: why, how, and where is the technology," *Journal of Power Sources*, vol. 91, no. 1, pp. 37 – 50, 2000.

[5] M. Armand, F. Endres, D. R. Macfarlane, H. Ohno, and B. Scrosati, "Ionic-liquid materials for the electrochemical challenges of the future," *Nature Materials*, no. 1, pp. 621–629, 2009.

[6] A. K. Shukla, S. Sampath, and K. Vijayamohanan, "Electrochemical supercapacitors: Energy storage beyond batteries," *Current Science*, vol. 79, no. 12, pp. 1656–1661, 2000.

[7] T. M. Bandhauer, S. Shukla, and T. F. Fueller, "A critical review of thermal issues in lithium-ion batteries," *Journal of the Electrochemical Society*, vol. 158, pp. R1–R25, 2011.

[8] G. Xiong, K. Hembram, R. Reifenberger, and T. S. Fisher, "Mno2-coated graphitic petals for supercapacitor electrodes," *Journal of Power Sources*, vol. 227, pp. 254 – 259, 2013.

[9] G. Xiong, C. Meng, R. G. Reifenberger, P. P. Irazoqui, and T. S. Fisher, "Graphitic petal electrodes for all-solid-state flexible supercapacitors," *Advanced Energy Materials*, vol. 4, no. 3, pp. 1 300 515–n/a, 2014.

[10] S. Roldan, C. Blanco, M. Granda, R. Menendez, and R. Santamaria, "Towards a further generation of high-energy carbon-based capacitors by using redox-active electrolytes," *Angewandte Chemie*, vol. 50, pp. 1699–1701, 2011.

[11] S. T. Senthilkumar, R. K. Selvan, and J. S. Melo, "Redox additive/active electrolytes: a novel approach to enhance the performance of supercapacitors," *J. Mater. Chem. A*, vol. 1, pp. 12 386–12 394, 2013.

[12] H. Yu, J. Wu, J. Lin, L. Fan, M. Huang, Y. Lin, Y. Li, F. Yu, and Z. Qiu, "A reversible redox strategy for swcnt-based supercapacitors using a high-performance electrolyte," *ChemPhysChem*, vol. 14, pp. 394–399, 2013.

[13] H. Yu, J. Wu, L. Fan, K. Xu, X. Zhong, Y. Lin, and J. Lin, "Improvement of the performance for quasi-solid-state supercapacitor by using pvakohki polymer gel electrolyte," *Electrochimica Acta*, vol. 56, no. 20, pp. 6881 – 6886, 2011.

[14] L.-Q. Fan, J. Zhong, J.-H. Wu, J.-M. Lin, and Y.-F. Huang, "Improving the energy density of quasi-solid-state electric double-layer capacitors by introducing redox additives into gel polymer electrolytes," *Journal of Materials Chemistry A*, vol. 2, p. 9011, 2014.

[15] G. Lota and E. Frackowiak, "Striking capacitance of carbon/iodide interface," *Electrochemistry Communications*, vol. 11, pp. 87–90, 2009.

[16] J. Zhou, J. Cai, S. Cai, X. Zhou, and A. N. Mansour, "Development of all-solid-state mediator-enhanced supercapacitors with polyvinylidene fluoride/lithium trifluoromethanesulfonate separators," *Journal of Power Sources*, vol. 196, pp. 10 479–10 483, 2011.

[17] K. Sun, E. Feng, H. Peng, G. Mab, Y. Wu, H. Wang, and Z. Lei, "A simple and high-performance supercapacitor based on nitrogen-doped porous carbon in redox-mediated sodium molybdate electrolyte," *Electrochimica Acta*, vol. 158, pp. 361–367, 2015.

[18] G. Ma, J. Li, K. Sun, H. Peng, J. Mu, and Z. Lei, "High performance solid-state supercapacitor with pva-koh-k3[fe(cn)6] gel polymer as electrolyte and separator," *Journal of Power Sources*, vol. 256, pp. 281–287, 2014.

[19] D. Zhao, H. Wang, Z. U. Khan, J. C. Chen, R. Gabrielsson, M. P. Jonsson, M. Berggren, and X. Crispin, "Ionic thermoelectric supercapacitors," *Energy Environ. Sci.*, vol. 9, pp. 1450–1457, 2016.

[20] M. S. Romano, N. Li, D. Antiohos, J. M. Razal, A. Nattestad, S. Beirne, S. Fang, Y. Chen, R. Jalili, G. G. Wallace, R. Baughman, and J. Chen, "Carbon nanotube reduced graphene oxide composites for thermal energy harvesting applications," *Advanced Materials*, vol. 25, no. 45, pp. 6602–6606, 2013.

[21] H. Im, H. G. Moon, J. S. Lee, I. Y. Chung, T. J. Kang, and Y. H. Kim, "Flexible thermocells for utilization of body heat," *Nano Research*, vol. 7, pp. 443–452, 2014.

[22] R. Hu, B. A. Cola, N. Haram, J. N. Barisci, S. Lee, S. Stoughton, G. Wallace, C. Too, M. Thomas, A. Gestos, M. E. d. Cruz, J. P. Ferraris, A. A. Zakhidov, and R. H. Baughman, "Harvesting waste thermal energy using a carbon-nanotube-based thermo-electrochemical cell," *Nano Letters*, vol. 10, no. 3, pp. 838–846, 2010.

[23] T. J. Kang, S. Fang, M. E. Kozlov, C. S. Haines, N. Li, Y. H. Kim, Y. Chen, and R. H. Baughman, "Electrical power from nanotube and graphene electrochemical thermal energy harvesters," *Advanced Functional Materials*, vol. 22, no. 3, pp. 477–489, 2012.

[24] K. Maize, A. Kundu, G. Xiong, K. Saviers, T. S. Fisher, and A. Shakouri, "Electroreflectance imaging of gold-h3po4 supercapacitors. part i: experimental methodology," *Analyst*, vol. 141, pp. 1448–1461, 2016.

[25] K. R. Saviers, A. Kundu, K. Maize, A. Shakouri, and T. S. Fisher, "Electroreflectance imaging of gold-h3po4 supercapacitors. part ii: microsupercapacitor ageing characterization," *Analyst*, vol. 141, pp. 1462–1471, 2016.

[26] T. Cottineau, M. Toupin, T. Delahaye, T. Brousse, and D. Bélanger, "Nanostructured transition metal oxides for aqueous hybrid electrochemical supercapacitors," *Applied Physics A*, pp. 599–606, 2006.

[27] L.-Z. Fan, Y.-S. Hu, J. Maier, P. Adelhelm, B. Smarsly, and M. Antonietti, "High electroactivity of polyaniline in supercapacitors by using a hierarchically porous carbon monolith as a support," *Advanced Functional Materials*, vol. 17, no. 16, pp. 3083–3087, 2007.

[28] E. Frackowiak, K. Fic, M. Meller, and G. Lota, "Electrochemistry serving people and nature: High-energy ecocapacitors based on redox-active electrolytes," *ChemSusChem*, vol. 5, no. 7, pp. 1181–1185, 2012.

[29] J. Zhong, L.-Q. Fan, X. Wu, J.-H. Wu, G.-J. Liu, J.-M. Lin, M.-L. Huang, and Y.-L. Wei, "Improved energy density of quasi-solid-state supercapacitors using sandwich-type redox-active gel polymer electrolytes," *Electrochimica Acta*, vol. 166, pp. 150–156, 2015.

[30] J. Lee, S. Choudhury, D. Weingarth, D. Kim, and V. Presser, "High performance hybrid energy storage with potassium ferricyanide redox electrolyte," *ACS Applied Materials & Interfaces*, vol. 8, no. 36, pp. 23 676–23 687, 2016.

[31] B. Akinwolemiwa, C. Peng, and G. Z. Chen, "Redox electrolytes in supercapacitors," *Journal of the Electrochemical Society*, vol. 162, pp. A5054–A5059, 2015.

[32] Y. Tian, J. Yan, R. Xue, and B. Yi, "Capacitive properties of activated carbon in k4fe(cn)6," *Journal of the Electrochemical Society*, vol. 158, no. 7, pp. A818–A821, 2011.

[33] L.-Q. Fan, J. Zhong, C.-Y. Zhang, J.-H. Wu, and Y.-L. Wei, "Improving the energy density of quasi-solid-state supercapacitors by assembling two redox-active gel electrolytes," *International Journal of Hydrogen Energy*, vol. 41, pp. 5725–5732, 2016.

[34] J. M. Nugent, K. S. V. Santhanam, A. Rubio, and P. M. Ajayan, "Fast electron transfer kinetics on multiwalled carbon nanotube microbundle electrodes," *Nano Letters*, vol. 1, no. 2, pp. 87–91, 2001.

[35] J. Okuno, K. Maehashi, K. Matsumoto, K. Kerman, Y. Takamura, and E. Tamiya, "Single-walled carbon nanotube-arrayed microelectrode chip for electrochemical analysis," *Electrochemistry Communications*, vol. 9, no. 1, pp. 13 – 18, 2007.

[36] P. Yang, K. Liu, Q. Chen, X. Mo, Y. Zhou, S. Li, G. Feng, and J. Zhou, "Wearable thermocells based on gel electrolytes for the utilization of body heat," *Angewandte Chemie*, vol. 128, pp. 1–5, 2016.

[37] H. K. Ali and A. C. Baratunde, "Electrochemical characterization of carbon nanotube and poly (3,4-ethylenedioxythiophene)poly(styrenesulfonate) composite aqueous electrolyte for thermo-electrochemical cells," *Journal of the Electrochemical Society*, pp. F867–F871, 2016.

[38] S. A. Hashmi, R. J. L. anf R. G. Linford, and W. S. Schlindwein, "Studies on all solid state electric double layer capacitors using proton and lithium ion conducting polymer electrolytes," *Journal of Chemical Society Faraday Transactions*, vol. 93, pp. 4177–4182, 1997.

[39] G. Ma, E. Feng, K. Sun, H. Peng, J. Li, and Z. Lei, "A novel and high-effective redox-mediated gel polymer electrolyte for supercapacitor," *Electrochimica Acta*, vol. 135, pp. 461–466, 2014.

[40] A. Kumar, M. R. Maschmann, S. L. Hodson, J. Baur, and T. S. Fisher, "Carbon nanotube arrays decorated with multi-layer graphene-nanopetals enhance mechanical strength and durability," *Carbon*, vol. 84, pp. 236 – 245, 2015.

[41] "Crc handbook of chemistry and physics," Boca Raton, FL, 1999.

[42] G. Wang, J. Huang, S. Chen, Y. Gao, and D. Cao, "Preparation and supercapacitance of cuo nanosheet arrays grown on nickel foam," *Journal of Power Sources*, vol. 196, no. 13, pp. 5756 – 5760, 2011.

[43] J. Xu, S. Gai, F. He, N. Niu, P. Gao, Y. Chen, and P. Yang, "A sandwich-type three-dimensional layered double hydroxide nanosheet array/graphene composite: fabrication and high supercapacitor performance," *J. Mater. Chem. A*, vol. 2, pp. 1022–1031, 2014.

[44] G. Xiong, C. Meng, R. G. Reifenberger, P. P. Irazoqui, and T. S. Fisher, "Graphitic petal electrodes for all-solid-state flexible supercapacitors," *Advanced Energy Materials*, vol. 4, no. 3, pp. 1 300 515–n/a, 2014.

[45] M. F. El-Kady, V. Strong, S. Dubin, and R. B. Kaner, "Laser scribing of high-performance and flexible graphene-based electrochemical capacitors," *Science*, vol. 335, no. 6074, pp. 1326–1330, 2012.

[46] L. Yuan, X.-H. Lu, X. Xiao, T. Zhai, J. Dai, F. Zhang, B. Hu, X. Wang, L. Gong, J. Chen, C. Hu, Y. Tong, J. Zhou, and Z. L. Wang, "Flexible solid-state supercapacitors based on carbon nanoparticles/mno2 nanorods hybrid structure," *ACS Nano*, vol. 6, no. 1, pp. 656–661, 2012.

[47] X. Lu, M. Yu, G. Wang, T. Zhai, S. Xie, Y. Ling, Y. Tong, and Y. Li, "H-tio2@mno2//h-tio2@c coreshell nanowires for high performance and flexible asymmetric supercapacitors," *Advanced Materials*, vol. 25, no. 2, pp. 267–272, 2013.

[48] X. Xiao, T. Li, P. Yang, Y. Gao, H. Jin, W. Ni, W. Zhan, X. Zhang, Y. Cao, J. Zhong, L. Gong, W.-C. Yen, W. Mai, J. Chen, K. Huo, Y.-L. Chueh, Z. L. Wang, and J. Zhou, "Fiber-based all-solid-state flexible supercapacitors for self-powered systems," *ACS Nano*, vol. 6, no. 10, pp. 9200–9206, 2012.

[49] S. Senthilkumar, R. Selvan, N. Ponpandian, and J. Melo, "Redox additive aqueous polymer gel electrolyte for an electric double layer capacitor," *RSC Advances*, vol. 2, pp. 8937–8940, 2012.

[50] Y. Xie, Y. Liu, Y. Zhao, Y. H. Tsang, S. P. Lau, H. Huang, and Y. Chai, "Stretchable all-solid-state supercapacitor with wavy shaped polyaniline/graphene electrode," *J. Mater. Chem. A*, vol. 2, pp. 9142–9149, 2014.

[51] E. Feng, G. Ma, K. Sun, F. Ran, H. Peng, and Z. Lei, "Superior performance of an active electrolyte enhanced supercapacitor based on a toughened porous network gel polymer," *New J. Chem.*, vol. 41, pp. 1986–1992, 2017.

[52] S.-E. Chun, B. Evanko, X. Wang, D. Vonlanthen, X. Ji, G. D. Stucky, and S. W. Boettcher, "Design of aqueous redox-enhanced electrochemical capacitors with high specific energies and slow self-discharge," *Nature Communications*, vol. 6, p. 7818, 2015.

[53] L. Chen, H. Bai, Z. Huang, and L. Li, "Mechanism investigation and suppression of self-discharge in active electrolyte enhanced supercapacitors," *Energy Environ. Sci.*, vol. 7, pp. 1750–1759, 2014.

[54] C. Meng, C. Liu, L. Chen, C. Hu, and S. Fan, "Highly flexible and all-solid-state paperlike polymer supercapacitors," *Nano Letters*, vol. 10, no. 10, pp. 4025–4031, 2010.

[55] Q. Chen, X. Li, X. Zang, Y. Cao, Y. He, P. Li, K. Wang, J. Wei, D. Wu, and H. Zhu, "Effect of different gel electrolytes on graphene-based solid-state supercapacitors," *RSC Adv.*, vol. 4, pp. 36 253–36 256, 2014.

[56] A. Balducci, R. Dugas, P. Taberna, P. Simon, D. Plee, M. Mastragostino, and S. Passerini, "High temperature carboncarbon supercapacitor using ionic liquid as electrolyte," *Journal of Power Sources*, vol. 165, no. 2, pp. 922 – 927, 2007.

[57] A. Balducci, W. A. Henderson, M. Mastragostino, S. Passerini, P. Simon, and F. Soavi, "Cycling stability of a hybrid activated carbon//poly(3-methylthiophene) supercapacitor with n-butyl-n-methylpyrrolidinium bis(trifluoromethanesulfonyl)imide ionic liquid as electrolyte," *Electrochimica Acta*, vol. 50, no. 11, pp. 2233 – 2237, 2005.

[58] Z. Fan, J. Yan, T. Wei, L. Zhi, G. Ning, T. Li, and F. Wei, "Asymmetric supercapacitors based on graphene/mno2 and activated carbon nanofiber electrodes with high power and energy density," *Advanced Functional Materials*, vol. 21, no. 12, pp. 2366–2375, 2011.

[59] J. Yan, Z. Fan, W. Sun, G. Ning, T. Wei, Q. Zhang, R. Zhang, L. Zhi, and F. Wei, "Advanced asymmetric supercapacitors based on ni(oh)2/graphene and porous graphene electrodes with high energy density," *Advanced Functional Materials*, vol. 22, no. 12, pp. 2632–2641, 2012.

[60] D. Weingarth, H. Noh, A. Foelske-Schmitz, A. Wokaun, and R. Kotz, "A reliable determination method of stability limits for electrochemical double layer capacitors," *Electrochimica Acta*, vol. 103, pp. 119 – 124, 2013.

[61] X. Kang, P. D. Sheng, and J. T.Richard, "Toward reliable values of electrochemical stability limits for electrolytes," *Journal of the Electrochemical Society*, vol. 146, pp. 4172–4178, 1999.

[62] X. Lu, M. Yu, G. Wang, T. Zhai, S. Xie, Y. Ling, Y. Tong, and Y. Li, "H-tio2@mno2//h-tio2@c coreshell nanowires for high performance and flexible asymmetric supercapacitors," *Advanced Materials*, vol. 25, no. 2, pp. 267–272, 2013.

[63] L. Yuan, X.-H. Lu, X. Xiao, T. Zhai, J. Dai, F. Zhang, B. Hu, X. Wang, L. Gong, J. Chen, C. Hu, Y. Tong, J. Zhou, and Z. L. Wang, "Flexible solid-state supercapacitors based on carbon nanoparticles/mno2 nanorods hybrid structure," *ACS Nano*, vol. 6, no. 1, pp. 656–661, 2012.

[64] M. Kaempgen, C. K. Chan, J. Ma, Y. Cui, and G. Gruner, "Printable thin film supercapacitors using single-walled carbon nanotubes," *Nano Letters*, vol. 9, no. 5, pp. 1872–1876, 2009.

[65] D. Pech, M. Brunet, H. Durou, P. Huang, V. Mochalin, Y. Gogotsi, P.-L. Taberna, and P. Simon, "Ultrahigh-power micrometre-sized supercapacitors based on onion-like carbon," *Nature Nanotechnology*, vol. 5, pp. 651–654, 2010.

[66] H. Wang, D. Zhao, Z. U. Khan, S. Puzinas, M. P. Jonsson, M. Berggren, and X. Crispin, "Ionic thermoelectric figure of merit for charging of supercapacitors," *Advanced Electronic Materials*, vol. 3, no. 4, p. 1700013, 2017.

[67] D. Zhao, S. Fabiano, M. Berggren, and X. Crispin, "Ionic thermoelectric gating organic transistors," *Nature Communications*, vol. 8, p. 14214, 2017.

[68] M. Bonetti, S. Nakamae, M. Roger, and P. Guenoun, "Huge seebeck coefficients in nonaqueous electrolytes," *The Journal of Chemical Physics*, vol. 134, p. 114513, 2011.

[69] W. B. Chang, H. Fang, J. Liu, C. M. Evans, B. Russ, B. C. Popere, S. N. Patel, M. L. Chabinyc, and R. A. Segalman, "Electrochemical effects in thermoelectric polymers," *ACS Macro Letters*, vol. 5, no. 4, pp. 455–459, 2016.

[70] H. Wang, U. Ail, R. Gabrielsson, M. Berggren, and X. Crispin, "Ionic seebeck effect in conducting polymers," *Advanced Energy Materials*, vol. 5, no. 11, p. 1500044, 2015.

[71] H. Im, H. G. Moon, J. S. Lee, I. Y. Chung, T. J. Kang, and Y. H. Kim, "Flexible thermocells for utilization of body heat," *Nano Research*, vol. 7, no. 4, pp. 443–452, 2014.

[72] A. Kundu, M. A. Alrefae, and T. S. Fisher, "Magnetothermoelectric effects in graphene and their dependence on scatterer concentration, magnetic field, and band gap," *Journal of Applied Physics*, vol. 121, p. 125113, 2017.

[73] T. Ikeshoji, "Thermoelectric conversion by thin-layer thermogalvanic cells with soluble redox couples," *Bulletin of the Chemical Society of Japan*, vol. 60, p. 1505, 1987.

[74] T. Quickenden and C. Vernon, "Thermogalvanic conversion of heat to electricity," *Solar Energy*, vol. 36, pp. 63–72, 1986.

[75] B. Burrows, "Discharge behavior of redox therogalvanic cells," *Journal of the Electrochemical Society*, vol. 123, pp. 154–159, 1976.

[76] B. Poudel, Q. Hao, Y. Ma, Y. Lan, A. Minnich, B. Yu, X. Yan, D. Wang, A. Muto, D. Vashaee, X. Chen, J. Liu, M. S. Dresselhaus, G. Chen, and Z. Ren, "High-thermoelectric performance of nanostructured bismuth antimony telluride bulk alloys," *Science*, vol. 320, no. 5876, pp. 634–638, 2008.

[77] T. J. Abraham, D. R. MacFarlane, and J. M. Pringle, "High seebeck coefficient redox ionic liquid electrolytes for thermal energy harvesting," *Energy and Environmental Science*, vol. 6, pp. 2639–2645, 2013.

[78] H. Zhou, T. Yamada, and N. Kimizuka, "Supramolecular thermo-electrochemical cells: Enhanced thermoelectric performance by hostguest complexation and salt-induced crystallization," *Journal of the American Chemical Society*, vol. 138, no. 33, pp. 10 502–10 507, 2016.

[79] R. Hu, B. A. Cola, N. Haram, J. N. Barisci, S. Lee, S. Stoughton, G. Wallace, C. Too, M. Thomas, A. Gestos, M. E. d. Cruz, J. P. Ferraris, A. A. Zakhidov, and R. H. Baughman, "Harvesting waste thermal energy using a carbon-nanotube-based thermo-electrochemical cell," *Nano Letters*, vol. 10, no. 3, pp. 838–846, 2010.

[80] M. S. Romano, N. Li, D. Antiohos, J. M. Razal, A. Nattestad, S. Beirne, S. Fang, Y. Chen, R. Jalili, G. G. Wallace, R. Baughman, and J. Chen, "Carbon nanotube reduced graphene oxide composites for thermal energy harvesting applications," *Advanced Materials*, vol. 25, no. 45, pp. 6602–6606, 2013.

[81] P. F. Salazar, S. Kumar, and B. A. Cola, "Nitrogen- and boron-doped carbon nanotube electrodes in a thermo-electrochemical cell," *Journal of The Electrochemical Society*, vol. 159, no. 5, pp. B483–B488, 2012.

[82] P. F. Salazar, S. T. Stephens, A. H. Kazim, J. M. Pringle, and B. A. Cola, "Enhanced thermo-electrochemical power using carbon nanotube additives in ionic liquid redox electrolytes," *J. Mater. Chem. A*, vol. 2, pp. 20 676–20 682, 2014.

[83] P. Yang, K. Liu, Q. Chen, X. Mo, Y. Zhou, S. Li, G. Feng, and J. Zhou, "Wearable thermocells based on gel electrolytes for the utilization of body heat," *Angewandte Chemie International Edition*, vol. 55, no. 39, pp. 12 050–12 053, 2016.

[84] S. L. Kim, H. T. Lin, and C. Yu, "Thermally chargeable solid-state supercapacitor," *Advanced Energy Materials*, vol. 6, no. 18, p. 1600546, 2016.

[85] F. Jiao, A. Naderi, D. Zhao, J. Schlueter, M. Shahi, J. Sundstrom, H. Granberg, J. Edberg, U. Ail, J. W. Brill, T. Lindstrom, M. Berggren, and X. Crispin, "Ionic thermoelectric paper," *J. Mater. Chem. A*, 2017.

[86] L. T. Le, M. H. Ervin, H. Qiu, B. E. Fuchs, and W. Y. Lee, "Graphene supercapacitor electrodes fabricated by inkjet printing and thermal reduction of graphene oxide," *Electrochemistry Communications*, vol. 13, no. 4, pp. 355 – 358, 2011.

[87] A. Yuan and Q. Zhang, "A novel hybrid manganese dioxide/activated carbon supercapacitor using lithium hydroxide electrolyte," *Electrochemistry Communications*, vol. 8, no. 7, pp. 1173 – 1178, 2006.

[88] C. Meng, C. Liu, and S. Fan, "Flexible carbon nanotube/polyaniline paper-like films and their enhanced electrochemical properties," *Electrochemistry Communications*, vol. 11, no. 1, pp. 186 – 189, 2009.

[89] Y.-C. Chen, Y.-K. Hsu, Y.-G. Lin, Y.-K. Lin, Y.-Y. Horng, L.-C. Chen, and K.-H. Chen, "Highly flexible supercapacitors with manganese oxide nanosheet/carbon cloth electrode," *Electrochimica Acta*, vol. 56, no. 20, pp. 7124 – 7130, 2011.

[90] J. Zhong, L.-Q. Fan, X. Wu, J.-H. Wu, G.-J. Liu, J.-M. Lin, M.-L. Huang, and Y.-L. Wei, "Improved energy density of quasi-solid-state supercapacitors using sandwich-type redox-active gel polymer electrolytes," *Electrochimica Acta*, vol. 166, pp. 150 – 156, 2015.

[91] S. Roldan, C. Blanco, M. Granda, R. Menendez, and R. Santamaria, "Towards a further generation of high-energy carbon-based capacitors by using redox-active electrolytes," *Angewandte Chemie International Edition*, vol. 50, no. 7, pp. 1699–1701, 2011.

[92] L.-H. Su, X.-G. Zhang, C.-H. Mi, B. Gao, and Y. Liu, "Improvement of the capacitive performances for co-al layered double hydroxide by adding hexacyanoferrate into the electrolyte," *Phys. Chem. Chem. Phys.*, vol. 11, pp. 2195–2202, 2009.

[93] J. Lee, S. Choudhury, D. Weingarth, D. Kim, and V. Presser, "High performance hybrid energy storage with potassium ferricyanide redox electrolyte," *ACS Applied Materials & Interfaces*, vol. 8, no. 36, pp. 23 676–23 687, 2016.

[94] G. Ma, J. Li, K. Sun, H. Peng, J. Mu, and Z. Lei, "High performance solid-state supercapacitor with pvakohk3[fe(cn)6] gel polymer as electrolyte and separator," *Journal of Power Sources*, vol. 256, pp. 281–287, 2014.

[95] K. Chen, F. Liu, D. Xue, and S. Komarneni, "Carbon with ultrahigh capacitance when graphene paper meets k3fe(cn)6," *Nanoscale*, vol. 7, pp. 432–439, 2015.

[96] A. J. Bard and L. R. Faulkner, *Electrochemical Methods: Fundamentals and Applications*. wiley, Dec. 2001.

[97] S. T. Senthilkumar and R. K. Selvan, "Flexible fiber supercapacitor using biowaste-derived porous carbon," *ChemElectroChem*, vol. 2, no. 8, pp. 1111–1116, 2015.

[98] H. Pang, B. Zhang, J. Du, J. Chen, J. Zhang, and S. Li, "Porous nickel oxide nanospindles with huge specific capacitance and long-life cycle," *RSC Advances*, vol. 2, pp. 2257–2261, 2012.

[99] R. B. Rakhi, B. Ahmed, M. N. Hedhili, D. H. Anjum, and H. N. Alshareef, "Effect of postetch annealing gas composition on the structural and electrochemical properties of ti2ctx mxene electrodes for supercapacitor applications," *Chemistry of Materials*, vol. 27, no. 15, pp. 5314–5323, 2015.

[100] O. Bohlen, J. Kowal, and D. U. Sauer, "Ageing behaviour of electrochemical double layer capacitors: Part i. experimental study and ageing model," *Journal of Power Sources*, vol. 172, no. 1, pp. 468 – 475, 2007.

[101] J. Schiffer, D. Linzen, and D. U. Sauer, "Heat generation in double layer capacitors," *Journal of Power Sources*, vol. 160, no. 1, pp. 765 – 772, 2006.

[102] G. Hamid, L. Hasna, and G. Rolan, "Supercapacitor characterization and thermal modelling with reversible and irreversible heat effect," *IEEE Transactions on Power Electronics*, vol. 26, no. 11, pp. 3402–3409, 2011.

[103] M. A. Sakka, H. Gualous, J. V. Mierlo, and H. Culcu, "Thermal modeling and heat management of supercapacitor modules for vehicle applications," *Journal of Power Sources*, vol. 194, no. 2, pp. 581 – 587, 2009.

[104] W. Lajnef, J.-M. Vinassa, O. Briat, S. Azzopardi, and E. Woirgard, "Characterization methods and modelling of ultracapacitors for use as peak power sources," *Journal of Power Sources*, vol. 168, no. 2, pp. 553 – 560, 2007.

[105] R. de Levie, "On porous electrodes in electrolyte solutions: I. capacitance effects," *Electrochimica Acta*, vol. 8, no. 10, pp. 751 – 780, 1963.

[106] L. Zubieta and R. Bonert, "Characterization of double-layer capacitors for power electronics applications," *IEEE Transactions on Industry Applications*, vol. 36, pp. 199–205, 2000.

[107] K. Wang, L. Zhang, B. Ji, and J. Yuan, "The thermal analysis on the stackable supercapacitor," *Energy*, vol. 59, pp. 440 – 444, 2013.

[108] H. Gualous, H. Louahlia-Gualous, R. Gallay, and A. Miraoui, "Supercapacitor thermal characterization in transient state," 2007, pp. 722–729.

[109] A. Hijazi, P. Kreczanik, E. Bideaux, P. Venet, G. Clerc, and M. D. Loreto, "Thermal network model of supercapacitors stack," *IEEE Transactions on Industrial Electronics*, vol. 59, no. 2, pp. 979–987, 2012.

[110] D. H. Lee, U. S. Kim, C. B. Shin, B. H. Lee, B. W. Kim, and Y.-H. Kim, "Modelling of the thermal behaviour of an ultracapacitor for a 42-v automotive electrical system," *Journal of Power Sources*, vol. 175, no. 1, pp. 664 – 668, 2008.

[111] A. A. Pesaran and M. Keyser, "Thermal characteristics of selected ev and hev batteries," in *Sixteenth Annual Battery Conference on Applications and Advances. Proceedings of the Conference (Cat. No.01TH8533)*, 2001.

[112] P. Guillemet, C. Pascot, and Y. Scudeller, "Compact thermal modeling of electric double-layer-capacitors," in *2008 14th International Workshop on Thermal Inveatigation of ICs and Systems*, 2008, pp. 118–122.

[113] H. Wang and L. Pilon, "Physical interpretation of cyclic voltammetry for measuring electric double layer capacitances," *Electrochimica Acta*, vol. 64, pp. 130 – 139, 2012.

[114] A. d Entremont and L. Pilon, "First-principles thermal modeling of electric double layer capacitors under constant-current cycling," *Journal of Power Sources*, vol. 246, pp. 887 – 898, 2014.

[115] A. d'Entremont and L. Pilon, "First-principles thermal modeling of electric double layer capacitors under constant-current cycling," *Journal of Power Sources*, vol. 246, pp. 887 – 898, 2014.

[116] A. L. d Entremont and L. Pilon, "Thermal effects of asymmetric electrolytes in electric double layer capacitors," *Journal of Power Sources*, vol. 273, pp. 196 – 209, 2015.

[117] A. L. d'Entremont and L. Pilon, "Thermal effects of asymmetric electrolytes in electric double layer capacitors," *Journal of Power Sources*, vol. 273, pp. 196 – 209, 2015.

[118] K. Maize, A. Kundu, G. Xiong, K. Saviers, T. S. Fisher, and A. Shakouri, "Electroreflectance imaging of gold-h3po4 supercapacitors. part i: experimental methodology," *Analyst*, vol. 141, pp. 1448–1461, 2016.

[119] K. R. Saviers, A. Kundu, K. Maize, A. Shakouri, and T. S. Fisher, "Electroreflectance imaging of gold-h3po4 supercapacitors. part ii: microsupercapacitor ageing characterization," *Analyst*, vol. 141, pp. 1462–1471, 2016.

[120] P. Guillemet, Y. Scudeller, and T. Brousse, "Multi-level reduced-order thermal modeling of electrochemical capacitors," *Journal of Power Sources*, vol. 157, no. 1, pp. 630 – 640, 2006.

[121] H. Gualous, H. Louahlia-Gualous, R. Gally, and A. Miraoui, "Supercapacitor thermal modeling and characterization in transient state for industrial applications," *IEEE Transactions on Industry Applications*, vol. 45, no. 3, pp. 1035–1044, 2009.

[122] O. Bohlen, J. Kowal, and D. U. Sauer, "Ageing behaviour of electrochemical double layer capacitors: Part ii. lifetime simulation model for dynamic applications," *Journal of Power Sources*, vol. 173, no. 1, pp. 626 – 632, 2007.

[123] "Epcos: Ultracaptm double layer capacitors, a new energy storage device for peak power applications, product profile," 2002.

[124] J. R. Miller, "Electrochemical capacitor thermal management issues at high-rate cycling," *Electrochimica Acta*, vol. 52, no. 4, pp. 1703 – 1708, 2006.

[125] O. Munteshari, J. Lau, A. Krishnan, B. Dunn, and L. Pilon, "Isothermal calorimeter for measurements of time-dependent heat generation rate in individual supercapacitor electrodes," *Journal of Power Sources*, vol. 374, pp. 257 – 268, 2018.

[126] C. Pascot, Y. Dandeville, Y. Scudeller, P. Guillemet, and T. Brousse, "Calorimetric measurement of the heat generated by a double-layer capacitor cell under cycling," *Thermochimica Acta*, vol. 510, no. 1, pp. 53 – 60, 2010.

[127] Y. Dandeville, P. Guillemet, Y. Scudeller, O. Crosnier, L. Athouel, and T. Brousse, "Measuring time-dependent heat profiles of aqueous electrochemical capacitors under cycling," *Thermochimica Acta*, vol. 526, no. 1, pp. 1 – 8, 2011.

[128] W.Lajnef, J.-M. Vinassa, O.Briat, and E. Woirgard, "Specification and use of pulsed current profiles for ultracapacitors power cycling," *Microelectronics Reliability*, vol. 45, pp. 1746–1749, 2005.

[129] O. S. Burheim, M. Aslan, J. S. Atchison, and V. Presser, "Thermal conductivity and temperature profiles in carbon electrodes for supercapacitors," *Journal of Power Sources*, vol. 246, pp. 160 – 166, 2014.

[130] H. Michel, "Temperature and dynamics problems of ultracapacitors in stationary and mobile applications," *Journal of Power Sources*, vol. 154, no. 2, pp. 556 – 560, 2006.

[131] J. Newman and W. Tiedemann, "Porous-electrode theory with battery applications," *AIChE Journal*, vol. 21, no. 1, pp. 25–41, 1975.

[132] C. W. Tanner, K.-Z. Fung, and A. V. Virkar, "The effect of porous composite electrode sutructure on solid oxide fuel cell performance i. theoretical analysis," *Journal of the Electrochemical Society*, vol. 144, pp. 21–30, 1997.

[133] M. W. Verbrugge and P. Liu, "Microstructural analysis and mathematical modeling of electric double-layer supercapacitors," *Journal of the Electrochemical Society*, vol. 152, pp. D79–87.

[134] V. Srinivasan and J. W. Weidner, "Mathematical modeling of electrochemical capacitors," *Journal of the Electrochemical Society*, vol. 146, pp. 1650–1658, 1999.

[135] C. Lin, J. A. Ritter, B. N. Popov, and R. E. White, "A mathematical model of an electrochemical capacitor with double-layer anf faradaic processes," *Journal of the Electrochemical Society*, vol. 146, pp. 3168–3175, 1999.

[136] H. Kim and B. N. Popov, "A mathematical model of oxide/carbon composite electrode for supercapacitors," *Journal of the Electrochemical Society*, vol. 150, pp. A1153–A1160, 2003.

[137] H.-J. Liu, W.-J. Cui, L.-H. Jin, C.-X. Wang, and Y.-Y. Xia, "Preparation of three-dimensional ordered mesoporous carbon sphere arrays by a two-step templating route and their application for supercapacitors," *J. Mater. Chem.*, vol. 19, pp. 3661–3667, 2009.

[138] C. Vix-Guterl, S. Saadallah, K. Jurewicz, E. Frackowiak, M. Reda, J. Parmentier, J. Patarin, and F. Beguin, "Supercapacitor electrodes from new ordered porous carbon materials obtained by a templating procedure," *Materials Science and Engineering: B*, vol. 108, no. 1, pp. 148 – 155, 2004.

[139] D. A. G. Bruggeman, "Calculation of different physical constants of heterogeneous substances. i. dielectric constants and conductivities of the mixed bodies of isotropic substances," *Annalen der Physik*, vol. 416, no. 7, pp. 636–664, 1935.

[140] F.A.L.Dullien, *Porous media: fluid transport and pore structure.* San Diego : Academic Press, 1992.

[141] M. Kroupa, G. J.Offer, and J. Kosek, "Modelling of supercapacitors: Factors influencing performance," *Journal of the Electrochemical Society*, vol. 163, pp. A2475–A2487, 2016.

[142] M. Frivaldsky, J. Cuntala, and P. Spanik, "Simple and accurate thermal simulation model of supercapacitor suitable for development of module solutions," *International Journal of Thermal Sciences*, vol. 84, no. Supplement C, pp. 34 – 47, 2014.

[143] S. G. P. Jr. and L. L. Macomber, "Predicting operating temperature and expected lifetime of aluminum-electrolytic bus capacitors with thermal modeling," *Powersystems*, 1999.

[144] A. Pandolfo and A. Hollenkamp, "Carbon properties and their role in supercapacitors," *Journal of Power Sources*, vol. 157, no. 1, pp. 11 – 27, 2006.

[145] L. L. Zhang and X. Zhao, "Carbon-based materials as supercapacitor electrodes," *Chem. Soc. Rev.*, vol. 38, pp. 2520–2531, 2009.

[146] M. W. Verbrugge, D. R. Baker, and B. J. Koch, "Mathematical modeling of high-power-density insertion electrodes for lithium ion batteries," *Journal of Power Sources*, vol. 110, no. 2, pp. 295 – 309, 2002.

[147] V. Srinivasan and J. W. Weidner, "Mathematical modeling of electrochemical capacitors," *Journal of the Electrochemical Society*, vol. 146, pp. 1650–1658, 1999.

[148] A. Nieder, "Miniature stereo radio transmitter for simultaneous recording of multiple single-neuron signals from behaving owls," *Journal of Neuroscience Methods*, vol. 101, no. 2, pp. 157–164, 2000.

[149] P. Mohseni, K. Najafi, S. J. Eliades, and X. Wang, "Wireless multichannel biopotential recording using an integrated FM telemetry circuit," *IEEE Transactions on Neural Systems and Rehabilitation Engineering*, vol. 13, no. 3, pp. 263–271, 2005.

[150] M. Hautefeuille, C. O'Mahony, B. O'Flynn, K. Khalfi, and F. Peters, "A MEMS-based wireless multisensor module for environmental monitoring," *Microelectronics Reliability*, vol. 48, no. 6, pp. 906–910, 2008.

[151] G. Xiong, C. Meng, R. G. Reifenberger, P. P. Irazoqui, and T. S. Fisher, "A review of graphene-based electrochemical microsupercapacitors," pp. 30–51, 2014.

[152] G. Xiong, C. Meng, R. G. Reifenberge, P. P. Irazoqui, and T. S. Fisher, "Graphitic Petal Micro-Supercapacitor Electrodes for Ultra-High Power Density," *Energy Technology*, vol. 2, no. 11, pp. 897–905, 2014.

[153] B. O. Seraphin and R. B. Hess, "Franz-keldysh effect above the fundamental edge in germanium," *Phys. Rev. Lett.*, vol. 14, pp. 138–140, 1965.

[154] K. L. Shaklee, F. H. Pollak, and M. Cardona, "Electroreflectance at a semiconductor-electrolyte interface," *Phys. Rev. Lett.*, vol. 15, pp. 883–885, 1965.

[155] J. Feinleib, "Electroreflectance in metals," *Physical Review Letters*, vol. 16, no. 26, pp. 1200–1202, 1966.

[156] A. Prostak and W. N. Hansen, "Electroreflectance in metals," *Phys. Rev.*, vol. 160, pp. 600–601, 1967.

[157] W. Anderson and W. Hansen, "Electroreflectance and conductance," *Journal of Electroanalytical Chemistry and Interfacial Electrochemistry*, vol. 47, no. 2, pp. 229 – 243, 1973.

[158] W. N. Hansen and A. Prostak, "Electromodulation of the optical properties of gold," *Phys. Rev.*, vol. 174, pp. 500–503, Oct 1968.

[159] P. Rodriguez and M. T. M. Koper, "Electrocatalysis on gold," *Phys. Chem. Chem. Phys.*, vol. 16, pp. 13 583–13 594, 2014.

[160] E. Castillejos, R. Bacsa, A. Guerrero-Ruiz, I. Rodriguez-Ramos, L. Datas, and P. Serp, "Catalytic activity of gold supported on zno tetrapods for the preferential oxidation of carbon monoxide under hydrogen rich conditions," *Nanoscale*, vol. 3, pp. 929–932, 2011.

[161] H. Chen, L. Shao, Q. Li, and J. Wang, "Gold nanorods and their plasmonic properties," *Chem. Soc. Rev.*, vol. 42, pp. 2679–2724, 2013.

[162] S. Munteanu, J. P. Roger, Y. Fedala, F. Amiot, C. Combellas, G. Tessier, and F. Kanoufi, "Mapping fluxes of radicals from the combination of electrochemical activation and optical microscopy," *Faraday Discuss.*, vol. 164, pp. 241–258, 2013.

[163] J. C. Abanulo, R. D. Harris, A. K. Sheridan, J. S. Wilkinson, and P. N. Bartlett, "Waveguide surface plasmon resonance studies of surface reactions on gold electrodes," *Faraday Discuss.*, vol. 121, pp. 139–152, 2002.

[164] J. J. Kakkassery, J.-P. Abid, M. Carrara, and D. J. Fermin, "Electrochemical and optical properties of two dimensional electrostatic assembly of au nanocrystals," *Faraday Discuss.*, vol. 125, pp. 157–169, 2004.

[165] T. Takamura, K. Takamura, and E. Yeager, "Specular reflectivity studies of the adsorption of halide anions on gold electrodes in 0.2 M HClO4," *J. Electroanal. Chem. Interfacial Electrochem.*, vol. 29, no. 2, pp. 279–291, 1971.

[166] J. D. E. McIntyre and D. M. Kolb, "Specular reflection spectroscopy of electrode surface films," in *Symposia of the Faraday Society*, vol. 4. Royal Society of Chemistry, 1970, pp. 99–113.

[167] M. Stedman, "Effect of the electrical double layer on the reflectance and ellipsometry of electrolyte-conductor interfaces," *Chemical Physics Letters*, vol. 2, no. 7, pp. 457–460, 1968.

[168] A. Bewick and J. Robinson, "Optical studies of the electrode-electrolyte solution interphase using reflectance methods," *Surface Science*, vol. 55, pp. 349–361, 1976.

[169] M. Cardona, K. L. Shaklee, and F. H. Pollak, "Electroreflectance at a Semiconductor-Electrolyte Interface," *Physical Review*, vol. 154, no. 3, pp. 696–720, Feb. 1967.

[170] B. SERAPHIN, "ELECTROREFLECTANCE IN SURFACE PHYSICS," *Le Journal de Physique Colloques*, vol. 31, no. C1, pp. C1–123, 1970.

[171] H. Meinhold and G. Weiser, "Modulation Spectroscopy on MoS2, and MoSe2," *physica status solidi (b)*, vol. 73, no. 1, pp. 105–115, 1976.

[172] A. Chaparro, P. Salvador, and A. Mir, "The scanning microscope for semiconductor characterization: photocurrent, photovoltage and electrolyte electroreflectance imaging at the n-MoSe2/I interface," *Journal of Electroanalytical Chemistry*, vol. 424, no. 1-2, pp. 153–157, Mar. 1997.

[173] K. Saviers, A. Kundu, K. Maize, A. Shakouri, and T. S. Fisher, "Electroreflectance imaging of supercapacitors. part ii: Microsupercapacitor ageing characterization," *Analyst, in peer review*, 2015.

[174] Y. G. Majid Beidaghi, "Capacitive energy storage in micro-scale devices: recent advances in design and fabrication of micro- supercapacitors," *Energy & Environmental Science*, vol. 7, pp. 867–884, 2014.

[175] S. Ju, O. Kading, Y. Leung, S. Wong, and K. Goodson, "Short-timescale thermal mapping of semiconductor devices," *IEEE Electron Device Letters*, vol. 18, no. 5, pp. 169–171, 1997.

[176] G. Tessier, S. Hole, and D. Fournier, "Quantitative thermal imaging by synchronous thermoreflectance with optimized illumination wavelengths," *Applied Physics Letters*, vol. 78, no. 16, p. 2267, 2001.

[177] M. Burzo, P. Komarov, and P. Raad, "Noncontact transient temperature mapping of active electronic devices using the thermoreflectance method," *IEEE Transactions on Components and Packaging Technologies*, vol. 28, no. 4, pp. 637–643, 2005.

[178] K. Maize, J. Christofferson, and A. Shakouri, "Transient Thermal Imaging Using Thermoreflectance," *2008 Twenty-fourth Annual IEEE Semionductor Thermal Measurement and Management Symposium*, pp. 55–58, 2008.

[179] Y. Ezzahri, J. Christofferson, G. Zeng, and A. Shakouri, "Short time transient thermal behavior of solid-state microrefrigerators," *Journal of Applied Physics*, vol. 106, no. 11, p. 114503, 2009.

[180] G. Tessier, M.-L. Polignano, S. Pavageau, C. Filloy, D. Fournier, F. Cerutti, and I. Mica, "Thermoreflectance temperature imaging of integrated circuits: calibration technique and quantitative comparison with integrated sensors and simulations," *Journal of Physics D: Applied Physics*, vol. 39, pp. 4159–4166, 2006.

[181] V. Moreau, G. Tessier, F. Raineri, M. Brunstein, A. Yacomotti, R. Raj, I. Sagnes, A. Levenson, and Y. D. Wilde, "Transient thermoreflectance imaging of active photonic crystals," *Applied Physics Letters*, vol. 96, no. 2010, pp. 3–6, 2010.

[182] B. Vermeersch, J. Christofferson, K. Maize, A. Shakouri, and G. De Mey, "Time and frequency domain CCD-based thermoreflectance techniques for high-resolution transient thermal imaging," *Annual IEEE Semiconductor Thermal Measurement and Management Symposium*, pp. 228–234, 2010.

[183] J. McIntyre and D. Aspnes, "Differential reflection spectroscopy of very thin surface films," *Surface Science*, vol. 24, no. 2, pp. 417 – 434, 1971.

[184] H. Ehrenreich and H. Philipp, "Optical properties of Ag and Cu," *Phys. Rev.*, vol. 128, no. 4, pp. 1622–1629, 1962.

[185] B. Conway, V. Birss, and J. Wojtowicz, "The role and utilization of pseudocapacitance for energy storage by supercapacitors," *Journal of Power Sources*, vol. 66, no. 1, pp. 1–14, 1997.

[186] J. E. B. Randles, "Kinetics of rapid electrode reactions," *Discuss. Faraday Soc.*, vol. 1, pp. 11–19, 1947.

[187] W. Gao, N. Singh, L. Song, Z. Liu, A. Reddy, L. Ci, R. Vajtai, Q. Zhang, B. Wei, and P. Ajayan, "Direct laser writing of micro-supercapacitors onhydrated graphite oxide films," *Nature Nanotechnology*, vol. 6, pp. 496–500, Aug 2011.

[188] H. J. Goldsmid and R. W. Douglas, "The use of semiconductors in thermoelectric refrigeration," *British Journal of Applied Physics*, vol. 5, no. 11, p. 386, 1954.

[189] Y. Sakuraba, K. Hasegawa, M. Mizuguchi, T. Kubota, S. Mizukami, T. Miyazaki, and K. Takanashi, "Anomalous nernst effect in l1 0 -fept/mnga thermopiles for new thermoelectric applications," *Applied Physics Express*, vol. 6, no. 3, p. 033003, 2013.

[190] E. H. Hwang, E. Rossi, and S. Sarma, "Theory of thermopower in two-dimensional graphene," *Physical Review B*, vol. 80, p. 235415, 2009.

[191] K. Novoselov, A. K. Geim, S. Morozov, D. Jiang, M. Katsnelson, I. Grigorieva, S. Dubonos, and A. Firsov, "Two-dimensional gas of massless dirac fermions in graphene," *Nature*, vol. 438, no. 7065, pp. 197–200, 2005.

[192] P. Dollfus, V. H. Nguyen, and J. Saint-Martin, "Thermoelectric effects in graphene nanostructures," *Journal of Physics: Condensed Matter*, vol. 27, no. 13, p. 133204, 2015.

[193] N. Xiao, X. Dong, L. Song, D. Liu, Y. Tay, S. Wu, L.-J. Li, Y. Zhao, T. Yu, H. Zhang, W. Huang, H. H. Hng, P. M. Ajayan, and Q. Yan, "Enhanced thermopower of graphene films with oxygen plasma treatment," *ACS Nano*, vol. 5, no. 4, pp. 2749–2755, 2011.

[194] C. R. Wang, W. S. Lu, L. Hao, W. L. Lee, T.-K. Lee, F. Lin, I. C. Cheng, and J. Z. Chen, "Enhanced thermoelectric power in dual-gated bilayer graphene," *Physical Review Letters*, vol. 107, p. 186602, 2011.

[195] Y. M. Zuev, W. Chang, and P. Kim, "Thermoelectric and magnetothermoelectric transport measurements of graphene," *Physical Review Letters*, vol. 102, p. 096807, 2009.

[196] P. Wei, W. Bao, Y. Pu, C. N. Lau, and J. Shi, "Anomalous thermoelectric transport of dirac particles in graphene," *Physical Review Letters*, vol. 102, p. 166808, 2009.

[197] J. G. Checkelsky and N. P. Ong, "Thermopower and nernst effect in graphene in a magnetic field," *Physical Review B*, vol. 80, p. 081413, 2009.

[198] X. Liu, D. Wang, P. Wei, L. Zhu, and J. Shi, "Effect of carrier mobility on magnetothermoelectric transport properties of graphene," *Physical Review B*, vol. 86, p. 155414, 2012.

[199] D. Wang and J. Shi, "Effect of charged impurities on the thermoelectric power of graphene near the dirac point," *Physical Review B*, vol. 83, p. 113403, 2011.

[200] A. V. Babichev, V. E. Gasumyants, and V. Y. Butko, "Resistivity and thermopower of graphene made by chemical vapor deposition technique," *Journal of Applied Physics*, vol. 113, no. 7, p. 076101, 2013.

[201] Y. Nam, J. Sun, N. Lindvall, S. J. Yang, C. R. Park, Y. W. Park, and A. Yurgens, "Unusual thermopower of inhomogeneous graphene grown by chemical vapor deposition," *Applied Physics Letters*, vol. 104, no. 2, p. 021902, 2014.

[202] L. Zhu, R. Ma, L. Sheng, M. Liu, and D. N. Sheng, "Universal thermoelectric effect of dirac fermions in graphene," *Physical Review Letters*, vol. 104, p. 076804, 2010.

[203] T. Löfwander and M. Fogelström, "Impurity scattering and mott's formula in graphene," *Physical Review B*, vol. 76, p. 193401, 2007.

[204] Y. Xing, Q. F. Sun, and J. Wang, "Nernst and seebeck effects in a graphene nanoribbon," *Physical Review B*, vol. 80, p. 235411, 2009.

[205] V. Ugarte, V. Aji, and C. M. Varma, "Electric, thermoelectric, and thermal conductivities of graphene with short-range unitary and charged impurities," *Physical Review B*, vol. 84, p. 165429, 2011.

[206] A. P. Hinz, S. Kettemann, and E. R. Mucciolo, "Quantum corrections to thermopower and conductivity in graphene," *Physical Review B*, vol. 89, p. 075411, 2014.

[207] X. Z. Yan and C. S. Ting, "Nernst effect of dirac fermions in graphene under a weak magnetic field," *Physical Review B*, vol. 81, p. 155457, 2010.

[208] T. Stauber, N. M. R. Peres, and F. Guinea, "Electronic transport in graphene: A semiclassical approach including midgap states," *Physical Review B*, vol. 76, p. 205423, 2007.

[209] N. M. R. Peres, J. M. B. L. d. Santos, and T. Stauber, "Phenomenological study of the electronic transport coefficients of graphene," *Physical Review B*, vol. 76, p. 073412, 2007.

[210] G. Sharma, P. Goswami, and S. Tewari, "Nernst and magneto-thermal conductivity in a lattice model of weyl fermions," *arXiv preprint arXiv:1507.05606*, 2015.

[211] N. A. Sinitsyn, A. H. MacDonald, T. Jungwirth, V. K. Dugaev, and J. Sinova, "Anomalous hall effect in a two-dimensional dirac band: The link between the kubo-streda formula and the semiclassical boltzmann equation approach," *Physical Review B*, vol. 75, p. 045315, 2007.

[212] J. Moore and R. Graves, "The ettingshausen-nernst coefficient and transport properties of alumel from 200 to 473 k," *Journal of Physics and Chemistry of Solids*, vol. 41, no. 2, pp. 129 – 133, 1980.

[213] O. C. Choiniere, R. Daou, F. Laliberte, D. LeBoeuf, N. Doiron Leyraud, J. Chang, J. Yan, J. Cheng, J. Zhou, J. B. Goodenough, S. Pyon, T. Takayama, H. Takagi, Y. Tanaka, and L. Taillefer, "Enhancement of the nernst effect by stripe order in a high-tc superconductor," *Nature*, vol. 458, pp. 743–745, 2009.

[214] K. I. Bolotin, K. J. Sikes, J. Hone, H. L. Stormer, and P. Kim, "Temperature-dependent transport in suspended graphene," *Physical Review Letters*, vol. 101, p. 096802, 2008.

[215] A. K. Geim and K. S. Novoselov, "The rise of graphene," *Nature Materials*, vol. 6, pp. 183–191, 2007.

[216] N. Ashcroft and N. Mermin, *Solid State Physics.* Saunders College, 1976.

[217] J. H. Chen, C. Jang, S. Xiao, M. Ishigami, and M. S. Fuhrer, "Intrinsic and extrinsic performance limits of graphene devices on sio2," *Nature Nanotechnology*, vol. 3, pp. 206–209, 2008.

[218] S. Adam, E. H. Hwang, V. M. Galitski, and S. D. Sarma, "A self-consistent theory for graphene transport," *Proceedings of the National Academy of Sciences*, vol. 104, no. 47, pp. 18 392–18 397, 2007.

[219] Y. W. Tan, Y. Zhang, K. Bolotin, Y. Zhao, S. Adam, E. H. Hwang, S. Das Sarma, H. L. Stormer, and P. Kim, "Measurement of scattering rate and minimum conductivity in graphene," *Physical Review Letters*, vol. 99, p. 246803, 2007.

[220] A. A. Patel and S. Mukerjee, "Thermoelectricity in graphene: Effects of a gap and magnetic fields," *Physical Review B*, vol. 86, p. 075411, 2012.

[221] W. Zhu, V. Perebeinos, M. Freitag, and P. Avouris, "Carrier scattering, mobilities, and electrostatic potential in monolayer, bilayer, and trilayer graphene," *Physical Review B*, vol. 80, p. 235402, Dec 2009.

[222] K. Sugihara, K. Kawamura, and T. Tsuzuku, "Temperature dependence of the average mobility in graphite," *Journal of the Physical Society of Japan*, vol. 47, no. 4, pp. 1210–1215, 1979.

[223] S. Cho and M. S. Fuhrer, "Charge transport and inhomogeneity near the minimum conductivity point in graphene," *Physical Review B*, vol. 77, p. 081402, 2008.

[224] Y. Wang, Z. A. Xu, T. Kakeshita, S. Uchida, S. Ono, Y. Ando, and N. P. Ong, "Onset of the vortexlike nernst signal above T_c in $la_{2-x}sr_xcuo_4$ and $bi_2sr_{2-y}la_ycuo_6$," *Physical Review B*, vol. 64, p. 224519, 2001.

[225] L. Hao and T. K. Lee, "Thermopower of multilayer graphene," *Physical Review B*, vol. 82, p. 245415, 2010.

[226] F. Mazzamuto, V. Hung Nguyen, Y. Apertet, C. Caër, C. Chassat, J. S. Martin, and P. Dollfus, "Enhanced thermoelectric properties in graphene nanoribbons by resonant tunneling of electrons," *Physical Review B*, vol. 83, p. 235426, 2011.

[227] H. J. Goldsmid and J. W. Sharp, "Estimation of the thermal band gap of a semiconductor from seebeck measurements," *Journal of Electronic Materials*, vol. 28, no. 7, pp. 869–872, 1999.

[228] G. Ma, M. Dong, K. Sun, E. Feng, H. Peng, and Z. Lei, "A redox mediator doped gel polymer as an electrolyte and separator for a high performance solid state supercapacitor," *Journal of Materials Chemistry A*, vol. 3, pp. 4035–4041, 2015.